INVESTIGATION OF DISEASE MECHANISMS AND SCREENING FOR TREATMENTS IN BETA-PROPELLER PROTEIN-ASSOCIATED NEURODEGENERATION (BPAN)

A thesis submitted to University College London

for the degree of Doctor of Philosophy

Dr Apostolos Papandreou

University College London

MRC Laboratory for Molecular Cell Biology

January 2020

Table of Contents

Acknowledgements

I am very grateful to my two Co-Primary Supervisors for all their help, support and mentorship during my PhD. Firstly, Professor Robin Ketteler, my named Primary Supervisor, was always supportive, helpful and understanding. Both his knowledge base and guidance were invaluable for me and sometimes I feel I could not have completed this work without him. Secondly, I have to acknowledge Professor Manju A Kurian, who was named Secondary Supervisor but, in every way, also contributed to this project as a Primary Supervisor and equally to Robin Ketteler. I cannot emphasise enough how useful her guidance and expertise were in completing this project. Moreover, she was always open and honest to me, there when needed, and helped me enormously to navigate efficiently through some challenging times in the lab.

I also need to acknowledge Professor Paul Gissen at this stage, who was initially my Primary Supervisor when I went Out of Programme for Research in 2015 and instrumental in this project's conception and design. In fact, it was both Manju Kurian and Paul Gissen who helped guide me in my very initial steps outside the realms of pure clinical medicine, meet Robin Ketteler and build a Research Fellowship proposal that eventually got funded. I am grateful to him for this, but also for being my mentor over the last 5 years.

This brings me to the funders of this work, the British Paediatric Neurology Association (BPNA) and Action Medical Research. I am truly humbled and immensely honoured to have received a Research Training Fellowship for this work; I truly hope that my work lives up to their expectations and helps their long-term goals of alleviating childhood disability and improving quality of life for patients.

And of course, my patients and their families were by far the biggest contributors in this work. I cannot put into words how grateful I am for their help, support and contributions to this project. I would not have achieved anything without them. Seeing them willingly and selflessly participating in this work by visiting the hospital and agreeing to give samples, even knowing that there is a chance they might never get to directly benefit from it, still gives me fuel to carry on working on/ studying this disorder until we can achieve some tangible improvement in their care.

Moving on, I'd like to acknowledge my team members in the Ketteler and Kurian labs, who effectively became my second family over the last few years and supported me through fun, stimulating, but also occasionally difficult and stressful times. I have to thank each and every one of them for being helpful and kind and always keen to assist with trouble shooting or whatever else

needed. People who have especially contributed to this work are mentioned below in alphabetical order:

Alexander Agrotis (Ketteler lab), who kindly taught be everything I know about Western Blots and helped in performing the drug screen (Labcyte Echo drug dispensing and plate Imaging on the PerkinElmer Opera Phenix) in the screening lab.

Christin Luft (Ketteler lab), who was always very supportive and also helped design and automate other drug screening steps (fixing, washing, immunostaining etc) on the BioMek Station.

Dimitri Budinger (Kurian lab), who kindly helped out with performing a large bulk of the qRT PCR experiments for Day 65 neuronal characterisation.

Janos Kriston-Vizi, but also Tanya Singh (Bioinformaticians at the LMCB), for their immense help with data analysis (drug screening and RNASeq).

Katy Barwick (Kurian lab), who kindly performed a large bulk of the genomic and cDNA sequencing on iPSC lines and subsequent relevant analysis.

Serena Barral (Kurian lab), who guided me through the iPSC landscape with her invaluable knowledge and expertise, and to whom everyone always turns for a solution when cells are 'misbehaving'.

Other non-UCL collaborators were also instrumental for this project. Firstly, the team at Oregon Health and Science University, Portland, USA, and above all Penny Hogarth, Susan Hayflick and Suh Young Jeong, who helped tremendously by sharing patient fibroblasts and allowing us to use them for downstream iPSC reprogramming. Additionally, the Vallier iPSC lab in Cambridge, UK, and mainly An-Sofie Lenaerts, who kindly performed iPSC reprogramming for a few lines and also the CRISPR/Cas9 mediated genome editing. My collaborators' efforts and input clearly add value to this work.

Last but not least, I would like to acknowledge my wife, Sofia, who has stood by me over all these years and helped me achieve my goals. She has always understood and fully supported my need to find answers to (what I consider to be) fundamental questions; she also helped me through some difficult times when no experiment was working in the lab and everything was 'my fault' (an essential process that every PhD student has to go through, it seems). I am really grateful for her help, support and friendship.

Abstract

Introduction. BPAN is a monogenic form of neurodegeneration, associated with brain iron accumulation and early-onset parkinsonism. It is caused by mutations in *WDR45*, an X-linked gene with role in early autophagy. The mechanisms linking autophagy, iron load and neurodegeneration are poorly understood, while there are no effective treatments for BPAN. I aimed to address these issues by developing a patient-derived, induced pluripotent stem cell (iPSC)-based dopaminergic neuronal cell model of the disease.

Methods. 3 paediatric patient-derived iPSC lines, 2 age-matched controls and 2 'isogenic controls' (generated via CRISPR/Cas9-mediated mutation correction in 2 BPAN lines) were differentiated into dopaminergic neurons using a 65-day protocol. High content imaging assays were developed for a drug screen, looking for small molecules that reverse patient-specific cellular phenotypes.

Results. At Day 65 there is absence of WDR45 protein in patient lines. RNA sequencing reveals differential gene expression in 190 genes when comparing patients to controls. When plated on multi-well plates at low density, BPAN ventral midbrain progenitors (Day 11 of differentiation) exhibit defective autophagy, with fewer LC3 puncta per cell forming compared to controls. This assay was used to perform a drug screen using the FDA-approved Prestwick library (1,280 compounds) and a series of novel autophagy activators. Some compound hits significantly enhance autophagy in all tested lines and show promise for further development.

Conclusion. I have used a patient-derived dopaminergic model of BPAN for disease modelling and also as a platform for high content imaging-based drug screening. My work contributes towards identifying novel, effective treatments for BPAN, and increases our understanding of the link between autophagy and neurodegeneration.

Impact Statement

There is urgent clinical need to improve disease understanding and develop novel therapies for Beta-Propeller Protein-Associated Neurodegeneration (BPAN), a treatment-resistant, life-limiting disorder. Through this work, I have generated a new *in vitro* patient-derived dopaminergic neuronal model of the disease. The model is firstly of significance as it has provided an opportunity to elucidate disease mechanisms in BPAN. Importantly, understanding monogenic rare disorders such as BPAN can also give us insight to other similar, more common neurodegenerative conditions such as Parkinson's disease. I also performed drug screening to find new, more effective, disease-specific treatments for affected patients. I have already identified some promising compounds that need further testing but overall could prove to be of therapeutic benefit in the future. In summary, my translational work using a patient-derived model of BPAN has the potential to benefit patients in the longer term, by improving their quality of life and long-term survival.

Declaration

I, Apostolos Papandreou, hereby declare that the work presented in this thesis is my own. Where information has been derived through contribution from other sources, I confirm that this has been appropriately indicated in the thesis.

1. Introduction

1.1. Beta-Propeller Protein-Associated Neurodegeneration (BPAN)- An Overview

Beta-Propeller Protein-Associated Neurodegeneration (BPAN) is one of the most recently described subtypes of Neurodegeneration with Brain Iron Accumulation (NBIA), an umbrella term used to describe conditions associated with neurological regression and excess amounts of iron abnormally accumulating in the central nervous system (CNS) (Meyer, Kurian et al. 2015, Hayflick, Kurian et al. 2018). BPAN is caused by mutations in *WDR45* (WD repeat domain 45) (Haack, Hogarth et al. 2012, Hayflick, Kruer et al. 2013, Saitsu, Nishimura et al. 2013), which is located on Xp11.23 and also known as *WIPI4* (WD repeat domain phosphoinositide-interacting protein 4) (Saitsu, Nishimura et al. 2013, Zhao, Sun et al. 2015). The encoded protein has a role in the early stages of autophagy, a cellular innate homeostatic process whereby damaged or redundant cargo (protein aggregates, damaged organelles etc) is engulfed in a double-shaped membrane structure (the autophagosome) in response to various stresses and/or stimuli and delivered to the lysosome for degradation and recycling (Saitsu, Nishimura et al. 2013, Proikas-Cezanne, Takacs et al. 2015, Bakula, Muller et al. 2017). Clinically, BPAN is characterised by two distinct stages; 1) a diverse set of neurodevelopmental issues in childhood and 2) neurodegeneration, dementia and prominent parkinsonism in adolescence/ early adulthood. Initially, and before *WDR45* was discovered as the causative gene, this two-stage clinical course had resulted in the frequent use of the term SENDA (static encephalopathy with neurodegeneration in adulthood), which is now no longer favoured (Schneider and Bhatia 2010, Hayflick, Kruer et al. 2013).

Overall, BPAN is a devastating early-onset neurodegenerative condition associated with severe morbidity and mortality, and for which there are currently no available treatments. Additionally, the link between autophagy, iron metabolism and striatonigral degeneration is poorly understood. Hence, addressing these issues constitutes an urgent and unmet need for the patients and the scientific community.

WDR45 is expressed in all tissues and especially skeletal muscles (Saitsu, Nishimura et al. 2013). Moreover, dermal fibroblasts and lymphoblastoid lines from BPAN patients exhibit abnormal autophagy *in vitro* (Saitsu, Nishimura et al. 2013, Seibler, Burbulla et al. 2018). Therefore, one would hypothesise that WDR45 deficiency would lead to a multisystemic disorder. However, BPAN seems to be exclusively a neurological disease, and in fact some areas of the brain, such as the substantia nigra (SN), are much more affected than others. From a research perspective, this firstly raises the possibility that 1) WDR45/WIPI4 has a very important role in neuronal homeostasis, and/ or that 2) the protein's function is nerve tissue-specific (with other proteins compensating for the deficiency of WDR45 in other tissues) (Saitsu, Nishimura et al. 2013). Secondly, since BPAN clinically only affects the nervous system (and mainly the SN), one should consider choosing relevant neuronal models to study the disease in an appropriate/ physiologically relevant context (**Figure 1**).

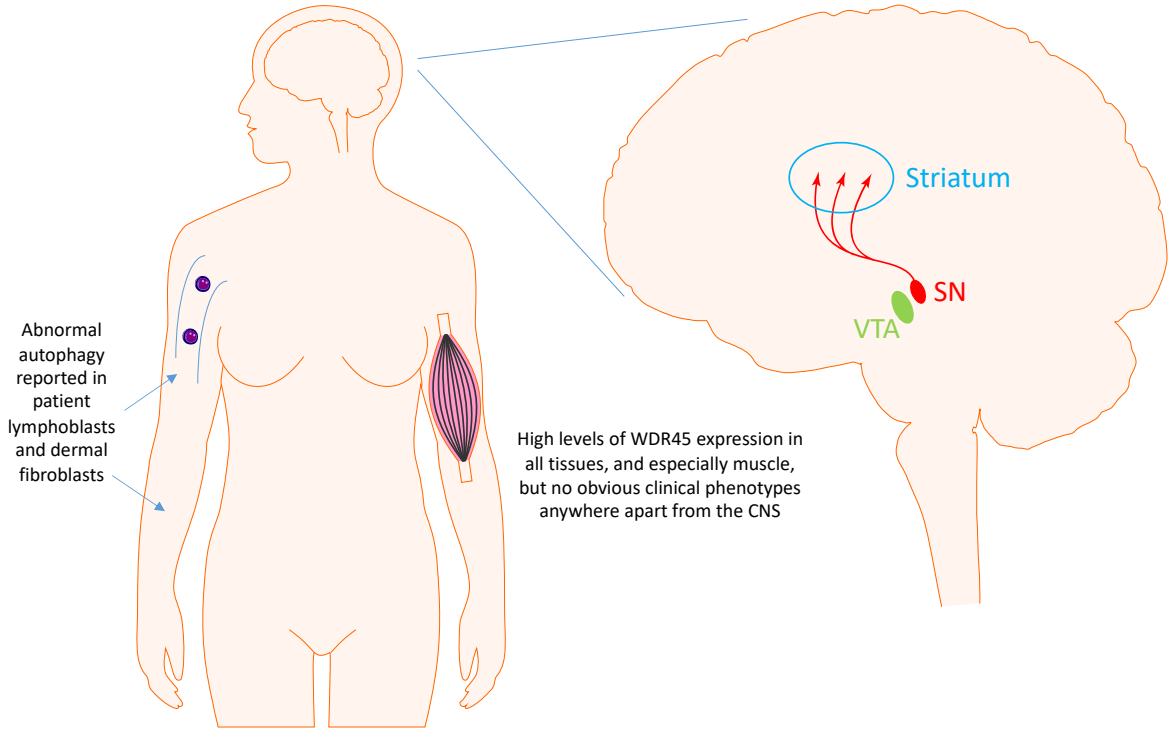

Figure 1. BPAN mainly affects the Substantia Nigra. Left: *to our best current knowledge, WDR45 deficiency leads to a disease that is almost exclusively neurological. This is despite the fact that 1) WDR45 is ubiquitously expressed in the human body and mostly in skeletal muscles and 2) cell lines from human tissues apart from the brain have been shown to have abnormal autophagy in vitro.* ***Right****: a midline sagittal view of the human brain is seen. All parts of the brain are affected in BPAN but the substantia nigra (SN) more so than others. The substantia nigra (SN) is richly populated by dopaminergic neurons that innervate the striatum (caudate nucleus, putamen) and play a major role in movement control. Parkinson's disease is characterised by SN loss of dopaminergic neurons. Finally, dopaminergic neurons are also populated in the Ventral Tegmental Area (VTA), an area relatively spared in BPAN. Due to the preferential SN involvement and prominent parkinsonian features seen in BPAN patients, studying SN dopaminergic neurons would be optimal for understanding disease mechanisms and developing new treatments. CNS= Central Nervous System.*

1.2. BPAN: Clinical, Radiological and Neuropathological phenotypes

BPAN is an X-linked disease; *WDR45* is located on the X chromosome and monoallelic mutations in females described in the literature suffice to lead to disease. BPAN primarily affects females, and male patients are only infrequently described (Haack, Hogarth et al. 2012, Hayflick, Kruer et al. 2013, Abidi, Mignon-Ravix et al. 2016, Gregory, Kurian et al. 2016, Nakashima, Takano et al. 2016, Zarate, Jones et al. 2016, Carvill, Liu et al. 2018). The reasons for this female patient preponderance are not fully understood and will be discussed in detail in a subsequent section (**Section 1.3**); however, factors such as *WDR45* somatic mosaicism (e.g. with germline mutations in males possibly being lethal *in utero*) and patterns of X Chromosome Inactivation (XCI) might contribute to this phenomenon.

Clinically, BPAN patients often present with seizures, global neurodevelopmental delay, absent or very limited expressive language and abnormal behaviours and mannerisms that resemble MECP2-like disease and/ or are referred to as 'Rett-like'(Ohba, Nabatame et al. 2014). Other early features also include sleep disturbances, ophthalmological abnormalities (such as retinal colobomas and bilateral partial retinal colobomas), as well as feeding and nutritional difficulties. During adolescence or early adulthood (mean age 25 years; range 15-37 years), patients develop dementia and a prominent movement disorder including progressive parkinsonism and dystonia (Hayflick, Kruer et al. 2013, Nishioka, Oyama et al. 2015, Gregory, Kurian et al. 2016).

1.2.1. Seizures and Epilepsy

BPAN patients frequently have epileptic seizures in childhood; often, these start as febrile seizures before becoming unprovoked (Nishioka, Oyama et al. 2015). Epilepsy often includes multiple seizure types, such as focal seizures with impaired consciousness, and generalised seizures including absence, atonic, tonic (including epileptic spasms), myoclonic, and tonic-clonic (Hayflick, Kruer et al. 2013). More recently, *WDR45* mutations have also been described as causes of Early-

Onset Infantile Epileptic Encephalopathies (EIEE), and can manifest as Lennox-Gastault or West Syndrome (Abidi, Mignon-Ravix et al. 2016, Nakashima, Takano et al. 2016, Carvill, Liu et al. 2018).

Typically, seizures often require antiepileptic drug treatment and/ or are initially difficult to control, but tend to become less marked or even resolve in adolescence or adulthood (Gregory, Kurian et al. 2016). The reason behind the seizure burden improvement with age is unclear, and more studies are warranted in order to understand the pathophysiological mechanisms for this phenomenon. However, two potential theoretical mechanisms leading to this clinical manifestation could be either a) a 'super-imposed' increased susceptibility of cortical neurons to cause seizures in childhood (Panayiotopoulos 1993, Caraballo, Aldao Mdel et al. 2011) or, conversely, b) the degeneration of epilepsy-causing cortical neurons/ networks later on in the lives of BPAN patients.

1.2.2. Speech and Language and Motor delay

Developmental delay is very common in children with BPAN and can be very severe (Carvill, Liu et al. 2018). The majority of patients have no expressive language or develop very limited language skills. Additionally, children might never achieve independent sitting or walking; those who walk are described as clumsy and have a reported broad-based or ataxic gait. Impairment of fine motor skills is also often reported and might include limited purposeful hand use reminiscent of MECP2-related disease. Overall, movement disorders are not frequently reported in childhood, although dystonia can be seen (Ohba, Nabatame et al. 2014). The more severely affected patients often exhibit extrapyramidal signs such as limb spasticity and axial hypotonia (Gregory, Kurian et al. 2016, Carvill, Liu et al. 2018).

There are rare reports of patients with less severe learning difficulties and near-normal language skills (Long, Abdeen et al. 2015). On the other hand, there are also reports of children manifesting motor and speech regression during early childhood, often after onset of difficult-to-treat epilepsy or in the context of an EIEE (Carvill, Liu et al. 2018).

1.2.3. Behavioural Issues and Autistic-like features

Children with BPAN manifest behavioural difficulties such as reduced attention span and hyperactivity (Lim, Tan et al. 2018). Additional features include lack of purposeful hand movements and hand stereotypies (e.g. midline hand-wringing) and bruxism are often reported (Hayflick, Kruer et al. 2013, Ohba, Nabatame et al. 2014). These features, sometimes paired with limited or absent speech and/or skill regression after seizure onset, or even the presence of abnormal (deep) breathing during waking hours (Gregory, Kurian et al. 2016) can lead clinicians to suspect Autism Spectrum Disorders (ASD), MECP2-related disease (Neul, Kaufmann et al. 2010), or other similar disorders (such as *CDKL5* and *FOXG1*) (Bahi-Buisson, Nectoux et al. 2008, Bahi-Buisson, Nectoux et al. 2010). Interestingly, though, children with BPAN often have good eye contact and a very friendly demeanour; hence, despite the presence of deficits in social communication and interaction, they behave differently than other children with ASD (Authors, personal observation).

1.2.4. Other Early-Onset Features (Sleep, Feeding, Ocular Abnormalities)

Sleep is very often disturbed in BPAN and this can be a very debilitating feature for both children and carers. Patients have difficulties not only in sleep initiation but also in maintaining sleep, and only sleep for short time periods. Importantly, sleep disturbances also persist in adulthood in some cases (Nishioka, Oyama et al. 2015). Sleep studies are often abnormal when performed, exhibiting shortened mean sleep latency and abnormal REM sleep, hypersomnolence, hyposomnolence, and "dance-like" movements of the extremities with sleep onset (Hayflick, Kruer et al. 2013, Nishioka, Oyama et al. 2015, Gregory, Kurian et al. 2016).

Additionally, feeding difficulties are reported in children with BPAN, often associated with texture sensitivity, gastroesophageal reflux or oropharyngeal dysfunction (with or without aspiration) in more severely affected cases. Once cognitive decline manifests and dystonia and parkinsonism become prominent after the second decade of life, feeding difficulties progressively

worsen and result in nutritional deficits and aspiration risks that often necessitate parenteral modes of feeding (Hayflick, Kruer et al. 2013, Gregory and Hayflick 2014, Gregory, Kurian et al. 2016).

Furthermore, ocular abnormalities are also reported in a proportion of patients (7 out of 23 in one cohort). These include myopia, astigmatism, optic nerve atrophy, partial retinal colobomas, retinal detachment, abnormal Visual Evoked Potentials (with increased latencies) and patchy loss of the pupillary ruff (Hayflick, Kruer et al. 2013, Gregory, Kurian et al. 2016)

Finally, no obvious muscle involvement has been described in BPAN, despite the fact that WDR45 is ubiquitously expressed and abundantly so in skeletal muscles (Saitsu, Nishimura et al. 2013). This is even more intriguing because other congenital disorders of autophagy (genetic disorders caused by mutations in autophagy-related genes) often manifest with a muscle phenotype that can be prominent (Ebrahimi-Fakhari, Saffari et al. 2016, Teinert, Behne et al. 2019). Indeed, no muscle biopsy reports in BPAN patients currently exist in the literature (which indicates that an unidentified muscle involvement in the disease cannot be excluded). Plausible explanations for this are a) that WDR45 is redundant in muscle or that its deficiency can be compensated by other proteins, b) that there is indeed a muscle phenotype but this is much less prominent than the CNS-related phenotypes, , especially in the initial stages of the disease course, and hence remains unreported/ unidentified, or c) that the brain is most vulnerable to *WDR45* mutations, but muscle-related phenotypes (and, indeed, involvement of other systems such as the liver etc) would eventually manifest if the natural history of the disease were altered and patients did not pass away so early due to CNS-related complications.

1.2.5. Neurological Regression and Prominent Parkinsonian Features

After a fairly 'stable' disease phase as described above, BPAN patients develop new-onset cognitive decline and, additionally, a prominent movement disorder consisting mainly of dystonia and parkinsonism. Dystonia is common, typically starting in the upper extremities. Symptomatology often improves with levodopa treatment for a period of time but unfortunately this effect is short-

lived, and the drug frequently has to be discontinued within a few years due to disabling dyskinesias. Regarding parkinsonian features, bradykinesia, rigidity and freezing of gait are prominent, whereas tremor is not so frequently encountered compared to other forms of parkinsonism. The age of onset of this neurological degeneration has been reported to be at a mean age of 25 years (range 15-37 years) by one study, while other authors also reported a similar age range of 29-39 years (Hayflick, Kruer et al. 2013, Nishioka, Oyama et al. 2015).

1.2.6. End Stages of Disease and the Need for Natural History Studies in BPAN

From that point onwards, there is an overall progressive decline in cognition and function. There is currently limited data regarding the rate of disease progression, which often varies from patient to patient. However, patients who previously had the ability to walk become wheelchair- or bed-bound, and there is also a progressive loss of (the already limited) expressive language that develops into severe dementia in early stages (Gregory, Kurian et al. 2016). Secondary complications from the movement disorder such as dysphagia, inadequate nutrition and respiratory infections also develop. There is also limited data on associated mortality. A study previously reported that death occurs around the 3rd to 5th decade of life, approximately 11 years after the beginning of their cognitive decline, with severe parkinsonism-related dysphagia and aspiration pneumonia listed as causes(Hayflick, Kruer et al. 2013).

With more and more BPAN patients being diagnosed through next generation sequencing modalities, and with the broadening of the phenotypic spectrum this is likely to result in, detailed studies on the natural history of the disease are a research priority for both patients and scientific community. Such information would be useful not only for prognostication and counselling in the clinic but also in order to assess the efficacy of any novel therapeutic approaches that might become available in the future. Reassuringly, such a large-scale natural history study (with both a prospective and retrospective arm) is currently being conducted by the Oregon Health and Science University (http://nbiacure.org/our-research/in-the-clinic/bpanready/) and aims to 1) understand how

symptoms and signs in BPAN develop over time, 2) identify clinical, biochemical and radiological markers ('biomarkers') and overall 3) provide data that will enable the conduction of future clinical trials.

1.2.7. BPAN Radiological and Neuropathological Findings: a disorder of Brain Iron Accumulation

In BPAN, all areas of the brain are affected, with some more so than others. In fact, one of the disease hallmarks is abnormal brain iron accumulation. Using conventional imaging modalities, this accumulation is more easily demonstrated in older patients. In fact, as with many NBIA disorders, brain iron accumulation is often not present (or detectable) in BPAN in early childhood. On the contrary, brain Magnetic Resonance Imaging (MRI) can be normal early on (Hayflick, Kruer et al. 2013, Ohba, Nabatame et al. 2014) or show non-specific features, such as thinning of the corpus callosum and hypomyelination (Gregory, Kurian et al. 2016). With time, iron tends to accumulate, and highly specific signal abnormalities develop. These consist of a hypointense signal on T2-weighted or 'iron-sensitive' sequences (such as T2* and FLAIR), mainly in the SN but also in the globus pallidus (GP). Additionally, T1-weighted sequences show a hyperintense "halo" surrounding a central linear region of signal hypointensity within the SN and cerebral peduncles. This hyperintense signal in the SN is much more prominent in older patients. There is also cerebral atrophy in the majority of patients, which also seems to become more obvious with disease progression; a proportion of patients also exhibit cerebellar atrophy/ volume loss. Computed Tomography (CT) scans of the brain also show a hyperdense signal in the SN, consistent with iron deposition.

Neuropathology studies are rare in BPAN (with only two relevant reports in the literature so far) but overall are consistent with radiological findings; namely, they describe an abnormal process affecting the whole brain but mainly the SN and the GP (Hayflick, Kruer et al. 2013, Paudel, Li et al. 2015). In more detail, a post-mortem examination of a female patient at 27 years of life described cerebellar atrophy, thinned cerebral peduncles and dark grey-brown appearance of the SN and, to a

much lesser extent, GP. Microscopic examination revealed excessive staining for iron in the GP and SN and, additionally, numerous large axonal spheroids [signifying axonal damage or impaired transport (Beirowski, Nogradi et al. 2010, Kruer 2013)], haemosiderin-containing macrophages (siderophages), severe neuronal loss and reactive astrocytosis. Fewer axonal spheroids were seen also in other brain areas (pons, medulla, thalamus). Additional but less significant neuronal loss (often with associated gliosis) were also seen in the thalamus, putamen and cerebellum. Finally, tau-positive neurofibrillary tangles were frequently encountered (hippocampus, neocortex, putamen, hypothalamus and, to a lesser degree, in the remaining neurons in the GP, SN, pons and thalamus). No amyloid-b plaques or Lewy bodies were observed (Hayflick, Kruer et al. 2013). Similar findings were reported by a later study on a 51-year old female, that demonstrated severe neuronal loss with gliosis affecting the SN, iron deposition in the SN and GP, axonal swellings in the SN, gracile nucleus and cuneate nucleus, as well as extensive phospho-tau deposition (Paudel, Li et al. 2015).

In summary, radiological and neuropathology findings distinguish BPAN from other NBIA disorders and provide interesting clues regarding implicated pathophysiological mechanisms leading to neurodegeneration. Firstly, the SN bright halo on T-weighted MRI is thought to be unique for BPAN. The mechanism behind its appearance is not well elucidated but it might be due to iron binding to neuromelanin, which is being released from dying pigmented neurons of the SN (Hayflick, Kruer et al. 2013). Secondly, the prominent involvement of the SN compared to the GP also differentiates BPAN from other NBIA disorders [such as phospholipase A2-associated neurodegeneration (PLAN), mitochondrial membrane protein-associated neurodegeneration (MPAN) and pantothenate kinase-associated neurodegeneration (PKAN)], where the GP is at least equally or more affected. Finally, other NBIA disorders like PLAN and MPAN are characterised by abundant α-synuclein-positive Lewy body pathology (Kruer 2013), whereas BPAN seems to be a tauopathy (Hayflick, Kruer et al. 2013, Paudel, Li et al. 2015). All the above indicate a distinct, but so far poorly understood, mechanism linking iron accumulation and striatonigral degeneration.

1.2.8. A devastating neurodegenerative rare disorder with no currently available treatments

In summary, BPAN is an early-onset, progressive and life-limiting condition associated with severe morbidity and mortality. Many patients are very severely affected from an early age, and this 1) impacts hugely on their life quality (and that of their carers), and 2) is overall linked with a significant socioeconomic burden. Unfortunately, there are no effective cures or disease-modifying treatments for BPAN; the current management approach is only limited in 1) control of symptoms/ treatment of manifestations (such as seizures, pyramidal and extrapyramidal signs, nutritional problems etc) and 2) prevention of secondary complications (e.g. Speech and Language assessment of swallowing, dietetic input and/ or gastrostomy tube feeding, hip and spine surveillance X-rays to detect dislocations and deformities, chest physiotherapy to facilitate secretion clearance and prevent opportunistic infections) (Gregory and Hayflick 2014). In other words, current practices aim at deceleration of disease progression rather than reversing or curing the disease. Moreover, there are still no clinical trials for BPAN on the horizon, although there is relevant interest from both patients/ families and the scientific community. This lack of development of novel therapies might be related to BPAN being one of the most recently described NBIA subgroups, with *WDR45* identified as the causative gene only a few years ago (Haack, Hogarth et al. 2012, Saitsu, Nishimura et al. 2013), and is likely to change soon. Indeed, such efforts are currently ongoing for other NBIA disorders such as PKAN or PLAN (e.g. https://clinicaltrials.gov/ct2/show/NCT03041116, https://clinicaltrials.gov/ct2/show/NCT03726996, respectively). Nonetheless, such efforts to develop novel, targeted and more effective treatments constitute a research priority.

1.3. BPAN Phenotype and Severity of Disease Progression: modifying factors

Details about several patients harbouring *WDR45* mutations have now been published in the literature and the severity of symptoms often varies. Symptom severity could, at least theoretically, be influenced by 1) the specific type of the *WDR45* pathogenic variant, 2) the presence of somatic mosaicism (and the time during embryogenesis the disease-causing mutation occurred) and 3) patterns of XCI (Haack, Hogarth et al. 2012, Hayflick, Kruer et al. 2013, Gregory, Kurian et al. 2016).

1.3.1. Mutation types could affect BPAN severity.

Although some case reports point to missense mutations being associated with less severe phenotypes compared to nonsense (Carvill, Liu et al. 2018), at present, no robust phenotype-genotype correlation studies exist in BPAN according to the current published literature (Haack, Hogarth et al. 2012, Hayflick, Kruer et al. 2013, Saitsu, Nishimura et al. 2013, Ohba, Nabatame et al. 2014, Long, Abdeen et al. 2015, Nishioka, Oyama et al. 2015, Abidi, Mignon-Ravix et al. 2016, Gregory, Kurian et al. 2016, Nakashima, Takano et al. 2016, Zarate, Jones et al. 2016, Carvill, Liu et al. 2018, Lim, Tan et al. 2018). However, theoretically, nonsense versus missense pathogenic variants, or variants affecting areas of the encoded protein that are more biologically relevant than others, might lead to more severe clinical phenotypes.

1.3.2. Somatic mosaicism might influence patient phenotypes.

In BPAN there are far fewer affected males than females but, perhaps unexpectedly, the phenotype is similar in both sexes (Gregory, Kurian et al. 2016). Since the disease primarily affects females, it has been hypothesised that 1) *WDR45* germline mutations in males are embryonically lethal (Haack, Hogarth et al. 2012, Hayflick, Kruer et al. 2013), and/or that 2) the disease would be much more severe or early-onset in affected boys, in a pattern similar to that observed in MECP2-related disease. Although BPAN still seems to be much more prevalent in females, male patients have now been described. Many of the boys with BPAN are severely affected (Abidi, Mignon-Ravix et al. 2016, Gregory, Kurian et al. 2016, Nakashima, Takano et al. 2016, Carvill, Liu et al. 2018) and a

recent case report of two BPAN siblings described a much more severely affected brother compared to his sister's clinical course (Zarate, Jones et al. 2016). Despite this, the disease course overall seems to be similar for both affected boys and girls. A plausible explanation for this would be the presence of somatic mosaicism in males (where, for example, at least a proportion of brain cells might carry the healthy *WDR45* allele, leading to a less severe phenotype). Similarly, the presence of such somatic mosaicism could also explain phenotypic differences between females harbouring the same *WDR45* mutation.

1.3.3. XCI possibly also contributes to the phenotypic spectrum in BPAN.

WDR45 is X-linked, and therefore, in females, subject to XCI. XCI is effectively an X-linked gene dosage compensation between females (XX) and males (XY), in which one X chromosome randomly becomes inactivated in female cells during embryogenesis (Panning 2008, Robert Finestra and Gribnau 2017). In BPAN female patients, a skewing of XCI in favour of the wild type or the mutated allele would theoretically lead to milder or more severe phenotypes, respectively. While non-random skewing of XCI is very frequently reported in BPAN, (Haack, Hogarth et al. 2012, Hayflick, Kruer et al. 2013, Carvill, Liu et al. 2018), testing is often performed in peripheral blood and not in brain tissue and, of course, whether skewing patterns in the blood reflect those in the brain is unknown. However, different cerebral patterns of XCI could also contribute to the phenotypic spectrum observed between patients. Also, very importantly, patterns and skewing of XCI can affect the modelling of X-linked disorders, and this will be discussed in more detail in the disease-modelling section.

1.4. WDR45/ WIPI4: known biological function(s)

1.4.1. Autophagy: a conserved cellular homeostatic mechanism

Autophagy is a highly conserved intracellular trafficking pathway through which subcellular components, including misfolded proteins and damaged organelles, are degraded and/ or recycled (Fujikake, Shin et al. 2018). Autophagy is important for cellular homeostasis and essential for mammalian development (Mizushima and Levine 2010). Overall, the most important roles of autophagy are to ensure protein and organelle quality control, metabolic adaptation to stressors (such as nutrient starvation, hypoxia or reactive oxidant species production) and provide innate immunity (through direct destruction of pathogens and also as a key mediating factor in the host defence mechanisms of innate and adaptive immunity) (Desai, Fang et al. 2015, Saha, Panigrahi et al. 2018). Particularly, autophagy is also thought to be important for post-mitotic and metabolically active tissues, such as neurons (Teinert, Behne et al. 2019). Furthermore, dysregulation of autophagy is associated with numerous diseases including cancer and neurodegeneration (Choi, Ryter et al. 2013). Indeed, there is mounting evidence in the literature regarding the physiological importance of autophagy in neuronal health and, conversely, the role of autophagy dysfunction in neurodegenerative diseases (Menzies, Fleming et al. 2017).

There are, of course, other intracellular degradation pathways apart from autophagy. When it comes to proteins, the ubiquitin-proteasome system, another major protein degradation pathway, is thought to be responsible for the selective degradation of short-lived intracellular and plasma membrane proteins tagged by ubiquitin. However, larger membrane proteins and protein complexes (including oligomers and aggregates) cannot pass through the narrow pore of the proteasome's barrel and macroautophagy induction seems to be necessary for their degradation; In contrast, damaged organelles can only be cleared by macroautophagy (Pan, Kondo et al. 2008).

At least three distinct types of autophagy exist, namely microautophagy, chaperone-mediated autophagy and macroautophagy. Microautophagy involves direct engulfment of cellular components

into the lysosome for degradation via inward invagination of the lysosomal membrane (Li, Li et al. 2012, Fujikake, Shin et al. 2018). Chaperone-mediated autophagy is a mechanism for targeted protein degradation. Firstly, cytoplasmic proteins with a targeting motif interact with the cytosolic heat shock cognate 70 chaperone, which enables their delivery to the lysosomal membrane. Substrate proteins are subsequently unfolded and go through the lysosomal membrane through a multimeric complex and rapid degradation follows (Kaushik and Cuervo 2012). Finally, macro-autophagy is the most studied autophagy subtype and believed to be the core pathway for degrading cytoplasmic proteins and organelles (Pan, Kondo et al. 2008, Nakatogawa, Suzuki et al. 2009). Through macroautophagy, cytosolic material is delivered to the lysosome for degradation and recycling. This occurs through the de novo generation of a cup-shaped membrane precursor (phagophore) at a nucleation site, known as the phagophore assembly site (PAS). where membrane assembles via a not well-elucidated mechanism to form a cup-shaped sac called the phagophore. Autophagosome membranes have been proposed to originate from several sources in mammalian cells, including the endoplasmic reticulum (ER), Golgi apparatus, mitochondria, and the plasma membrane. The phagophore surrounds the cargo (such as protein aggregates and damaged organelles) and seals to form a complete double-membrane vesicle (autophagosome). The autophagosome's outer membrane subsequently fuses with degradative compartments to expose the inner membrane and its contents to hydrolase enzymes (**Figure 2**) (Yang and Klionsky 2010). WDR45 seems to have a role in macroautophagy, as discussed in the next section. In fact, for the purpose of this thesis, microautophagy and chaperone-mediated autophagy are not relevant, and the focus will be on macroautophagy (hereafter called "autophagy" in this text, unless otherwise specified).

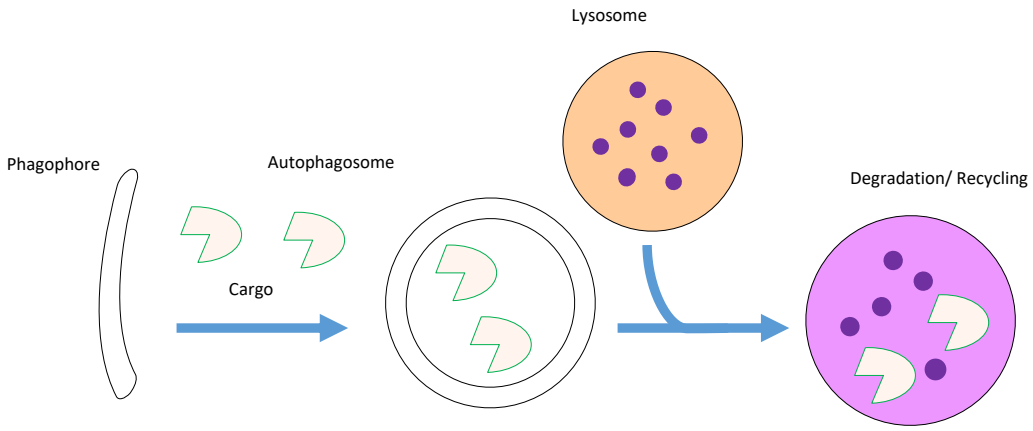

Figure 2. Macroautophagy *(hereby referred to as autophagy) is an innate highly conserved and dynamic cellular homeostatic mechanism, closely linked to lysosomal metabolism. Initially, a newly formed double-membrane cup-shaped structure known as the phagophore engulfs damaged or redundant cytoplasmic content ("the cargo", e.g. damaged organelles or protein aggregates) and forms the autophagosome. Subsequent autophagosomal/ lysosomal fusion leads to cargo degradation and recycling. All stages of autophagy are constantly and tightly regulated by upstream and downstream protein complexes that inhibit or enhance flux according to cellular stressors (e.g. starvation or hypoxia) and internal or external stimuli.*

Autophagy is a complex sequence of strictly regulated steps. Upstream and downstream protein complexes regulate each stage of the process, adjusting the autophagic flux promptly and according to cellular metabolic needs and other stimuli such as stressors. Autophagy-inducing conditions include hypoxia, nutrient starvation, reactive oxygen species production, and also the identification of intracellular abnormal protein aggregates, damaged organelles or infective pathogens (Mazure and Pouyssegur 2010, Son, Shim et al. 2012, Russell, Yuan et al. 2014).

The proteins involved in autophagy ['autophagy-related proteins' (Atg)] were initially described in yeast (*Saccharomyces cerevisiae*) by Yoshinori Ohsumi's lab, who won the Nobel prize in Physiology or Medicine in 2016 for his relevant work in elucidating the mechanisms of autophagosome formation (Rubinsztein and Frake 2016). Subsequent research in multiple laboratories worldwide has now been performed, demonstrating that complex interactions and feedback loops between numerous proteins take place during autophagosome formation. This

process is described in detail below (Mizushima, Yoshimori et al. 2011, Rubinsztein, Shpilka et al. 2012, Bento, Renna et al. 2016, Reggiori and Ungermann 2017, Kocaturk and Gozuacik 2018) and depicted in **Figure 3**; nomenclature used refers to mammalian/ human genes and proteins, unless stated otherwise.

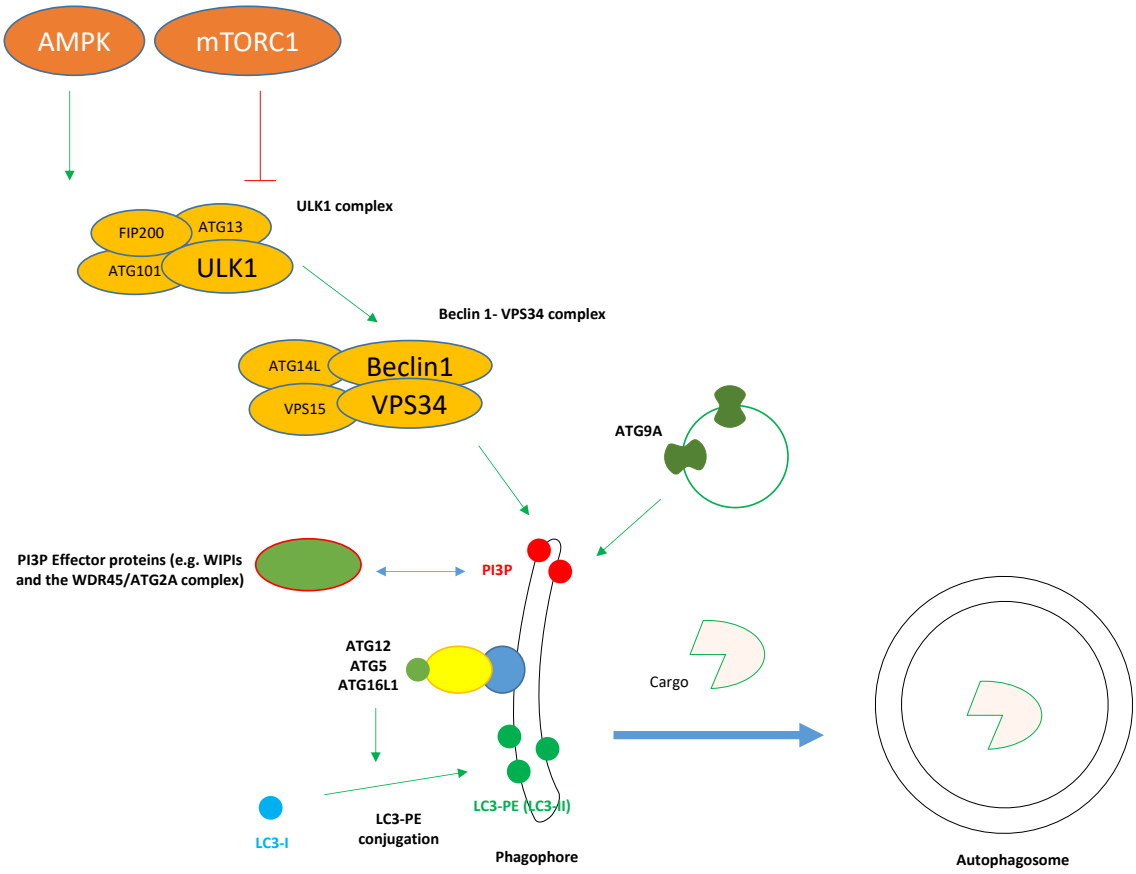

Figure 3. Depiction of the key protein complexes and conjugation reactions involved in autophagy. *Interactions between various protein complexes, plus two key conjugation reactions, govern the steps of autophagosome formation. The ULK1 protein complex is activated upon autophagy induction; this leads to Beclin1 and, subsequently, VPS34 activation and class III phosphatidylinositol 3-phosphate (PtdIns3P) production. PtdIns3P is essential for recruiting effector proteins to the early-forming autophagosome. ATG9A is also recruited in the early stages of autophagosome formation and thought to be involved in the trafficking of essential factors or lipid components to the autophagosome. Further steps include the conjugation of a) ATG12 to ATG5 and subsequent recruitment of ATG16L1 and b) LC3 to Phosphatidylethanolamine on the phagophore membrane. The former conjugation reaction is necessary for the latter, while the latter (and the conjugated form of LC3) is crucial for the final maturation, elongation and closure of the autophagosome. Details are provided in the text below.*

The most upstream component in the formation and maturation of an autophagosome is the ULK1 complex which, in mammalian cells, consists of the serine/threonine kinase ULK1/2, and the additional proteins FIP200, ATG13 and ATG101 (Zachari and Ganley 2017). This complex regulates levels of autophagy in response to changes in nutrients and growth factor signalling. For example, upon AMP-activated protein kinase (AMPK) activation or mTOR (mechanistic target of rapamycin) inhibition, ULK1 is activated, thereby inducing autophagy (Kim, Kundu et al. 2011, Russell, Tian et al. 2013).

Immediately downstream of the ULK1 complex, the Beclin1-VPS34 complex acts to mobilise essential membrane components to the forming autophagosome. This complex consists of Beclin 1, the class III phosphatidylinositol 3-phosphate (PtdIns3*P*)-kinase (PI3K) VPS34 and other associated proteins (VPS15 and ATG14L) (Funderburk, Wang et al. 2010). Activated ULK1 phosphorylates Beclin-1, which in turn activates the VPS34 kinase and *PtdIns3P* production (Russell, Tian et al. 2013). The production PtdIns3*P* by the PI3K complex is essential for autophagosome formation (Proikas-Cezanne, Takacs et al. 2015). Apart from being part of the membrane itself, this specialised phosphoinositide is thought to act as a unique signature of membrane identity that helps recruit effector proteins crucial in further stages of autophagosome formation. PROPPINs (β-propellers that bind phosphoinositides) are currently the only known PtdIns3*P*-binding proteins with conserved and essential function in autophagy from yeast to human (Thumm, Busse et al. 2013). The human PROPPIN family members are called WD-repeat protein interacting with phosphoinositides (WIPI) and consist of the four members (WIPI1 to WIPI4; the latter is also known as WDR45). The intracellular function of WDR45 is not well understood and will be discussed in detail later on.

Another conserved protein, ATG9A, is also involved early in the autophagosome formation stage. It is the only known transmembrane protein among the core ATG proteins required for autophagosome formation; it is present in vesicles that move between the Golgi and the autophagosome formation site and may be involved in the trafficking of critical factors or lipid components used early on to build the autophagosome (Yamamoto, Kakuta et al. 2012). Interestingly, ATG9A normally disappears from the autophagosomal structure prior to the appearance of MAP1LC3 (Microtubule-associated protein 1 light chain 3) (LC3, discussed in the following paragraph) which suggests that it is not needed in the latter stages of autophagosome maturation and closure (Kageyama, Omori et al. 2011, Mizushima, Yoshimori et al. 2011).

Two further conjugation reactions act downstream of the Beclin1-VPS34 complex to elongate and eventually fully close the forming autophagosome, namely the ATG12- ATG5-ATG16L1 and the

LC3-Phosphatidylethanolamine systems. Firstly, ATG12 is conjugated to ATG5 and this complex subsequently recruits ATG16L1; this complex is present on the outer side of the phagophore and is essential for its proper elongation. Importantly, the ATG12- ATG5-ATG16L1 complex participates in the second conjugation reaction involving the covalent attachment of LC3 to PE on the autophagosomal membrane. The LC3-PE conjugation system is essential for regulating the final steps of autophagosome formation, maturation and closure (Kuma, Mizushima et al. 2002, Fujita, Itoh et al. 2008, Agrotis, Pengo et al. 2019). Importantly, and as described in more detail below (**Section 1.4.2**), LC3 (and especially LC3-II, the conjugated, membrane-bound form) is a very useful marker for monitoring autophagy as it attaches to autophagosomes during their formation and remains associated throughout later stages of autophagy.

The fully formed/ closed autophagosome subsequently fuses with lysosomes to ensure degradation of its contents. Firstly, the outer autophagosomal membrane fuses with the (single) membrane of the lysosome. This is followed by degradation of the inner autophagosomal membrane by lysosomal hydrolases and exposure of the contents of the autophagosome to the lumen of the lysosome. For the process of fusion, cytoskeleton components and related motor proteins, tethering factors, core fusion machinery proteins/ protein complexes and phospholipids are required; these are not described in detail as autophagosome/ lysosome fusion is beyond the scope of this thesis (Wang, Li et al. 2016, Yu, Chen et al. 2018).

1.4.3. WDR45/ WIPI4: the encoded protein is a β-propeller that binds phosphoinositides (PROPPIN) with roles in early autophagy

WDR45 is part of the WD repeat protein family, containing repeating units of a conserved core of approximately 40 amino acids that usually end with tryptophan-aspartic acid (WD). These repeats organise in a beta-propeller structure and form a scaffold for protein-protein interactions (Smith, Gaitatzes et al. 1999, Li and Roberts 2001). WDR45 (also named WIPI4) is an ATG (Mizushima and

Komatsu 2011) with a role in early autophagy, and more specifically in the phagophore maturation process (**Figures 3, 4**).

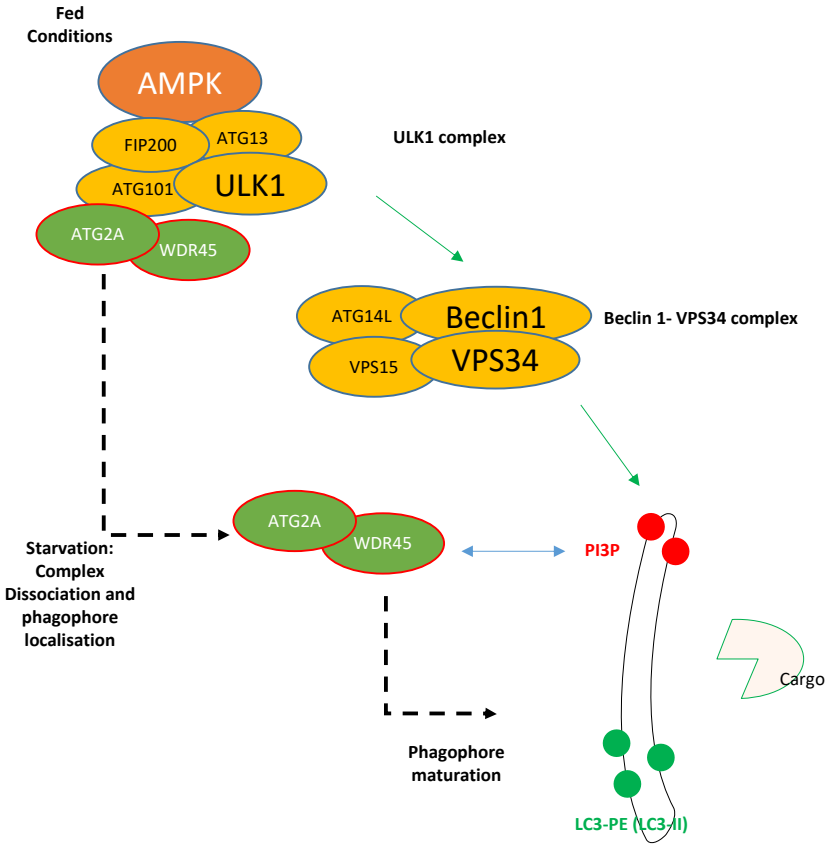

Figure 4. WDR45 and proposed role in autophagy according to currently published data. *Details are provided in the text below.*

As mentioned above, PtdIns3*P* production via the Beclin1-VPS34 complex is crucial for the forming autophagosome (Yang and Klionsky 2010, Russell, Tian et al. 2013, Proikas-Cezanne, Takacs et al. 2015). In humans, WIPIs 1 to 4 are the only known PROPPINs and act as autophagy-specific PtdIns3*P*-binding effector proteins. WIPI subunits in mammals associate with membranes through a phosphoinositide-binding motif (FRRG) within a seven–β propeller structure (Baskaran, Ragusa et al. 2012). WDR45 is thought to be involved in early stages of the autophagy pathway and *S. Cerevisiae* and *C. Elegans* homologues (Atg18 and EPG6, respectively) are essential for autophagosome formation (Obara, Sekito et al. 2008, Lu, Yang et al. 2011, Nakamura, Kodera et al. 2013). In *C.*

elegans studies, EPG6 forms a complex with ATG2, another autophagy-related protein, and regulates the generation of autophagosomes from omegasomes. One function of the EPG6/ ATG2 complex also seems to be the distribution of ATG9 (again, thought to supply lipids to the forming autophagosome). WDR45 also seems essential for the maturation of autophagosomes in starvation-induced autophagy in Normal Rat Kidney (NRK) cells. Accumulation of (abnormally enlarged) DFCP1-labelled omegasomes (cup-shaped endoplasmic reticulum membrane protrusions resembling the Greek letter Ω) was seen in *WDR45*-Knockdown (KD) NRK cells (Lu, Yang et al. 2011) whereas, upon starvation (a known autophagy flux activator), accumulation of LC3-labelled autophagosomes and ATG5 puncta was also seen in *C. Elegans*-based studies. ATG5 dissociates from the autophagosomal membrane upon the autophagosome's completion in *S. Cerevisiae* models (Nakatogawa, Suzuki et al. 2009). The above in combination suggest that autophagosome formation is defective in *WDR45* KD NRK cells (Lu, Yang et al. 2011). Similarly, studies in human lymphoblastoid cell lines derived from patients with *WDR45* mutations showed accumulation of LC3-marked autophagosomes compared to controls, both in basal conditions and after autophagy flux induction. These LC3-positive structures co-localised with ATG9A, which is absent from completed autophagosomes, again suggesting that the autophagosome formation in WDR45 deficiency is abnormal or impaired (Saitsu, Nishimura et al. 2013). Furthermore, studies in human melanoma G361 WDR45 KD cells also showed LC3 puncta accumulation compared to non-specific KD cells. U2OS cell studies also confirmed that WDR45 forms a complex with ATG2A through two critical (and conserved in human WIPI proteins) residues, N15 and D17. This complex also contains AMPK and ULK1 in fed conditions; however, upon starvation, and possibly due to AMPK activation, the WDR45/ ATG2A complex is proposed to dissociate from AMPK and ULK1 and localise to the autophagosome, possibly supporting their maturation (Bakula, Muller et al. 2017) (**Figure 4**).

1.4.4. The link between WDR45 deficiency and neurodegeneration

As mentioned above, BPAN affects the whole brain, but the SN [which is populated by midbrain dopaminergic (mDA) neurons] more so than other areas. This is reflected clinically, with early-onset

neurodevelopmental issues but also with very prominent parkinsonian features later in the disease course. Additionally, iron accumulation is a disease hallmark, mainly in the SN but also in other areas such as the GP. However, disease mechanisms in BPAN are poorly elucidated and the link between autophagy (that seems to be defective in BPAN), iron metabolism, and neuronal malfunction (and mainly) striatonigral degeneration is not well understood (Saitsu, Nishimura et al. 2013, Bakula, Muller et al. 2017, Seibler, Burbulla et al. 2018). Recent studies have investigated BPAN pathophysiology. Firstly, CNS-specific *WDR45* knockout mice display defects in autophagy-mediated clearance of protein aggregates and re-capitulate several hallmarks of BPAN, such as cognitive impairment and defective axonal homeostasis (Zhao, Sun et al. 2015). However, not all prominent features of the disease were present; for example, there was absence of iron accumulation at 12 months of life. Another more recent study using constitutive *WDR45* knockout mice showed accumulation of endoplasmic reticulum stress in neurons over time, leading to neuronal apoptosis (Wan, Wang et al. 2019). Other studies based on cell models (Seibler, Burbulla et al. 2018) showed that BPAN fibroblasts and neurons exhibit reduced LC3 compared to controls, as well as iron accumulation and possible mitochondrial and lysosomal dysfunction (**Figure 5**). Additionally, there is some indication that induction of autophagy in BPAN cells might lead to reversal of iron accumulation or endoplasmic reticulum stress (Seibler, Burbulla et al. 2018, Wan, Wang et al. 2019). Overall, this data suggests that autophagy may be a key pathway that is dysfunctional in BPAN and overcoming the underlying autophagy defect may provide a benefit for therapeutic strategies.

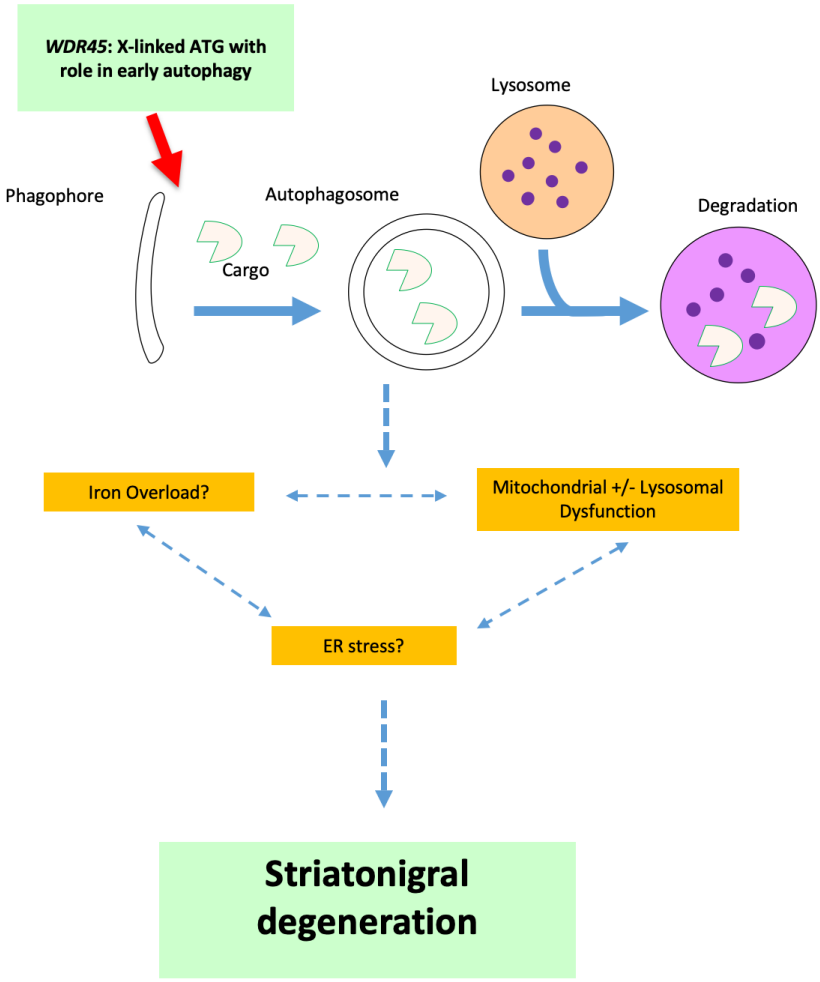

Figure 5. The link between WDR45, autophagy and disease in BPAN patients is not well understood. *WDR45 is a conserved protein with role in the early stages of autophagosome formation (also see Figures 3 and 4). It is not clear how WDR45 deficiency leads to neurodegeneration; however, iron accumulation, lysosomal and mitochondrial dysfunction, as well as Endoplasmic Reticulum (ER) stress have been implicated in recent studies. Moreover, brain iron accumulation seems to be absent in other congenital disorders of autophagy, which points to a unique, as yet unidentified role of WDR45 within the CNS. Overall, mechanisms causing disease in BPAN are not well elucidated, and more studies are warranted in order to understand the affected molecular pathways leading to neuronal malfunction and early death.*

1.4.5. Autophagy and Neurodegenerative Disorders

Autophagy is a key mechanism for cells to overcome adverse or potentially harmful conditions such as starvation or intrinsic or extrinsic stressful stimuli (e.g. hypoxia or ROS production). Hence, it is likely very important for tissues such as the brain, that are 1) metabolically active and 2) post-mitotic, hence cannot rely on cell division and replication to maintain homeostasis. Indeed, defects in autophagy are increasingly encountered in neurodegenerative conditions, whereas basal

autophagy suppression has been shown to lead to neurodegeneration in animal models (e.g. mice that are *Atg5*- or *Atg7*-deficient specifically in the CNS) (Hara, Nakamura et al. 2006, Komatsu, Waguri et al. 2006, Son, Shim et al. 2012). Importantly, understanding such disorders and the pathways leading to downstream neuronal malfunction and early death might give us useful insights into what cellular processes are malfunctioning in BPAN and, therefore, identify potential new treatments.

Firstly, the brain is often the most severely affected organ in pathogenic mutations of **genes involved in autophagy pathways**, as well as in disorders of lysosomal function (which is very closely linked to autophagy) (Ebrahimi-Fakhari, Saffari et al. 2016, Teinert, Behne et al. 2019, Zhu, Runwal et al. 2019). In fact, mutations in these genes are often linked to neurodegenerative disorders, indicating the heavy reliance of neurons on autophagy to maintain normal function and homeostasis (Nixon 2013, Guo, Liu et al. 2018, Meng, Lin et al. 2019). Apart from *WDR45* and BPAN, examples of other congenital disorders of autophagy include

- *EPG5*, involved in autophagosome-lysosome fusion, mutations in which cause Vici Syndrome, (OMIM #242840), a multisystemic disorder with primary CNS involvement (Ebrahimi-Fakhari, Wahlster et al. 2014, Byrne, Jansen et al. 2016, Ebrahimi-Fakhari, Saffari et al. 2016, Teinert, Behne et al. 2019),
- *SNX14*, involved in intracellular trafficking, cholesterol and neutral lipid homeostasis, mutations in which cause an autosomal-recessive cerebellar ataxia syndrome (OMIM #616354) (Thomas, Williams et al. 2014, Akizu, Cantagrel et al. 2015)
- *ATG5,* involved in early autophagy; mutations cause *ATG5*-associated autosomal recessive ataxia syndrome (OMIM #617584) (Kim, Sandford et al. 2016)
- *SQSTM1/ p62,* involved in autophagy cargo detection; mutations cause *SQSTM1/p62*-associated childhood-onset neurodegeneration (OMIM #617145) (Haack, Ignatius et al. 2016)

- hereditary spastic paraplegias (SPG), often caused by mutations in genes involved in multiple cellular pathways and processes including endoplasmic reticulum function, vesicle formation, membrane trafficking, mitochondrial function, lipid metabolism, myelination, axonal transport and autophagy [such as *SPG11*, *ZFYVE26* (SPG15) and *TECPR2* (SPG49)] (Lo Giudice, Lombardi et al. 2014, Ebrahimi-Fakhari, Saffari et al. 2016).
- finally, mTOR pathway defects, such as the ones in tuberous sclerosis (caused by mutations in *TSC1* and *TSC2*), and lysosomal storage defects, such as the ones in Niemann-Pick type C (caused by mutations in *NCP1* and *NPC2,* involved in cholesterol and lipid intracellular trafficking) also result in multisystemic disorders with primary neurological involvement and impaired autophagy on a molecular level (Ebrahimi-Fakhari, Saffari et al. 2016).

Overall, congenital disorders of autophagy manifest with a broad clinical phenotypic spectrum and are characterised by genetic heterogeneity, with an expanding number of causative mutations in different genes leading to multi-systemic and/ or neurological signs and symptoms. Despite their heterogeneity, unifying clinical characteristics begin to emerge, such as a) the early disease onset (often in early childhood/ adolescence), b) the progressive disease course with neurodegeneration, developmental regression and cognitive decline, c) the frequent involvement of long white matter tracts (e.g. corpus callosum, corticospinal tracts) and the cerebellum (Purkinje cells), d) the 'storage disease-like' phenotypes frequently observed (e.g. coarse facial features, macroglossia, sensorineural hearing loss, organomegaly, kyphoscoliosis) and e) often a multisystemic disease with additional non-neuronal manifestations (including myopathy and ophthalmic manifestations) (Ebrahimi-Fakhari, Saffari et al. 2016). Hence, delineation of underlying molecular mechanisms and the interconnected pathways leading from protein deficiency to disease is important in order to identify potential targets for novel therapeutic developments for these conditions.

Finally, and despite the similarities with BPAN on both molecular and clinical levels, other congenital disorders of autophagy are not linked with brain iron accumulation (Ebrahimi-Fakhari, Saffari et al. 2016, Teinert, Behne et al. 2019). This points to a unique, as yet unidentified, role of BPAN in brain cells. For example, WDR45 could possibly be responsible for selective autophagy of a specific iron binding protein, the accumulation of which would lead to iron accumulation and a downstream vicious cycle of oxidative stress, more iron accumulation, organelle malfunction and, eventually, neuronal malfunction and early death (**Figure 5**). Overall, more studies are warranted in order to further elucidate the intracellular roles of WDR45 and the mechanisms leading to disease in BPAN.

Moreover, **autophagy is also often defective in more common neurodegenerative disorders**. The two most common neurodegenerative disorders, Alzheimer's and Parkinson's disease, and their links to autophagy, are discussed in the paragraphs below.

Apart from loss of certain nerve subpopulations, one of the main hallmarks of neurodegenerative conditions is **intracellular aggregation of misfolded proteins or damaged organelles**, many of which can be removed or degraded by autophagy.

Firstly, Alzheimer's disease, the most common neurodegenerative condition (Mayeux and Stern 2012), is characterised by 1) extracellular amyloid-β (Aβ) plaques, which consist of cleaved products of amyloid precursor proteins, and 2) intracellular neurofibrillary tangles, which represent aggregated hyperphosphorylated tau protein. There is also accumulation of autophagosomes and other pre-lysosomal autophagic vacuoles (AVs), particularly in the dendrites (Nixon, Wegiel et al. 2005, Nixon 2013). Defective retrograde transport of autophagosomes from the synapses and neuritic processes to the soma (containing the largest concentration of lysosomes) leads to accumulation of Aβ plaques and might be contributory to Alzheimer's disease pathogenesis (Son, Shim et al. 2012). Reduced autophagy caused by beclin1 deficiency has also been shown to reduce intraneuronal Aβ accumulation, extracellular Aβ deposition and neurodegeneration (Pickford, Masliah et al. 2008,

Jaeger, Pickford et al. 2010). Lysosomal proteolysis defects might also play a role in Alzheimer's disease pathogenesis; Presenillin-1 (PS1) is essential for lysosomal acidification and protein turnover by autophagy, and its deficiency leads to delayed proteolytic clearance of autophagic substrates and their accumulation (in the form of autophagic vacuoles) in mice neurons and patient fibroblasts (Lee, Yu et al. 2010). Conversely, mTOR pathway inhibition (and autophagy induction) via rapamycin has been shown to rescue cognitive deficits and ameliorate Aβ and tau pathology in Alzheimer's disease mouse models (Caccamo, Majumder et al. 2010, Spilman, Podlutskaya et al. 2010). All the above collectively demonstrate that autophagy is not only implicated in the pathophysiology of Alzheimer's disease but also that targeting/ inducing autophagy might be of therapeutic benefit for these patients.

Moreover, Parkinson's disease, the second most commonly encountered neurodegenerative condition (Berger, Breteler et al. 2000), is characterised by 1) selective loss of mDA neurons in the SN pars compacta and 2) intracellular Lewy bodies, the main component of which is aggregated α-synuclein. Aggregates of α-synuclein are degradable by autophagy (but also by chaperone-mediated autophagy), and inhibition of this process leads to α-synuclein accumulation (Cuervo, Stefanis et al. 2004, Vogiatzi, Xilouri et al. 2008). Additionally, several forms of familial Parkinson's disease are associated with autophagy defects. Mutations in *LRRK2* (causing the most common cause of autosomal dominant form of Parkinson's disease) lead to autophagosome accumulation in SH-SY5Y cells and also impair autophagy flux with ageing. *VPS35* mutations also cause autosomal dominant Parkinson's disease; it has been shown that dysfunction in VPS35 destabilises the WASH complex (which regulates endosomal trafficking of several cargos), thereby leading to defects in autophagosome formation and compromised trafficking of autophagy-related protein ATG9 (Zavodszky, Seaman et al. 2014). Importantly, there is evidence that autophagy flux induction (e.g. via overexpression of TFEB, an autophagy modulator) ameliorates α-synuclein aggregation and rescues dopaminergic neurons (Decressac, Mattsson et al. 2013, Kilpatrick, Zeng et al. 2015).

Apart from abnormal clearance of protein aggregates, **mitophagy**, the autophagy process of clearing damaged mitochondria from cells, is often reported as dysfunctional in common neurogenerative conditions. In Alzheimer's disease, compromised mitophagy causes defects in energy production and leads to oxidative stress. This results in Aβ peptide formation and accumulation of hyperphosphorylated tau aggregates. Accumulation of pathogenic Aβ and hyperphosphorylated tau also seems to impair mitophagy, leading to a subsequent increase in damaged mitochondria, and a self-propagating vicious cycle ending in downstream neuronal damage and early death (Kerr, Adriaanse et al. 2017). Similarly, defects in mitophagy also cause Parkinson's disease. Mutations in *PINK1* (PTEN induced putative kinase 1) and *PARKIN* (parkin RBR E3 ubiquitin protein ligase), two key proteins in the mitophagy process, cause autosomal recessive Parkinson's disease accounting for up to 50% of familial cases in the European population (Kazlauskaite and Muqit 2015). Briefly, PINK1, a ubiquitine kinase, can be imported on the Outer Mitochondrial Membrane (OMM) but is rapidly degraded under conditions of mitochondrial health. However, after mitochondrial damage and membrane depolarisation, PINK1 stabilises, accumulates at the OMM, is autophosphorylated and activated. PINK1 activation in turn leads to phosphorylation of both ubiquitin and the ubiquitin-like domain of Parkin, which results in maximal activation of Parkin E3 ubiquitin ligase activity and ubiquitylation of OMM substrates (Rasool, Soya et al. 2018). Finally, these substrates interact with ubiquitin binding domain- containing proteins (e.g. p62), that attract the autophagy machinery to the mitochondrion and further advance the mitophagic process. Defective mitophagy may contribute to synaptic dysfunction and aggregation of misfolded proteins, which in turn might further impair mitochondrial homeostasis. Interventions that stimulate mitophagy to maintain mitochondrial health might, therefore, be used as an approach to delay the neurodegenerative processes in Parkinson's Disease (Gao, Yang et al. 2017), and perhaps even other similar conditions such as BPAN. Indeed, there is evidence of mitochondrial dysfunction in BPAN (Seibler, Burbulla et al. 2018) and other congenital disorders of autophagy, and direct organelle

damage (e.g. via accumulation of toxic substances) but also defective mitophagy might plausibly play a role.

How the above findings in other neurodegenerative disorders relate to BPAN (and whether there are common pathophysiological mechanisms leading to downstream neuronal malfunction) is not well understood. As mentioned above, BPAN pathophysiology is likely different to other NBIA subtypes; for example, it is the only NBIA disorder caused by mutations in a conserved ATG, there is primary SN (versus GP) involvement and the MRI T1 hyperintense 'Halo sign' in the SN is thought to be a unique process (Haack, Hogarth et al. 2012, Hayflick, Kruer et al. 2013). Additionally, as mentioned above, BPAN is the only congenital disorder of autophagy manifesting with brain iron accumulation. Axonal spheroids present in the brain of affected patients might be caused by defective autophagy or retrograde transport of autophagosomal vacuoles, as described in more common conditions (Beirowski, Nogradi et al. 2010, Kruer 2013). Furthermore, in BPAN there is extensive phospho-tau deposition (Paudel, Li et al. 2015), reminiscent of Alzheimer's disease, but no evidence of Aβ plaques in the literature so far. There is also significant neuronal loss, primarily in the SN, reminiscent of Parkinson's disease, but limited neuropathology data suggest the absence of Lewy bodies (Hayflick, Kruer et al. 2013, Kruer 2013). Finally, there is limited data about lysosomal and mitochondrial function and/ or mitophagy in BPAN, but recent studies suggest that iron accumulation might lead to secondary mitochondrial and lysosomal dysfunction, which might in turn cause neuronal dyshomeostasis (Seibler, Burbulla et al. 2018). All these elements are worth examining in BPAN in order to help elucidate the underlying pathophysiological mechanisms and identify potential targets for future therapeutic drug development. Very importantly, it would be interesting to establish if BPAN neurons exhibit autophagy defects and, subsequently, if autophagy induction could help ameliorate other disease-related phenotypes.

1.4.6. Dopaminergic Neurons are more susceptible to damage than other neuronal cell populations in Parkinson's disease, and also in BPAN

As mentioned above, neurodegeneration is associated with loss of certain neuronal subtypes, which can often be very specific and selective. In fact, both the identity of affected neurons and the pattern in which neuronal degeneration occurs are often specific to each condition, hence giving rise to specific clinical signs that characterise the disease. For example, Alzheimer's disease is characterised by early onset loss of distinct subgroups of neurons in layer II of the entorhinal cortex, the subiculum, and the CA1 region of the hippocampus; in contrast, many other cortical and hippocampal regions do not show pathological signs early in the disease course. Moreover, the most vulnerable cell subtype in Parkinson's disease (regardless of aetiology) are the dopaminergic neurons of the SN pars compacta (A9 group), which are very selectively lost (Brichta and Greengard 2014). Conversely, the dopaminergic neurons of the ventral tegmental area (A10 group) are more resistant to the neurodegenerative process. Dopaminergic neurons in the SN are of particular importance for BPAN, too, as a) the SN is the most affected brain area with extensive dopaminergic neuron loss and b) parkinsonism (caused by loss of SN dopaminergic neurons) is clinically one of the most prominent features in later disease stages. Hence, understanding the mechanisms underlying the dopaminergic neuron susceptibility to malfunction or injury in Parkinson's disease, and investigating whether these mechanisms also apply to BPAN and other similar parkinsonian disorders, is relevant and, consequently, of research interest for our project.

Dopaminergic neurons are very metabolically active and, hence, might be at risk of sustaining damage in cases of high energy demand or mitochondria/energy failure. Firstly, the dopaminergic neuronal intrinsic pacemaking function probably entails greater overall levels of activity (and energy demand) than what is seen in other neuronal subtypes. Moreover, monoamine neurotransmission (production of dopamine, packaging in vesicles, synaptic release, reuptake, recycling etc) also produces a huge energy demand (Haddad and Nakamura 2015). Overall, this increased neuronal activity predisposes neurons (and, primarily, axons) to energy failure, for example when mitochondria are compromised (Pathak, Shields et al. 2015). Hence it is plausible that dopaminergic susceptibility is related to the increased metabolic demands compared to other neurons. However,

despite extensive relevant research, it is still not clear why A9 SN dopaminergic neurons are more vulnerable to damage than other dopaminergic cell subtypes. Examples of relevant studies performed include, firstly, examining differences in gene expression profiles between A9 (SN) and A10 (Ventral Tegmental Area) neurons; it is hypothesised that a cell type-specific combination of several gene expression differences and subtle differences in protein function are responsible for establishing the increased or decreased midbrain DA neuron vulnerability. Secondly, SN dopaminergic neurons form much larger axonal arbors and a higher number of synapses when compared to A10 neurons; this might lead to redistribution of mitochondria to the axonal terminals and a large increase in energy demand, but also vulnerability to factors affecting energy supply (e.g. mitochondrial dysfunction, defective mitophagy etc) (Bolam and Pissadaki 2012). Thirdly, mature A9 neurons exhibit autonomous pacemaking activities governed by calcium channels, whereas juvenile SN (A9) neurons and A10 neurons rely on voltage-dependent sodium channels. This differential reliance on calcium channels might lead to elevated levels of calcium in the cytoplasm and, subsequently, levels of oxidative stress, thereby explaining the increased susceptibility of mature SN dopaminergic neurons to neurodegeneration in PD (Mosharov, Larsen et al. 2009, Guzman, Sanchez-Padilla et al. 2010, Brichta and Greengard 2014). Additionally, pacemaking supported by calcium influx is thought to be more energetically demanding for cells, as calcium has to be transferred extracellularly against steep concentration gradients (Surmeier and Schumacker 2013).

Overall, a lot remains unknown about what leads to SN mDA neuron degeneration in Parkinson's disease and more research is needed in order to understand the relevant molecular pathways. Undoubtedly, the elucidation of the cellular mechanisms underlying this preferential vulnerability/ susceptibility (and understanding whether this vulnerability applies to other neurodegenerative conditions such as BPAN) 1) constitutes a research priority and 2) would be of significant importance in the efforts towards developing more effective neuroprotective strategies and treatments.

Conversely, the study of rarer, monogenic forms of neurodegeneration such as BPAN (or even *LRRK2, SNCA, PINK1*-related familial forms of Parkinson's disease) often provides very useful insight into mechanistic processes underlying more common disorders.

1.5. Choice of Research Model to study BPAN and induced pluripotent stem cell (iPSC)-based modelling of neurological disorders

1.5.1. Dopaminergic neurons are the optimal cell subtype to study BPAN

Although WDR45 seems to have a role in regulating the early stages of autophagosome formation, the precise mechanisms by which mutations in the gene cause disease and the protein's role in neurodegeneration and iron accumulation are yet to be elucidated. As mentioned above, one hypothesis is that the suggested defects in cellular autophagy and the observed iron accumulation in vivo are linked. Furthermore, the symptomatology in BPAN is almost exclusively neurological and the most affected area of the brain is the mDA neuron-rich SN. This is also mirrored clinically, with parkinsonism featuring very prominently after a certain point in the disease course. Hence, we propose that the protein might exert its function in a tissue (brain)-specific manner or, alternatively, that its role in preserving intracellular homeostasis might be more important in post-mitotic, non-regenerating or vulnerable cells (e.g. the A9 SN mDA neurons). For all these reasons, we suggest that a dopaminergic neuronal cell model is optimal in order to study pathophysiological mechanisms in BPAN and develop targeted, effective therapies for the disorder.

1.5.2. Historical scarcity of appropriate models to study neurological disease

Historically, there have been many difficulties around accurately modelling neurological disorders. The main reason for this is the unavailability of appropriate tissue for research. It has long been recognised that patient derived cells are a potentially better *in vitro* tool for studying human disease. However, the human brain is very inaccessible (especially when compared to skin, liver, muscle and other tissues). Hence, isolating healthy neural cells from post-mortem brains (or even brain biopsies from live patients) for cell culture and future studies is often challenging or impossible

due to 1) the rarity of some conditions such as BPAN but also 2) the susceptibility of the cells to oxygen deprivation and external stressors. In particular, post-mitotic neurons are difficult to expand in *in vitro* culture systems. Conversely, and despite their undeniable utility and certain benefits, transformed cell lines and transgenic animals 1) do not accurately reflect human gene expression profiles, metabolism and homeostasis, 2) often do not harbour disease-causing genetic mutations and 3) frequently only partially recapitulate patients' neurological phenotypes (Barral and Kurian 2016). For example, in the BPAN CNS-specific WDR45 knockout mouse, there is poor motor coordination, greatly impaired learning and memory, as well as evidence of autophagy defects (accumulation of LC3-I, LC3-II and p62/SQSTM1-positive structures in axons and neurons), and extensive axonal swelling with numerous axon spheroids. However, no iron accumulation (in the SN or other brain regions) was detectable at 13 months (Zhao, Sun et al. 2015).

Importantly, the development of novel therapeutics for human neurological disorders is very challenging and many drugs tested in animal models have failed in subsequent human clinical trials due to lack of efficacy or intolerability (Scannell, Blanckley et al. 2012). Again, this reflects fundamental differences in the neurobiology of humans when compared to animals and necessitates the development of improved, more physiologically relevant models.

Overall, the study of neurological disorders has been historically challenging for the above reasons and the lack of appropriate models that accurately recapitulate conditions in the human brain. Hence, understanding brain physiology, elucidation of disease mechanisms and development of improved therapeutics has been hindered.

1.5.3. Induced Pluripotent Stem Cells (iPSC)

Since 1998, the isolation and use of human embryonic stem cells (ESCs) for studying human disease has provided a (technically and ethically) challenging but also very promising way to overcome the aforementioned issue of neuronal tissue unavailability. More recently, cellular reprogramming techniques further revolutionised this methodology. In a landmark study by

Yamanaka and colleagues, adult skin fibroblasts were reprogrammed into iPSC through overexpression of four transcription factors (OCT4, SOX2, C-MYC and KLF4) (Takahashi, Tanabe et al. 2007). Different ways to achieve delivery of these four factors have been described. These initially involved integrating retroviral or lentiviral delivery but have lately been substituted by non-integrating strategies, namely 1) non-integrating vectors and 2) vector-free strategies (including microRNAs and small molecules mimicking the action of the 4 transcription factors). The overall aim of these newer strategies is the generation of transgene-free iPSCs (as well as the reduction of insertional mutagenesis risks) and improved reprogramming efficiency.

IPSCs have the ability to proliferate almost indefinitely and can differentiate into any cell type in the human body. These qualities, combined with the continuous development and refinement of differentiation protocols for an expanding array of cell subpopulations and/ or even 3-dimensional structures resembling organs (often referred to as 'organoids'), have made the study of every human disease theoretically possible, with specific patient cells as a starting point (Barral and Kurian 2016).

In the BPAN project, we utilised a Sendai virus-based methodology to reprogram dermal fibroblasts into iPSCs. Sendai virus (SeV) is a single strand RNA virus which has been extensively used as a non-integrating vector system to reprogram somatic cells into iPSC with relatively high efficiency (Fusaki, Ban et al. 2009).

1.5.4. The use of iPSCs for studying neurological disorders

As discussed above, iPSCs provide a way around the historical issue of tissue unavailability for research in neurological/ neurodegenerative conditions. Indeed, a wide range of neural cells can now be differentiated using culture conditions and differentiation protocols following embryology-derived developmental principles. Subsequently, several iPSC-derived neuronal models have already been generated for monogenic defects, chromosomal disorders and complex polygenic diseases (Devine, Ryten et al. 2011, Kirkeby, Grealish et al. 2012, Mariani, Coppola et al. 2015, Barral and Kurian 2016, Li, Chao et al. 2018, Seibler, Burbulla et al. 2018). The use of these is already proving to

be an invaluable tool to further understand neurobiology, elucidate disease mechanisms and develop novel precision therapies (**Figure 6**).

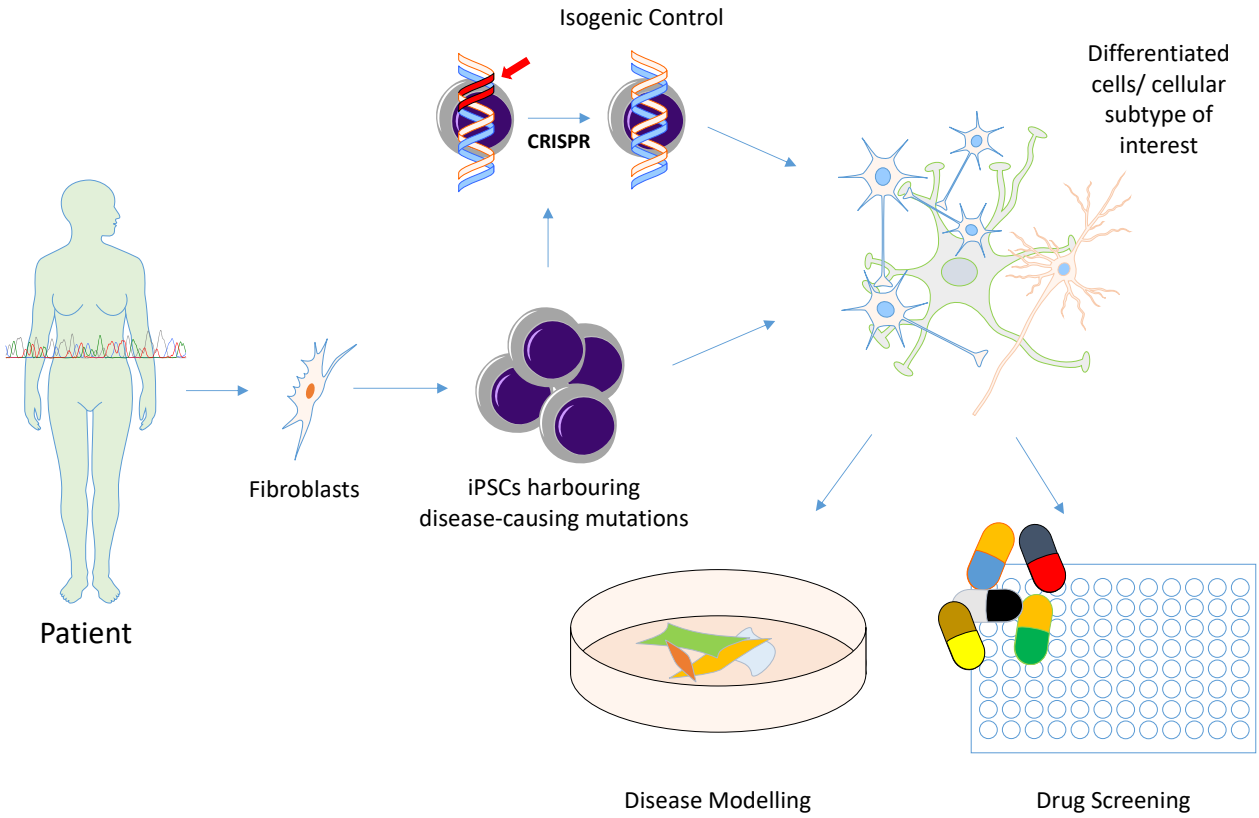

Figure 6. Neurological Disease modelling using iPSCs. *With a relatively non-invasive technique, skin fibroblasts are collected from the patients, and then using a transcription factor cocktail, these are firstly reprogrammed into iPSCs and, subsequently, differentiated into desirable subtypes (in the case of my project, mDA neurons). Hence, iPSC-based models allow in vitro disease modelling and disease study in a physiologically relevant context, and also downstream applications such as drug screening. There are limiting factors in the iPSC technology like line variability (to be discussed in detail in section 1.6), but especially in monogenic disorders, the use of multiple patient lines and appropriate age-matched controls (including 'isogenic' controls generated via CRISPR genome editing) allow for robust results in downstream experiments. An approach identical to the one depicted was applied to the BPAN project.*

1.5.5. Development of novel therapies in neurological disorders using iPSCs

There is currently a huge unmet need for development of novel, targeted and efficient therapies for severe neurological conditions including BPAN, where symptom alleviation often seems to be the only realistic management option. As mentioned above, many CNS-targeting drugs initially developed on animal (or other, overall inappropriate) models fail to exhibit efficacy or tolerability in clinical trials. Hence, iPSCs provide a very promising platform for development of new therapeutics as they are human cells, can differentiate into cells that are physiologically relevant to each disease and have a large capacity for self-renewal (which allows large-scale applications such as high-throughput drug screening). Despite still at early stages, iPSC models have already been used in neurological disease models (including ones of childhood-onset disorders) for

1) testing specific drugs or novel approaches such as anti-sense oligonucleotides, for example in Spinal Muscular Atrophy (Corti, Nizzardo et al. 2012, Xu, Denton et al. 2016),
2) providing a proof-of-concept for the efficacy of gene therapy approaches (that, for instance, restore disease-related phenotypes in the dish for CLN3-related Batten's or LRRK2-related Parkinson's disease) (Seibler, Graziotto et al. 2011, Lojewski, Staropoli et al. 2014),
3) cell replacement therapies, for example by injecting mDA progenitors in the striatum of Parkinson's disease patients, an approach that is already at clinical trial stage (Kikuchi, Morizane et al. 2017, Sonntag, Song et al. 2018, Takahashi 2019)
4) small (<10,000 compounds) or medium- to large-scale (Little, Ketteler et al. 2019) drug screening

Compound library screening for hits that restore disease-related phenotypes in iPSC-based neuronal models is of particular interest, especially due to 1) the capacity for fast testing of drugs at a large scale and 2) the potential for drug repurposing and faster clinical translation when considering FDA-approved compounds. Screening generally involves seeding neuronal cells at a specified stage of differentiation onto multi-well (96-, 384- or 1536-) plates. After an often-short

incubation post seeding, cells are treated with the compounds, and also possibly with positive and negative controls, and phenotypic readouts are captured through plate readers (e.g. when measuring luminescence) or high content imaging confocal microscopes (e.g. for immunofluorescence-based assays) before or after cell fixation. The term 'high content screening' or high content analysis' is used to describe the recording of multiple parametres in a large number or cells, exposed to many different conditions, in a short period of time. Such capacity of data capture, paired with the ever-increasing power of computing, bioinformatics and image/ data analysis techniques and software, makes large scale applications (such as drug screens using many thousands of compounds) feasible. Immunofluorescence-based high content imaging assays are most often fixed-cell assays (Esner, Meyenhofer et al. 2018) and require cell seeding at low density (and as a monolayer) in order to reduce noise and allow subsequent meaningful analysis of captured images. Drug screening using iPSC- or ESC-based neuronal models has already been performed in several neurological disorders and a list of relevant publications is provided in **Table 1**.

Condition	Cell type	Compounds	Results	References
Spinal muscular atrophy	iPSC-derived Motor neurons	200,000	Not published	(Grskovic, Javaherian et al. 2011)
Parkinson's Disease	hESC-derived Motor neurons	2,000	6 hits, 1 further validated	(Ryan, Dolatabadi et al. 2013)
ALS (Amyotrophic lateral sclerosis)	iPSC-derived Motor neurons	1,757	38 hits	(Burkhardt, Martinez et al. 2013)
Alzheimer's Disease	iPSC-derived Neural Progenitors	1,684	42 hits, 4 further validated	(van der Kant, Langness et al. 2019)
Alzheimer's Disease	Commercially available iPSC-derived neurons (iCell)	'Several hundred' (GSK compound library)	19 hits including a Cyclin-Dependent Kinase 2 inhibitor	(Xu, Lei et al. 2013)
Alzheimer's Disease	iPSC-derived Cortical neurons with trisomy 21	1,280 (Prestwick Chemical library)	55 compounds that reduce amyloid-β accumulation	(Brownjohn, Smith et al. 2017)
Alzheimer's Disease	iPSC-derived Cortical neurons	1,258	27 Aβ-lowering screen hits, 6 leading compounds prioritised by chemical structure-based clustering	(Kondo, Imamura et al. 2017)

Table 1. Examples of studies using iPSC- or ESC-derived neurons for drug screening in neurological disorders. *Table adapted from (Little, Ketteler et al. 2019)*

1.6. Making dopaminergic neurons in vitro

1.6.1. Development of dopaminergic neurons in vitro: available '2-dimensional' protocols

Our ability to recreate human mDA neurons in vitro has increased drastically in recent years and been built largely on the growing knowledge of these cells' embryological development in vivo. Due to this, we now have unprecedented opportunities in disease modelling, drug discovery and cell replacement therapies for neurological disorders in our disposal. Indeed, this also applies for monogenic neurodegenerative disorders such as BPAN.

As mentioned before, human IPSCs and ESCs are an attractive cell source for disease modelling and regenerative medicine overall, since they 1) are capable of self-renewal and generation of all desirable cell subtypes and also 2) carry the genotypes of patients with known clinical phenotypes. Numerous protocols describing the differentiation of mDA neurons from iPSCs have been developed during the last decade (Arenas, Denham et al. 2015). Again, these are based on exposure of iPSCs to transcription factors and morphogens that recapitulate in vivo developmental conditions and give rise to ventral midbrain cellular specifications. Whether starting from an iPSC monolayer or Embryoid Bodies (EBs), most of the recent protocols start off with dual inhibition of the SMAD pathway (inhibition of BMP, nodal, activin and TGFβ signalling) that induces neuronal identities in the iPSCs and eliminates the need for use of feeder layers. This is supplemented by exposure to SHH or SHH agonists, that drive cells towards ventral identities, and WNT1 pathway activation (e.g. via GSK3 beta inhibitors that activate the WNT/β-catenin signalling), that 'caudalise' the cells and help them assume appropriate midbrain specifications. The latter term ('caudalisation') refers to the fact that cells develop more rostral (forebrain) identities with no exposure to WNT1 activators (Nordstrom, Jessell et al. 2002, Arenas, Denham et al. 2015). Apart from this, other transcription/ neurotrophic factors, nutrients and antioxidants are also added to the culture media, for example

brain-derived neurotrophic factor (BDNF) and glial cell-line- derived neurotrophic factor (GDNF), that have been shown to help with mDA neuron survival.

We have now reached a stage where mDA neuronal differentiation protocols lead to fairly efficient generation of cells that even exhibit appropriate functionality *in vivo*. For instance, when transplanted in rodent models of Parkinson's Disease, these cells survive, retain marker expression, do not form overgrowths and lead to recovery of phenotypic defects in several (drug-induced or spontaneous) motor and behavioural tests (Kirkeby, Grealish et al. 2012, Arenas, Denham et al. 2015).

However, morphogens and transcription factors might have 'off-target effects', in other words activate pathways different than the ones desired and lead to differentiation into cells with different/ unwanted specifications. Additionally, a lot remains to be understood about the actual properties of SN pars compacta A9 neurons (and, for example, their differences from A10 neurons).

Hence, better understanding of 1) the nature of A9 mDA neurons (e.g. via single cell transcriptome analysis) and 2) the precise effect of, and requirement for, different signalling molecules is essential in order to further refine current mDA neuronal differentiation protocols. Additionally, the cells that are generated need to be scrutinised for the presence of expected characteristics, at least up to a certain level. In the case of A9 SN mDA neurons for the BPAN project, this would include the expression of appropriate markers (e.g. TH, AADC, PITX3, DAT, VMAT2, GIRK2), electrophysiological properties such as spontaneous firing (Grace and Onn 1989) and the release of dopamine.

1.6.2. Direct reprogramming of somatic cells into dopaminergic neurons: a different approach

Apart from the aforementioned route of generating neurons through pluripotent stem cells, it is worth mentioning here that generation of dopaminergic neurons (and other neuronal subtypes) is

also possible through direct reprogramming of somatic cells. In fact, both mouse and human cells (e.g. fibroblasts) from all germ layers have been directly reprogrammed into neurons. This process again relies on the direct (by forced expression) or indirect (i.e. via microRNAs and small molecules) regulation of the activity of lineage-specific transcription factors so as to reassign cell fate. Direct reprogramming is potentially exciting, mainly due to the theoretical ability to convert any somatic cell into an 'induced dopaminergic neuron' but also because the described protocols to generate these are simpler, less expensive and much faster than 'traditional' methods of generating them via iPSC reprogramming. However, and despite constant advances in the field, 1) the actual properties of (and long-term expression of markers in) induced dopaminergic neurons are still not optimally studied, 2) gene expression profiling seems to significantly differ from A9 and A10 neurons, 3) engraftment into the striatum of Parkinson's disease mice is not as effective in correcting disease-related phenotypes in the animals and 4) the differentiation efficiency can be low (with only a small percentage of fibroblasts becoming neurons) (Caiazzo, Dell'Anno et al. 2011, Dell'Anno, Caiazzo et al. 2014, Arenas, Denham et al. 2015). For all the above reasons, we chose to generate iPSC-derived mDA neurons in order to study BPAN.

1.6.3. 3-Dimensional iPSC-derived systems for modelling neurological disorders

Despite the utility of iPSCs, an aforementioned issue to consider when used to model neurological disease is their 'fetal nature'/ immaturity but also lack of complexity; due to their two-dimensional organisation, more conventional iPSC-derived models lack the regional organisation characteristics and complex neural circuitry seen in actual patients or in animal models. This, in turn, means that aspects of neurobiology are not accurately represented and, subsequently, that some disease-related phenotypes (like Lewy body aggregation in Parkinson's disease) might not be easily elicitable in vitro. To address this, researchers have developed iPSC-derived 3-dimensional structures resembling the whole brain (labelled 'brain organoids') and exploiting the intrinsic ability of neural stem cells to self-organise and differentiate into three-dimensional structures not dis-similar to the actual organ *in vivo* (Lancaster and Knoblich 2014). Hinderances also exist, for instance the lack of

vascularisation and, thereby, nutrient supply (which inhibits growth and maturation potential) but organoids are overall thought to be a very useful tool for studying neurodevelopment and its disorders. Moreover, generation of organoids representing the midbrain (Midbrain-Like-Organoids, MLOs) and exhibiting mature features such as neuromelanin production, has recently been reported and will undoubtedly prove useful for better understanding disorders affecting that part of the CNS (Jo, Xiao et al. 2016).

In our project, we chose to use a 2-dimensional mDA neuronal differentiation protocol for studying BPAN, and this was based on two reasons. Firstly, we wanted to primarily study mDA neurons, and protocols for generation of MLOs are still not widely established (in fact, none had been published at the start of the project). Secondly, a main focus of our project was to identify potential novel and improved treatments for BPAN. Although drug screening using 3-dimensional models is a hot topic and likely to become more common practice in the future (Sachs, de Ligt et al. 2018), it is still largely unexplored, especially in neurological disorders. On the other hand, the use of iPSC-derived 2-dimensional models for drug screening is better established. Therefore, our initial goal was to use a 2-dimensional model [that was well established and proven to be efficient in generating A9 SN dopaminergic neurons (Kirkeby, Grealish et al. 2012, Kirkeby, Nelander et al. 2012)] and then perhaps validate any promising screen hits on more complex systems (such as an animal or, indeed, an organoid model) in future studies.

1.7. Hypothesis and Research Aims

In summary, BPAN is a devastating, early-onset and ultimately life-limiting, neurodegenerative disorder, for which there are currently no effective disease-modifying treatments. Additionally, current disease models often do not accurately recapitulate patient phenotypes and pathophysiological mechanisms governing BPAN are yet to be elucidated. The SN is the mostly affected brain area, but patient dopaminergic neurons are inaccessible for research; hence, a novel research approach needed to be adopted.

My **hypothesis** was that iPSC lines from patients with WDR45 deficiency and subsequent differentiation into mDA neurons will provide 1) a powerful research tool for understanding mechanisms leading to neuronal malfunction and early death as well as 2) an ideal platform for identifying novel, targeted and improved therapies for BPAN.

The **main aims** of this PhD project were:

a) to create a patient-derived, mDA neuronal model of BPAN, using iPSCs

b) to determine whether patient-derived mDA neurons recapitulate key features of BPAN

c) to evaluate disease mechanisms in WDR45-related disease

d) to evaluate the utility of this model as a drug screening platform by developing high content imaging phenotypic assays and performing small molecule library screens,

e) to identify drugs (hits) that ameliorate disease-related phenotypic defects in BPAN lines.

2. Materials and Methods

2.1. Key materials used

Key materials (factors, chemicals, kits, enzymes, plasticware, antibodies) used for this project are listed in **Table 2**.

Factors, Chemicals, Kits and Enzymes	
2-Mercaptoethanol 50mM	ThermoFisher (31350010)
100bp Ladder/ 6X Blue/Orange Loading Dye	Promega (G3161)
Accumax 100 mL	Sigma (A7089)
AccuPrime SuperMix I	ThermoFisher (12342010)
Agarose powder	Bioline (BIO-41025)
Alamar Blue Cell Viability Reagent	ThermoFisher Scientific (DAL1100)
B-27 Supplement (50X), minus vitamin A	ThermoFisher (12587-010)
Bafilomycin A1 from *Streptomyces griseus*	Sigma (B1793)
BCA Protein Assay Kit	ThermoFisher (23225)
BDNF	Miltenyi (130-093-811)
BigDye Terminator v1.1 Cycle Sequencing Kit	Thermo Fisher (4337451)
BioMix Red	Bioline (BIO-25006)
CHIR 99021	Tocris Bioscience (4423)
Clarity Western ECL Substrate	BioRad (1705061)
cOmplete, Mini, EDTA-free Protease Inhibitor Cocktail	Merck (11836170001)
CytoTune-iPS 2.0 Sendai Reprogramming Kit	ThermoFisher (A16517)
DAPI ((1 mg/ml))	Sigma (28718-90-3)
DAPT 10mg	Tocris (2634)
db-cAMP	Sigma (D0627-250MG)
Dithiothreitol (DTT)	Sigma (10197777001)
Dimethyl Sulfoxide (DMSO)	Sigma (D8418)
DMEM⁄F-12 (1:1) (1X), liquid - with L-Glutamine, without HEPES	ThermoFisher (11320-074)
DMEM, high glucose	ThermoFisher (41965039)
DMEM, high glucose, GLUTAMAX supplement	ThermoFisher (10566016)
DNase I, Amplification Grade	ThermoFisher (18068015)
DNeasy Blood & Tissue Kit	Qiagen (69506)
Dulbecco's Phosphate Buffered Saline (DBPS)	ThermoFisher (14190250)
EDTA 0.02% Solution	Sigma (E8008)
Fetal Bovine Serum	Sigma (F9665)
Fibronectin, Bovine Plasma Protein	ThermoFisher (33010018)
GDNF	Miltenyi (130-096-291)
Gelatin	Sigma (G9391)
GC Rich PCR System	Roche (12140306001)
Hoechst 33342	ThermoFisher (H3570)
Knockout DMEM	ThermoFisher (10829018)

Knockout Serum Replacement	ThermoFisher (10828018)
L-Ascorbic Acid	Sigma (A4403-100MG))
L-Glutamine, liquid, 200mM	ThermoFisher (2503081)
Laemmli 4x Sample Buffer	BioRad (161-0747)
Laminin from Engelbreth-Holm-Swarm murine sarcoma basement membrane	Sigma (L2020-1MG)
LDN193189	Sigma (SML0559-5MG)
Matrigel hESC-Qualified Matrix, LDEV-free, 5ml	Corning (354277)
MESA BLUE qPCR 2X MasterMix Plus for SYBR Assay	Eurogentec (RT-SY2X-03+WOUB)
MicroCLEAN Kit	Clent Life Science (MCL-1)
MiniProtean TGX Precast Gels 4-20%	BioRad (#4561096EDU)
mTeSR1 medium	StemCell technologies (85870)
MycoAlert mycoplasma detection kit	Lonza (LT07-218)
N2 Supplement	ThermoFisher (17502048)
Neurobasal medium	ThermoFisher (21103049)
Non-Essential Amino Acids 100x	ThermoFisher (11140035)
NucleoSpin Plasmid Kit	Macherey-Nagel (740588.50)
Penicillin/Streptomycin 10,000 U/ml	ThermoFisher (15140122)
Paraformaldehyde solution 4% in PBS	Santa Cruz (30525-89-4)
Precision Plus Protein Dual Color Standards	BioRad (1610374)
ProLong Gold Antifade Mountant	Thermo Fisher (P36930)
Purmorhamine (1mg)	Cayman Chemicals (10009634-1 mg-CAY)
ReleSR	StemCell Technologies (05873)
RIPA Buffer	Sigma (R0278-50ML)
RNeasy Mini Kit	Qiagen (74106)
SB431542 (10mg)	Cell Guidance Systems (sm33-10)
Sodium Pyruvate, 100mM	(ThermoFisher, 11360070)
Sonic Hedgehog C24II, Recombinant modified human	R&D Systems (1845-SH-025)
Superscript III Reverse Transcriptase	ThermoFisher (18080044)
SYBR™ Safe DNA Gel Stain	ThermoFisher (S33102)
TeSR E8 medium	StemCell Technologies (05990)
Thiazovivin (ROCK-Inhibitor)	Cambridge Bioscience (1681-1)
Torin1 mTOR inhibitor	Merck-Millipore (475991)
Trans-Blot Turbo Mini PVDF Transfer Packs	BioRad (1704156)
Tris-glycine-SDS running buffer 10X, 5L	BioRad (161-0772)
TrypLE	ThermoFisher (12563029)
Tween 20	Merck (P1379)
Trypsin-EDTA solution	Sigma (T4049)
Vitronectin XF	StemCell Technologies (07180)
Key Plasticware	
CellCarrier-96 Ultra Microplates	PerkinElmer (6055300)
Corning Costar TC-Treated Multiple Well Plates (6 well)	Sigma (CLS3516-50EA)
Corning Costar TC-Treated Multiple Well Plates (12 well)	Sigma (CLS3513-50EA)
Corning Costar TC-Treated Multiple Well Plates	Sigma (CLS3527-100EA)

(24 well)		
Corning 96 Well TC-Treated Microplates	Sigma (CLS3997-50EA)	
Corning cell culture flasks 25 cm^2	Sigma (CLS430372)	
Nunc Lab-Tek II Chamber Slide System	ThermoFisher (154453)	
Western Blot Antibodies		
Primary Antibody	**Company/ Catalogue Number**	**Dilution**
Beta Actin mouse monoclonal antibody (clone AC-15)	Sigma (A1978)	1:4,000
LAMP1 mouse monoclonal antibody	BD Biosciences (611042)	1:1,000
Ferritin Heavy Chain 1 (FTH1), Clone D1D4, rabbit monoclonal antibody	Cell Signalling (4393S)	1:1,000
LC3B rabbit polyclonal antibody	Sigma (L7543)	1:1,000
P62/SQSTM1 rabbit polyclonal antibody	Sigma (P0067)	1:1,000
Transferrin (D-9) mouse monoclonal antibody	Santa Cruz	1:1,000
WDR45 rabbit monoclonal antibody	Gift from Professor Sharon Tooze's laboratory, Francis Crick Institute, London, UK	1:250
Secondary Antibody	**Company/ Catalogue Number**	**Dilution**
Anti-mouse IgG, HRP-linked Antibody	Cell signalling technology (7076)	1:5,000
Anti-rabbit IgG, HRP-linked Antibody	Cell signalling technology (7074)	1:5,000
Immunofluorescence Antibodies		
Primary Antibody	**Company/ Catalogue Number**	**Dilution**
FOXA2 mouse monoclonal antibody	BD Pharmigen (561580)	1:500
LMX1A rabbit polyclonal antibody	Millipore (AB10533)	1:2,000
MAP2 Mouse monoclonal antibody	Sigma	1:400
NANOG Mouse monoclonal antibody	Millipore	1:500
OCT4 Mouse monoclonal antibody	Santa Cruz	1:50
SMA Rabbit monoclonal antibody	Abcam	1:100
SOX17 Goat polyclonal antibody	R&D Systems	1:20
TH Chicken polyclonal antibody	Aves	1:400
TRA-1-60 Mouse monoclonal antibody	Santa Cruz	1:200
TRA-1-81 Mouse	Millipore	1:200

monoclonal antibody		
TUJ1 Mouse monoclonal antibody	BioLegend	1:400
Secondary Antibody	**Company/ Catalogue Number**	**Dilution**
Alexa Fluor 488 Donkey Anti-Goat IgG	ThermoFisher (A-11055)	1:400
Alexa Fluor 488 Goat Anti-Mouse IgG	ThermoFisher (A-11001)	1:400
Alexa Fluor 488 Goat Anti-Rabbit IgG	ThermoFisher (A-11008)	1:400
Alexa Fluor 594 Goat Anti-Chicken IgG	ThermoFisher (A-11042)	1:400
Alexa Fluor 594 Goat Anti-Mouse IgM (for TRA-1-60 and TRA-1-81 antibodies)	Thermofisher (A-21044)	1:400
Alexa Fluor 594 Goat Anti-Rabbit IgG	ThermoFisher (A-11012)	1:400
High Content Immunofluorescence Antibodies		
Primary Antibody	**Company/ Catalogue Number**	**Dilution**
LAMP1 (CD107a), Clone H4A3, mouse monoclonal antibody	BD Biosciences (555798)	1:1,000
LC3B rabbit monoclonal antibody (clone D11)	Cell Signalling Technology (3868S)	1:200
P62/SQSTM1 rabbit polyclonal antibody	Sigma (P0067)	1:1,000
Secondary Antibody	**Company/ Catalogue Number**	**Dilution**
Alexa Fluor 488 Goat Anti-Mouse IgG	ThermoFisher (A-11001)	1:400
Alexa Fluor 488 Goat Anti-Rabbit IgG	ThermoFisher (A-11008)	1:400

Table 2. Key materials used for the project. *Factors, chemicals, kits, enzymes, plasticware and antibodies for immunofluorescence and western blotting (both primary and corresponding secondaries) are sub-categorised and listed in alphabetical order.*

2.2. Ascertainment of patient and control fibroblasts and iPSC lines.

Patient and control dermal fibroblasts used in this project were collected at either Great Ormond Street Hospital (GOSH), London, UK, or at Oregon Health and Science University (OHSU), Portland, Oregon, USA. Age-matched control dermal fibroblasts were ascertained from both the UCL Great Ormond Street Institute of Child Health (UCL GOS ICH) Dubowitz Biobank and OHSU. Fibroblasts from OHSU were shipped under appropriate Material Transfer Agreements between OHSU and University College London (UCL).

Reprogramming into iPSC either took place a) at UCL GOS ICH in Dr Manju Kurian's lab or b) at Professor Ludovic Vallier's laboratory, Wellcome Trust-Medical Research Council Cambridge Stem Cell Institute (Anne McLaren Laboratory for Regenerative Medicine, Cambridge, UK). Patients provided written informed consent for this study (REC reference 13/LO/0171). Both centres use a similar protocol based on Sendai virus-mediated delivery of four transcription factors (Sox2, Oct3/4, Klf4, c-Myc)(Fusaki, Ban et al. 2009) (the CytoTune-iPS 2.0 Sendai Reprogramming Kit, ThermoFisher, was used in the Kurian lab). As mentioned above, the use of multiple control and patient lines, including isogenic controls, was essential for downstream experiments to allow robust phenotypic comparisons between BPAN and wild-type lines.

I personally took part in consenting BPAN patients at GOSH for skin biopsy, fibroblast culture and subsequent reprogramming into iPSC. I also attended a BPAN research and family meeting in Portland, Oregon, USA (23-26/06/2016) where I physically examined patients and consented them for skin biopsy and fibroblast culture; subsequently, I helped draft the MTA between OHSU and UCL GOS ICH. I also cultured, expanded, stored dermal fibroblasts and shipped them to the Vallier lab for reprogramming. I was not otherwise involved in the iPSC reprogramming or CRISPR/Cas9-mediated genome editing process.

Finally, CRISPR/Cas9-mediated mutation correction in BPAN iPSC lines and creation of isogenic controls took place at the Vallier lab.

2.3. Cell Culture

All lines were cultured at 37°C, 5% CO2. Media, relevant reagents used and protocols for maintenance are detailed individually below for each line used.

2.3.1. Human Skin Fibroblasts

Media and Reagents

Lines were maintained in DMEM containing Glucose and GlutaMax (ThermoFisher) supplemented with Penicillin-Streptomycin (1%, 100 U/ml), Sodium Pyruvate (ThermoFisher, 100 mM, diluted 1:100) and 10% heat-inactivated Fetal Bovine Serum (FBS) (Sigma).

Line Maintenance

Cells were cultured in 25 cm^2 Corning cell culture flasks (Thermofisher) and were passaged every 5-7 days when fully confluent (depending on rate of cell division and number of cells passaged). For passaging, cells were washed in 1x Dulbecco's Phosphate Buffered Saline (DPBS, ThermoFisher) and 1ml of Trypsin-EDTA solution (Sigma) was added; after approximately 5 minutes of incubation at 37°C, 4 ml of complete DMEM was added and cells dissociated via gentle washing. Finally, 1 ml of cell suspension was transferred into a new 25 ml flask containing 4 ml of complete DMEM.

Reprogramming of fibroblasts into iPSCs with the CytoTune-iPS 2.0 Sendai Reprogramming Kit.

As mentioned above, I was not personally involved in the actual process of iPSC reprogramming; however, this briefly involved

- transfection of fibroblasts with the Sendai virus containing the 4 transcription factors (*OCT4, SOX2, KLF4, c-MYC*)
- transferring transfected cells onto plates pre-seeded with Mouse Embryonic Feeder cells (day 6 after transfection)

- manual picking of iPSC colonies and selection of iPSC clones (30-40 days after transfection)

- subsequent passaging of iPSCs (when colonies had reached appropriate confluency) with a non-enzymatic solution in order to select only pluripotent colonies (ReLeSR; Stem Cell Technologies).

- When iPSC clones were stable, transferring onto feeder free conditions using Matrigel and mTeSR™ 1 complete medium

- Expansion of at least 3 clones and freezing down/ banking at around passage 25.

2.3.2. IPSCs

Media and Reagents

mTeSR1 and TeSR-E8 complete medium for iPSCs

As per manufacturer's instructions, 5x mTeSR1 supplements (100 ml) were added to 400 ml of mTeSR1 basal medium. Medium was supplemented with 1% Penicillin-Streptomycin (stock concentration 10,000 U/ml, ThermoFisher). Similarly, for TeSR-E8, TeSR-E8 Basal Medium (480 mL) was mixed with TeSR-E8 25X Supplement (20 ml) and 1% Penicillin-Streptomycin (100 U/ml).

Coating with Matrigel and Vitronectin XF for iPSCs in culture

Firstly, 10 mg/ml of Matrigel (Corning) was resuspended in 25 ml Knockout DMEM (ThermoFisher). 1 ml was plated in a 6-well plate and incubated for at least 1 hour at 37°C. For VitronectinXF coating, 1 ml of Vitronectin XF was diluted in 25 ml of sterile 1 x DPBS, then plated onto 6-well plates for at least 1 hour at 37°C.

Media for iPSC spontaneous in vitro differentiation

Knock-out Serum Replacement (KOSR) complete medium

Medium composition (500 ml): 390 ml Knockout DMEM, 100 ml Knockout-Serum Replacement (20%; Invitrogen), 5 ml L-glutamine (2 mM; ThermoFisher), 5 ml Non-Essential Amino Acids 100x (1%, Invitrogen), 500 µl 2-Mercaptoethanol (50 mM; ThermoFisher).

DMEM plus 20% FBS

Constitution of 500 ml: 395 ml DMEM, 100ml (20%) FCS, 5ml (1%) Penicillin-Streptomycin (100 U / ml).

iPSC line maintenance

The iPSC lines obtained from UCL-GOS ICH were plated on 6-well plates (Corning Costar TC-Treated Multiple Well Plates, Sigma) precoated with Matrigel (Corning) and cultured in mTeSR1 complete media (StemCell Technologies) with daily media change and passaging every 5-7 days when fully confluent (depending on rate of cell division and number of cells passaged). The iPSC lines obtained from Cambridge (Professor Vallier's lab) were initially plated on Vitronectin XF (Stemcell Technologies)-coated plates and cultured in TeSR-E8 complete media (Stemcell Technologies) with daily media change and weekly passaging. Eventually, these lines were also transferred to matrigel-mTeSR1 culture conditions.

Passaging of iPSC lines. Cells were washed in 1x DPBS and 1 ml of Ethylenediaminetetraacetic acid (EDTA) was added; after approximately 5 minutes of incubation at 37°C, EDTA was aspirated and cells gently washed with culture media, then transferred to new matrigel (or Vitronectin XF)-coated plates. The ratio of passaging was usually 1 well into 2 wells. In order to minimise spontaneous differentiation appearing, newly-dissociated cells were often left to sediment to the bottom of a 15-ml Falcon tube filled with culture medium for 3-4 minutes; subsequently, most of the supernatant (containing differentiating single cells) was aspirated/ discarded and only the bottom 2ml (containing iPSC clumps) were plated.

All lines used were vigorously examined for pluripotency and any inappropriate lines discarded/ not used for downstream differentiations. Furthermore, all lines were maintained in culture for a maximum of 3 months after thawing (10-15 passages) in order to avoid acquisition of chromosomal/ genetic abnormalities. Additionally, testing for mycoplasma was regularly performed using the MycoAlert Mycoplasma Detection Kit (Lonza).

Removing spontaneously differentiating cells from iPSC lines

Gelatin 0.1% method: 6-well plates were coated with sterile 0.1% gelatin (Sigma) in Milli-Q water (H_20) and incubated at 37°C for 1-24 hours. IPSC lines exhibiting colonies of obvious spontaneous differentiation were harvested in TrypLE (ThermoFIsher), pelleted after centrifugation at 300x g for 5 minutes, re-suspended in mTeSR1 and Thiazovivin (Biovision) (stock concentration 10 mM, diluted 1:1,000 in culture medium to a final concentration of 10 μM), plated on the gelatin-coated wells and incubated at 37°C for 30-60 minutes (allowing for differentiating cells to adhere to the bottom of the plate). Subsequently, the medium (containing un-differentiated iPSCs) was gently aspirated and plated onto matrigel-coated plates.

ReleSR method: iPSCs in 6-well plates were washed in 1x DBPS, ReleSR was applied for 20-30 seconds and, then, wells were left to dry out for 4 minutes at room temperature. Subsequently, non-differentiating iPSC colonies were dissociated by adding 1ml/well of culture medium and gently tapping the plate, then plated onto newly coated plates.

Spontaneous Differentiation of iPSCs in vitro

After harvesting with TrypLE, iPSCs were centrifuged for 5 min at 300x g and resuspended in full KOSR medium (composition detailed above), plus added Thiazovivin (10 μM). For Embryoid Body (EB) formation, on Day 0, 2 x 10^6 iPSCs were plated on a 6-cm non-adherent Petri dish and the medium was changed in 48 hours. On day 4, EBs were seeded into a 24-well plate (Corning) for spontaneous differentiation into all three germ layers. For mesodermal differentiation, wells were

coated with 0.1% gelatin and cells maintained in DMEM plus 20% FBS. For neuroectoderm and endoderm differentiation, wells were coated with matrigel and cells maintained in full KOSR medium. Medium change took place every 48 hours. On Day 16, cells were fixed and stained for expression of 1) endoderm-related protein SRY-BOX 17 (SOX17), 2) the mesoderm-related Alpha Smooth Muscle Actin (SMA) and 3) the neuroectodermal Neuronal Class III β-Tubulin (TUJ1) (protocol for immunofluorescence described in **Section 2.8**).

CRISPR/Cas9-mediated correction of disease-causing mutations in iPSC lines.

As mentioned above, I was not personally involved in the actual process of CRISPR/Cas9 genome editing; however, this briefly involved

- targeting the region of interest in the genomic DNA by a 20-nucleotide guide sequence in the sgRNA (electroporated into the iPSCs)
- introducing a double-stranded break in the target DNA via the Cas9 (also electroporated into the iPSCs)
- promoting HDR through the delivery of an artificial repair template (Single Strand Oligodeoxynucleotides) (again, delivered via electroporation)
- the introduction of a specific DNA sequence at the specified genomic location (that included correction of the *WDR45* mutation but also 'silent'/ synonymous mutations in adjacent nucleotides in order to avoid repeated editing once the desired correction had occurred); this DNA sequence would lead to translation of a full-length WDR45 protein.
- Single iPSC clone expansion and selection of the correctly edited ones via gene sequencing

The sgRNA and HDR donor templates for the CRISPR corrections are detailed below:

Patient 02 (587-02):

sgRNA 1: ATGACTCAACAGCCACTTTG AGG (reverse strand)

sgRNA 2: AGGCTGGTCACTCCTCAAAG TGG (forward strand)

HDR Donor Template:

C*T*C*TCTCACTTTGGTCTTGGTTGAAACGCAGGCTGGTCACTCCTCGTAATGGCTGTTGAGTCATGGTG CAGGATTGTTCCTCTGCAT*A*C*A

Patient 03 (535-02):

sgRNA 1: AAACTGGTGGAGCTGCGCTG AGG (reverse strand)

HDR Donor Template:

C*A*T*ACCCTGTGCTCACCAGTAGAGGGTGGCAGGGTCAGTGCCTCGTCTCAGCTCCACCAGTTTCTCCT TGGATTGTGTGTCAAAGAG*G*C*G

2.3.3. IPSC neuronal differentiation (mDA neurons)

Media and Reagents

The constitution of the medium for each stage of differentiation, as well as relevant concentrations, are detailed in **Table 3**.

mDA Neuronal Differentiation Protocol		
Medium	**Constituents**	**Dilution**
EB medium (D0-D4)	DMEM/F12:Neurobasal medium	1:1
	N2 supplements	1:100
	B-27 supplements (ThermoFisher)	1:50
	L-Glutamine	(1mM) 1:100
	Penicillin/ Streptomycin	1:100
	Thiazovivin (Rock inhibitor) (on D0, only)	10µM 1:1000
	SB431542	10µM 1:1000
	LDN193189	100nM 1:100000
	CHIR99021	0,8µM 1:1250
	SHH	100ng/ml 1:250
	Purmophamine (from D2 onwards)	0.5µM 1:20000
ND medium (D4-D11)	DMEM/F12:Neurobasal medium	1:1
	N2 supplements (ThermoFisher)	1:200
	B-27 supplements (ThermoFisher)	1:100
	L-Glutamine	1mM 1:100
	Penicillin/ Streptomycin	1:100
	SB431542 (out on D6)	10µM 1:1000
	LDN193189 (out on D9)	100nM 1:100000
	CHIR99021 (out on D9)	0,8µM 1:1250
	SHH (out on D9)	100ng/ml 1:250
	Purmophamine (out on D9)	0.5µM 1:20000
FD medium (D11-D14)	Neurobasal medium	1
	B-27 supplements	1:50
	L-Glutamine	1mM 1:100
	Penicillin/ Streptomycin	1:100
	L-Ascorbic Acid (Sigma)	0,2mM 1:250
	BDNF	20ng/ml 1:500
FDf medium (D14-D65)	Neurobasal medium	1
	B-27 supplements	1:50
	L-Glutamine	1:100
	Penicillin/ Streptomycin	1:100
	Ascorbic Acid	0,2mM 1:250
	BDNF	20ng/ml 1:500
	GDNF	20ng/ml 1:500
	db-cAMP	0,5mM 1:200
	DAPT (from D30 onwards)	10µM 1:1000

Table 3. Constitution of media used during the neuronal differentiation protocol. *Shaded rows indicate constituents removed or added on specific days during the mDA neuronal differentiation protocol.*

Coating of wells with poly-L-ornithine and Fibronectin/Laminin (**PO/Fn/Lam**) was performed as follows: poly-L-ornithine (PO) (Sigma) 15 µg/ml, in 1x DPBS, was added to wells and incubated at 37^{o}C for 48 hours (approximately 70 µl/well in a 96-well plate, 350 µl in a LabTek slide, 700 µl in a 12-well plate). After 48 hours, wells were washed three times in 1x DPBS and Fibronectin/ Laminin (Fn/Lam) [prepared by diluting Fibronectin (ThermoFisher) and Laminin (Sigma) in 1x DPBS to 5 µg/ml] added; plates were incubated at 37^{o}C for another 48 hours.

Neuronal Differentiation Protocol

The iPSC mDA neuronal **differentiation protocol** is adapted from (Kirkeby, Grealish et al. 2012, Kirkeby, Nelander et al. 2012) and summarised in **Figure 7.** More details on basic embryology of generating dopaminergic neurons can also be found in the Results Section. Concentrations of factors are detailed in **Table 3.** The protocol started on Day 0 with formation of embryoid bodies (EB) by placing dissociated iPSCs on a non-adherent petri dish. For the first two days, the use of a p160-Rho-associated coiled-coil kinase (ROCK)-Inhibitor, thiazovivin, aided the survival and self-renewal of dissociated iPSCs (Watanabe, Ueno et al. 2007, Xu, Zhu et al. 2010). Dual SMAD inhibition to induce neural identities also took place on Day 0, through addition of SB431542 (Cell Guidance Systems) (for 6 days) and LDN193189 (Sigma) (for 9 days). SB431542 blocks Transforming growth factor (TGF) beta and LDN193189 inhibits the Bone Morphogenetic Protein (BMP) pathway; combined action of these two compounds has been shown to trigger differentiation of iPSCs into CNS neural precursors (Qi, Zhang et al. 2017). Sonic hedgehog (SHH-C24II, R&D Systems) and the SHH pathway activator Purmorphamine (Cayman Chemicals) were used to 'ventralise' the cells (guide them towards floorplate identities) (for 9 days) (Sinha and Chen 2006). Moreover, CT99021 (CHIR 99021, Tocris), a GSK3 inhibitor, activated the WNT1 pathway and was used to guide cells towards midbrain fates (for 9 days). Later addition of BDNF (Miltenyi) (from Day 11) and GDNF (Miltenyi) (from Day 14) helped the development and survival of mDA progenitors (Arenas, Denham et al. 2015), while dibutyryl-cAMP (db-cAMP) (Sigma) (from Day 14) and the notch inhibitor N-[N- (3,5-Difluorophenacetyl)-L-alanyl]-S-phenylglycine t-butyl ester (DAPT) (Tocris) (from Day 30) also helped with mDA neuronal

survival and induction of mature neuronal morphologies (Kirkeby, Nelander et al. 2012). The exact constitution of the medium used in each step is described above in **Table 3**.

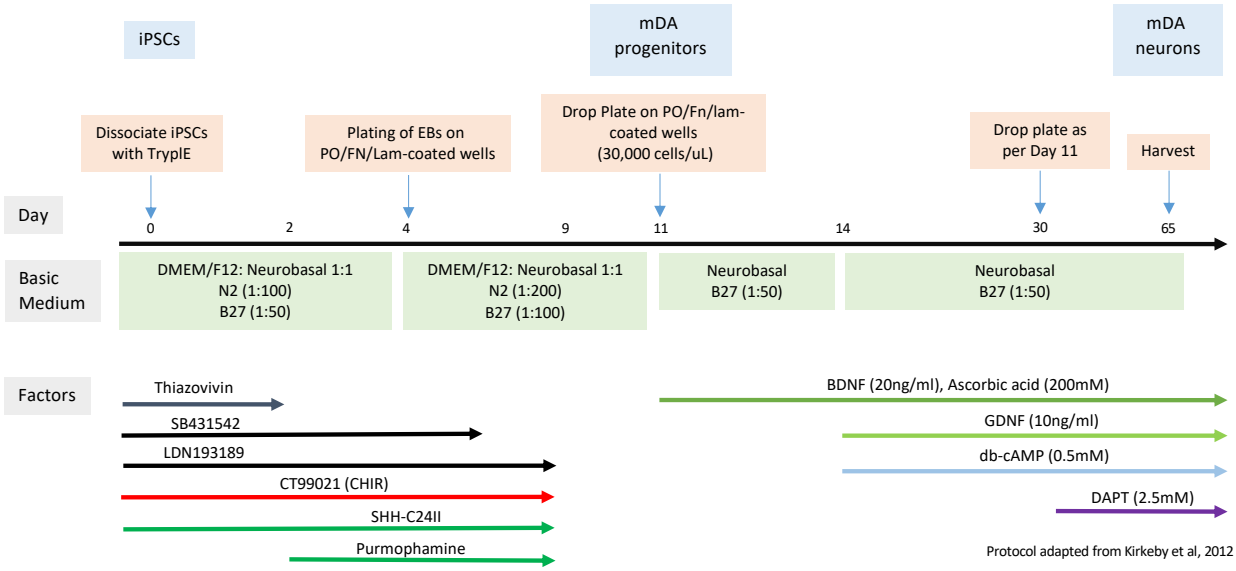

Figure 7. Protocol for dopaminergic neuronal differentiation. *Adapted from Kirkeby et al, 2012(Kirkeby, Grealish et al. 2012, Kirkeby, Nelander et al. 2012). My aim is to create A9-type mDA neurons that populate the substantia nigra and are derived from the ventral midbrain. Hence, firstly, dual SMAD inhibition via SB431542 and LDN193189 induces neuronal identities. Additionally, Sonic Hedgehog (SHH-C24II) and purmorphamine (SHH analogue) push cells towards ventral identities, while CT99021 (CHIR) guides cells towards midbrain fates. Finally, other neurotrophic factors (such as BDNF, GDNF, DAPT) and additives (e.g. B27, which contains nutrients and antioxidants) ensure neuronal survival and mature neuronal morphologies at the end of the differentiation protocol. Finally, the cell density during drop plating is very important for the survival and differentiation of mDA progenitors. On one hand, cells need to be maintained at a high density to avoid cell death and loss specific cell subtypes. On the other hand, higher than optimal densities could also lead to cell death or dysregulated neuronal maturation. Abbreviations: EBs= embryoid bodies, mDA= midbrain dopaminergic.*

On day 0 of differentiation, EBs were prepared by 1) harvesting iPSCs with TrypLE and mTeSR1, 2) centrifugation at 300g x 5min, 3) re-suspending in EB medium and plating on non-adherent Petri dishes. On day 2, the EB medium was changed by collecting EBs in 15-ml Falcon tubes, centrifuging at 200g for 1 minute, re-suspending the pellet in freshly-prepared EB medium and replating on the same non-adherent Petri-dish. On day 4, the EBs were collected in a 15-ml Falcon tube, centrifuged at 200g for 1 minute, re-suspended in freshly prepared ND Day 4 medium and plated on poly-L-ornithine/ Fibronectin/ Laminin-coated 12-well plates (Corning) (methodology for coating described below). Media were changed every 48 hours. On day 6, ND medium without SB431542 and, on day 9, ND medium without SB431542, LDN193189, CHIR99021, SHH and Purmophamine were used. On day 11, the dopaminergic progenitors were re-plated on PO/Fn/Lam-coated 12-well plates via drop plating (see next paragraph and **Figure 7**) for final differentiation. On day 14, the medium was switched to Final Differentiation medium f (FDf). On Day 30, the cells were replated [again, via drop plating, on both PO/FN/Lam-coated 12-well plates and also LabTek slides (Nunc Lab-Tek II Chamber Slide System, Thermofisher)] and DAPT was added to the medium. Subsequently, medium changes occurred every 48 hours and cells were harvested at Day 65 for RNA, DNA and protein extraction, as well as immunofluorescence experiments. At the time of harvesting, Day 65 cells were either untreated or had been exposed to 3-hour treatments with autophagy-inducing or inhibiting drugs. These were 1) **Torin1 (**Merck-Millipore**)** (dissolved in DMSO, at 250 uM stock concentration; then at 1:1,000 dilution in cell culture medium and 250 nM final concentration) (mTOR inhibitor, hence causing autophagy flux induction), 2) **Bafilomycin A1** (Sigma) (from *Streptomyces griseus*, dissolved in DMSO, at a stock concentration of 10 uM; subsequently at 1:1,000 dilution and 10 nM final concentration) (blocks the fusion of autophagosomes with lysosomes and hence causes autophagy flux inhibition), 3) **a combination of Bafilomycin A1** (10 nM) **and Torin1** (250 nM) and 4) **DMSO** (1:1,000 dilution) as (negative) control.

Drop plating of Day 11 and Day 30 mDA neuronal progenitors

The Fn/Lam coating (described in **Section 2.3.2**) was aspirated and the (PO/Fn/Lam-coated) plate left open to dry inside the sterile tissue culture hood. The cells (at Day 11 or Day 30) were washed with DPBS and incubated with 500µl of Accumax (Sigma) for 20min at 37°C. KOSR complete medium was used to stop the enzymatic reaction and cells were pelleted by centrifuging at 300g for 5 minutes, re-suspended in appropriate medium (FD and FDf for Day 11 and Day 30 cells, respectively) and plated in drops at a dilution of 30,000 cells/µl. The cell drops were incubated for 1hour at 37°C and, once cells were attached to the plate, more medium was added.

2.4. Genomic DNA extraction

Genomic DNA was extracted from cell pellets using the DNeasy Blood & Tissue Kit (Qiagen). Pelleted cells were resuspended in 200 µl 1x DPBS supplemented with 1:10 proteinase K. For **cell lysis**, 200 µl of buffer AL was added to the cells and mixed thoroughly by vortexing, followed by incubation at 56°C for 10 min. For **DNA precipitation**, 200 µl of 100% ethanol was added to the sample and mixed thoroughly by vortexing. The mix was then transferred into DNeasy Mini spin columns placed within collection tubes and centrifuged at 8,000x g for 1 min; flow through and collection tubes were then discarded. Columns were washed with 500 µl AW1 buffer (stringent washing buffer containing low concentrations of quinidine), centrifuged for 1 min at 8,000 x g, and tubes and flow through discarded. Columns were washed again with 500 µl AW2 buffer (tris-based ethanol solution to remove salts) and centrifuged for 3 min at 14,000x g, tubes and flow through discarded. DNA **elution** was performed in 100 µl of elution buffer after 1 min incubation at room temperature and centrifugation for 1 min at 8,000x g. The purity and concentration of the extracted DNA was measured with the UV-Vis spectrophotometer NanoDrop™ 1000 (Thermo Fisher Scientific). Extracted DNA samples were stored at -20°C for future use.

2.5. RNA extraction and complementary DNA (cDNA) conversion

Total RNA extraction from pellets was performed using the RNeasy Mini Kit (Qiagen). Collected cells were lysed in RLT buffer (containing guanidinium isothiocyanate to break the cell walls and denature RNAses) and 500 µM β-mercaptoethanol (which allows breaking down of disulphide bonds from RNases and prevents degradation of the RNA). Samples were homogenised by vortexing for 1 min. Subsequent addition of equal volume of 70% ethanol precipitated the RNA. After binding to a silica membrane through centrifugation (for 15 s at 8,000x g), the RNA was washed with 700 µl RW1 buffer containing guanidine salt and ethanol (in order to remove carbohydrates, proteins and fatty acids) and centrifuged for 15 s at 8,000x g. The column was then washed with 500 µl of buffer RPE containing ethanol, for the removal of traces of salt. The sample was then centrifuged for 15 s at

8,000x g. A second washing step with RPE was performed and column was centrifuged for 2 min at 8,000x g. The RNA was then eluted with RNA-free H_20 with centrifugation for 1 min, 8,000x g. Purity and concentration of the extracted RNA was measured with the UV-Vis spectrophotometer NanoDrop™ 1000. The product was then stored at -80°C for further use.

Subsequently, **RNA purification** took place using the DNase I Kit (ThermoFisher). DNase I digests single- and double-stranded DNA to oligodeoxyribonucleotides. For this, 1 µg of RNA sample was mixed with 1 µl 10x DNase I Reaction Buffer, 1 µl DNase I and Nuclease-Free H_20 to 10 µl. The mix was incubated for 15 min at room temperature. To inactivate the DNAse I, 1 µl of EDTA solution was added and incubated for 10 min at 65°C.

Reverse transcription took place using Superscript III Reverse Transcriptase kit (ThermoFisher). In brief, 1 ug of RNA (diluted to a volume of 10µl) was mixed with 1 µl of oligo(dT) primers, 1 µl of dNTP Mix and 1 µl of Nuclease-Free H_20. The mix was incubated for 5 min at 65°C, and subsequently for 1 min on ice. After this, 4 µl 5x first-strand buffer, 1 µl 0.1 M (DTT), 1 µl Nuclease-Free H_20, and 1 µl SuperScript™ III Reverse Transcriptase were added (total volume 20 µl), and samples were processed for 60 min at 50°C and 15 min at 70°C, in order to generate complimentary DNA (cDNA). Finally, cDNA was either 1) stored at -20°C (for testing of SeV clearance) or 2) pre-diluted at 1:25 (total 500uL), aliquoted and stored at -20°C for downstream experiments.

2.6. Protein extraction

Firstly, each cell pellet was resuspended in 200 µl RIPA buffer (Sigma) containing cOmplete Mini Protease Inhibitor Cocktail (Merck) (1:10 dilution). After vortexing for 1 min, samples were incubated on ice for 30 min and subsequently centrifuged at 13,000x g for 15 min at 4°C. The collected protein lysate was then used for quantification of protein concentration using the Pierce BCA Protein Assay Kit (ThermoFisher). For this, 1) 10 µl of each sample, as well as 2) 7 separated prediluted protein standards and a 'blank' sample (H_2O), were loaded onto 96-well plates (Corning 96 Well TC-Treated Microplates, Sigma), each in triplicates. Afterwards, 200 µl of reagent mix A and

B (A:B ratio of 1:50) was added to all samples and standards and the plate was incubated for 30 min at 37°C. Finally, sample absorbance (y) at 555 nm was measured in a multiplate reader. Data analysis to determine the protein concentration **x** for each sample was undertaken using the linear equation:

$$y = m * x + t$$

and therefore:

$$x = \frac{y - t}{m}$$

Values m and t were specified according to the absorbance readings of the standards and the 'blank' sample.

2.7. Western Blot

Protein levels were quantified using the Pierce BCA Protein Assay Kit as described above. For immunoblotting, 10 µg of protein were mixed with (7.5 or 6 µl) 4x Laemmli Buffer (Bio-Rad), (6 or 5 µl of) 0.1 M Dithiothreitol (DTT) (Sigma) and H_20 (for a total sample volume of 30 µl or 20 µl, respectively, and according to protein concentrations). Samples were vortexed, centrifuged and heated for 5 min at 95°C. Samples [alongside with Precision Plus Protein Standards (BioRad) to aid band identification] were loaded onto 4-20% Mini-PROTEAN TGX Precast Gels (BioRad) and electrophoresed, in 1x Tris-glycine-SDS running buffer (BioRad), at 100 V for 80-90 minutes (or 300 V for 15 minutes), to allow adequate separation of different molecular weight protein bands. Proteins were then transferred onto Trans-Blot® Turbo™ Mini PVDF Transfer membranes [with the Trans-Blot Turbo Transfer System (Bio-Rad) at 25 V, 2.5 A for 7 min], before blocking with 5% skimmed milk in PBS with added Tween20 (Merck) (0.05%, 0.5ml in 1 litre) (PBST) for 1hour at room temperature or at 4**°**C overnight. The membrane was probed with primary antibody in blocking buffer at room temperature for 1 hour, or overnight at 4**°**C. After washing with PBST, the membrane was incubated in corresponding HRP-conjugated secondary antibodies in blocking buffer for 1-2 hours at room temperature (or overnight at 4**°**C). Further washes were carried out prior to development using HRP substrate (Clarity Western ECL Substrate, BioRad) followed by exposure on an ImageQuant chemilumenscent imaging system (GE) or the BioRAD Gel Doc Imager and imaging using the ImageLab software (BioRAD). Images were exported to .tiff format prior to quantification of band intensities with ImageJ/Fiji software. A list of primary (and secondary HRP-linked antibodies) used is provided in **Table 2.** Antibodies that were trialled but not fully optimised are not detailed.

2.8. Immunofluorescence

Cells were washed in 1x DPBS, fixed with 4% Paraformaldehyde (PFA) in PBS (Santa Cruz) and subsequently stained for markers of interest. Blocking was performed in 1x DBPS, 10% FBS, with (for nuclear markers) or without (for membrane markers) 0.1% of 100X Triton for cell membrane permeabilisation (for Day 65 mDA neurons, only, 0.3% Triton was used). After incubation with the primary antibody solution (at an appropriate concentration, diluted in blocking solution, for 1 hour at room temperature or at +4°C overnight), cells were incubated with the secondary antibody (60 min at room temperature in the dark) and finally with DAPI (1 mg/ml) or Hoechst 33342 (1:1,000 and 1:1,0000, respectively) for 10 minutes at room temperature in the dark). For iPSCs, Day 11 progenitors and spontaneous *in vitro* differentiation experiments, images were acquired using the inverted Fluorescence microscope Olympus IX71 (UCL GOS ICH) (10x or 20x air objectives). For Day 65 mDA neuronal immunofluorescence-based experiments, cells were cultured on LabTek slides from Day 30 onwards. After fixing, blocking, cell membrane permeabilization, and staining for markers of interest, LabTek slide cases were removed and coverslips mounted with ProLong Gold Antifade Mountant (ThermoFisher). Slides were stored in +4°C or -20°C, in the dark prior to imaging. Images were taken on the multiphoton confocal microscope (Zeiss LSM880) (UCL GOS ICH) or Leica TCS SP8 STED confocal laser scanning microscope (UCL MRC Laboratory for Molecular Cell Biology) using a 20x water or oil immersion objective, respectively.

After image acquisition (10X and 20X objectives), image analysis was performed using the ImageJ/Fiji software. Where relevant, marker quantification (for Day 11 mDA progenitors and Day 65 mDA neurons, as detailed in the Results section) was performed (on images acquired at 20x magnification) for three independent experiments. For each experiment, three random fields were imaged and 1500-1800 cells (DAPI-positive) randomly selected; subsequently, cells staining positive for markers of interest were manually counted. For staining of more than one marker in each well, antibodies raised in different species were used. All primary and corresponding secondary

antibodies used for iPSC, Day 11 progenitor and Day 65 mDA neurons are detailed in **Table 2** and in the relevant Results sections.

Finally, High Content Imaging-based immunofluorescence experiments for phenotypic assay set up and subsequent drug screening were also performed. These will be detailed in **Section 2.17** and, subsequently, in the relevant Results section.

2.9. Reverse transcriptase (RT) Polymerase Chain Reaction (PCR)

Firstly, in order to detect **pluripotency marker expression (***GAPDH, SOX2, cMYC, NANOG, OCT4* and *KLF4*) in iPSCs, RT PCR was performed on cDNA from each iPSC line. Primers used are summarised in **Table 4**.

Primer name	Sequence (5'-3')	PCR product size (bp)
***GAPDH* F**	ATCCCATCACCATCTTCCAG	382
***GAPDH* R**	CCATCACGCCACAGTTTCC	
***OCT4* F**	CGAAACCCACACTGCAGCAG	402
***OCT4* R**	CCTGGCACAAACTCCAGGTTT	
***SOX2* F**	GGGAAATGGGAGGGGTGCAAAAGAGG	151
***SOX2* R**	TTGCGTGAGTGTGGATGGGATTGGTG	
***NANOG* F**	CAGCCCCGATTCTTCCAGTCCC	343
***NANOG* R**	CGGAAGATTCCCAGTCGGGTTCACC	
***c-MYC* F**	GCGTCCTGGGAAGGGAGATCCGGAGC	328
***c-MYC* R**	TTGAGGGGCATCGTCGCGGGAGGCTG	
***KLF4* F**	ATATCCCGCCGTGGGTGAAAGTTC	243
***KLF4* R**	ACTCAGCCATGGACTGGAGCATCC	

Table 4. Primer pairs for detection of pluripotency marker expression via RT PCR. *F= forward, R= reverse*

For each tested pluripotency marker, a mix of 20 µL per iPSC sample was loaded onto 96-well PCR plates and ran as detailed in **Table 5**.

Mix Constitution	
GAPDH, SOX2, cMYC, NANOG, OCT4	**KLF4**
Forward/ Reverse Primer Mix 0.4µl	Forward/ Reverse Primer Mix 0.4 µl
BioMix Red 10 µl	BioMix Red 10 µl
H_20 (RNAase/DNAase free) 7.2 µl	GC rich resolution solution 4 µl
cDNA 2 µl	GC reaction buffer 3.2 µl
	cDNA 2 µl
PCR Conditions	
GAPDH, SOX2, cMYC, NANOG	**OCT4, KLF4**
95°C 5 min (initial step)	95°C 5 min (initial step)
35 cycles: 95°C 30 sec 60°C 45 sec 72°C 1 min	35 cycles: 95°C 30 sec 58°C 45 sec 72°C 1 min
72°C 5 min	72°C 5 min

Table 5. Mix constitutions and PCR conditions for RT PCR experiments

Moreover, in order to confirm that iPSC lines have no virus or transgenes detectable in their genome, an **SeV clearance analysis** was performed using the CytoTune-iPS 2.0 Sendai Reprogramming Kit. Detection of the SeV genome and SeV-carried pluripotency genes in iPSCs was

performed through RT PCR using cDNA from each iPSC line and primers already provided by the kit (**Table 6**).

Primer name	Sequence (5'-3')	PCR product size (bp)
SeV F	GGATCACTAGGTGATATCGAGC	181
SeV R	ACCAGACAAGAGTTTAAGAGATATGTATC	
SeV *SOX2* F	ATGCACCGCTACGACGTGAGCGC	451
SeV *SOX2* R	AATGTATCGAAGGTGCTCAA	
SeV *KLF4* F	TTCCTGCATGCCAGAGGAGCCC	410
SeV *KLF4* R	AATGTATCGAAGGTGCTCAA	
SeV *c-MYC* F	TAACTGACTAGCAGGCTTGTCG	532
SeV *c-MYC* R	TCCACATACAGTCCTGGATGATGATG	
SeV *OCT4* F	CCCGAAAGAGAAAGCGAACCAG	483
SeV *OCT4* R	AATGTATCGAAGGTGCTCAA	
***GAPDH* F**	ATCCCATCACCATCTTCCAG	382
***GAPDH* R**	CCATCACGCCACAGTTTCC	

Table 6. Primers used for Sendai Virus Clearance-related RT PCR experiments. *F= forward, R= reverse, SeV= Sendai Virus*

The RT PCR mix consisted of 10 µl cDNA, 10 µl AccuPrime SuperMix I (ThermoFisher) and 2 µl forward/ reverse primer mix. The thermal cycle conditions are summarised in **Table 7**.

SeV Clearance- RT PCR conditions		
Number of cycles	**Temperature (°C)**	**Time (s)**
1	95 (denaturation)	300
35	95 (denaturation) 55 (Tm) 72 (elongation)	30 30 30 (per Kb)
1	72 (elongation)	300

Table 7. PCR conditions for Sendai Virus Clearance-related RT PCR experiments

The PCR products were electrophoresed on Agarose (Bioline) gels (1.5% and 2% for iPSC pluripotency markers and SeV clearance, respectively) in 1x TBE buffer, supplemented with SYBR Safe DNA Gel Stain (ThermoFisher) (5 µl per 100mL) at 100V for 75 minutes, with a mixture of 100bp Ladder and 6x Loading Dye (Promega) used as a molecular weight marker. Band detection was performed using the ImageLab software. For both processes, cDNA samples from H9 embryonic stem cells and a control human dermal fibroblast line were used as controls. As a positive control for SeV clearance, SeV genome was used.

2.10. Real-time Quantitative Reverse Transcriptase PCR (qRT PCR)

A list of qRT PCR primers for detection of markers relevant for each stage of differentiation is provided in **Table 8**.

qRT PCR primers	
Primer name	**Sequence (5'-3')**
***GAPDH* F**	TTGAGGTCAATGAAGGGGTC
***GAPDH* R**	GAAGGTGAAGGTCGGAGTCA
***FOXA2* F**	CCGTTCTCCATCAACAACCT
***FOXA2* R**	GGGGTAGTGCATCACCTGTT
***EN1* F**	CGTGGCTTACTCCCCATTTA
***EN1* R**	TCTCGCTGTCTCTCCCTCTC
***EN2* F**	CCTCCTGCTCCTCCTTTCTT
***EN2* R**	GACGCAGACGATGTATGCAC
***LMX1A* F**	CGCATCGTTTCTTCTCCTCT
***LMX1A* R**	CAGACAGACTTGGGGCTCAC
***LMX1B* F**	CTTAACCAGCCTCAGCGACT
***LMX1B* R**	TCAGGAGGCGAAGTAGGAAC
***OCT4* F**	TCTCCAGGTTGCCTCTCACT
***OCT4* R**	GTGGAGGAAGCTGACAACAA
***NANOG* F**	TTGGGACTGGTGGAAGAATC
***NANOG* R**	GATTTGTGGGCCTGAAGAAA
***TH* F**	CGGGCTTCTCGGACCAGGTGTA
***TH* R**	CTCCTCGGCGGTGTACTCCACA
***DAT* F**	TCACCAACGGTGGCATCTAC
***DAT* R**	CACTCCGATGGCTTCGATGA
***NURR1* F**	TGCGAGCAGAGAGGGAGTAG
***NURR1* R**	TCGACATTTCTGCCTTCTCCTG
***SNCA* F**	GGAGTGGCCATTCGACGAC
***SNCA* R**	CCTGCTGCTTCTGCCACAC
***MAPT* F**	CTCGCATGGTCAGTAAAAGCAA
***MAPT* R**	GGGTTTTTGCTGGAATCCTGGT
***WDR45* F**	TGCGCCATGACAAGATCGT
***WDR45* R**	ACTCAAACAGCTTTCGGGGAT

Table 8. qRT PCR primers used for Day 11 (shaded row) and Day 65 (non-shaded rows) characterisation.
Abbreviations: F= forward; R= reverse

Firstly, 20 µl cDNA (derived from 1 ug of RNA) had been pre-diluted to a total volume of 500 µl; this was further diluted 1:1 with Nuclease-Free Water. A master mix was also prepared [10 µl of MESA BLUE qPCR 2X MasterMix Plus for SYBR Assay (Eurogentec) and 1 µl of Forward and Reverse primer mix per sample]. Subsequently, 9 µl of diluted cDNA and 11 µl of master mix were added to each well and plates were centrifuged at 2,000x g for 2 minutes to allow mixing. All gene targets were tested in triplicates for each sample. An internal control was loaded to each plate for each

target, again in triplicates, in order to allow value normalisation between plates (and account for plate-to-plate variability).Finally, qRT-PCR was performed with the StepOnePlus Real-Time PCR System (Applied Biosystems) with the following protocol (**Table 9**):

qRT PCR Thermal Cycling Protocol	
1 cycle:	5 min (initial denaturation step)
40 cycles:	95**°**C 15 sec (denaturation) 60**°**C 60 sec (annealing/ extension)

Table 9. Thermal cycling programme for qRT PCR experiments.

Gene expression was analysed using the $\Delta\Delta C_T$ method:

$$\Delta C_T = C_T \text{ target} - C_T \text{ GADPH}$$

$$\Delta\Delta C_T = \Delta C_T \text{ sample} - \Delta C_T \text{ control}$$

$$\text{Fold change (FC)} = 2\text{^} - (\Delta\Delta C_T)$$

Mr Dimitri Budinger, Research Assistant in the Kurian lab, UCL GOS ICH, kindly performed most of the Day 65 qRT PCR experiments.

2.11. Epi-Pluri-Score

The Epi-Pluri-Score analysis was outsourced to (and performed by) Cygenia. Genomic DNA (> 5 µl at a concentration of > 200 ng/µl) from iPSC lines was extracted and sent off for this analysis. The Epi-Pluri-Score is a simple and robust biomarker that distinguishes between pluripotent and non-pluripotent cells. DNA-methylation levels (β-values) are measured by pyrosequencing at three specific CpG sites, within the genes *ANKRD46*, *C14orf115*, and *POU5F1 (OCT4)*. The CpG sites at *ANKRD46* and *C14orf115* in pluripotent cells are methylated and non-methylated, respectively, and these β-values are combined into the Epi-Pluri-Score. A positive Epi-Pluri-Score indicates pluripotency. However, methylation within *POU5F1* might indicate early differentiation, so this β-value is also factored in (Lenz, Goetzke et al. 2015).

2.12. Single Nucleotide Polymorphism (SNP) array analysis for iPSC karyotype integrity

10 ug of genomic DNA from iPSC lines (concentration of > 75ng/µl) were sent off to UCL Genomics for analysis using the Infinium HumanCytoSNP-12 v2.1 BeadChip array. Subsequently, I analysed the raw SNP array data (in .idat file format) using the Illumina's Bluefuse Multi software (https://www.illumina.com/clinical/clinical_informatics/bluefuse.html).

2.13. XCI Studies

Genomic DNA from fibroblasts, iPSCs and mDA neurons deriving from female BPAN patients was sent off to the NE Thames Regional Genetics Laboratory at Great Ormond Street Hospital. XCI status was studied in the regional genetics laboratory by examining differences in methylation at the human Androgen Receptor (AR) locus. AR is located on the X Chromosome and the assay is based on fluorescent PCR in the presence and absence of the methylation-sensitive restriction enzyme HpaII. Firstly, maternal and paternal X chromosomes carry different numbers of CAG repeats at the AR locus. Secondly, HpaII methylation-sensitive restriction sites are located close to the CAG repeat-containing regions. HpaII digestion removes the unmethylated alleles, allowing subsequent PCR amplification and detection of a CAG repeat-containing portion of the methylated (inactivated) AR allele, using appropriate primers. PCR detection of two bands of different sizes (due to the different sizes of the CAG repeats) means that both alleles are expressed, while detection of only one band indicates the expression of only one allele (Comertpay, Pastorino et al. 2014).

2.14. WDR45 genomic and cDNA sequencing

Firstly, **Direct Sanger Sequencing of genomic DNA** was performed in fibroblast and iPSC lines to confirm that 1) the disease-causing mutations of the *WDR45* locus were maintained, after

reprogramming, in all patient iPSC lines and 2) CRISPR correction had resulted in the desired *WDR45* sequence in the 'isogenic' control lines. The genomic DNA sequences were obtained from the Genome Reference Consortium Human Build 37 (GRCh37), (https://grch37.ensembl.org/Homo_sapiens/Info/Index) (transcript ID ENST00000356463.3, NM_007075). The primers (**Table 10**) were designed with Primer3Plus software (http://www.bioinformatics.nl/cgi-bin/primer3plus/primer3plus.cgi).

Exon	**Size (bp)**	**Tm**	**Primer Sequence**	
3 (Coding Exon 1)	261	55℃	3F	TCCCAAAGTGCTGGATTAC
			3R	TTCCTCCCACAAGGGTACAG
4-5 (Coding Exons 2-3)	429	60℃	4-5F	CTGTACCCTTGTGGGAGGAA
			4-5R	CCAGGAATCCGAGAAATCTG
6-7 (Coding Exons 4-5)	505	60℃	6-7F	GCCCCTTACCCTAAACCTTG
			6-7R	TGAGTGTGAGCATCTCCCTG
8-9 (Coding Exons 6-7)	596	60℃	8-9F	TCTGGTCCTCATCCAGCTCT
			8-9R	CAGAGGAAGGAGGAGTCGTG
10-11 (Coding Exons 8-9)	707	60℃	10-	GTCTGCTCCATTCACGATCA
			10-	GCTGTCCCCCTTACTGATGA
12 (Coding Exon 10)	634	60℃	12F	AGATGCCTGAGAGGACTGGA
			12R	AATCCCCAGGTTGGATTAGG

Table 10. PCR primers for WDR45 gene sequencing. *Tm= annealing temperature. F= forward, R= reverse*

For each set of primer pairs, reaction solution was prepared as shown in **Table 11.** *WDR45* is comprised of 12 exons but exons 1 and 2 are in the untranslated region and only exons 3-12 encode the full protein.

Component	Volume (µl) (EXON 3)	Volume (µl) (OTHER EXONS)
ddH_2O	0	4
GC Rich resolution solution	4	0
BioMix Red	10	10
Forward Primer	2	2
Reverse Primer	2	2
DNA	2	2
Total Volume	20	20

Table 11. PCR constituents and relevant volumes for genomic DNA sequencing of WDR45

A touch-down PCR protocol was used to improve the specificity of the primer binding for sequencing of exon 3 (**Table 12)**. Initially starting from a temperature 4°C greater than that of the annealing temperature (Tm), the temperature was gradually lowered by 2°C every two cycles until the desired Tm was reached.

EXON 3 (Coding Exon 1)		
Number of cycles	**Temperature (°C)**	**Time (s)**
1	95 (denaturation)	240
2	95 (denaturation) 59 72 (elongation)	30 30 30
2	95 (denaturation) 57 72 (elongation)	30 30 30
35	95 (denaturation) 55 (Tm) 72 (elongation)	30 30 30
1	72 (elongation)	300
EXONS 4_5, 6_7, 8_9, 10_11, 12		
Number of cycles	**Temperature (°C)**	**Time (s)**
1	95 (denaturation)	300
35	95 (denaturation) 60℃ (Tm) 72 (elongation)	30 30 30
1	72 (elongation)	300

Table 12. PCR conditions for amplifying WDR45 exons.

The purity of the amplified PCR product was checked on a 1.5% agarose gel before proceeding with the sequencing (electrophoresis protocol as described above, in **Section 2.9**). Amplified DNA was then purified with MicroCLEAN Kit (Clent Life Science) and further processed with the BigDye Terminator v1.1 Cycle Sequencing Kit (ThermoFisher). Sequencing was performed with the ABI

PRISM 3730 DNA Analyzer (Applied Biosystems). The results were analysed using Sequencher (https://www.genecodes.com) and Chromas softwares (http://technelysium.com.au/wp/chromas). Where appropriate, *in silico* analysis of pathogenicity in identified *WDR45* variants was also performed using Alamut software (https://www.interactive-biosoftware.com/alamut-visual/). Finally, for sequence alignment, the wild type *WDR45* sequence was obtained from the Ensembl genome browser, amino acid sequence predictions were generated by entering wild type, patient and CRISPR-corrected sequences into the online ExPASy Translate tool (https://web.expasy.org/translate/), and sequence alignments were generated using the online ClustalOmega tool (https://www.ebi.ac.uk/Tools/msa/clustalo/). Dr Katy Barwick, research assistant at the Kurian lab, UCL GOS ICH, performed most of the purification, sequencing, *in silico* analysis and alignment.

Moreover, WDR45 **cDNA sequencing** was performed for the determination of mutated allele expression in female iPSC lines. Firstly, cDNA was extracted as described above, amplified through PCR and sequenced in order to help determine which of the two *WDR45* alleles, the mutated or wild-type, was expressed in the two female iPSC lines (Patient 01, BPAN07, and Patient 03, 535-02). The primers used for cDNA sequencing are summarised in **Table 13**.

Exons	**Expected size**	**Primers used**		**Coverage**
1-4	391bp	F	GACTCAACAGCCACTTCGAGGA	Beginning of Exon 3 to mid-Exon 7
		R	GTCGGGGAAGGAGTACACAT	
5-7	465bp	F	AGCTAAGCGCGAGAAGGCGTTCACCTTCACCAAGCCAG	Late Exon 6 to Exon 10
		R	GCTTTACCGCTCAACCGTTCAGAGGAAGGAGGAGTCGTG	
8-10	675bp	F	GTGTACTCCTTCCCCGACAA	Mid-exon 7 to mid-exon 12
		R	CGTCGAAAGCCTCTCTGTTG	

Table 13. Primers used for WDR45 cDNA sequencing.

2.15. Bulk RNA Sequencing (RNAseq)

Total RNA from Day 65 neurons was extracted from BPAN and control Day 65 mDA neurons, as described above, and samples from all patient and control lines, (200ng or more, concentration of >25ng/µL) were sent to UCL Genomics for bulk RNAseq. Briefly, UCL Genomics performed messenger RNA (mRNA) library preparation using the Kapa mRNA HyperPrep Kit (Kapa Biosystems) and subsequent sequencing on the Illumina HiSeq 3000 system. Quality control of the RNAseq data was performed using the MultiQC software (and confirmed that all samples analysed were of optimal quality). Finally, RNAseq raw data were produced in FASTQ format and analysed by Dr Tanya Singh, bioinformatician at LMCB. DESeq2, an R software package, was used for differential gene expression analysis between patient and control lines (Love, Huber et al. 2014). (https://www.bioconductor.org/packages/release/bioc/html/DESeq2.html). A p value of <0.05 and fold change of <-2 or >+2 [-1<log2(FC)<1] was set as a statistically significant cut-off in order to generate a list of differentially expressed genes (either up- or down-regulated in BPAN mDA neurons). For Gene Ontology (GO) term annotation and molecular pathway enrichment analysis, the PANTHER (Protein ANalysis THrough Evolutionary Relationships) Classification System was used (Mi, Muruganujan et al. 2013)(http://www.geneontology.org/).

2.16. Characterisation of mDA neuronal model

Firstly, in order to fully **characterise the iPSC lines** and ensure their pluripotency/ capacity to be used for downstream dopaminergic neuronal differentiation, several methods were used (as described above) and including Spontaneous Differentiation into all germ layers *in vitro*, Epi-Pluri-Score, immunocytochemistry and RT PCR for pluripotency marker expression, Sendai Virus Clearance, SNP array analysis for karyotype integrity and genomic DNA sequencing to ensure maintenance of disease-causing mutations after reprogramming. Subsequently, the **characterisation of the mDA neuronal model** took place both at progenitor (Day 11) stage and also at the end of the

differentiation (day 65), using a combination of immunofluorescence and qRT PCR experiments for detection of appropriate marker expression, as well as downregulation of iPSC-related pluripotency markers. Details will be provided in the relevant Results section.

2.17. Phenotypic Assay Set-Up for downstream drug screening

After establishing our BPAN neuronal model, the aim was to 1) examine the function of WDR45, e.g. in autophagy and lysosomal function and 2) identify high content assays that distinguish between BPAN and control lines (which could then be used for a drug screen, looking for hits that ameliorate disease-related phenotypes). For this purpose, we developed both immunofluorescence- and plate reader-based assays. Firstly, cells were plated onto 96-well low skirted microplates (CellCarrier-96 Ultra Microplates, PerkinElmer, Catalogue number: 6055300), as follows: skin **fibroblasts** at a density of 300,000/mL (30,000 cells/ well), and **mDA progenitors** (Day 11 of differentiation) at a density of 100,000-150,000 cells/mL (10,000-15,000 cells/ well). In the case of mDA progenitors, wells had been pre-coated with PO/Fn/Lam.

2.17.1. High content imaging-based immunofluorescence experiments

For high content imaging phenotypic assay set-up, cells at 24 hours after plating were either fixed (see below for details) at basal conditions or after 3-hour treatments with compounds that inhibit or induce the autophagy flux. These were 1) **Torin1**, 2) **Bafilomycin A1**, 3) **a combination of Bafilomycin A1 and Torin1** and 4) **DMSO** as (negative) control. Stocks were diluted 1:1,000 in cell culture medium during treatment, giving final treatment concentrations of 250 nM and 10 nM for Torin 1 and Bafilomycin A1, respectively. Subsequently, cells were washed with 1x DPBS and fixed with 4% PFA in DBPS for 10-15 minutes. After PFA, cells were washed, then permeabilised and fixed a second time in ice-cold methanol (kept at -20**°**C) for 15 minutes at +4°C ; washed in DPBS, quenched in 50 mM NH4Cl in DPBS for 20 minutes; washed, and incubated in blocking buffer (fibroblasts: 3% goat serum in DPBS; mDA progenitors: DBPS, 10% FBS and 0.1% Triton) for 1 hour at

room temperature. Plates were incubated overnight at 4°C with primary antibody diluted in blocking buffer (50 µl/well). Washing with DPBS ensued, and cells were subsequently incubated with secondary antibody in blocking buffer (50 µl/well) for 1 hour at room temperature. A list of primary antibodies used is available in **Table 2**.

After washing, nuclei were stained with DAPI (1:1,000) or Hoechst 33342 (1:10,000). For co-staining experiments, antibodies raised in different species against different target proteins were incubated simultaneously. Subsequently, a) fibroblasts were imaged on the PerkinElmer Opera LX and b) mDA progenitors on the PerkinElmer Opera Phenix High Content Screening Confocal Microscope. Images from 20-25 fields per well were acquired, with each condition tested at least in duplicate in each plate. A 40x water immersion objective was used, allowing fast capture of high-resolution images (Numerical Aperture 1.1). Laser and gain settings were optimised for the brightest sample to avoid signal saturation, and the same settings were used to image all samples within a single experiment. Image analysis took place using ImageJ and R Studio softwares. Image analysis was performed by Dr Janos Kriston-Vizi, lead bioinformatician and head of the Bioinformatics Image Core (BIONIC) facility at UCL MRC LMCB. Graphs were subsequently generated, and statistical significance calculated on GraphPad Prism software.

2.17.2. Plate Reader Assays (Assessment of Cell Viability)

For plate reader assay set up, Day 11 mDA progenitors on 96-well plates (24 hours post seeding) were exposed to the following conditions/ stressors for a total of 24 hours:

1. H_20 (negative control)
2. FD Medium without antioxidants B27 and L-Ascorbic Acid
3. FD Medium without Glucose
4. MPP+ at 0.5mM, 1mM and 2mM
5. FeCl3 at 100 µM and 200 µM

The action of WDR45 is induced in Glucose starvation (Bakula, Muller et al. 2017). Additionally, BPAN fibroblasts showed evidence of increased oxidative stress and mitochondrial dysfunction after treatments with the mitochondrial stressor (complex I inhibitor) 1-methyl-4-phenylpyridinium (MPP+, 1mM) or ferric chloride (FeCl3, 100 µM) (Seibler, Burbulla et al. 2018). Hence, the rationale behind these treatments was firstly, to test whether glucose absence or oxidative stress had any effect on cell viability. Each treatment/ condition was tested on all 7 BPAN and control lines, and in 4 separate experiments/ biological replicates. After 24 hours of treatments, Alamar Blue Cell Viability Reagent (ThermoFisher) 10 µl was added in each well and plates incubated for 4-7 hours. Alamar Blue is a reagent containing resazurin, a cell permeable, non-toxic and weakly fluorescent blue indicator dye. Upon entering living cells, resazurin is reduced (by FMNH2, FADH2, NADH, NADPH and cytochromes) to resorufin, a compound that is pink and highly fluorescent. The intensity of fluorescence produced is proportional to the number of living cells where reactions of the electron transport chain are taking place. For our experiment, the medium colour change from blue to pink indicated metabolically active and, hence, viable cells; at that point, fluorescence (excitation at 560 nm, emission at 590 nm) was measured on the PerkinElmer Envision II Microplate Reader. To correct for differences between 1) basal metabolic rates between lines, 2) numbers of cells seeded per well for each line and 3) background fluorescence, all values for each cell line were converted to a Fold Change from the H_20-treated value. Relevant graphs were generated, and statistical significance calculated on GraphPad Prism software.

2.18. Drug Screening

2.18.1. Choice of Cells

Once the primary drug screen phenotypic assay had been set up (described in detail in the Results section), I proceeded with the drug screen using Day 11 mDA progenitors. The choice of using of Day 11 progenitors for my project's drug screen will be detailed in the Results Section. However, briefly, I chose Day 11 cells as a) they are still in a mitotic stage (thus survive replating and seeding at low densities more easily), b) can be produced in relative abundance compared to later stages of differentiation, allowing experiments on a large scale and c) are very well characterised with robust ventral midbrain identities. Hence, the rationale was to perform the drug screen on Day 11 cells and subsequently validate hits on both Day 11 cells but also in more mature Day 65 mDA neurons.

2.18.2. Drug Screen

A drug screen was performed on our BPAN neuronal model using an autophagy (LC3)-based high content imaging assay (described in detail in the Results section); however, briefly, BPAN mDA progenitors consistently exhibit defective LC3 puncta formation when compared to controls. For the screen, I used 2 separate small molecule libraries, both available in the Ketteler lab (UCL MRC LMCB). Firstly, the **Prestwick Chemical Library** of 1,280 compounds (off-patent, 95% FDA/ EMA approved) was used. This is a chemically and pharmacologically diverse library, also containing drugs with known action in the CNS (16% of compounds). The use of FDA-approved drugs gives the opportunity for drug repurposing for any suitable hits and, therefore, has the capacity to reduce the time required for clinical translation. Compounds were provided on source plates at 10 mM in DMSO, ready for drug screening (http://www.prestwickchemical.com/libraries-screening-lib-pcl.html). Secondly, a **library of autophagy activators** was screened. This consists of a) novel compounds (available in the Kettleler lab and developed through collaboration with UCL School of Pharmacy and UCL Translational Research Office) that are known to enhance autophagy in several cell lines, b) well-known autophagy inducers and c) other drugs (e.g. autophagy inhibitors or toxins), effectively to be used as negative controls.

Concentrations and mechanisms of action for the autophagy inducer drugs are detailed in **Table 14**.

Compound	Concentration	Comments
TRO-AUT-29	10 mM	unknown MoA; increases LC3 puncta in cell lines
TRO-AUT-30	10 mM	unknown MoA; increases LC3 puncta in cell lines
TRO-AUT-31	10 mM	unknown MoA; increases LC3 puncta in cell lines
TRO-AUT-32	10 mM	unknown MoA; increases LC3 puncta in cell lines
TRO-AUT-33	10 mM	unknown MoA; increases LC3 puncta in cell lines
TRO-AUT-34	10 mM	unknown MoA; increases LC3 puncta in cell lines
TRO-AUT-35	10 mM	unknown MoA; increases LC3 puncta in cell lines
TRO-AUT-36	10 mM	unknown MoA; increases LC3 puncta in cell lines
Chloroquine	10 mM	Lysosomotropic agent
JKV8C3	10 mM	unknown MoA; increases LC3 puncta in cell lines
Comp 5F4	10 mM	CLK2 inhibitor (Prak, Kriston-Vizi et al. 2016)
Rapamycin	10 mM	mTOR inhibitor
Torin 1	250 uM	mTOR inhibitor
Resveratrol	10 mM	multiple targets; autophagy inducer
Flubendazole	10 mM	ATG4B agonist
AZD1152	10 mM	Aurora Kinase A inhibitor
TRO-AUT-37	10 mM	unknown MoA; increases LC3 puncta in cell lines
TRO-AUT-38	10 mM	unknown MoA; increases LC3 puncta in cell lines
TRO-AUT-39	10 mM	unknown MoA; increases LC3 puncta in cell lines
TRO-AUT-40	10 mM	unknown MoA; increases LC3 puncta in cell lines
TRO-AUT-41	10 mM	unknown MoA; increases LC3 puncta in cell lines
TRO-AUT-42	10 mM	unknown MoA; increases LC3 puncta in cell lines
TRO-AUT-43	10 mM	unknown MoA; increases LC3 puncta in cell lines
TRO-AUT-44	10 mM	unknown MoA; increases LC3 puncta in cell lines
BEZ235	10 mM	mTOR/PI3K inhibitor
MG132	5 mM	Proteasome inhibitor
Trehalose	10 mM	autophagy inducer or autophagic flux inhibitor
ABT-737	10 mM	BCL2 inhibitor
SRT-1720	10 mM	SIRT1 activator
STK693863	10 mM	ATG4B inducer
Desferrioxamine	10 mM	Stabilizes HIF1 alpha
MK-2206	10 mM	Pan-AKT inhibitor
TRO-AUT-45	10 mM	unknown MoA; increases LC3 puncta in cell lines
TRO-AUT-46	10 mM	unknown MoA; increases LC3 puncta in cell lines
TRO-AUT-47	10 mM	unknown MoA; increases LC3 puncta in cell lines
TRO-AUT-48	10 mM	unknown MoA; increases LC3 puncta in cell lines
TRO-AUT-49	10 mM	unknown MoA; increases LC3 puncta in cell lines
TRO-AUT-50	10 mM	unknown MoA; increases LC3 puncta in cell lines
TRO-AUT-51	10 mM	unknown MoA; increases LC3 puncta in cell lines
TRO-AUT-52	10 mM	unknown MoA; increases LC3 puncta in cell lines
PV-1019	10 mM	CHK2 inhibitor
Etoposide	10 mM	Topoisomerase II inhibitor
3-methyl adenine	10 mM	PI3K III inhibitor
DMSO	10 mM	control
AZD8055	10 mM	mTOR inhibitor
S6K inhibitor	2 mM	S6 kinase inhibitor

Spermidine	6.4 mM	autophagy inducer
Valinomycin	10 mM	potassium ion transport
TRO-AUT-53	10 mM	unknown MoA; increases LC3 puncta in cell lines
TRO-AUT-54	10 mM	unknown MoA; increases LC3 puncta in cell lines
TRO-AUT-55	10 mM	unknown MoA; increases LC3 puncta in cell lines
TRO-AUT-56	10 mM	unknown MoA; increases LC3 puncta in cell lines
TRO-AUT-57	10 mM	unknown MoA; increases LC3 puncta in cell lines
TRO-AUT-58	10 mM	unknown MoA; increases LC3 puncta in cell lines
TRO-AUT-59	10 mM	unknown MoA; increases LC3 puncta in cell lines
TRO-AUT-60	10 mM	unknown MoA; increases LC3 puncta in cell lines
JKV8C3-A	10 mM	unknown MoA; increases LC3 puncta in cell lines
JKV8C3-B	10 mM	unknown MoA; increases LC3 puncta in cell lines
MRT68921	10 mM	ULK1/2 inhibitor
MRT673074	10 mM	ULK1/2 inhibitor
MHY-1485	10 mM	mTOR activator
SMER-28	10 mM	small-molecule enhancer (SMER) of autophagy, inducing autophagy independently of rapamycin
Biochanin A	10 mM	phytoestrogen
Tamoxifen	10 mM	oestrogen receptor antagonist
TRO-AUT-61	10 mM	unknown MoA; increases LC3 puncta in cell lines
TRO-AUT-62	10 mM	unknown MoA; increases LC3 puncta in cell lines
TRO-AUT-63	10 mM	unknown MoA; increases LC3 puncta in cell lines
TRO-AUT-64	10 mM	unknown MoA; increases LC3 puncta in cell lines
TRO-AUT-65	10 mM	unknown MoA; increases LC3 puncta in cell lines
TRO-AUT-66	10 mM	unknown MoA; increases LC3 puncta in cell lines
Erlotinib	10 mM	EGFR inhibitor
CCCP	5 mM	mitochondrial uncoupler
JKV8C3-C	10 mM	unknown MoA; increases LC3 puncta in cell lines
STK964	10 mM	ATG4B inducer
Compound C	10 mM	AMP kinase inhibitor
Brefeldin A	10 mg/ml	ER-Golgi transport inhibitor
Antimycin A	10 mM	cytochrome C reductase inhibitor
Oligomycin	10 mM	ATP synthase inhibitor
Rotenone	10 mM	complex I inhibitor
Digoxin	10 mM	cardiac glycoside

Table 14. Composition of the autophagy activator drug screen library. *Novel autophagy flux-inducing compounds were available in the Ketteler lab. Other known autophagy inducers (e.g. resveratrol, spermidine), controls (e.g. DMSO) and toxins (e.g. CCCP, valinomycin) were used as additional positive and negative controls. Abbreviations: MoA= mode of action*

The source plate layout (96-well format) for the autophagy activator library is detailed in **Table 15**.

	1	2	3	4	5	6	7	8	9	10	11	12
A	DMSO	TRO-AUT-29	Chloroquine	TRO-AUT-37	BEZ235	TRO-AUT-45	PV-1019	TRO-AUT-53	JKV8C3-A	TRO-AUT-61	JKV8C3-C	BafnA1
B	DMSO	TRO-AUT-30	JKV8C3	TRO-AUT-38	MG132	TRO-AUT-46	Etoposide	TRO-AUT-54	JKV8C3-B	TRO-AUT-62	STK964	BafnA1
C	DMSO	TRO-AUT-31	Comp 5F4	TRO-AUT-39	Trehalose	TRO-AUT-47	3-methyl adenine	TRO-AUT-55	MRT68921	TRO-AUT-63	Compound C	BafnA1
D	DMSO	TRO-AUT-32	Rapamycin	TRO-AUT-40	ABT-737	TRO-AUT-48	DMSO	TRO-AUT-56	MRT673074	TRO-AUT-64	Brefeldin A	BafnA1
E	DMSO	TRO-AUT-33	Torin 1	TRO-AUT-41	SRT-1720	TRO-AUT-49	AZD8055	TRO-AUT-57	MHY-1485	TRO-AUT-65	Antimycin A	BafnA1
F	DMSO	TRO-AUT-34	Resveratrol	TRO-AUT-42	STK693863	TRO-AUT-50	S6K inhibitor	TRO-AUT-58	SMER-28	TRO-AUT-66	Oligomycin	BafnA1
G	DMSO	TRO-AUT-35	Flubendazole	TRO-AUT-43	Desferiox-amine	TRO-AUT-51	Spermidine	TRO-AUT-59	Biochanin A	Erlotinib	Rotenone	BafnA1
H	DMSO	TRO-AUT-36	AZD1152	TRO-AUT-44	MK-2206	TRO-AUT-52	Valinomycin	TRO-AUT-60	Tamoxifen	CCCP	Digoxin	BafnA1

Table 15. Source plate layout for autophagy activator screen. *DMSO and Bafilomycin A1 are used as negative controls (Columns 1 and 8, respectively). Most compounds had a stock concentration of 10mM (100nl dispensed and final concentration in cell culture medium 10 µM)*

The **protocol** for the drug screen is summarised in **Figure 8**. For both screens, 96-well plates, coated with PO/Fn/Lam, were used for cell seeding and subsequently as destination plates. For the Prestwick screen, one patient line (with the biggest LC3-related phenotypic defect) was used and 48x 96-well destination plates required (16 source plates, 80 compounds each, tested in triplicates). For the autophagy screen, 3 lines (Control 01, Patient 02, Patient 03) and 9x 96-well destination plates were used (1 source plate, 3 lines, tested in triplicates).

For both screens, DMSO (1:1,000 dilution, in all wells of column 1) and Bafilomycin A1 (in column 12) were used in all destination plates as negative and positive controls, respectively. This was because 1) Bafilomycin A1 blocks autophagosomal/ lysosomal fusion and leads to accumulation of autophagosomes, whereas 2) DMSO in low concentrations should have no (or little) effect and, finally, 3) almost all drugs in the screen were diluted in DMSO.

Most drugs were seeded at a concentration of 10 mM, hence diluted in FD Day 11 medium to a final concentration of 10 µM. Furthermore, cells were fixed 24 hours post treatments. LC3 was detected using the anti-LC3 D11 clone rabbit monoclonal antibody (1:200, as per **Table 2**) and a corresponding Alexa Fluor 488 Goat Anti-Rabbit IgG secondary antibody (1:400); nuclei were detected via DAPI staining. Finally, plates were imaged for LC3 (488nm) and DAPI (375nm) and images analysed for hit detection.

A summary of the image analysis process is attempted in the paragraph below and in **Figure 8**. This multi-step process took place during phenotypic assay set up, but also during the actual drug screen.

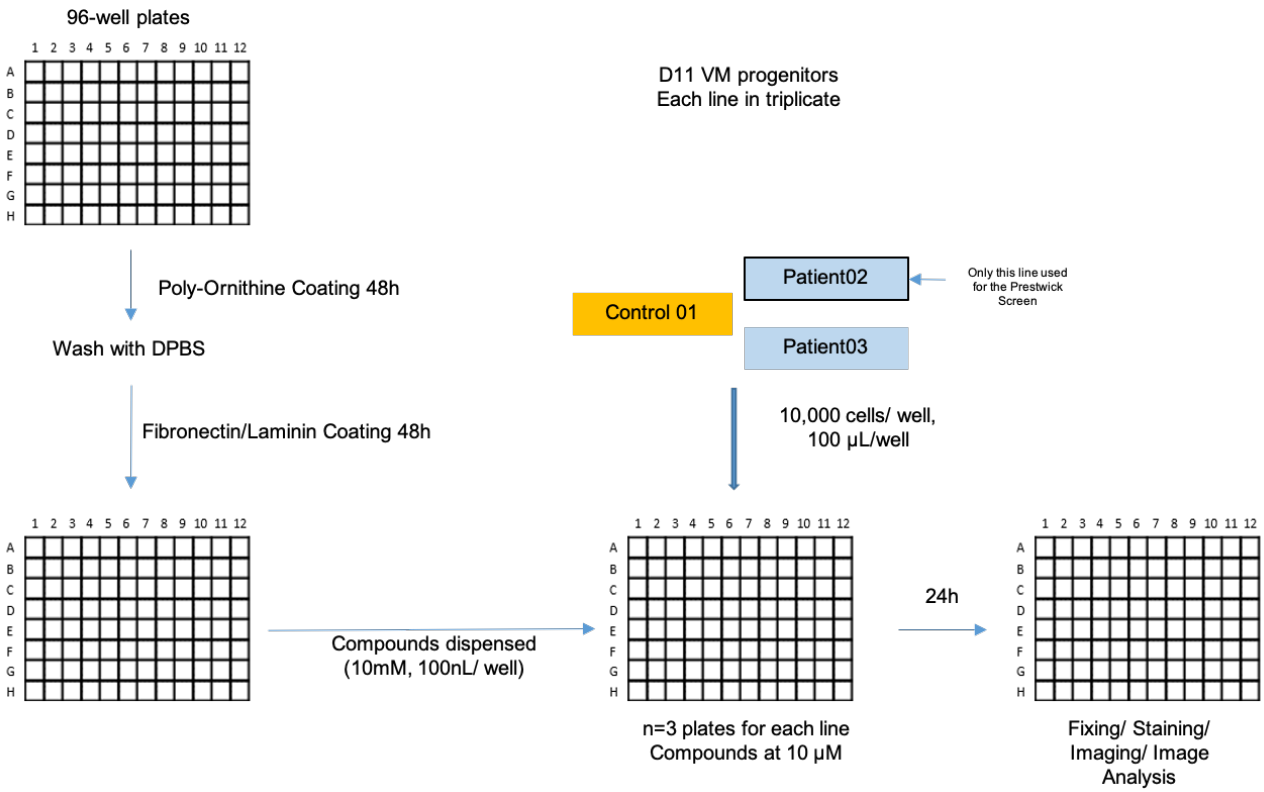
96-well plates
1 2 3 4 5 6 7 8 9 10 11 12
A
B
C
D
E
F
G
H
Poly-Ornithine Coating 48h
Wash with DPBS
Fibronectin/Laminin Coating 48h
D11 VM progenitors
Each line in triplicate
Control 01
Patient02
Patient03
Only this line used for the Prestwick Screen
10,000 cells/ well, 100 µL/well
Compounds dispensed (10mM, 100nL/ well)
n=3 plates for each line
Compounds at 10 µM
24h
Fixing/ Staining/ Imaging/ Image Analysis

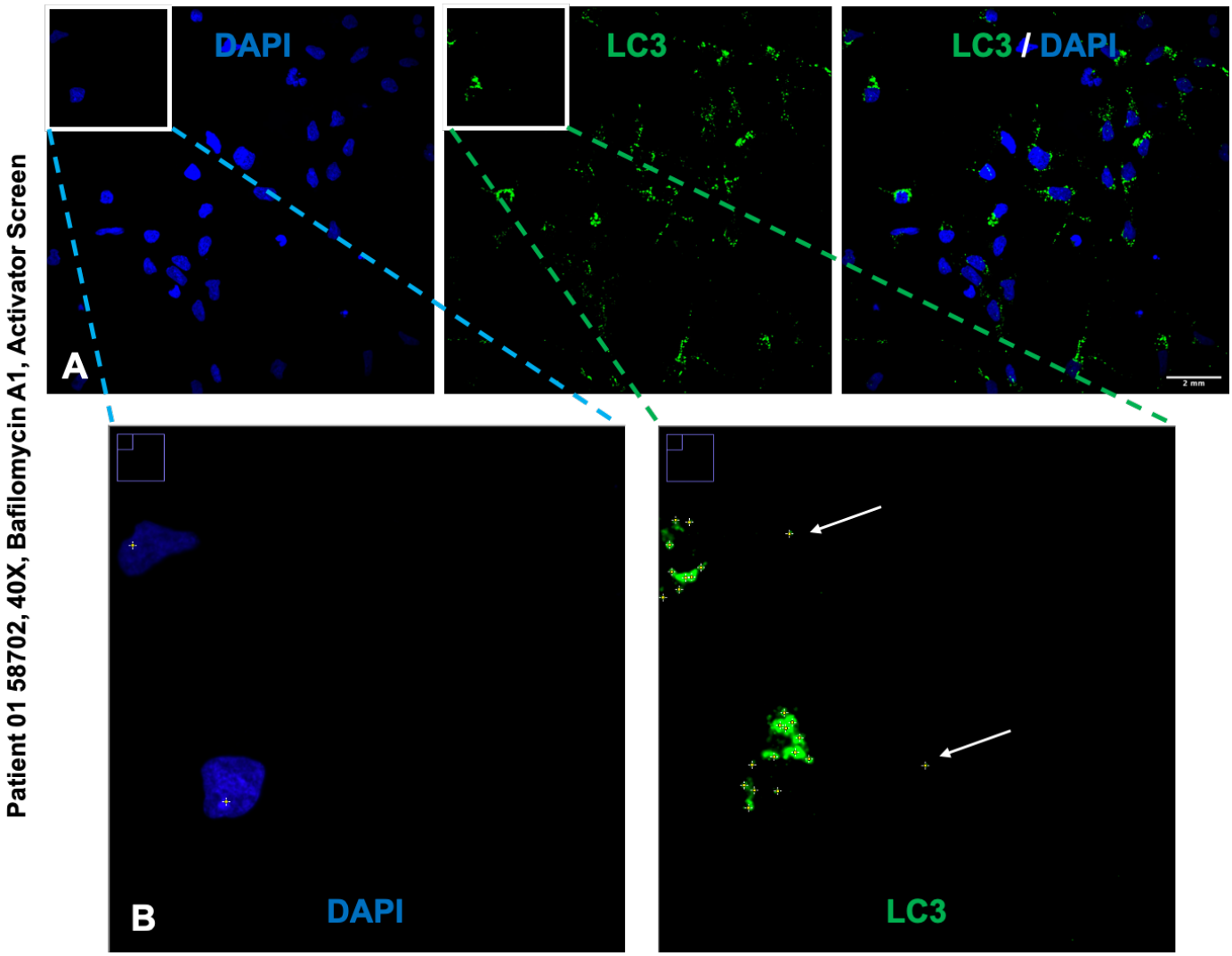
Patient 01 58702, 40X, Bafilomycin A1, Activator Screen
DAPI
LC3
LC3 / DAPI
A
2 mm
B
DAPI
LC3

Figure 8. Drug Screening. Above: *an overview of the protocol followed for both drug screens is shown. The process was optimised and, wherever possible, automated to allow testing of compounds at a large scale. Regardless of the screen, DMSO (in Column 1) and BafilomycinA1 (in Column 12) were used as negative and positive controls, respectively.* ***Below****: image analysis was performed by Dr Janos Kriston-Vici at LMCB (unpublished data and methodology).* ***A.*** *Images were captured by the PerkinElmer Opera Phenix (96 well plates used, 20 images/ fields captured per well) and analysed via ImageJ/ Fiji. Representative image of nuclei and puncta is shown.* ***B.*** *Magnification of the top-left corner of DAPI and LC3 images in A, above. Nuclei and puncta were both counted using ImageJ's Find Maxima process (small yellow crosses). LC3 puncta in two cells (n= 2 nuclei/ yellow crosses) are shown. When counting puncta, background noise was excluded through image segmentation, and puncta outside cells (white arrows pointing to small yellow crosses not adjacent to nuclei/ not within the cytoplasm) were not counted. Furthermore, values were normalised according to positive and negative controls from each plate and Z scores for each compound screened were generated. Where applicable, e.g. in cases of increased background signal/ non-cytoplasmic puncta numbers, plate treatment, staining and image analysis was repeated.*

In order to allow this drug screen (and other large-scale applications in general), the above protocol was optimised and automated in the Ketteler lab. In detail, plates were automatically coated (with PO/Fn/Lam) and washed using the Beckman Coulter Biomek NXp and Biotek EL406 automated workstation and the SAMI scheduling software. Cell seeding onto 96-well plates (and also the subsequent PFA fixing, post drug treatments) was performed with the Biotek Multi-Flo Multi-Mode Dispenser. For drug dispensing, the Labcyte Echo 550 with CellAccess system (with the capacity to dispense just few ul of each drug) was used. For immunostaining, the combination of the Beckman Coulter Biomek station and the SAMI scheduling software was utilised again. For imaging, the PerkinElmer Opera Phenix confocal microscope was used. Each 96-well plate was imaged in approximately 65-70 minutes [20-25 fields imaged per well, at 40 x, Numerical Aperture 1.1, Binning 1, for two channels (Channel 1: 375 nm, Channel 2: 488 nm lasers)]. The use of Plate Handler II with plate stackers and Harmony 4.6 Software in the 'Remote' setting allowed for automated imaging of a large number of plates. Captured data were exported to the Columbus Image Data Storage and Analysis System and, subsequently, to the LMCB online, secure drives. Image analysis (e.g. exclusion of background noise when counting puncta through image segmentation, puncta and nuclei counting using ImageJ's Find Maxima, normalisation of values according to positive and negative controls from each plate and generation of Z scores for each compound) was performed (by Dr Janos Kriston-Vici, LMCB) using ImageJ/Fiji and R Studio. Where applicable, e.g. in cases of increased background signal/ non-cytoplasmic puncta numbers, plate treatments, staining and image analysis was repeated.

The Labcyte Echo 550 dispenser was used by Dr Alexander Agrotis, post-doctoral fellow in the Ketteler lab. The Beckman Coulter Biomek station and the SAMI scheduling software was used by Dr Christin Luft, post-doctoral fellow in the Ketteler lab.

2.19. Statistical analysis

Statistical analysis was performed using GraphPad Prism V. 8.1.2. or Microsoft Excel software. Patient and control samples were compared through ordinary one-way ANOVA or Repeated Measurements ANOVA tests (in cases of unpaired and paired samples, respectively). The reasoning for using ANOVA rather that t-tests was because in my experiments I had multiple (> 2) lines/ groups tested, and t-tests are traditionally used when comparing two groups, only. On graphs, error bars represent the Standard Error of Mean. Significance levels are determined through p-values, and statistically significant values ($p<0.05$) are shown with asterisks, as follows; 1 asterisk (*) indicates p-values between 0.05 and 0.01, 2 asterisks (**) indicate p-values between 0.01 and 0.001, and 3 asterisks (***) indicate p-values< 0.001. Non-significant values ($p>0.05$) as shown as (ns).

3. Results

3. Establishment and Characterisation of the BPAN midbrain dopaminergic neuronal model

3.1. Induced pluripotent stem cells: derivation, characterisation and neuronal differentiation

In the BPAN project, a Sendai virus-based methodology to reprogram dermal fibroblasts into iPSCs was utilised. Sendai virus (SeV) is a single strand RNA virus which has been extensively used as a non-integrating vector system to reprogram somatic cells into iPSC with relatively high efficiency (Fusaki, Ban et al. 2009). The commercially available kit (CytoTune-iPS 2.0 Sendai Reprogramming Kit) is based on a modified non-transmissible form of SeV used for the delivery of OCT4, SOX2, C-MYC and KLF4.

Generation of iPSC lines has been possible from multiple cell types and tissues, for example peripheral blood cells, urine cells, hepatocytes or keratinocytes (Zhou, Benda et al. 2012, Barrett, Ornelas et al. 2014, Raab, Klingenstein et al. 2014, Cheng, Lei et al. 2017). However, dermal fibroblasts remain the most popular and widely available choice. This is because fibroblasts are easy and inexpensive to maintain in tissue culture and also exbibit good viability and culture stability over 5–10 passages. Additionally, despite a relatively low reprogramming efficiency, they facilitate successful generation of iPSC in most cases. Equally importantly, they have been very broadly investigated and utilised so far; for example, reprogramming of fibroblasts using many different techniques has been studied, while most iPSC banking is been performed using fibroblast-derived cells (Raab, Klingenstein et al. 2014). For the BPAN project, all iPSC lines were derived from human fibroblasts.

Control and patient fibroblast ascertainment and iPSC reprogramming took place as detailed below, in **Section 3.4.** Characterisation of derived iPSCs is described in **Section 3.5.**, whereas generation of midbrain dopaminergic neurons in **Section 3.6.**

3.2. Caveats of iPSC-based disease modelling to consider when studying BPAN

3.2.1. The 'fetal' status of iPSC-derived neurons

During reprogramming into iPSCs, somatic cells return to a developmental stage similar to that of ESCs, independent of their original age.

Age-related characteristics of the original somatic cells, (such as nuclear abnormalities, telomere length, mitochondrial activity) are lost during reprogramming into iPSC. Hence, and despite the fact that subsequent neuronal differentiation protocols span from weeks to months (Srikanth and Young-Pearse 2014), the derived neurons are often reminiscent of human fetal neurons, even if they exhibit relatively mature morphological, molecular and electrophysiological phenotypes (Lancaster, Renner et al. 2013, Barral and Kurian 2016). The relatively immature nature of these neurons should always be a consideration when modelling postnatal-, childhood- and adult-onset neurological diseases, where pathological features only manifest during postnatal development or through ageing.

When it comes to studying monogenic severe, fully penetrant disorders that present in the neonatal period, early infancy or childhood, this 'caveat' might not be so obstructive for disease modelling or might even be desirable/ relevant to disease pathophysiology. On the other hand, *in vitro* neuronal disease model might fail to recapitulate disease phenotype in late-onset disorders, such as Parkinson's disease or Alzheimer's disease. Strategies that have been used to overcome this issue and elicit disease-related phenotypes otherwise not easily discernible in the dish firstly include exposing cells to external stressors. For example, iPSC-derived mDA neurons from Parkinson's disease patients harbouring *LRRK2* mutations recapitulate some features of the condition such as α-synuclein aggregation and signs of oxidative stress. However, neuronal apoptosis and degeneration was only evident in the dish after exposure to hydrogen peroxide, MG-132, and 6-hydroxydopamine (known stressors/ neurotoxins) (Nguyen, Byers et al. 2011). A second strategy is ageing the cells, via prolonging maintenance in tissue culture, or even overexpressing progerin that subsequently leads

to neuromelanin formation (Miller, Ganat et al. 2013) (a key feature of SN mDA neurons not otherwise seen in 2-dimensional iPSC-derived models).

In the case of BPAN, a monogenic disorder with very early onset in the majority of cases, but also a two-stage clinical course, we hypothesise that a combination of the above might apply. In other words, it is plausible that some disease-related features might be present in the dish early on, but also that some phenotypic defects (e.g. the striatonigral degeneration and loss of dopaminergic neurons) might be only elicitable after external stressors.

3.2.2. IPSC line variability

An inherent issue in iPSC-based disease modelling is line-to-line variability. IPSC lines from different 'controls'/ healthy individuals, and even different iPSC clones deriving from the same individual (patient or control) often behave differently in the dish, and this difference includes their capacity to differentiate (Osafune, Caron et al. 2008, Bock, Kiskinis et al. 2011, Ortmann and Vallier 2017). This line variability, a limiting factor that could affect iPSC utility and clinical safety, is thought to be related to several genetic and epigenetic background differences (Barral and Kurian 2016). The issue has often led researchers to wonder whether a disease-related phenotype seen *in vitro* is actually disease-relevant, or just due to other genetic/ epigenetic differences between patient and control lines. Of course, the issue of line variability is even more pronounced when attempting to model disorders such as sporadic Parkinson's or Alzheimer's disease where multiple (often unknown) genetic and epigenetic factors are thought to have contributed to disease and phenotype severity.

In order to overcome this inherent problem, two strategies are mainly adopted by the scientific community, namely 1) the use of as many patient lines and as many age-matched controls as possible (looking for phenotypes that are reproducible or not, depending on the presence or absence of disease, respectively) and 2) the use of 'isogenic' controls. One of the main disadvantages of the first approach is that is expensive and time consuming. More recently, **'isogenic control' lines**,

generated via gene-editing technologies, have become the gold-standard method to unequivocally validate the effect of a specific genotype on the iPSC model system. Substitution of a single disease-causing mutation with the 'wild-type' sequence in a patient-derived iPSC cell line leads to the development of a control line which, otherwise, harbours the same genetic and epigenetic background with the patient iPSC line. This decreases any "background noise" that could affect cell phenotypes and ensures that any phenotypic variability seen in downstream experiments is due to the actual mutation. Hence, this is a particularly useful methodology in monogenic neurological disorders. In a similar way, the insertion of specific mutations into a control line can be used to induce disease phenotypes into control iPSC lines.

Different gene editing methodologies have been used for iPSC gene editing, including the generation of isogenic controls, such as Zinc Finger Nucleases (ZFN), Transcription Activator-Like Effector Nucleases (TALENs) and, more recently, the Clustered Regularly Interspaced Short Palindromic Repeats (CRISPR)-Cas9 system. **CRISPR/Cas9 genome editing** has now become the method of choice due to it being relatively more efficient, inexpensive, fast and targeted compared to other approaches (Agrotis and Ketteler 2015, Barral and Kurian 2016).

CRISPRs are part of an bacterial adaptive immune mechanism that aims to destroy invading DNA (Barrangou, Fremaux et al. 2007). There are three major different CRISPR systems in different bacterial species (Makarova, Haft et al. 2011); the type II CRISPR system from *Streptococcus pyogenes* has been adapted and is currently the most frequently used for targeted genome editing in eukaryotic cells (Jinek, Chylinski et al. 2012, Agrotis and Ketteler 2015). This is essentially a system of three (or two) components, 1) the CRISPR RNA (crRNA) that contains a nucleotide sequence targeting a specific region of the foreign DNA, 2) the trans-activating CRISPR RNA (tracrRNA), a scaffold with which the crRNA interacts via base pairing and 3) the Crispr Associated (Cas9) nuclease. Artificial fusion of the crRNA and tracrRNA leads to a fully functional 'single guide' RNA (sgRNA) and further simplifies the system. The region of interest in the genomic DNA (protospacer sequence) is

targeted by a 20-nucleotide user-generated guide sequence in the sgRNA (or crRNA) and always lies adjacent to a protospacer adjacent motif (PAM). Cas9 is associated with the RNA component and introduces a double-stranded break in the target DNA, always 3 nucleotides upstream of the PAM. This normally leads to Non-Homologous End Joining and random insertions or deletions, and therefore frame-shifting and gene function disruption. However, delivery of an artificial repair template along with the Cas9/sgRNA constructs can lead to Homology Directed Repair (HDR) and the efficient introduction of a specific DNA sequence at a specified genomic location. For example, one can substitute the disease-causing mutation in an iPSC line with the 'wild-type' sequence (or a sequence that translates to a full-length protein but purposefully contains 'silent' mutations/ synonymous changes, in order to prevent repeated rounds of editing once the desired correction occurs). In fact, the latter approach is exactly what we followed for 2 BPAN patient iPSC lines, as discussed later on.

3.2.3. Chromosomal rearrangements and other genetic changes can affect iPSC modelling

Another caveat of iPSC modelling is the accumulations of chromosomal abnormalities and other genetic changes that might affect pluripotency and also mask (or, alternatively, disguise as) disease-related phenotypes. It is now well established that the reprogramming process, as well as prolonged tissue culture time and increased number of passages, leads to chromosomal insertions, deletions and rearrangements in iPSC lines. These rearrangements lead to significant differences in gene expression and differentiation potential (Mayshar, Ben-David et al. 2010, Turinetto, Orlando et al. 2017). Hence, major chromosomal abnormalities need to be accounted for (and excluded) when modelling disease and, even more so, when considering cell replacement therapies. Strategies around this problem (that we also followed in the BPAN project) include 1) performing detailed genomic analysis [e.g. Single Nucleotide Polymorphism (SNP) Array or Whole Exome/ Genome Sequencing analysis] on iPSC lines prior to differentiations, but also 2) screening for common chromosomal changes during maintenance in tissue culture (e.g. https://www.stemcell.com/hpsc-

genetic-analysis-kit.html) and 3) ensuring that 'old' iPSCs are discarded (and new thawed) after a maximum number of (10-15) passages.

An additional issue is the gradual accumulation of mutations in *TP53/P53*, a tumour suppressor gene with known roles in DNA damage response (Merkle, Ghosh et al. 2017). These mutations might confer a selective advantage to mutated iPSC subclones and/ or positively affect their capacity to differentiate. More recently, it was also suggested that CRISPR-Cas9 edited iPSC lines (e.g. isogenic controls described above) frequently harbour TP53/P53 mutations. In fact, Cas9-mediated DNA double-stranded breaks seem to elicit a toxic response that kills most iPSC lines; this response is TP53-dependent and the efficiency of genome editing in the presence of wild-type P53 is severely reduced (Ihry, Worringer et al. 2018). These issues might create obstacles in disease modelling, especially when trying to interpret cell viability/ toxicity-related phenotypic readouts, but also very importantly for cell replacement therapies. For the BPAN project, we tried to address this potential issue by using as many iPSC controls as possible (2 CRISPR-corrected lines and 2 age-matched controls) and not relying solely on isogenic lines when looking for correction of disease-related phenotypes (as explained in detail in the Results section).

3.2.4. iPSC lines and X Chromosome Inactivation (XCI) status: implications for the study of X-linked conditions

A key feature of iPSC lines, worth mentioning here as likely to affect the modelling of X-linked disorders such as BPAN, is the status of XCI. In iPS female lines, one X Chromosome seems to remain inactive during reprogramming and iPSC maintenance. This inactivation is maintained throughout the process of differentiation into the desired cell type (Tchieu, Kuoy et al. 2010, Tomoda, Takahashi et al. 2012). It is also known that iPSC lines are clonal; in other words, one clone derives from a single dermal fibroblast; hence, the X inactivation status of a specific iPSC clone in early passages reflects the status of the originating fibroblast. However, when performing skin biopsies and isolating skin fibroblasts, the status of XCI is often unknown or random; hence, it cannot *a priori* be

known which X chromosome will be inactive (and which allele of interest will be expressed) in the derived iPSC lines.

Additionally, the status of XCI is thought to be dependent on derivation and culture conditions of iPSCs. For example, reprogramming using SNL feeder cells (producing high levels of leukaemia inhibitory factor) often leads to X reactivation, while iPSC lines generated using standard bFGF culture conditions retain an inactive X Chromosome (Tomoda, Takahashi et al. 2012). To complicate matters further, after prolonged passaging, iPSC lines are prone to lose XIST coating on the inactivated chromosome. Despite this change, the inactive state seemed to be maintained according to some studies, and only alleles that were active in previous passages continued to be expressed (Tchieu, Kuoy et al. 2010). However, another study examining mutations in HPRT (an X-linked gene causing Lesch-Nyhan syndrome, a condition with severe neurological manifestations) showed that, in female iPSC lines expressing the mutated HPRT allele, XIST loss and DNA de-methylation with passaging was also associated with ectopic expression of the wild-type allele from the previously inactive X, leading to restoration of cellular phenotypes in downstream neuronal differentiation experiments (Mekhoubad, Bock et al. 2012). This state where XIST is silenced and one X chromosome is only partially inactive was termed XCI erosion. Finally, a more recent large-scale study looking at XCI parameters in more than 700 RNA high-throughput sequencing samples showed that, in ESCs XCI is usually eroded, while iPSCs frequently display complete XCI with expression of XIST, consistent dosage compensation, and monoallelic transcription of X-linked genes (Bar, Seaton et al. 2019). This difference between ESCs and iPSCs could be explained by 1) the existence of epigenetic memory in iPSC lines from their distinct parental sources, or 2) differences in derivation or culture conditions of ESCs and iPSCs.

In any case, the above might have implications and are worth considering when trying to generate iPSC lines from female patients with X-linked disorders, but also during subsequent disease modelling. Creating clones that express the healthy allele (and thereby behave as controls) from the

beginning or due to subsequent XCI erosion are factors that might have an impact on BPAN neuronal modelling and dilute (or eradicate) phenotypic defects in BPAN female lines. In order to overcome these issues, 1) the status of XCI at all stages (fibroblasts, iPSC, neurons) as well as which of the two alleles are expressed at iPSC and neuronal stage need to be established and 2), the use of as many patient and control lines as possible, including male BPAN iPSC lines should be considered.

3.3. Development of midbrain dopaminergic neurons: basic embryology

Dopaminergic neuronal development is a very complex process during embryogenesis, that takes place in the ventral midbrain and is governed by spatial and temporal responses to combined actions of several transcription factors and morphogens. This process is summarised below [as reviewed in (Arenas, Denham et al. 2015)]. A lot of this knowledge comes from studies in mice/ rats, hence the relevant gene nomenclature is used where appropriate.

One of the earliest and most crucial patterning events in the neural tube is the formation of two signalling centres, the isthmic organiser (IsO) and the floor plate (FP). The combined action of transcription factors from these two centres essentially enables cells to acquire Ventral Midbrain identities, and subsequently promotes the genesis, appropriate differentiation and survival of mDA neurons (Joyner, Liu et al. 2000, Placzek and Briscoe 2005).

Antero-posterior patterning occurs via the IsO, which is formed at the Midbrain-Hindbrain Border (MHB) through the coordinated expression and mutual repression of Otx2 in the midbrain and Gbx2 in the hindbrain (Wassarman, Lewandoski et al. 1997, Broccoli, Boncinelli et al. 1999, Millet, Campbell et al. 1999). These two transcription factors subsequently control the patterning of the MHB; Otx2 is required for Wnt1 expression in the midbrain, whereas Gbx2 for Fgf8 expression in the hindbrain (Ye, Shimamura et al. 1998, Puelles, Annino et al. 2004). The presence of Fgf8 is required for the generation of the IsO. In fact, Fgf8 gradients at the MHB are crucial for cells to acquire anteroposterior fates; high Fgf8 concentrations lead to HB identities, whereas lower concentrations in neighbouring regions ensure a midbrain identity (Basson, Echevarria et al. 2008).

Ventro-dorsal patterning of the neural tube occurs in the FP and is regulated largely by SHH. A gradient of SHH from the FP regulates patterning in the ventro-dorsal axis: ventral progenitors are exposed to higher concentrations of SHH and respond by expressing different transcription factors compared to dorsal cells, that are exposed to lower concentrations; this results in different ventro-dorsal identities (Briscoe and Ericson 1999). Moreover, in the midbrain FP, high SHH signalling

upregulates Foxa2. Foxa2 plays a central role in the SHH network and is required for FP development as well as for ventral patterning (Ang and Rossant 1994, Weinstein, Ruiz i Altaba et al. 1994). FOXA2 also (up)regulates Shh, which again positively feeds back onto Foxa2 expression (Shh-Foxa2 network) (Metzakopian, Lin et al. 2012).

Midbrain FP specification is also a complex process governed by interactions of several transcription factors in the midbrain FP. Firstly, Lmx1b is expressed and directly regulates the expression of Wnt1 and Lmx1a. Wnt1 and Lmx1a also regulate each other via beta-catenin (which activates Lmx1a) or directly (Lmx1a activates Wnt1), forming an auto-regulatory loop (Arenas, Denham et al. 2015). Wnt1 also upregulates Otx2 and Lmx1a via β-catenin, and Lmx1a/b upregulate Msx1 (Wnt1-Lmx1a/b-Msx1 network). Msx1 suppresses the emergence of basal plate fates via downregulation of basal plate marker Nkx6.1. Midbrain basal plate markers Nkx2-2 and Nkx6-1 are also inhibited in the mFP by Foxa2 and Otx2 (that downregulate Nkx2-2) (Arenas, Denham et al. 2015).

Subsequently, **mDA neurogenesis** starts in the ventricular zone (VZ) of the mFP. The VZ contains radial glia cells (RG) that undergo neurogenesis to generate postmitotic neuroblasts. This process is controlled by two genes expressed in the VZ, Mash1 and Ngn2, which are in turn regulated by the Shh-Foxa2 and Lmx1a/b-Wnt1-Otx2 networks, as well as other nuclear receptors and morphogens (such as the morphogen Wnt5a, and the nuclear receptors Lxra and Lxrb) (Arenas, Denham et al. 2015). Post-mitotic neuroblast cells subsequently migrate radially through the intermediate zone (IZ), over the processes of the RG, and differentiate into mDA neurons in the marginal zone (MZ) (Hanaway, McConnell et al. 1971, Kawano, Ohyama et al. 1995). Finally, as cells become mDA neurons, they migrate tangentially towards their final position at the SN pars compacta (Hanaway, McConnell et al. 1971, Marchand and Poirier 1983). A receptor worth mentioning at this point is Cxcr4 (C-X-C motif chemokine receptor type 4), which can be detected in the IZ and MZ and is required for radial migration and fiber outgrowth of mDA neurons (Yang, Edman et al. 2013, Bodea,

Spille et al. 2014). Additionally, NURR1, PITX3 and EN1/2 are crucial regulators of terminal differentiation, as well as survival and maintenance of mDA neurons. Mature mDA neurons express markers such as tyrosine hydroxylase, AADC, Aldh1a1, VMAT2 and GIRK2 (Arenas, Denham et al. 2015). Expression of all these factors described above during mDA neurogenesis is shown in **Figure 9.**

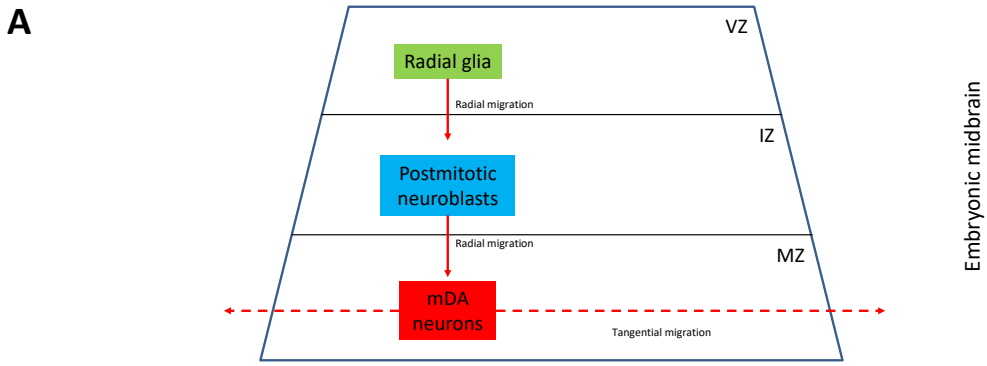

B

Marker	Wnt1	Shh	Msx1	LXRa	Mash1	LXRb	Ngn2	Wnt5a	Otx2	Lmx1b	Foxa2	Lmx1a	Aldh1a1	En1	Cxcr4	Nurr1	Pitx3	Th	Aadc	Vmat2	Dat	Girk2
Radial Glia	+	+	+	+	+	+	+	+	+	+	+	+	+	L								
Neuroblasts						L	L	L	+	+	+	+	+	+	+	+	L		L			
mDA neurons (E12)								L	+	+	+	+	+	+	+	+	+	+	+	+		
mDA neurons (E15)									+	+	+	+	+	+		+	+	+	+	+	+	+

Figure 9. Neurogenesis of midbrain dopaminergic (mDA) neurons. A. *Midbrain progenitors migrate radially towards the marginal zone, where they mature into mDA neurons before finally migrating tangentially to their final positions (Substantia Nigra for A9 neurons).* ***B.*** *Expression of genes important in mDA neurogenesis. Data from mice embryological studies. Genes expressed in Radial Glia (RG) are shown in green, genes in neuroblasts in blue, while in mDA neurons in red. Gene expression in mDA neurons is shown in two stages, Embryonic Day 12 (E12) and Embryonic Day 15 (E15, more mature). As shown, markers of midbrain progenitors include Foxa2, Lmx1a/b, and En1, whereas markers of advanced mDA maturity include Nurr1, Th, and Dat; expression of these and other markers, as described in following chapters, will be examined in our model via immunofluorescence and quantitative real-time PCR. This figure has been adapted from (Arenas, Denham et al. 2015). VZ: ventricular zone, IZ: intermediate zone, MZ: marginal zone, +: marker expressed, L: expressed in low levels.*

After the stringent process of iPSC characterisation, one iPSC line from each control and patient (7 in total, including the CRISPR-corrected lines) were taken forward for downstream neuronal differentiation, disease modelling and drug screening. For iPSC mDA neuronal differentiation, I used

a protocol with slight modifications from one previously published (Kirkeby, Grealish et al. 2012, Kirkeby, Nelander et al. 2012). As described above, this protocol is based on dual SMAD inhibition to induce neuronal identities and addition of factors to push cells towards ventral midbrain fates. As the protocol is 65 days long, the efficiency of differentiation was assessed at two stages, a) at Day 11 ventral midbrain progenitor and b) at 'mature' Day 65 mDA neuronal stage. In summary, all patient and control lines that were chosen for downstream experiments successfully differentiated into mDA neurons. The process of characterising the generated mDA neurons is detailed below.

3.4. Ascertainment of dermal fibroblast and iPSC lines for downstream experiments

Patient and control iPSC lines and originating fibroblasts used in this project are summarised in **Table 16**. Fibroblast line BUCL01 was collected at GOSH. Fibroblasts 535-201 and 587-201A were collected at OHSU. I also used HDF7301-05 and 582-202 as age-matched control lines; HDF7301-05 fibroblasts were ascertained from the UCL GOS ICH Dubowitz Biobank, whereas 582-202 from OHSU. As mentioned above, reprogramming into iPSCs took place at both UCL GOS ICH and the Vallier lab in Cambridge (**Table 16**). At least 2 iPSC clones were derived from each dermal fibroblast line. After rigorous characterisation of pluripotency (**Section 3.5**), only one suitable clone per patient/ control was taken forward for downstream experiments. Finally, BPAN iPSC lines 587-02 (Patient 02) and 535-02 (Patient 03) were used for CRISPR/Cas9-mediated mutation correction and creation of isogenic controls R7-72 (Patient 02 Corrected) and R234-68 (Patient 03 Corrected), respectively.

Finally, several more BPAN fibroblast lines were collected from GOSH, the OHSU and the Royal Children's Hospital in Melbourne, Australia (with appropriate MTAs where applicable) (data not shown). However, these lines were not used for reprogramming, mainly due to capacity/ inability to handle more lines.

Fibroblast Identifier	iPSC Clone used after characterisation	*WDR45* Mutation	Protein Effect	Age	Gender	Mutation Location	Reprogramming/ CRISPR Correction
HDF 7301	**HDF 7301-05 (Control 01)**	Healthy control	Not applicable	13y	F	Not applicable	UCL GOS ICH
582-202	**582-06 (Control 02)**	Healthy Control	Not applicable	1y10mo	M	Not applicable	Vallier lab, Cambridge
BUCL01	**BPAN07 (Patient 01)**	c.344+2T>A	Aberrant splicing, early stop codon	5y	F	Just after exon 6	UCL GOS ICH
587-201A	**587-02 (Patient 02)**	c.19C>T	p.Arg7*	19y8mo	M	Exon 3	Vallier lab, Cambridge
535-201	**535-02 (Patient 03)**	c.700C>T	p.Arg234*	6y4 mo	F	Exon 9	Vallier lab, Cambridge
	R7-72 (Patient 02 Corrected)	Substitution of c.19C>T with 'wild-type' sequence	Normal length	19y8mo	M	Not applicable	Vallier lab, Cambridge
	R234-68 (Patient 03 Corrected)	Substitution of c.700C>T with wild-type sequence	Normal length	6y4 mo	F	Not applicable	Vallier lab, Cambridge

Table 16. Patient and control fibroblast and co-responding iPSC lines used in this project. *Two patient lines (587-02 and 535-02) harbour nonsense pathogenic mutations leading to an early stop codon. The third patient line carries a splice site mutation that leads to aberrant splicing and an early stop codon 2 nucleotides later (as detailed in the Results section). For our 2 isogenic controls R7-72 and R234-68, disease-causing mutations (in Patients 02 and 03, respectively) have been corrected using CRISPR/Cas9-mediated genome editing; The pathogenic single nucleotide polymorphism was substituted by the wild-type nucleotide, while other 'silent'/ synonymous changes were also introduced in order to avoid repeated editing once the desired correction had occurred.*

3.5. IPSCs are truly pluripotent and maintain disease-causing mutations

All iPSC lines used for downstream neuronal differentiation and drug screening experiments were extensively tested for true pluripotency. Any unsuitable lines (e.g. lines that had acquired major chromosomal rearrangements during reprogramming) were discarded (relevant data from characterisation of these lines is not shown). The available methods for iPSC characterisation vary in literature and can include many techniques such as formation of teratomas after iPSC injection in mice (Takahashi, Tanabe et al. 2007) or even mass spectrometry-based methods and proteomics (Baud, Heywood et al. 2019). In my project, I performed a comprehensive characterisation of all available iPSCs, which is described in detail below. Briefly, this included Spontaneous Differentiation into all germ layers *in vitro*, Epi-Pluri-Score, immunocytochemistry and RT PCR for pluripotency marker expression, Sendai Virus Clearance (RT PCR), SNP array analysis for karyotype integrity, genomic DNA sequencing to ensure maintenance of disease-causing mutations after reprogramming (and correction of these mutations after CRISPR genome editing) and, finally, cDNA sequencing in female iPSC lines and XCI studies to determine expression of the mutated WDR45 allele.

For the isogenic control lines R7-72 and R234-68 (deriving from patient lines 587-02 and 535-02, respectively), characterisation involved 1) detection of pluripotency marker expression through immunocytochemistry, 2) SNP array analysis for karyotypic integrity and 3) genomic DNA sequencing to ensure mutation correction, since originating lines 587-02 and 535-02 had already been extensively tested.

3.5.1. Spontaneous Differentiation into all germ layers in vitro

In order to ensure pluripotency, iPSC lines were initially tested for their ability of spontaneous *in vitro* differentiation into all three germ layers (endoderm, mesoderm, and ectoderm) that give rise to specific tissue lineages. For this, embryoid body-based spontaneous differentiation was performed, with 16 days of culture and subsequent immunofluorescent staining, as described in **Section 2.3.2**. All iPSC lines successfully differentiated spontaneously into all three germ layers,

endoderm, mesoderm and ectoderm. This was detected through expression of related markers (SOX17, SMA and TUJ1, respectively) via immunofluorescence experiments, as detailed in **Figure 10**.

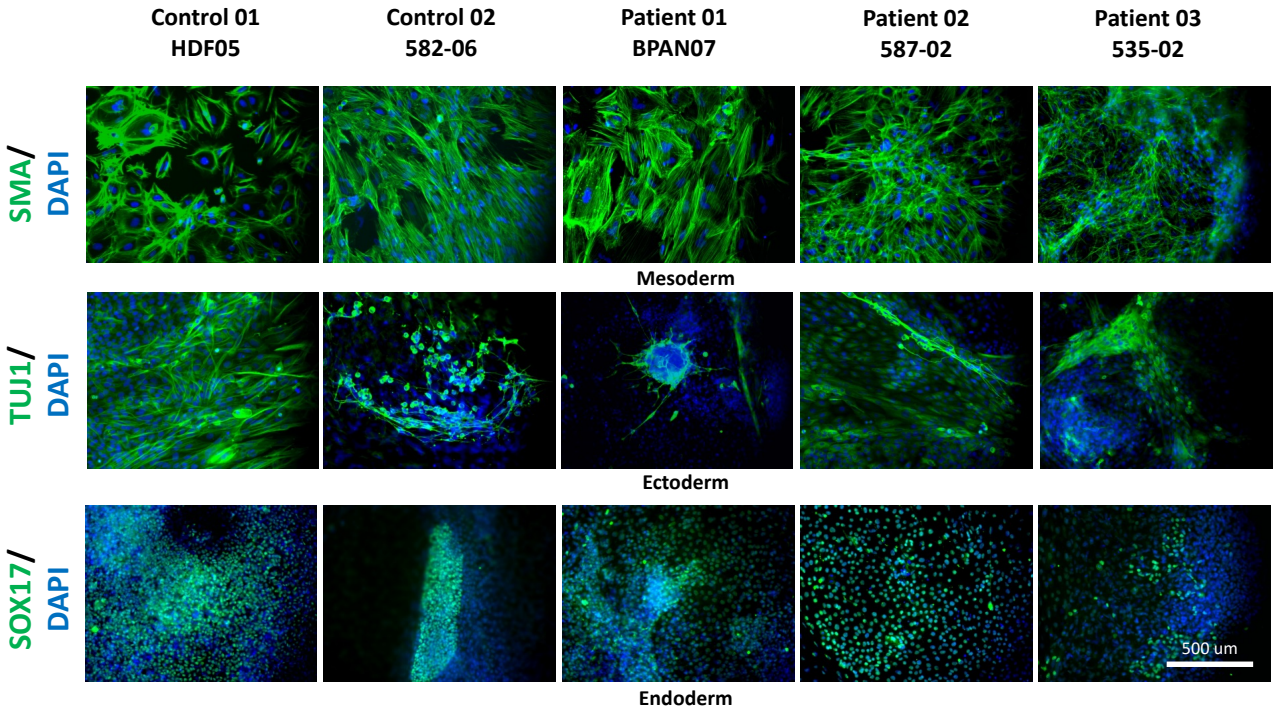

Figure 10. Immunofluorescence staining for Spontaneous in vitro Differentiation*. Cells were fixed, stained and imaged at Day 16 of the Spontaneous in vitro differentiation protocol. SOX17 (endoderm-related), TUJ1 (ectoderm-related), and SMA (mesoderm-related) markers are shown in green for all control and BPAN lines used for downstream experiments (apart from the two isogenic controls). Nuclei were stained for DAPI (blue). Images were acquired using the inverted Fluorescence microscope Olympus IX71, 20x air objective.*

3.5.2. Epi-Pluri-Score

Another test performed to ensure iPSC pluripotency was the Epi-Pluri-Score analysis, which distinguishes between pluripotent and non-pluripotent cell lines, based on differential DNA methylation of CpG sites (Lenz, Goetzke et al. 2015). Epi-Pluri-Score testing was performed on all patient and control iPSC lines. DNA methylation levels (β-values) of the CpG sites within *ANKRD46*, *C14orf115*, and *POU5F1 (OCT4)* confirmed pluripotency status for all lines tested, as detailed in **Figure 11**.

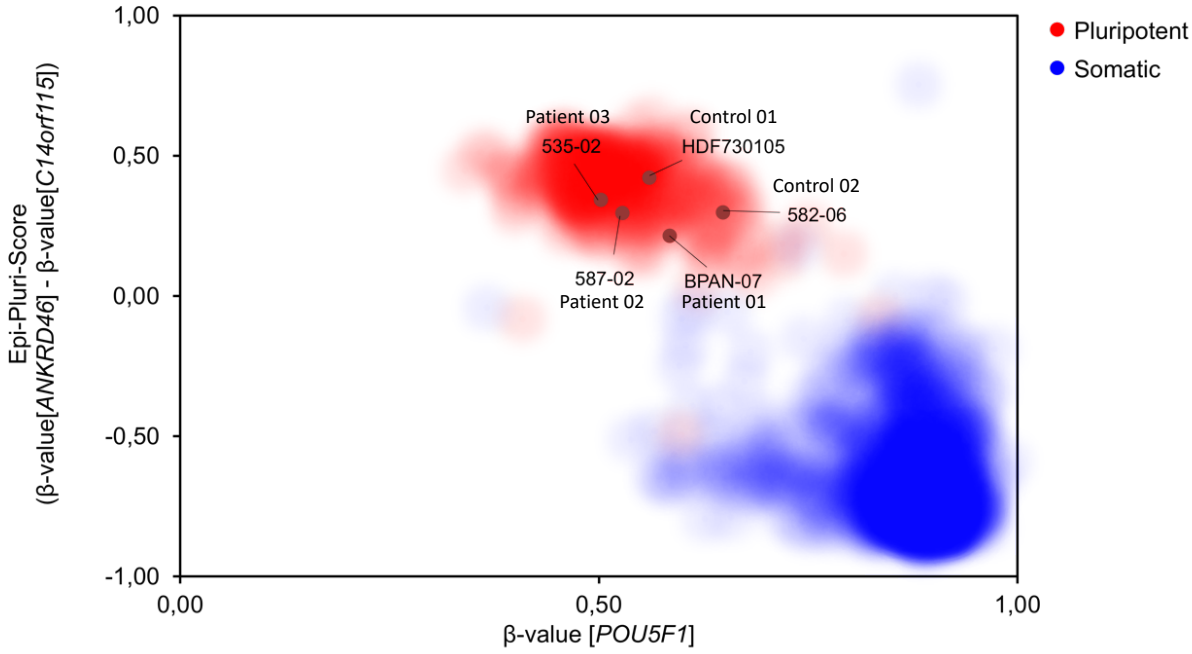

Figure 11. Epi-Pluri-Score testing. *All patient and control lines are in the pluripotent range (red) according to ANKRD46, C14orf115, and POU5F1 (OCT4) β-values. The Y axis represents the β-value of POU5F1 (OCT4), which increases during differentiation (or in somatic cells). The X axis represents the sum of (β-value [ANKRD46]-β-value[C14orf115]). ANKRD46 and C14orf115 are methylated (high β-value) and non-methylated (low β-value) in pluripotent cells, respectively. Conversely, after differentiation, the β-values for ANKRD4 and C14orf115 decrease and increase, respectively. The red cloud shows DNA methylation profiles of 264 pluripotent samples, while the blue cloud those of 1,951 non-pluripotent somatic samples (Lenz, Goetzke et al. 2015). The methylation profile of all 5 tested iPSC lines were located within the red cloud, providing further evidence for pluripotency of the control and patient lines.*

3.5.3. Pluripotency marker expression (Immunocytochemistry and RT PCR)

Moreover, as additional tests to establish iPSC pluripotency, all patient and control lines were tested for expression of pluripotency markers.

Firstly, I utilised immunofluorescence to assess this. Staining for 4 pluripotency-associated makers was undertaken. All 7 iPSC lines express pluripotency markers OCT4, NANOG, TRA-1-60 and TRA-1-81, as detected via immunofluorescence (**Figure 12**). Blocking was performed with (for nuclear markers OCT4 and NANOG) or without (for membrane markers TRA-1-60 and TRA-1-81) 0.1% Triton for cell membrane permeabilisation.

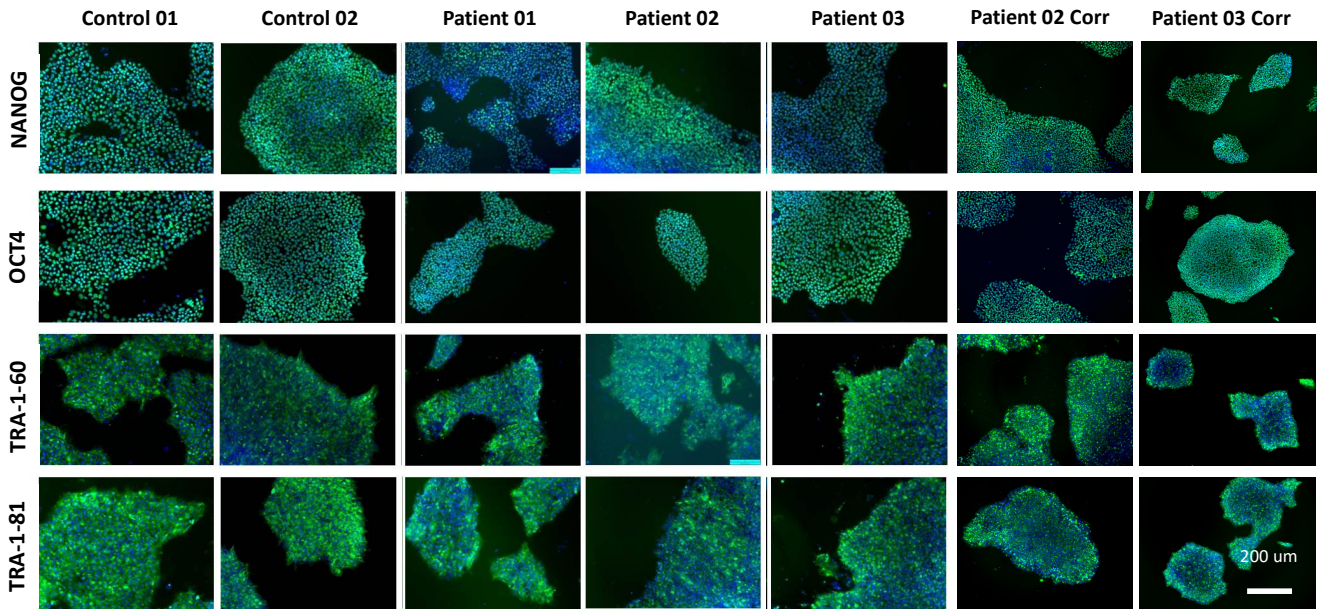

Figure 12. Pluripotency marker expression in iPSC lines (immunofluorescence). *All iPSC lines used for downstream neuronal differentiation and drug screening express nuclear markers OCT4 and NANOG, as well as surface markers TRA-1-60 and TRA-1-81 (stained green). DAPI (blue) was used for nuclear staining. Images were acquired using the inverted Fluorescence microscope Olympus IX71, 10x air objective. Although formal quantification was not performed, the vast majority of DAPI-positive cells also stain positive for pluripotency markers, indicating that cultures are in pluripotent state with lack of spontaneous differentiation under routine iPSC maintenance conditions.*

Additionally, endogenous expression of pluripotency markers *SOX2, KLF4, NANOG* and *OCT4* was also detectable via RT PCR (**Figure 13**). DNA samples analysed included skin fibroblasts and H9 human embryonic stem cells (negative and positive controls, respectively), while Glyceraldehyde-3-phosphate dehydrogenase (*GAPDH*) was used as a housekeeping gene. All patient and control iPSC lines, as well as the H9 line showed expression of all 4 pluripotency-related transcription factors tested, which were not detected in the fibroblast line.

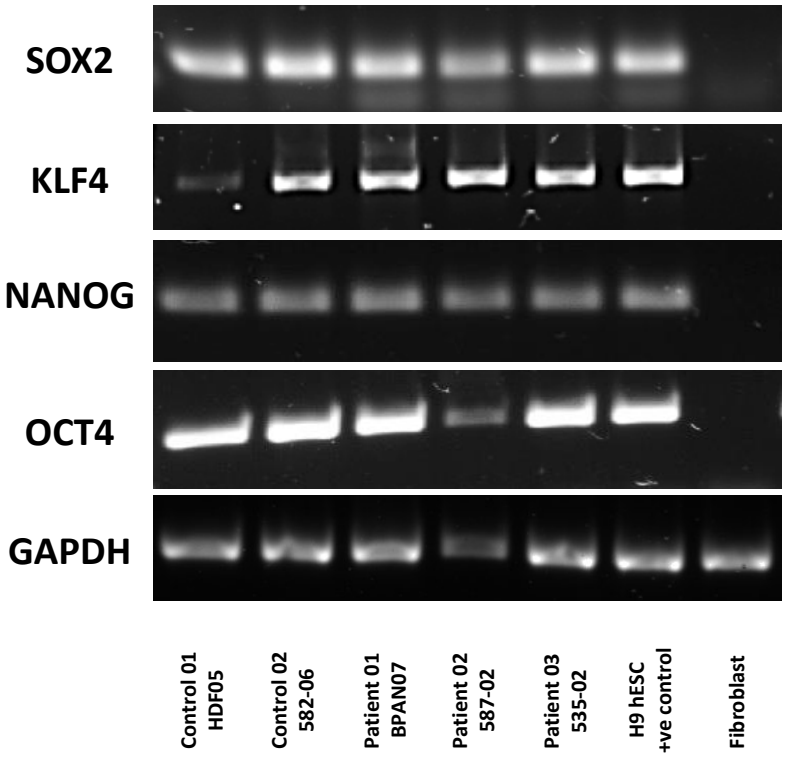

Figure 13. Detection of pluripotency maker expression via RT PCR. *cDNA from iPSC lines used for downstream experiments (apart from the CRISPR-corrected lines) was tested for expression of pluripotency markers. All iPSC lines express SOX2, KLF4, NANOG and OCT4. These are also positive in the H9 human embryonic stem cell (H9 hESC) line (used as positive control) but not detectable in human dermal fibroblasts (negative control). GAPDH was used as a housekeeping gene.*

3.5.4. Sendai Virus Clearance

Since Sendai Virus was used during iPSC reprogramming in order to transiently express pluripotency transgenes, it was important to determine its clearance from the iPSCs prior to further experiments. In order to confirm that Sendai virus had been cleared from iPSC lines after reprogramming, RT PCR was undertaken to detect SeV genome and transgenes (*Klf4, OCT4, c-MYC, SOX2*). Sendai virus genome and related pluripotency transgenes were not detectable in any iPSC line via RT PCR, confirming that there was no permanent integration of the virus into the iPSC genome. Results are detailed in **Figure 14**. Samples analysed included H9 human embryonic stem cells and Sendai Virus DNA (negative and positive controls, respectively); GAPDH was used again as a housekeeping gene.

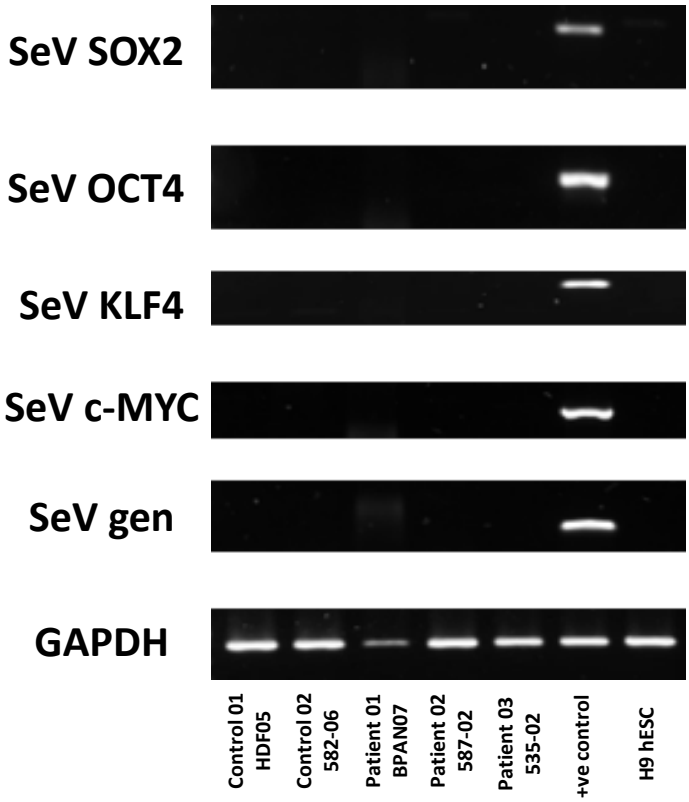

Figure 14. Sendai virus is not detectable in the derived iPSC lines. *cDNA from (undifferentiated) iPSC lines that were subsequently used for downstream experiments (apart from the CRISPR-corrected lines) was tested for detection of Sendai virus (SeV) genome (gen) and expression of pluripotency transgenes via RT PCR. A positive (+ve) control (SeV DNA) and a negative control (cDNA from the H9 human embryonic stem cell line, H9 hESC) were also included in the analysis. GAPDH was used as a housekeeping gene and detected in all lines. Transgenes carried on the Sendai Virus vector were present in the control Sendai virus DNA, but not detectable in any of the iPSC or embryonic stem cell lines.*

3.5.5. SNP array analysis

Confirmation of genomic integrity was essential prior to the use of iPSC lines for downstream experiments, as iPSCs are at high risk of chromosomal aberrations (deletions, duplications) that may 1) have significant effects on gene expression, protein expression and differentiation potential and thus 2) render them unusable for downstream neuronal differentiation and disease modelling (Mayshar, Ben-David et al. 2010). Therefore, in my project, I used a genome-wide SNP array analysis approach in order to determine genome stability and look for variations that could have occurred during the reprogramming process.

Analysis of SNP array data revealed that most available iPSC clones were suitable for use; however, other clones had acquired major abnormalities during reprogramming and when compared to SNP date from originating fibroblasts. Large deletions or insertions were regarded as pathogenic and iPSC clones subsequently discarded; the cut-off size for this was set at 5 megabases (Mb) or more. A summary of this process is provided in **Table 17**, while SNP array analysis of all lines subsequently used for downstream experiments is shown in **Figure 15**. When compared to the originating fibroblasts, lines HDF-05, 582-06, BPAN-07, 587-02 and 535-02 have no major chromosomal rearrangements. Similarly, isogenic controls R7-72 and R234-68 also maintain their genomic integrity post CRISPR/Cas9-mediated genome editing.

Fibroblasts	Derived iPSC Clones	SNP Array	Line Used (X)
HDF 7301	HDF 7301-03	Normal	
	HDF7301-05	Normal	X (Control 01)
582-202	582-03	Normal	
	582-06	Normal	X (Control 02)
BUCL01	BPAN06	103 Mb gain Chr 1 5 Mb deletion Chr 7	
	BPAN07	Normal	X (Patient 01)
	BPAN11	Normal	
587-201A	587-01	100 Mb loss of homozygosity Chr 1	
	587-02	Normal	X (Patient 02)
535-201	535-01	5 Mb duplication Chr 1	
	535-02	Normal	X (Patient 03)
CRISPR/Cas9 Edited iPSC lines			
587-02 (Patient 02)	R7-38	7.5 Mb deletion Chr 7	
	R7-72	Normal	X (Patient 02 Corrected)
	R7-83	Normal	
535-02 (Patient 03)	R234-20	90 Mb Gain X Chr	
	R234-40	Normal	
	R234-68	Normal	X (Patient 03 Corrected)

Table 17. Summary of dermal fibroblast and iPSC lines used in the BPAN project. *Most iPSC lines maintained karyotypic integrity after reprogramming and when compared to the originating fibroblast lines. Lines that had acquired large (> 5 megabases, Mb) were not used further and discarded. Lines produced after the CRISPR/Cas9-mediated isogenic control generation were similarly examined to ensure no major rearrangements had occurred during the genome editing process.*

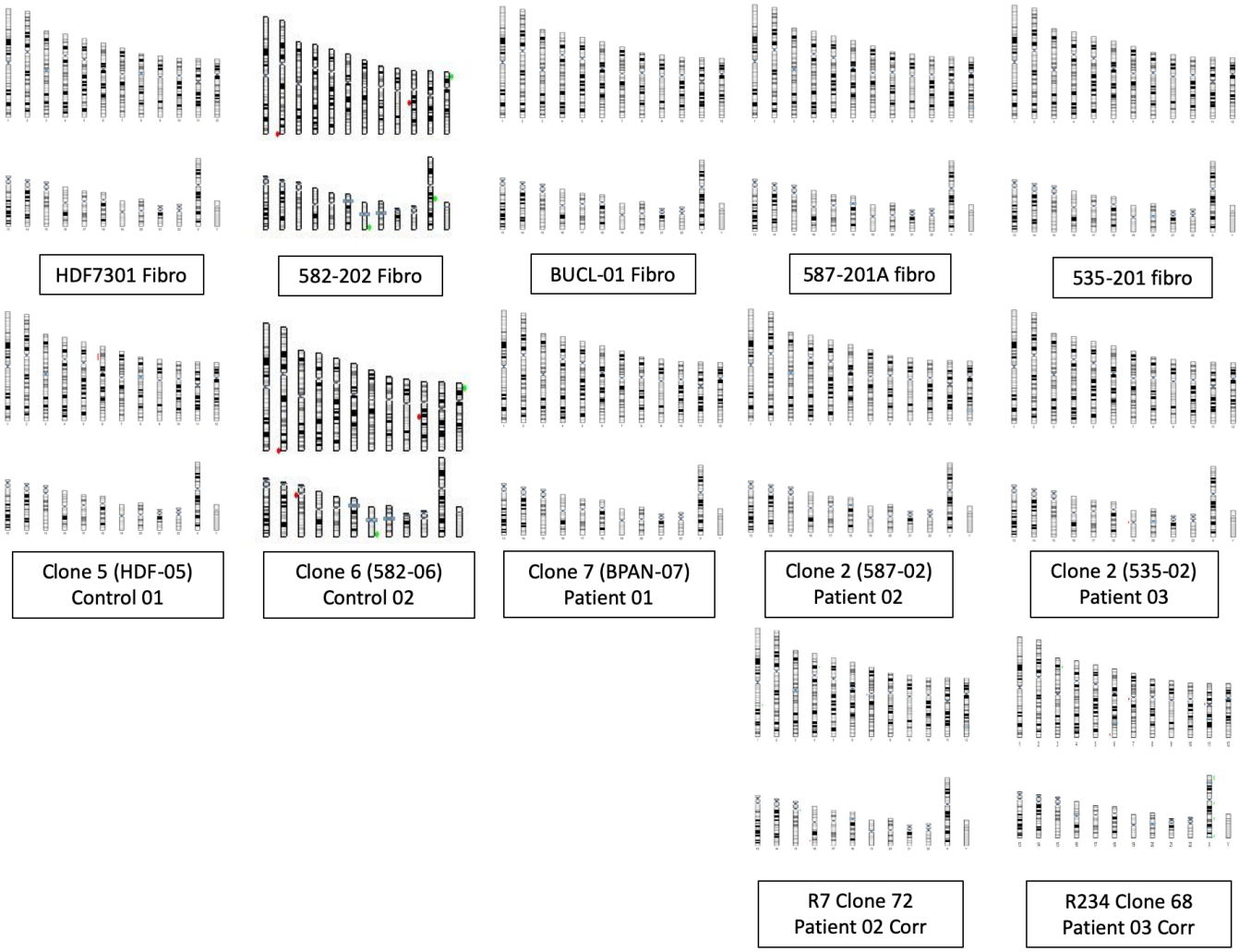

Figure 15. All iPSC lines used for downstream experiments have maintained their genomic integrity. *SNP array analysis of all iPSC lines used for downstream experiments. Genomic DNA sent to UCL Genomics for analysis using the Infinium HumanCytoSNP-12 v2.1 BeadChip array. Generated .idat files were subsequently analysed via Illumina's BlueFuse Multi software. Deletions are marked as red lines adjacent to their location on each chromosome, while insertions/ gains as green lines. All deletions/ gains were small (<5Mb) and also deemed as non-pathogenic BlueFuse Multi.*

3.5.6. BPAN lines maintain disease-causing mutations and express the mutated WDR45 alleles

Moreover, it was important to establish that our iPSC-based model was, indeed, one of WDR45 deficiency. For this purpose, I needed to determine that all derived iPSC lines harbour the mutations causing disease in our patients but also express the mutated allele.

Firstly, I performed Sanger sequencing of genomic DNA in order to establish that 1) *WDR45* mutations have been maintained from skin fibroblasts to the reprogrammed iPSCs, and that 2) control iPSC lines did not have any pathogenic *WDR45* variants. Sequencing revealed that BPAN iPSC lines maintain disease-causing mutations in *WDR45* after iPSC reprogramming (**Figure 16**). In detail, female line BPAN-07 (Patient 01) is heterozygous for mutation c.344+2T>A, while female 535-02 (Patient 03) is also heterozygous for mutation c.700C>T; p.234Arg*. Additionally, male line 587-02 is hemizygous for mutation c.19C>T; p.19Arg*. Finally, *WDR45* genomic DNA sequencing for control lines 01 and 02 (HDF-05 and 582-06, respectively) revealed no pathogenic variants. In more detail, in Control 01 (HDF-05), a homozygous intronic SNP with a very low minor allele frequency (MAF) was detected (c.977-9dupC; Reference SNP Cluster ID 782592002; MAF:0.00008), however splicing predictions suggested that this variant is not likely to affect gene splicing (according to the dbSNP database, https://www.ncbi.nlm.nih.gov/snp/?term=782592002) and, therefore, the line was used for downstream experiments. No SNPs worth mentioning were identified in Control 02 (582-06).

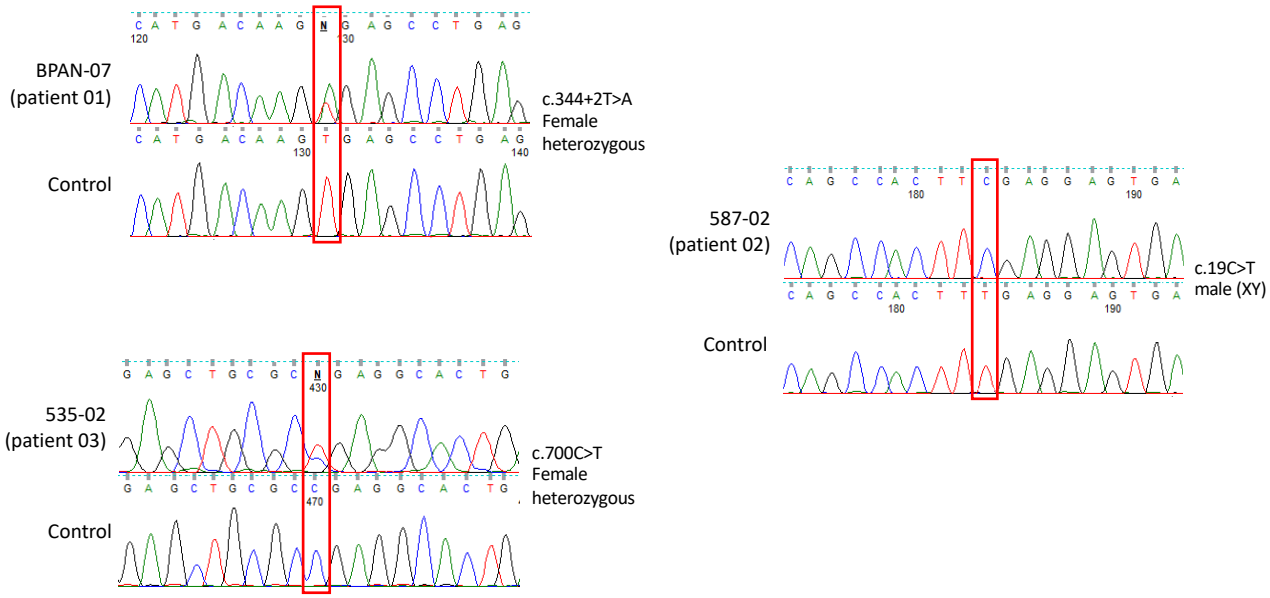

Figure 16. BPAN iPSC lines maintain disease-causing mutations. Genomic DNA from BPAN iPSC lines was subjected to WDR45 gene sequencing. *Sequencing chromatogram of regions surrounding the pathogenic variants are shown for Patient 01, 02 and 03 iPSC lines, but also for Control 01 (HDF05) iPSC line. WDR45 disease-causing mutations are highlighted in the red rectangles.*

Mutations in Patients 02 and 03 lead to early stop codons. Additionally, in BPAN-07, the c.344+2T>A variant leads to aberrant splicing (**Figure 17**). In detail, the donor splice-site at the end of exon 6 is abolished, leading to a premature stop codon 2 amino acids downstream. This is confirmed by a) splicing predictions and b) the inclusion of 28 aberrant intronic bases in the cDNA sequence (as detailed below).

```
WT_WDR45            MTQQPLRGVTSLRFNQDQSCFCCAMETGVRIYNVEPLMEKGHLDHEQVGSMGLVEMLHRS    60
WDR45_c.344+2T-A    MTQQPLRGVTSLRFNQDQSCFCCAMETGVRIYNVEPLMEKGHLDHEQVGSMGLVEMLHRS    60
                    ************************************************************

WT_WDR45            NLLALVGGGSSPKFSEISAVLIWDDAREGKDSKEKLVLEFTFTKPVLSVRMRHDKIVIVL    120
WDR45_c.344+2T-A    NLLALVGGGSSPKFSEISAVLIWDDAREGKDSKEKLVLEFTFTKPVLSVRMRHDKRA---    117
                    ************************************************** .

WT_WDR45            KNRIYVYSFPDNPRKLFEFDTRDNPKGLCDLCPSLEKQLLVFPGHKCGSLQLVDLASTKP    180
WDR45_c.344+2T-A    ------------------------------------------------------------    117

WT_WDR45            GTSSAPFTINAHQSDIACVSLNQPGTVVASASQKGTLIRLFDTQSKEKLVELRRGTDPAT    240
WDR45_c.344+2T-A    ------------------------------------------------------------    117

WT_WDR45            LYCINFSHDSSFLCASSDKGTVHIFALKDTRLNRRSALARVGKVGPMIGQYVDSQWSLAS    300
WDR45_c.344+2T-A    ------------------------------------------------------------    117

WT_WDR45            FTVPAESACICAFGRNTSKNVNSVIAICVDGTFHKYVFTPDGNCNREAFDVYLDICDDDD    360
WDR45_c.344+2T-A    ------------------------------------------------------------    117

WT_WDR45            F 361
WDR45_c.344+2T-A    - 117
```

Figure 17. WDR45 mutation c.344+2T>A leads to aberrant splicing and an early stop codon. *Alignment of wild type & BPAN07 9WDR45 c.344+2T>A) amino acid sequences showing premature truncation of the protein by 246 amino acids with the inclusion of 2 aberrant residues (arginine and Alanine); p.(Ile116Argfs*3). Wild type sequence was obtained from the Ensembl genome browser, amino acid sequence predictions were generated by entering wild type and BPAN07 cDNA sequences into the online ExPASy Translate tool (https://web.expasy.org/translate/), and sequence alignments were generated using the online ClustalOmega tool (https://www.ebi.ac.uk/Tools/msa/clustalo/). Abbreviations: WT= wild type sequence.*

Additionally, as XCI might affect which *WDR45* allele is expressed in female lines, it was theoretically possible that our female BPAN iPSC lines express the wild type alleles, hence effectively behaving as controls. As mentioned above, in female cells, the inactivated X chromosome is methylated and covered with XIST RNA, with the inactivation spreading across the entire chromosome (Panning 2008, Tchieu, Kuoy et al. 2010, Disteche and Berletch 2015). Hence, one would expect only one WDR45 allele (the one located on the active X chromosome) to be expressed in female iPSCs. In order to establish patterns of allele expression in my project, XCI analysis was performed for both female BPAN patients at all stages of differentiation (originating fibroblasts, derived iPSCs and Day 65 mDA neurons) (**Figure 18**). As mentioned above, this process involves PCR amplification and detection of a CAG repeat-containing portion of the methylated (inactivated) AR allele using appropriate primers, in the presence and absence of the methylation-sensitive restriction enzyme HpaII (which, in turn, removes the unmethylated alleles). For the first patient, BUCL01 fibroblasts show a random pattern of XCI. However, the pattern of inactivation in the derived BPAN-07 (Patient 01) iPSC line and in BPAN-07 Day 65 mDA neurons shows a completely non-random pattern of XCI, with effectively only one PCR band detectable in the presence of Hpall restriction enzyme. This, in turn signifies that, in BPAN-07 iPSC and neuronal lines, only one of the two X Chromosomes (and, therefore, WDR45 alleles) is expressed. The explanation for this is that 1) although fibroblasts are a mixed population with a random status of XCI, iPSCs are clonal, with the XCI status being the same as the one in the originating dermal fibroblast and 2) the XCI status is maintained throughout neuronal differentiation. Similarly, in the second female patient, 535-201 fibroblasts, derived iPSCs (535-02, Patient 03) and mDA neurons have XCI skewing in favour of one chromosome, and only one X Chromosome (and WDR45 allele) is expressed in these lines.

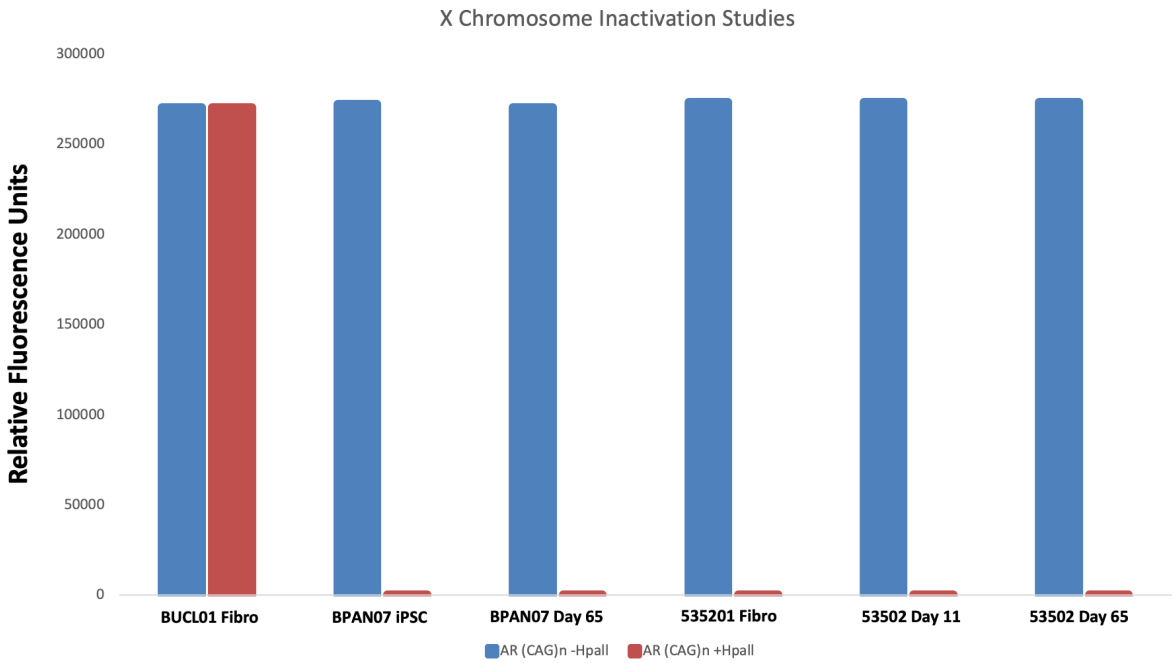

Figure 18. XCI status in BPAN female lines. *Analysis was performed using the human Androgen Receptor assay, which is based on fluorescent PCR of the AR locus after digestion with the methylation-sensitive restriction enzyme HpaII. For patient 01 (BPAN07), XCI analysis in fibroblasts shows a random pattern of X inactivation, with two PCR bands detectable in the presence and absence of the HpaII restrictive enzyme. For patient 03 (535-201), there is practically only one detectable band in the fibroblasts, signifying a skewing of XCI towards the expression of only one allele. Importantly, for both patients, iPSC lines and derived neurons have very skewed patterns of XCI, with PCR bands practically undetectable in the presence of HpaII. This signifies that only one WDR45 allele is expressed in female BPAN iPSC and neuronal lines.*

Subsequently, in order to determine exactly which of the two alleles are expressed in female BPAN iPSCs, *WDR45* cDNA sequencing of Patients 01 and 03 was also performed and compared to control iPSC cDNA (from the HDF-05 line). In detail, cDNA from Patient 01 (BPAN-07) is 28 base pairs longer than control cDNA while cDNA from Patient 03 (535-02) retains the c.700C>T change leading to an early stop (**Figure 19**).

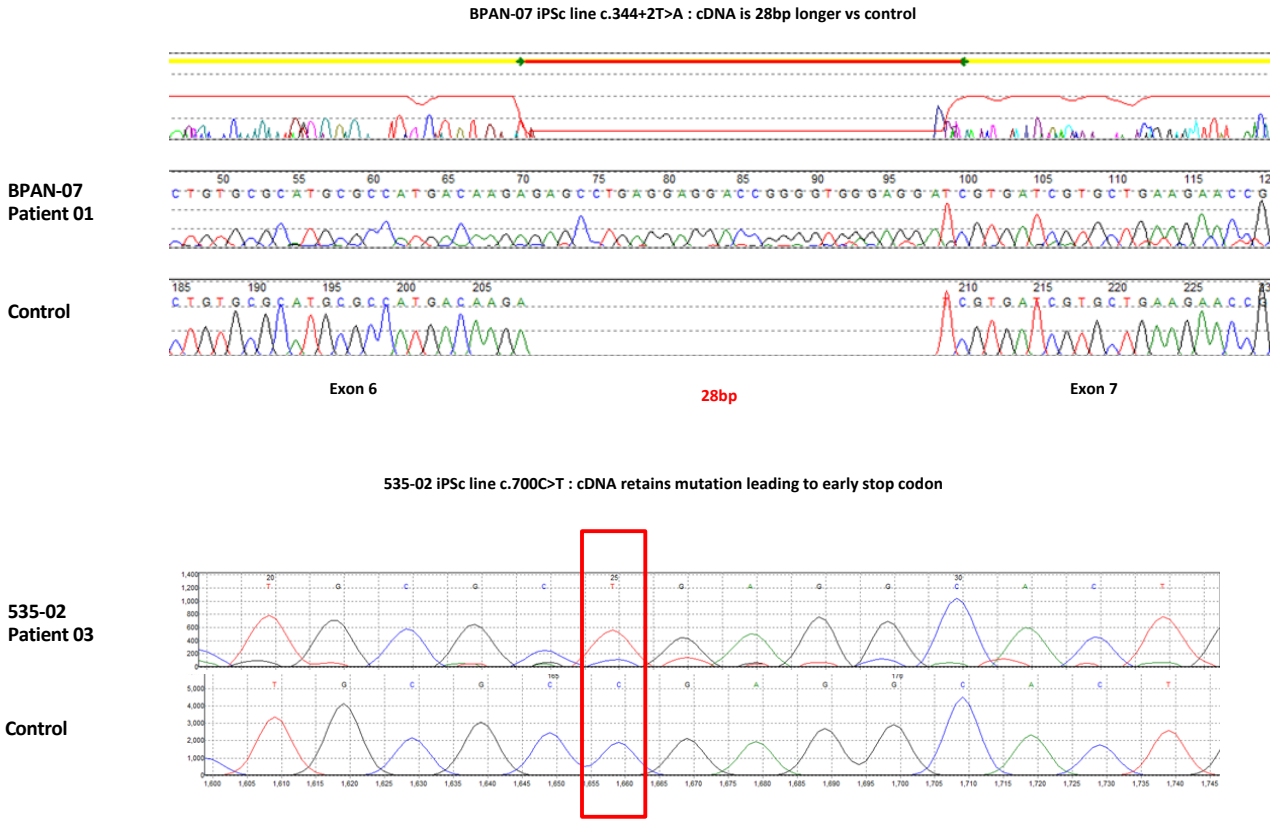

Figure 19. WDR45 cDNA sequencing in female BPAN iPSC lines indicates that the mutated alleles are expressed. *Sequencing of cDNA from female BPAN iPSC lines Patient 01 and Patient 03, and relevant chromatograms surrounding the positions of the pathogenic mutations, are shown. In Patient 01 (BPAN-07), the cDNA is abnormally long, while for Patient 03 (535-02), the c.700C>T leading to an early stop codon is retained.*

The cDNA sequencing results, paired with the analysis of the XCI status, indicate that the mutated alleles are expressed in both female BPAN iPSC lines. This is further supported by Western Blotting experiments for WDR45 expression at Day 65 of differentiation (detailed below in Results **Chapter 4**), that show complete absence of WDR45 protein in all patient neurons.

3.5.7. CRISPR Genome editing in two BPAN lines restores a nucleotide sequence leading to full-length protein

The use of CRISPR-generated isogenic controls was crucial in this project in order to ensure robust comparisons between patient and control lines in downstream experiments. After obtaining the two genome edited lines, R7-72 (Patient 02 Corrected) and R234-68 (Patient 03 Corrected), I firstly needed to confirm that the WDR45 disease causing mutations had, indeed, been corrected. Therefore, WDR45 genomic DNA sequencing of the two CRISPR/Cas9-generated isogenic controls was performed.

For Patient 02 (587-02, c.19C>T), HDR after the Cas9-mediated double stranded break resulted in the following changes:

c.16C>T; c.18C>A; c.19T>C

Apart from mutation correction, adjacent nucleotides were also substituted with synonymous changes, in order to avoid repeated editing at the site once the correction at position 19 had occurred, at the same time ensuring translation of the correct amino acid sequence (**Figure 19**). Similarly, for Patient 03 (535-02, c.700C>T), the following genomic DNA changes occurred during genome editing:

C.697C>A; c.699C>A; c.700T>C

Changes included mutation correction at position 700 but also synonymous nucleotide changes in adjacent positions (**Figure 20**).

Figure 20. Alignment of wild type, patient 02 (c.19C>T), patient 03 (c.700C>T) and CRISPR corrected WDR45 genomic DNA sequences. *The wild type sequence was obtained from the Ensembl genome browser and sequence alignments were generated using the online ClustalOmega tool (https://www.ebi.ac.uk/Tools/msa/clustalo/). For each corrected line, three nucleotide substitutions occurred after HDR, and are depicted in red rectangles. Patient 02 Corrected (initially c.19C>T): c.16C>T; c.18C>A; c.19T>C. Patient 03 Corrected (initially c.700C>T): C.697C>A; c.699C>A; c.700T>C. For both corrections, the first two are silent/ synonymous changes and, overall, the sequence leads to translation of a full-length WDR45 protein, as detailed below. These additional synonymous changes are important in order to avoid repeated editing at the site once the correction occurs, but also to accurately distinguish correctly edited lines through subsequent sequencing.*

Finally, *in silico* analysis predicts that genome editing restores WDR45 protein translation at its full length (**Figure 21**). This is further supported by Western Blotting experiments for WDR45 expression at Day 65 of differentiation (detailed below in **Chapter 4**), that show restoration of the WDR45 protein band in both CRISPR lines, and at the same size (in kDA) when compared to Controls 01 and 02.

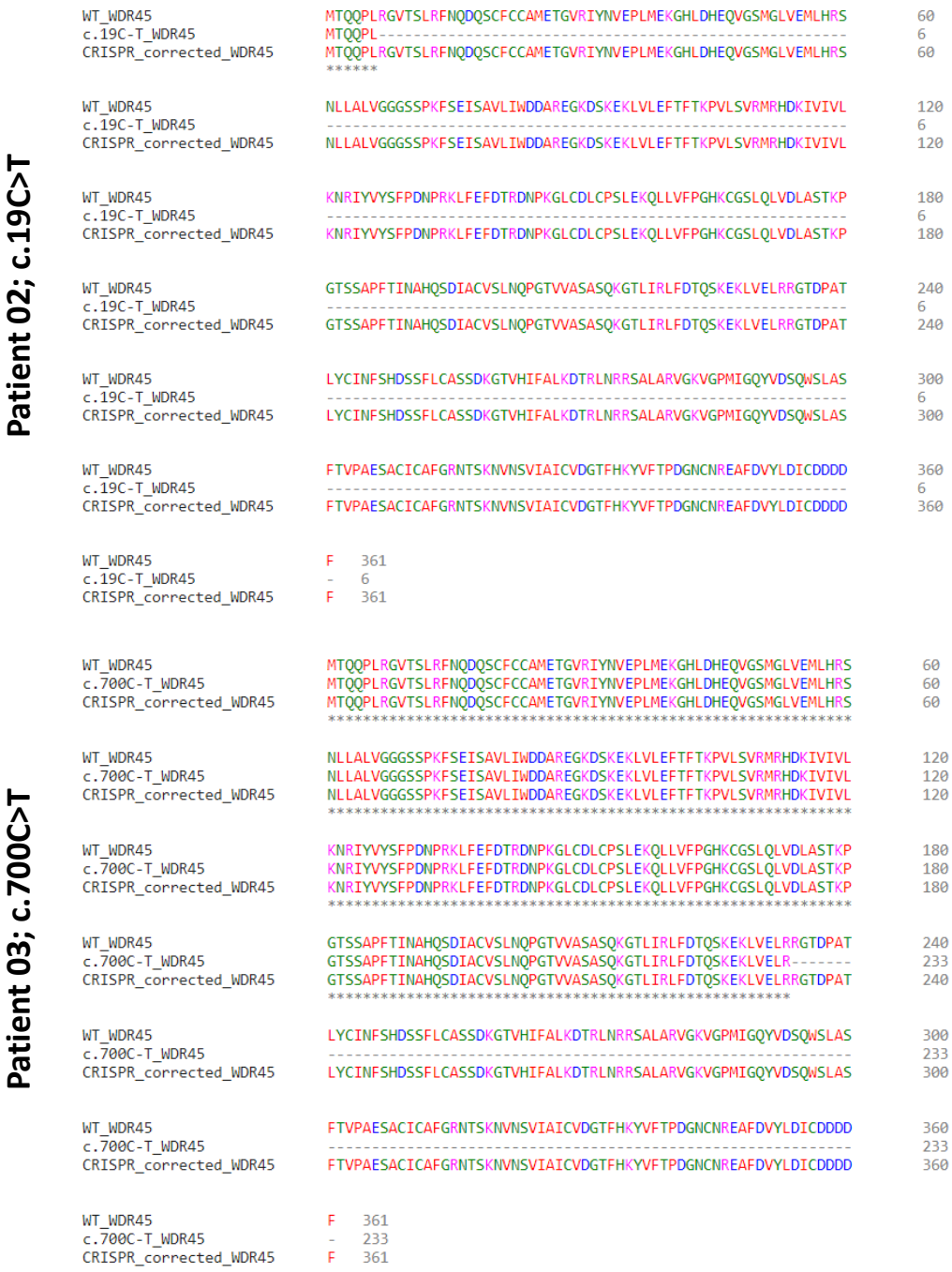

Figure 21. CRISPR/Cas9-mediated genome editing restores full length WDR45 protein in edited lines. *Above: Alignment of wild type, WDR45 c.19C>T (Patient 02, 587-02) & R7-72 (Patient 02 Corrected) WDR45 amino acid sequences showing premature truncation of the protein resulting from the c.19C>T change and restoration of the wild type sequence following c.16C>T, c.18T>A and c.19T>C CRISPR correction. Below: alignment of wild type, WDR45 c.700C>T (Patient 03, 535-02) & R234-68 (Patient 03 Corrected) WDR45 amino acid sequences showing premature truncation of the protein resulting from the c.700C>T change and restoration of the wild type sequence following c.697C>A, c.699C>A and c.700T>C CRISPR correction. The wild type sequence was obtained from the Ensembl genome browser; amino acid sequence predictions were generated by entering wild type, mutant and CRISPR corrected DNA sequences into the online ExPASy Translate tool (https://web.expasy.org/translate/), and sequence alignments were generated using the online ClustalOmega tool (https://www.ebi.ac.uk/Tools/msa/clustalo/)*

3.6. All lines differentiate efficiently into midbrain dopaminergic neurons

3.6.1. Characterisation of ventral midbrain progenitors

Firstly, expression of ventral midbrain markers forkhead box protein A2 (FOXA2) and homeobox transcription factor 1 alpha (LMX1A) was examined at Day 11 of differentiation through immunofluorescence (**Figure 22**). Co-expression of FOXA2 and LMX1A is thought to be unique to the ventral midbrain (Kriks, Shim et al. 2011), hence a high percentage of doubly-positive cells indicates effective initiation of differentiation into mDA neurons. In all tested lines, both patient and control, high percentages of expression of (and co-expression for) both ventral midbrain markers were evident. There was no significant difference in FOXA2 and LMX1A expression patterns between patient and control lines (**Figure 23**).

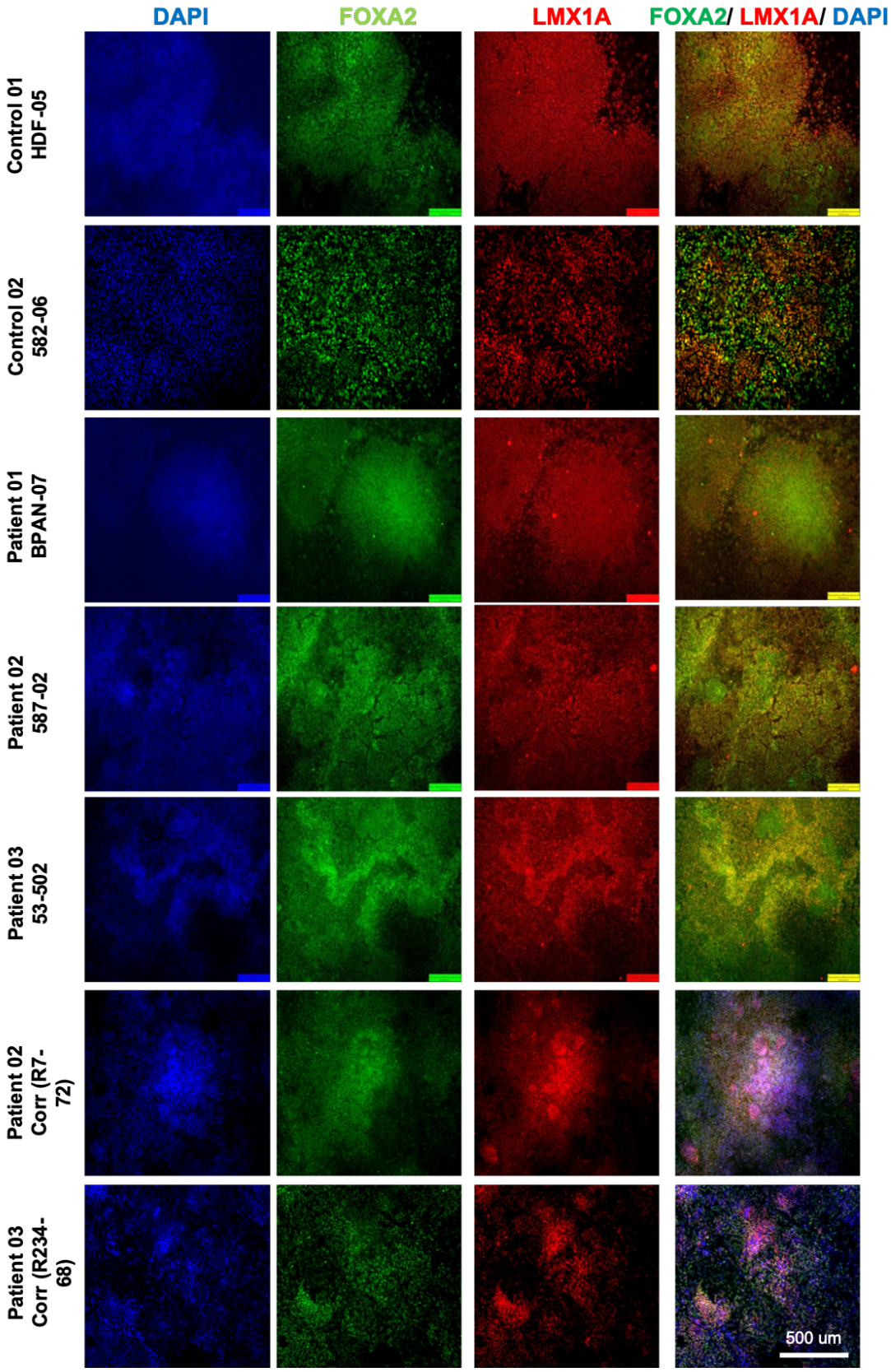

Figure 22. Expression of ventral midbrain markers in Day 11 progenitors. *FOXA2 is stained in green, LMX1A in red and nuclei (DAPI) in blue. All lines co-express FOXA2 and LMX1A in high percentage of cells (Figure 23), signifying an effective initiation of differentiation into mDA neurons. Images were acquired on the inverted Fluorescence microscope Olympus IX71, 10X air objective.*

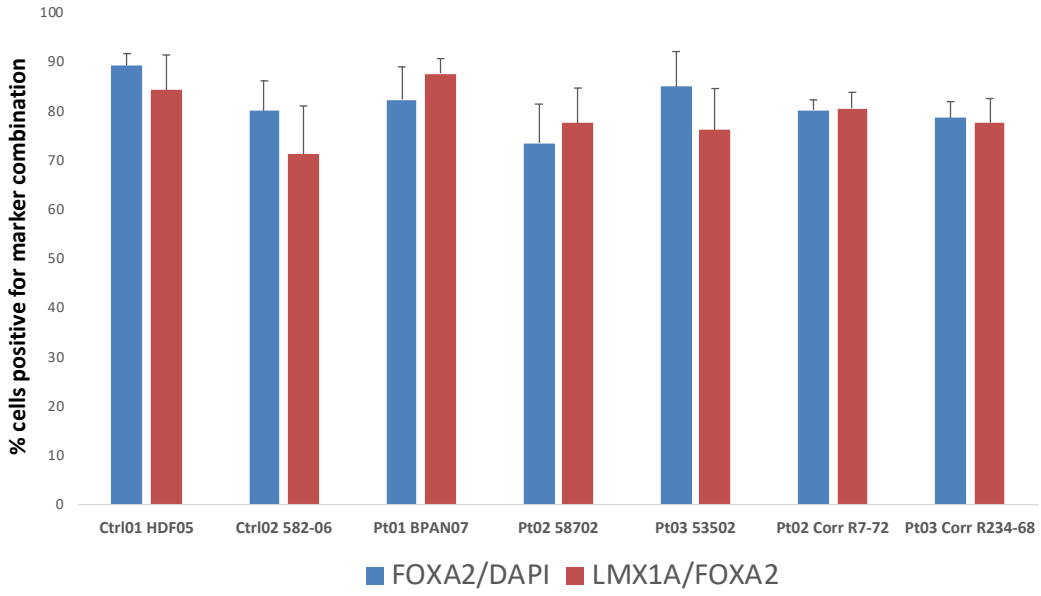

Figure 23. Co-expression of LMX1A and FOXA2 in Day 11 ventral midbrain progenitors. *Ventral midbrain marker FOXA2 is expressed in the majority of DAPI-positive cells, for all lines. The co-expression of LMX1A/ FOXA2 is present in high percentages in all line. There is no statistical difference between FOXA2/ DAPI and LMX1A/FOXA2 ratios between control and patient lines. Percentages were calculated after manual counting of cells on ImageJ/Fiji using images acquired with a 20X objective (n=3 for all lines; 3 individual images taken from random areas of a well were analysed for each biological replicate). No statistical significance was seen when comparing both ratios of FOXA2/DAPI and LMX1A/FOXA2 between patient and control lines. Statistical analysis was performed using the ordinary one-way ANOVA test. Error bars represent the Standard Error of Mean. Abbreviations: Pt= Patient, Ctrl= Control, Corr= Corrected*

Additionally, at day 11 of differentiation, lines were tested via qRT PCR for appropriate marker gene expression suggestive of effective initiation of mDA neuronal differentiation. For each marker/ target, ΔC_T mean values in Day 11 ventral midbrain progenitors (calculated using the target's C_T mean values, normalised versus the ones from the housekeeping gene GAPDH) were compared to ones in corresponding iPSCs. All lines exhibited a) downregulation in gene expression of pluripotency-related markers *OCT4* and *NANOG* and b) upregulation in gene expression of ventral midbrain markers *FOXA2, LMX1A, LMX1B, EN1* and *EN2* (**Figure 24**).

In summary, both immunofluorescence and qRT PCR experiments at Day 11 confirm a successful initiation of mDA neuronal differentiation and the generation of robust ventral midbrain progenitors.

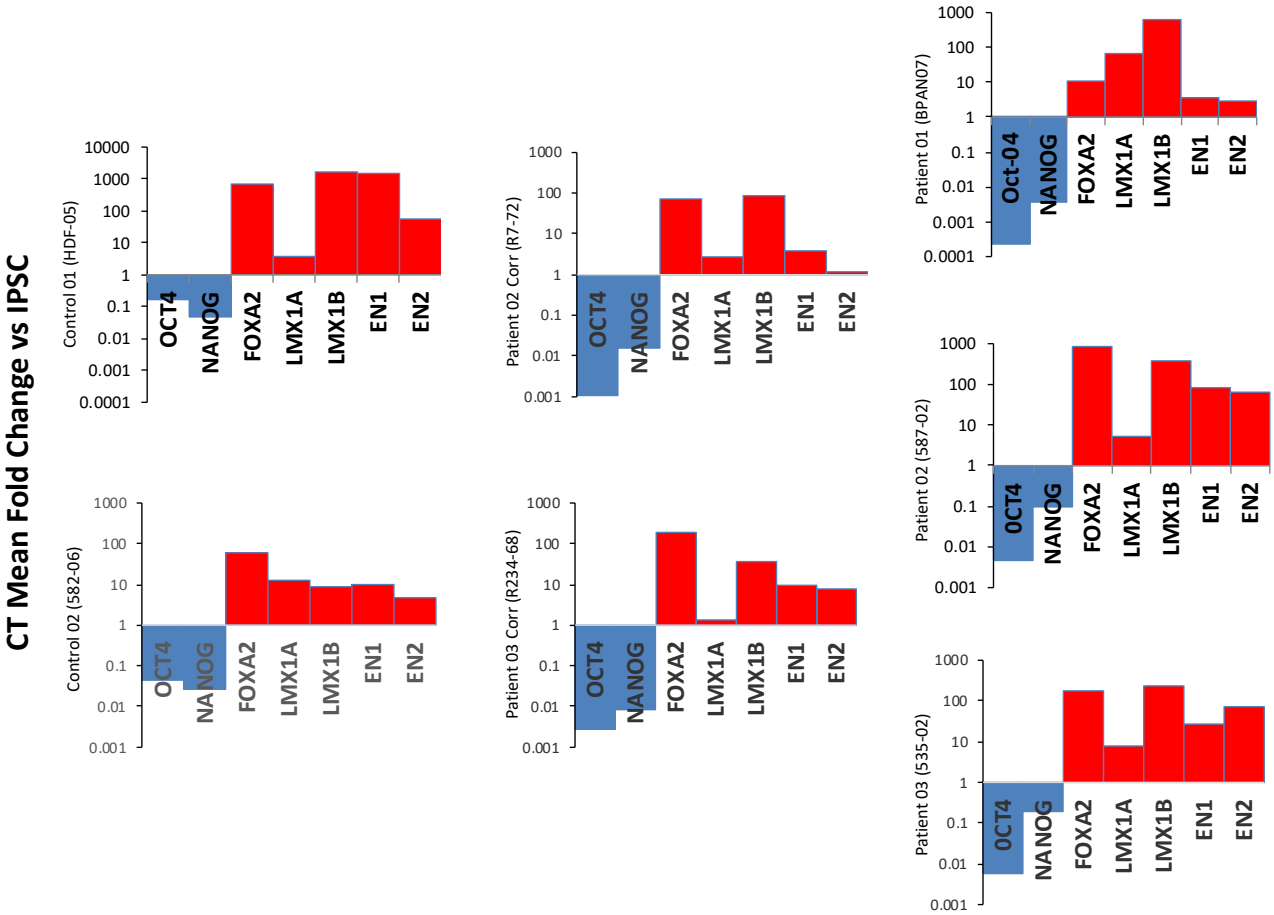

Figure 24. Day 11 ventral midbrain progenitors: real-time quantitative RT PCR. *All lines show upregulation of ventral midbrain markers (in red) and downregulation of pluripotency markers (in blue). On the graphs, the y axis is on a logarithmic scale. Gene expression is relative to the housekeeping gene (GAPDH) and normalised to the respective iPSC line; the fold Change of the* $\Delta\Delta C_T$ $[(\Delta\Delta C_T = \Delta C_T\ sample\ -\ \Delta C_T\ iPSC)$*, and [(FC)= 2^-(ΔΔCT)], when comparing the CT mean values of each target to the one of the corresponding iPSC, is shown. n=1 representative differentiation for each line, n=3 technical replicates for the CT Mean calculation for each marker.*

3.6.2. Characterisation of Day 65 mDA neurons

All patient and control lines differentiated successfully to Day 65 mDA neurons. At this stage, mature neurons were examined via immunofluorescence for typical morphology (a soma and dentritic processes) (Hartfield, Yamasaki-Mann et al. 2014), as well as the expression of the dopaminergic-specific marker tyrosine hydroxylase (TH) and the pan-neuronal marker microtubule-associated protein 2 (MAP2). All lines exhibited mature dopaminergic neuronal morphologies with round soma and long neural projections. Additionally, all lines expressed MAP2 and TH (**Figure 25**). After quantification of MAP2- and TH-positive cells, no significant differences were detected between patient and control mDA neurons, signifying absence of spontaneous neurodegeneration in the dish under normal tissue culture conditions (**Figure 26**). Additionally, MAP2/DAPI, TH/DAPI and TH/MAP2 ratios were similar to those reported in other studies (Kirkeby, Grealish et al. 2012), indicating that the differentiation process was overall effective.

Interestingly, only a proportion of cells in my cultures were (TH-positive) dopaminergic neurons. This implies that other cell subtypes are very likely to also be present, for example other neuronal subtypes or glial cells. It is unclear why these cells co-exist with dopaminergic neurons in the dish; however, it is plausible that dopaminergic neurons need these types of cells in their environment to survive and function. Although this was not the focus of my PhD project, a perhaps interesting future experiment would be to try to establish what other cell subtypes are present in my cultures, and in what proportion. For this, I would have to perform immunostaining (e.g. staining using antibodies against Glial Fibrillary Acidic Protein for detection of astrocytes, or Tryptophan Hydroxylase for serotonergic neurons) (Heller and Rusakov 2015, Ye, Pitlock et al. 2018) or (fluorescence-activated or magnetic-activated) cell sorting (Zhu and Murthy 2013).

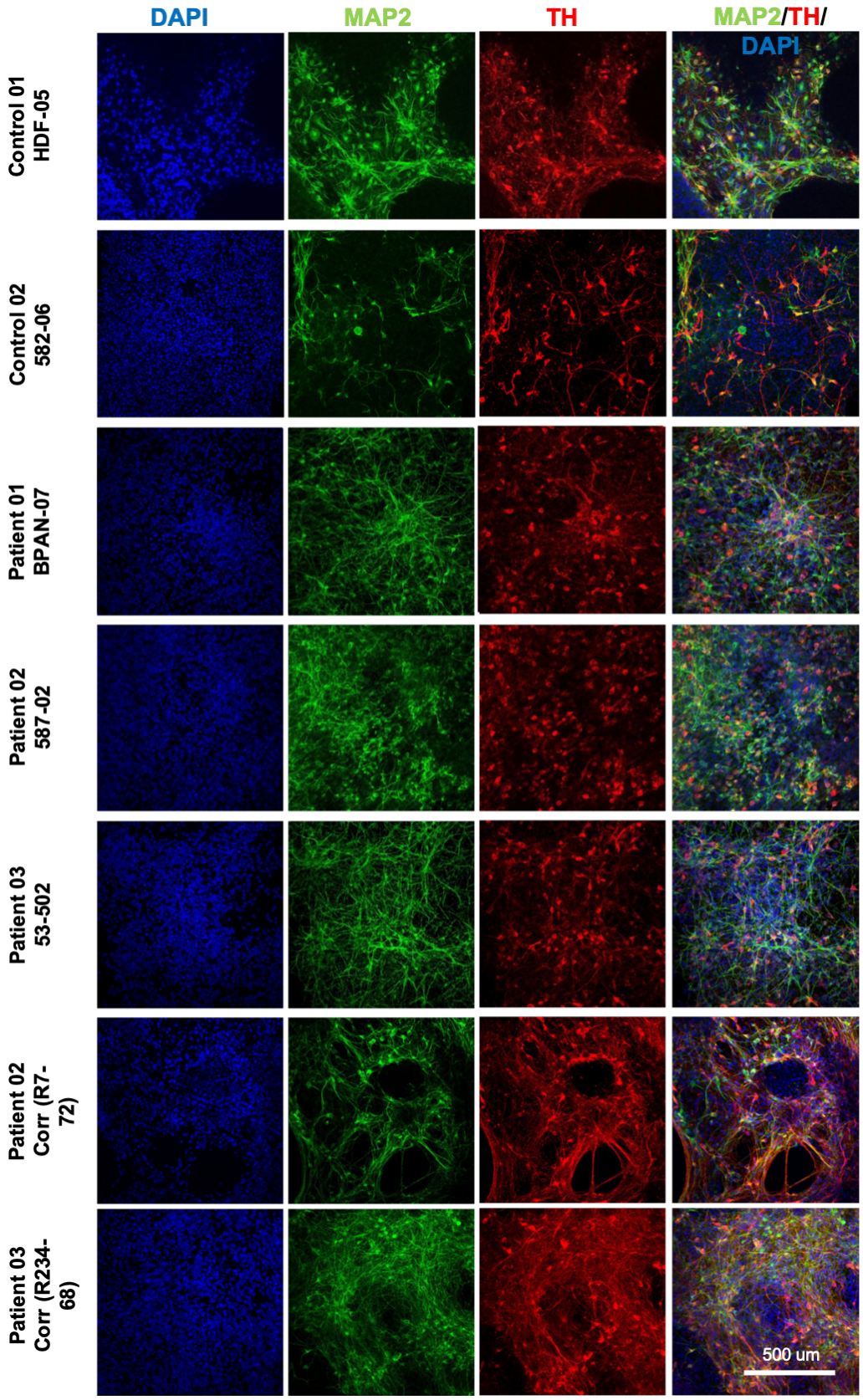

Figure 25. Day 65 immunofluorescence. *Mature dopaminergic neurons derived from all lines exhibit typical morphology and express pan-neuronal (MAP2, stained in green) and dopaminergic-specific (TH, stained in red) markers. Nuclear staining (DAPI) is shown in blue. Images were acquired on the Zeiss LSM880 multiphoton confocal microscope and a 20X water immersion objective was used.*

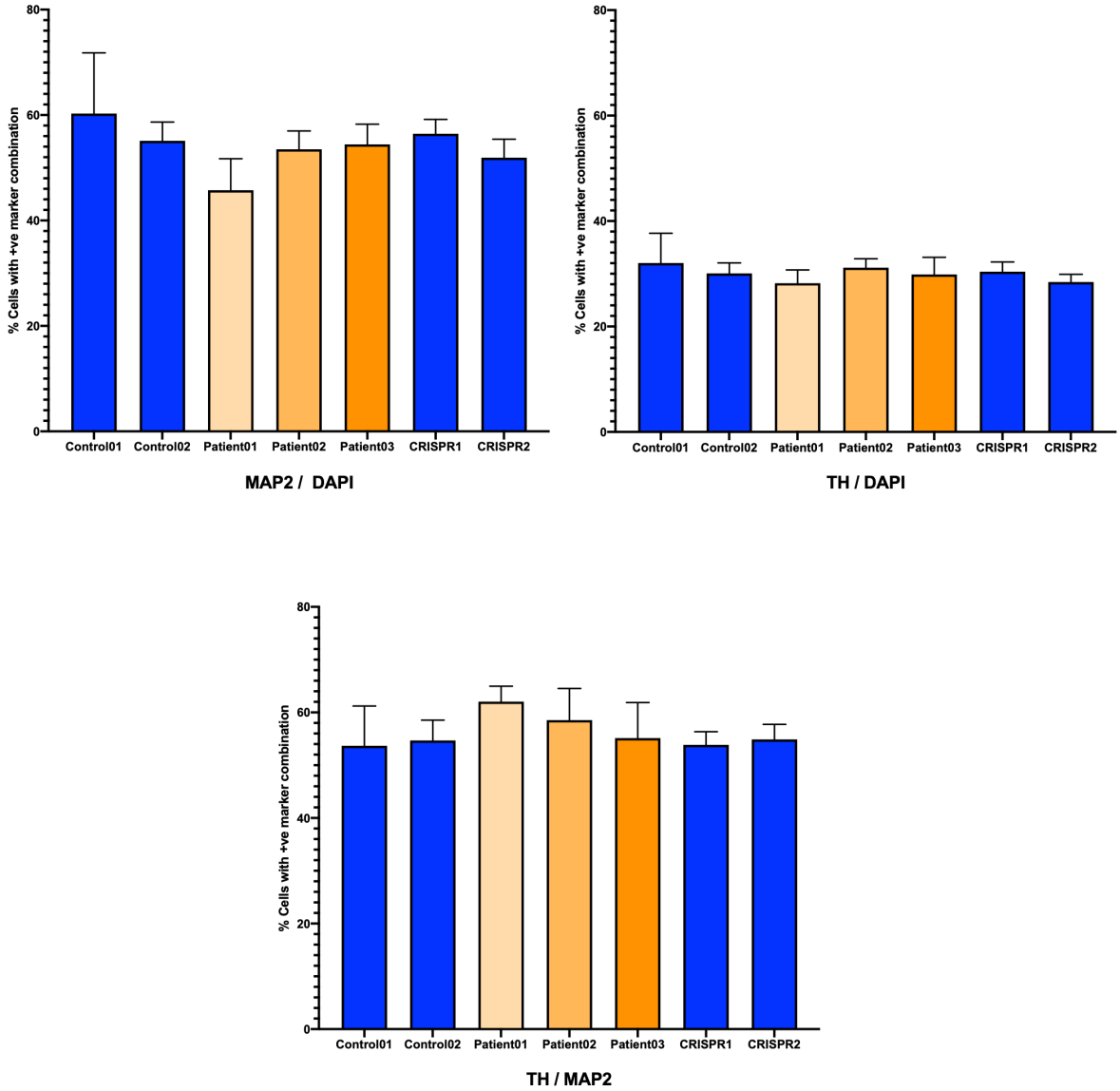

Figure 26. Quantification of Day 65 immunofluorescence. *The ratios of MAP2/DAPI, TH/DAPI and TH/MAP2 are comparable to those reported in other studies. There is no statistically significant difference between TH/ DAPI, MAP2/DAPI and TH/MAP2 ratios when comparing control and patient lines. Percentages were calculated after manual counting of cells on ImageJ/Fiji, using images acquired with a 20X objective. Statistical analysis was performed using the ordinary one-way ANOVA test. n=3 replicates for all lines. 3 individual images, taken from random areas of a LabTek slide well, were analysed for each biological replicate. Error bars represent the Standard Error of Mean.*

Additionally, qRT PCR was performed at Day 65 to ensure a pattern of gene expression compatible with mDA neuronal maturity. Markers tested include mature mDA-related Tyrosine Hydroxylase (*TH*), Nuclear receptor related-1 protein (*NURR1*), Dopamine Transporter (*DAT*), α-synuclein (*SNCA*), as well as Microtubule-Associated Protein Tau (*MAPT*. *MAPT* is thought to be a marker of mDA maturity but its expression is more widespread throughout the CNS; moreover, certain isoforms can also accumulate in tauopathies (with BPAN having several features of a tauopathy, as mentioned in the introduction) (Trabzuni, Wray et al. 2012, Fukasawa, de Labio et al. 2018, Hefti, Farrell et al. 2018). As in Day 11 qRT PCR experiments, for each target, ΔC_T mean values in mDA neurons (calculated using the housekeeping gene GAPDH) were compared to ones in corresponding iPSCs. All 7 lines exhibited upregulation in gene expression of markers *TH, SCNA, and NURR1*, and also of *MAPT* (**Figure 27**).

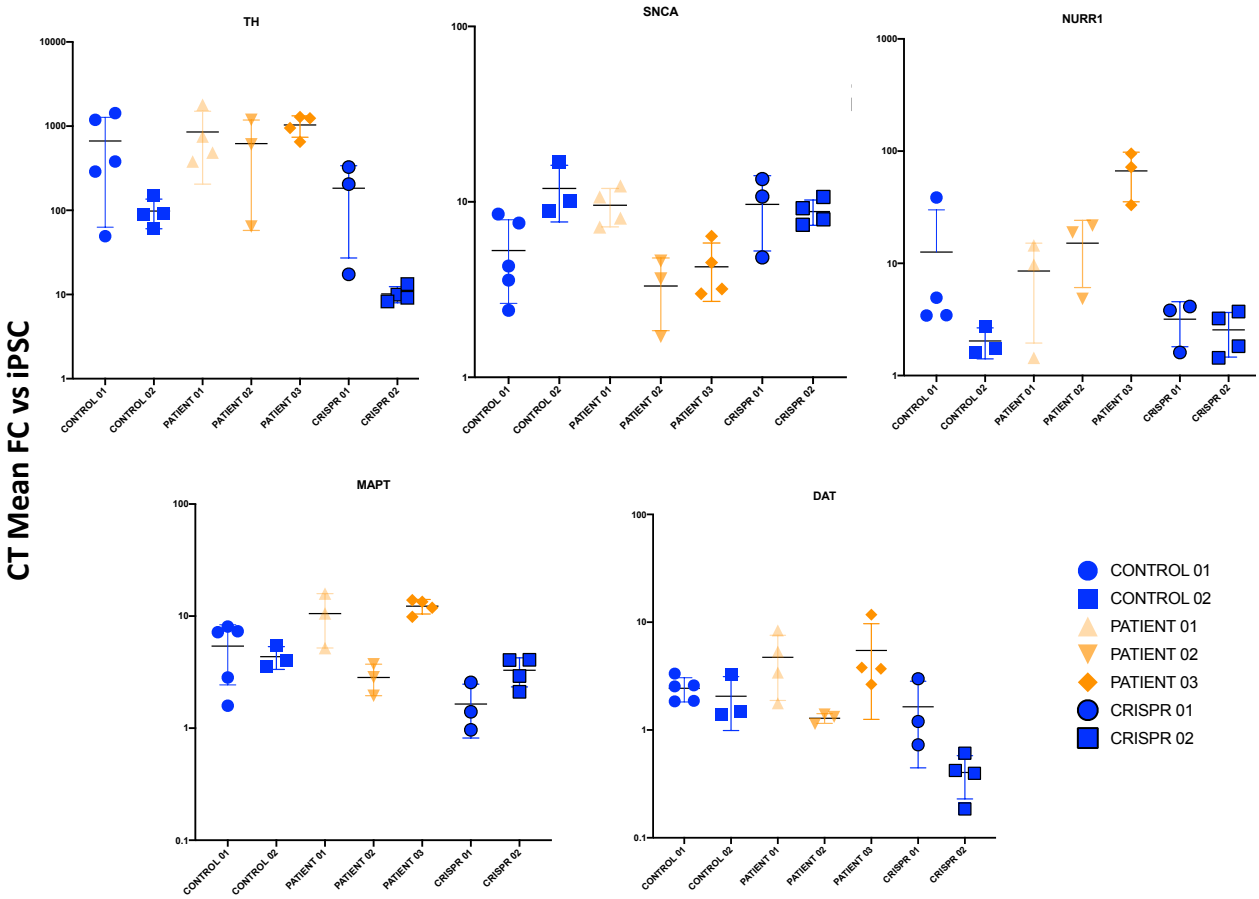

Figure 27. All lines show upregulation of mature markers compared to the corresponding iPSC lines. *On the graphs, the y axis is on a logarithmic scale. Values for control lines are shown in blue and patient lines in orange. Gene expression is relative to the housekeeping gene (GAPDH) and normalised to the respective iPSCs line. The Fold change of the ΔΔCT [FC= $2^{\wedge-(\Delta\Delta CT)}$] when comparing the ΔCT mean values of each target to the one of the corresponding iPSC line is shown. Error bars represent Mean values with Standard Error of Mean. n=3-5 biological replicates for each line. No statistical comparison between patient and control lines is feasible in this analysis, as each value is calculated versus values from corresponding iPSC lines and not taking inter-plate variability into account.*

In summary, both immunofluorescence and qRT PCR experiments at Day 65 confirm successful mDA neuronal differentiation for all patient and control lines, and the generation of robust mDA neurons that can be used in downstream experiments.

3.7. Discussion

3.7.1. Derived iPSC lines underwent stringent characterisation

I comprehensively demonstrated that all iPSC lines used for downstream experiments were truly pluripotent. I also showed that all lines maintained genomic integrity, while patient iPSCs also harboured the disease-causing mutations. Moreover, there were several caveats of iPSC-based models that I tried to address such as, firstly, the inherent issue of iPSC line variability. In order to overcome this, multiple patient and control lines were used. In total, three BPAN [Patient 01 (BPAN-07), Patient 02 (587-02) and Patient 03 (535-02)] and two age-matched control [Control 01 (HDF-05) and Control 02 (582-06)] iPSC lines were used for phenotypic comparisons. Very importantly, two BPAN iPSC lines [Patient 02 (587-02) and Patient 03 (535-02)] underwent CRISPR/Cas9-mediated genome editing, during which the disease-causing WDR45 nonsense mutation (leading to an early stop codon) was substituted with a sequence leading to a full-length WDR45 protein. The use of these additional 'isogenic control' lines [Patient 02 Corrected and Patient 03 Corrected], and 7 iPSC lines in total, ensured that any phenotypic differences seen in downstream experiments between patient and control lines were due to the WDR45 deficiency and not due to other genetic or epigenetic background changes.

Furthermore, all iPSC lines underwent stringent testing to establish that they are truly pluripotent, and any inappropriate lines were excluded from downstream experiments. Pluripotency testing firstly included 1) detection of pluripotency markers through immunofluorescence and RT PCR. A teratoma test, which was previously regarded as the gold standard test for iPSC pluripotency, was not performed due to ethical considerations (as it would require iPSCs to be injected into mice), lack of expertise and access to animal facilities, and due to it being expensive and time consuming. Instead, 2) the Epi-Pluri-Score and 3) testing the iPSCs' ability to spontaneously differentiate into all 3 germ layers *in vitro* (through a 16-day protocol) were performed for all lines. Pluripotency testing also involved 4) clearance of the Sendai Virus and related pluripotency transgenes and 5)

maintenance of disease-causing mutations in patient lines. Finally, all iPSC lines were tested to ensure they had maintained their 6) karyotypic integrity during reprogramming. The latter was examined via SNP array and any lines that had acquired chromosomal insertions or deletions (that could influence their capacity for downstream differentiations) were discarded. The cut off size of 5Mb for insertions or deletions to be considered pathogenic is already quite stringent, as conventional karyotyping (used in many iPSC-based projects) cannot detect aberrations smaller than 5–10 Mb (Forozan, Karhu et al. 1997).

Another factor that could influence BPAN modelling was the status of XCI in female lines. In order to overcome this, I performed XCI studies which showed that female iPSC and neuronal lines [Patient 01 (BPAN-07) and Patient 03 (535-02)] had skewing of XCI in favour of only one X chromosome. Coupled with WDR45 cDNA sequencing at iPSC stage and WDR45 western blotting at Day 65 mature mDA neuron stage, this proved that in both female patient lines, only the mutated WDR45 allele was expressed in iPSCs and throughout the process of differentiation.

In summary, after establishing the above, I was confident that downstream disease modelling would produce robust and reproducible results.

3.7.2. Successful differentiation into midbrain dopaminergic neurons for all lines

I successfully managed to differentiate all 7 lines, both patients and controls, into 'mature' midbrain dopaminergic neurons. The efficiency of my differentiation protocol in producing dopaminergic (TH-positive via immunofluorescence) neurons was very similar to published studies (Kirkeby, Grealish et al. 2012, Kirkeby, Nelander et al. 2012). Additionally, there was upregulation of mature dopaminergic markers in all lines (via RT-PCR) when compared to corresponding iPSC lines. However, there was lack of spontaneous neurodegeneration in the dish, in line with the absence of neurodegeneration that we also observe clinically in BPAN patients in the first few years of life. Hence, the above feature possibly reflects an 'immature' or 'young' state of derived neurons, due to which, mDA neurons at 'mature' stage might not exhibit defects that become more prominent in

patients with time. Indeed, Day 65 BPAN mDA neurons show no spontaneous neurodegeneration in vitro, with TH/DAPI and MAP2/DAPI ratios similar to controls. Plausibly, a reduction in TH- and/or MAP2-positive cells could have been seen in BPAN lines with longer culture times; however, this would have also increased neuronal culture/ maintenance costs and the risk of contamination. Such phenotypes could also theoretically have been elicited with application of stressors, such as oxidative stress, hypoxia or toxins. Of course, appropriate, and perhaps disease- (or cell-) specific, stressors would have to be tested, while the right type of assay (readout) would also have to have been identified. Additionally, the duration of the exposure and/ or the concentration of these stressors would have to be optimised, as prolonged exposure to stressful factors (and/ or very high toxin concentrations) might be toxic for all lines (and not just the patient-derived neurons); on the other hand, suboptimal concentrations or inadequate exposure times might fail to demonstrate a phenotypic defect. Indeed, I encountered many of these issues when I attempted to stress the Day 11 ventral midbrain progenitors while setting up the Alamar Blue-based cell viability assay (detailed in **Chapter 4**). In any case, applying stress to Day 65 neurons in order to elicit neurodegenerative phenotypes *in vitro* might be an important experiment to consider in future studies.

4. Investigation of the BPAN Neuronal Cell Model for identification of Disease-Specific Features

4.1. Phenotypic Assay Development

4.1.1. Rationale behind phenotypic assay development

After successfully establishing the BPAN dopaminergic neuronal model, my next goal was to examine the model in order to identify phenotypic features that could distinguish patient lines from controls. In the first instance, I aimed to investigate patterns of WDR45 gene and protein expression, hoping to prove that BPAN lines are deficient of WDR45. Additionally, I wanted to examine the effect of this deficiency in neuronal function and further elucidate pathophysiological mechanisms leading to disease. Hence, I set up assays to test autophagy flux in patient lines in order to verify my initial hypothesis of this process being defective in BPAN neurons. Apart from autophagy, I also tried to develop assays to test other intracellular functions, such as iron metabolism, lysosomal function and cell viability. Overall, though, one additional main goal throughout this assay development phase was that the assays should, wherever possible, be amenable to high content imaging applications. This would enable me to use the most promising assays (the ones showing most pronounced and reproducible defects in patient lines) for downstream drug screening, which was a major part of the project from the start.

4.1.2. Assays to monitor autophagy

Autophagy is an essential intracellular homeostatic mechanism that is pathophysiologically relevant in many disorders. Hence, measuring and monitoring autophagy accurately is critical but frequently difficult and confusing; for example, most assays capture mere snapshots of this very dynamic process, and there are often many confounding variables that might give rise to incorrect/ contradictory results (Gottlieb, Andres et al. 2015). Hence, a careful selection/ design of (often more than one) assays is needed to monitor autophagy and its flux. As mentioned above, a protein of

particular interest involved in cargo nucleation, phagophore elongation and closure/ maturation of the autophagosome is LC3. The cytosolic form of LC3 (LC3-I) is conjugated with PE and integrated into the forming autophagosomal membrane. The lipidated/ conjugated form of LC3 (LC3-II) is therefore widely used as a marker for identifying and tracking autophagosomes. Moreover, post-translational modifications are crucial for recruiting the autophagy machinery to specific cargo. A protein known as p62/sequestosome 1 (SQSTM1), a cargo receptor that attracts the machinery to protein aggregates, has also been used as a marker of autophagy flux (Gottlieb, Andres et al. 2015, Yoshii and Mizushima 2017). The above two assays have been used in this thesis and will be described in detail later on; briefly, autophagy flux induction leads to autophagosome (LC3-II) accumulation, but so does blockage of autophagosomal/ lysosomal fusion. Conversely, autophagy flux induction results in autophagosomal cargo (p62) degradation while a blockage of autophagosomal/ lysosomal fusion leads to p62 accumulation. Hence, a combination of these assays is needed in order to decipher which process or treatment leads to actual induction of autophagy in BPAN cells.

4.2. Patterns of WDR45 expression in BPAN and control neurons

In order to characterise the BPAN model, I firstly tried to determine patterns of WDR45 expression, looking at both mRNA and protein levels. I aimed to investigate patterns of *WDR45* expression during mDA neurogenesis but also whether BPAN neurons were, indeed, in a state of WDR45 deficiency.

4.2.1. WDR45 gene expression is upregulated during neuronal differentiations

Firstly, qRT PCR was performed in iPSCs and Day 65 mDA neurons for all lines. When compared to corresponding iPSCs, *WDR45* cDNA levels (examined via the $\Delta\Delta C_T = \Delta C_T \text{ sample} - \Delta C_T \text{ iPSC}$, and reflecting mRNA levels and gene expression) are upregulated in all Day 65 cells, both patient and controls, when compared to the corresponding iPSC line (**Figure 28**).

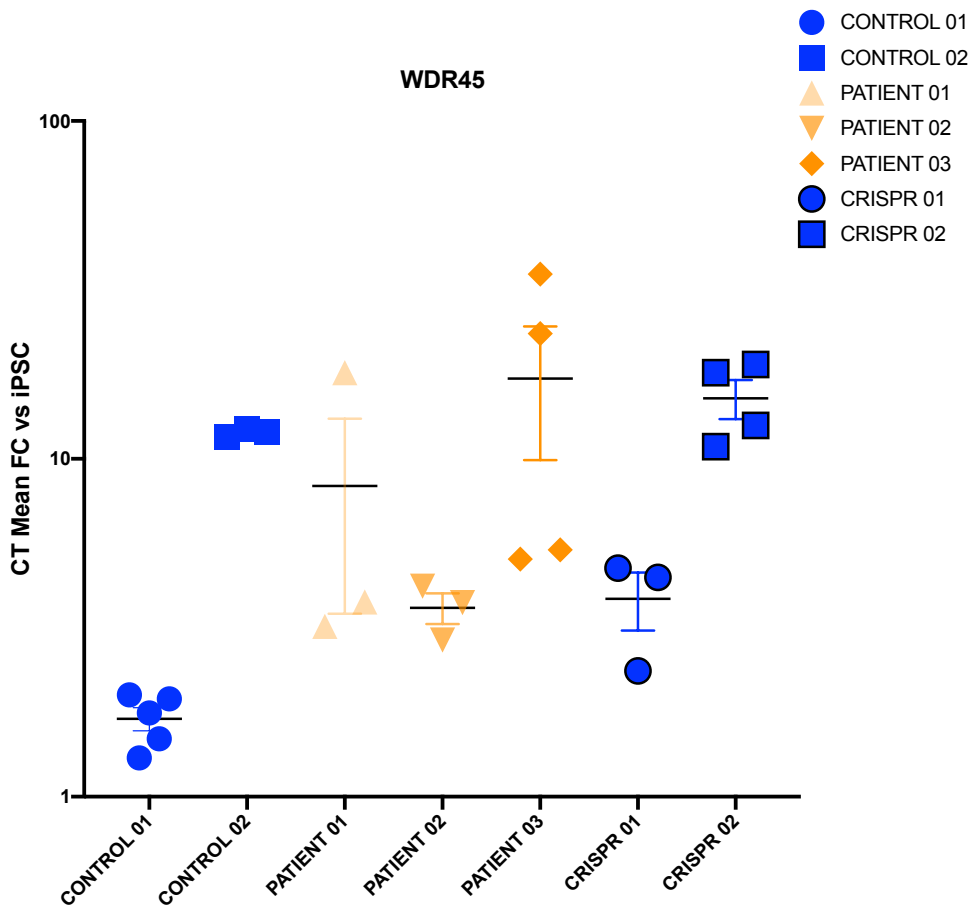

Figure 28. Universal upregulation of WDR45 gene expression in Day 65 neurons. *All mDA neuronal lines, both patients and controls, exhibit a statistically significant increase in WDR45 mRNA levels when compared to the*

corresponding iPSC lines. Values for control lines are shown in blue and patient lines in orange. Gene expression is relative to the housekeeping gene (GAPDH) and normalised to the respective iPSC line. The Fold change [FC= 2^-(ΔΔCT)], when comparing the ΔCT mean values of each target to the one of the corresponding iPSC line, is shown. Error bars represent Mean values with Standard Error of Mean. n=3-5 independent biological replicates for each line. No statistical comparison between patient and control lines is feasible in this analysis, as each value is calculated versus values from corresponding iPSC lines and not taking inter-plate variability into account.

All BPAN lines harbour mutations leading to early stop codons and therefore, possibly, mRNA nonsense-mediated decay. *WDR45* gene expression upregulation is also ubiquitously present in all 4 control lines, both age-matched and isogenic. In order to further examine WDR45 expression patterns during neuronal differentiation, real-time quantitative RT PCR was also performed on Control 01 (HDF-05) iPSCs, Day 11 and Day 65 samples, using a different set of cDNA primers (a primer set used to perform WDR45 cDNA sequencing, as per **Sections 2.14 and 3.2.6**). This experiment also showed upregulation or WDR45 expression in Day 65 cells, but also in Day 11 progenitors, when compared to iPSCs, which possibly indicates that WDR45 upregulation physiologically occurs early on in the differentiation process (**Figure 29**).

In summary, *WDR45* gene expression is upregulated during mDA neuronal differentiation. No direct comparison with *WDR45* expression in dermal fibroblasts (or other tissues) was performed, hence such expression patterns could also be seen in other tissues/ somatic cells during differentiation events. However, this upregulation might possibly indicate that WDR45 is important for neuronal differentiation and/ or survival.

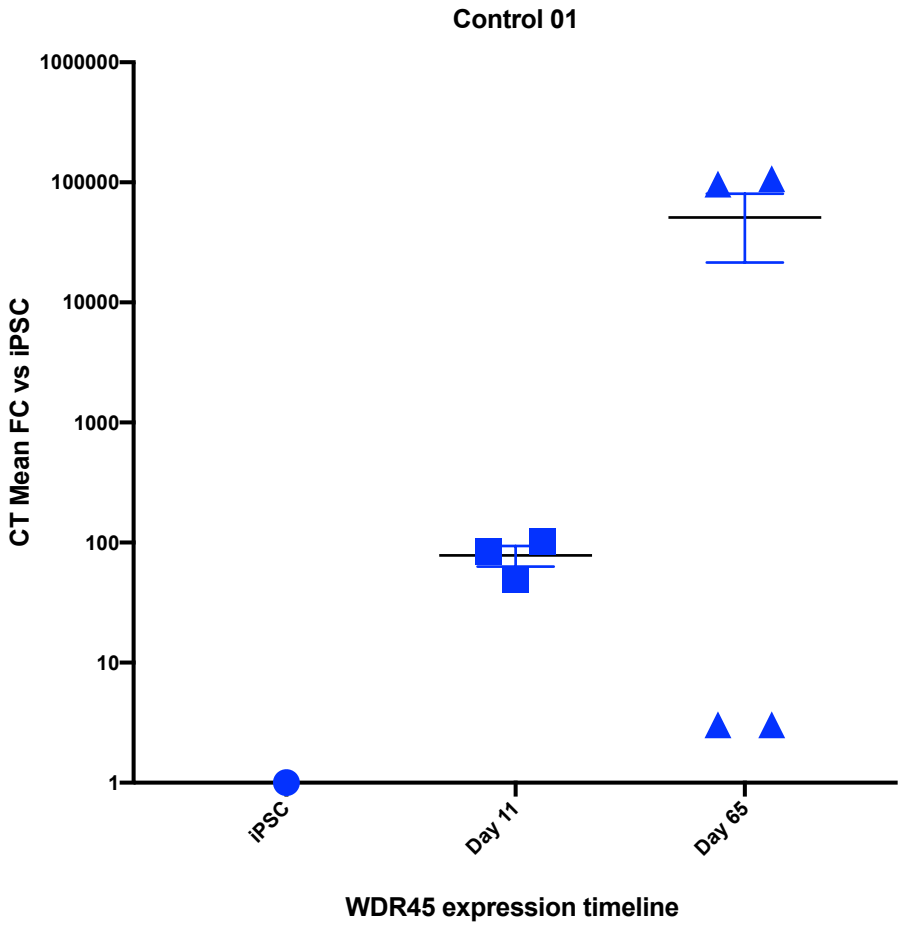

Figure 29. Upregulation of WDR45 gene expression during neuronal differentiations. *Control 01 line exhibits a statistically significant increase in WDR45 mRNA levels at both progenitor and mature mDA neuronal stage, when compared to the corresponding iPSCs. Gene expression is relative to the housekeeping gene (GAPDH) and normalised to the respective iPSC line. The Fold change [FC= 2^-(ΔΔCT)], when comparing the CT mean values of each target to the one of the corresponding iPSC line, is shown. Error bars represent Mean values with Standard Error of Mean. n=3-4 biological replicates for each line. Due to large error bars and standard deviation in the Day 65 WDR45 values, no statistically significant difference is present between Day 11 and Day 65 cells. Statistics were calculated using the ordinary one-way Anova test.*

4.2.2. WDR45 protein is absent in BPAN Day 65 mDA neurons

After examining *WDR45* gene expression, I proceeded to examine actual WDR45 protein levels in mDA neurons. For this purpose, western blotting was performed in all BPAN and control lines. WDR45 protein bands were 1) not detectable in any patient line but 2) present in age-matched Controls 01 and 02 at the expected size (approximately 37 kDa) and 3) fully restored after CRISPR mutation correction. This result is in agreement with my data on the XCI status and cDNA sequencing in iPSC lines, supporting the notion that the mutated *WDR45* allele is expressed in BPAN lines leading to a complete absence of WDR45 protein expression in mature mDA neurons (**Figure 30**). Hence, our BPAN mDA neuronal model is one of true WDR45 deficiency.

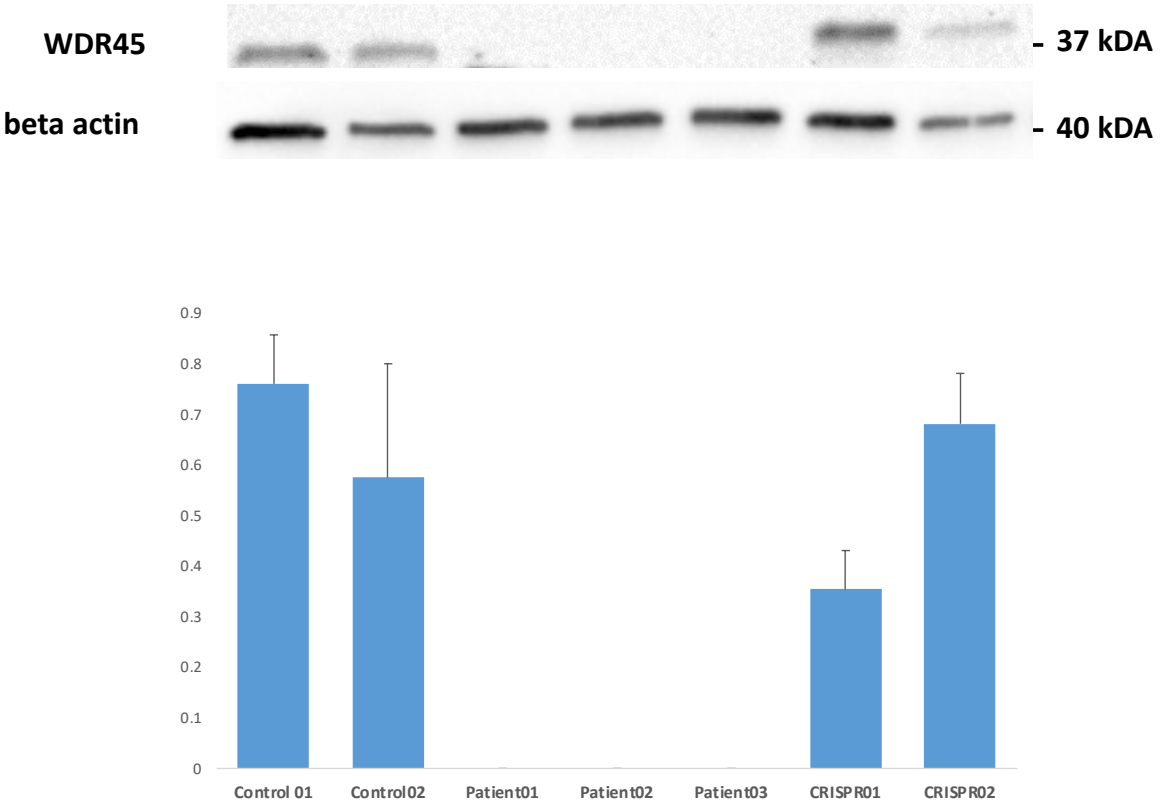

Figure 30. WDR45 protein absence in BPAN dopaminergic neurons. *WDR45 bands are detected at approximately 37kDA in Controls 01 and 02 but are absent in all BPAN patient neurons. A representative blot is shown. Beta actin was used as the loading control. CRISPR/Cas9 mutation correction leads to a protein band expression of identical size to the WDR45 band seen in the age-matched controls. Band intensity quantification using ImageJ software shows no statistically significant difference between age-matched and isogenic controls. n=4 biological replicates for each line. Error bars represent the Standard Error of Mean. Statistics were calculated using ANOVA.*

4.3. BPAN neurons recapitulate disease-related phenotypes

4.3.1. BPAN lines exhibit defective autophagy

In order to identify patient-related phenotypes and set up phenotypic assays for downstream drug screening experiments, and also due to the long periods required for neuronal differentiations, I initially cultured and tested BPAN and control dermal fibroblasts in parallel to neuronal lines. Control line 582-202 and BPAN lines BUCL01, 587-201A and 535-201 [reprogrammed into Control 02 (582-06), Patient 01 (BPAN07), Patient 02 (587-02) and Patient 03 (535-02) iPSC lines, respectively] were cultured under normal conditions and subsequently seeded onto 96-well plates at a density of 300,000 cells/ well. Twenty-four hours post seeding, cells were treated for 3 hours with autophagy flux inhibiting or inducing compounds [namely 1) DMSO as control, 2) Bafilomycin A1, 3) Torin 1 and 4) Bafilomycin A1 and Torin 1], then fixed and stained for autophagy marker LC3. The rationale for this assay was that I had initially hypothesised that autophagy is defective in BPAN. After image analysis using ImageJ/Fiji and R Studio software, I demonstrated that BPAN fibroblasts exhibited defective autophagy, with fewer LC3 puncta (representing autophagosomes) compared to the control line. This defect was more evident, and statistically significant, in basal (DMSO treatment) conditions (**Figure 31**). The DMSO- and Torin 1-related results suggest that BPAN cells respond to autophagy induction, hence are not exhibiting a completely defective autophagy pathway; rather, there seems to be a basal defect that could possibly be reversed. This is potentially of interest, as the possibility of overcoming this defect with autophagy inducers could be used for therapeutic purposes in BPAN. Moreover, the combination of Bafilomycin A1 and Torin1 treatments (in other words, the induction of autophagosome formation combined with blockage of autophagosomal/ lysosomal fusion) possibly results in the maximum number of autophagosomes the cells can produce at any time, hence the inability to detect any phenotypic differences between patients and controls.

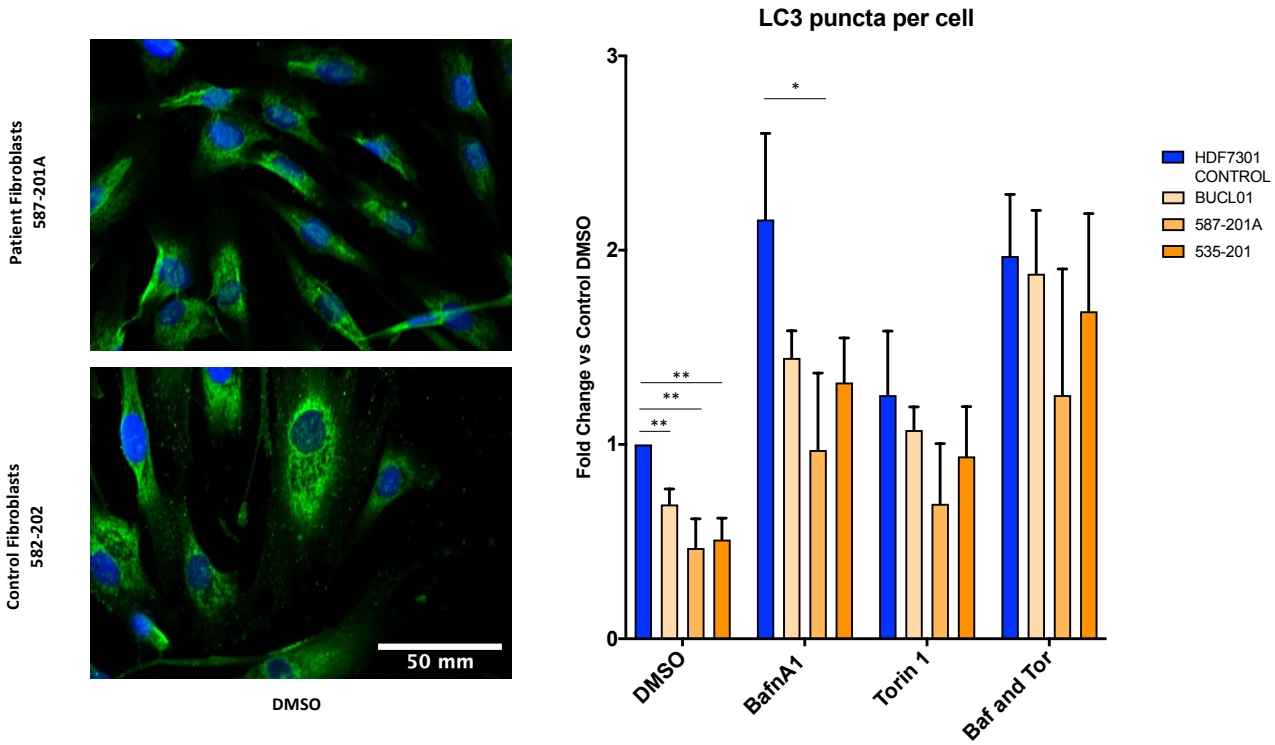

Figure 31. BPAN fibroblasts exhibit defective autophagy. *BPAN fibroblast lines produce fewer LC3 puncta (representative of autophagosomes) than the control fibroblast line, with this phenotypic difference more evident in basal (DMSO-treated) conditions. n=3 independent experiments. Statistical significance was calculated using Repeated Measurements ANOVA and error bars represent the Standard Error of Mean. Only statistically significant results are depicted on the graph.*

The LC3 fibroblast assay was a promising assay with a robust and reproducible phenotypic difference between patient and control lines in basal conditions; hence, it could potentially be used for the proposed downstream drug screen in our neuronal model. The next step was to examine whether these defects in LC3 puncta formation were also present in BPAN Day 11 ventral midbrain progenitors. For this, a similar procedure was followed; all patient and control lines [Patients 01, 02 and 03, Controls 01, 02, Patient 02 Corrected (CRISPR01) and Patient 03 Corrected (CRISPR02)] at Day 11 of differentiation were seeded onto 96-well plates at a density of 10,000-15,000 cells/ well and, 24 hours post seeding, treated for 3 hours with 1) DMSO, 2) Bafilomycin A1, 3) Torin 1 and 4) Bafilomycin A1 and Torin 1. Again, BPAN lines exhibited defective autophagosome formation, with fewer LC3 puncta forming compared to controls. This defect was more pronounced in DMSO-treated conditions. Importantly, CRISPR-mediated correction of WDR45 mutations in both Patients 02 and 03 resulted in the restoration of LC3 puncta formation to normal levels (**Figure 32**).

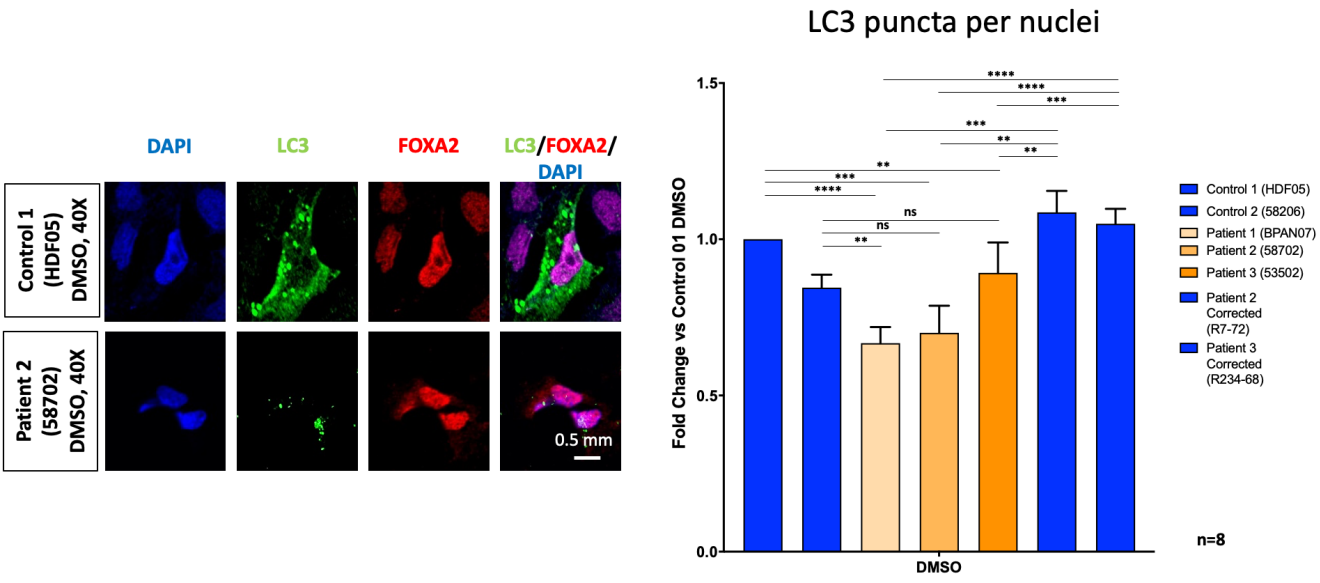

Figure 32. Defective Autophagy in Day 11 Ventral midbrain progenitors. *BPAN ventral midbrain progenitors produce fewer LC3 puncta (representative of autophagosomes) than the controls, with this phenotypic difference more evident in basal (DMSO-treated) conditions. n=8 independent differentiations/ biological replicates for each line; for each biological replicate, all 7 lines had the same start date of differentiation and were seeded on the same 96-well plate for Day 11 experiments. Within each differentiation/ 96-well plate, the fold change of LC3 puncta formation when compared to Control 01 (HDF05) was calculated. LC3 basal levels for Patient 03 were similar to Control 02 (but significantly lower when compared to the other 3 controls). The LC3 phenotypic defect was reversed after CRISPR/Cas9-mediated WDR45 mutation correction in Patient 02 and Patient 03. For statistical analysis, Repeated measurements ANOVA was used. Error bars represent the Standard Error of Mean.*

After treatments with Torin1 and/or Bafilomycin A1, LC3 puncta production increased significantly for all lines, with the largest number of puncta per nuclei seen in the combined Torin1 and Bafilomycin treatment. This, firstly, signifies, that the treatments were effective, because they produced the results expected (increased in autophagosome numbers, maximal in the combined treatment) in all lines. Some defects in LC3 puncta formation in BPAN lines were also seen. However, this was not reproducible in all patient lines, with Patient 03 exhibiting LC3 puncta levels comparable to all controls (**Figure 33).**

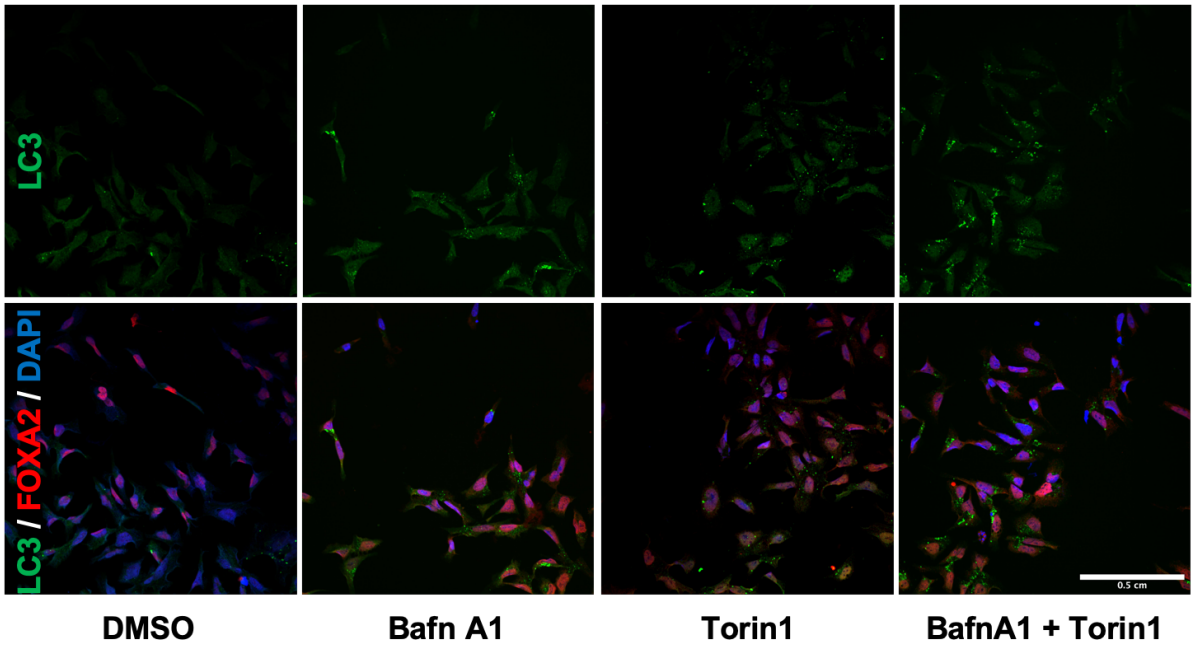

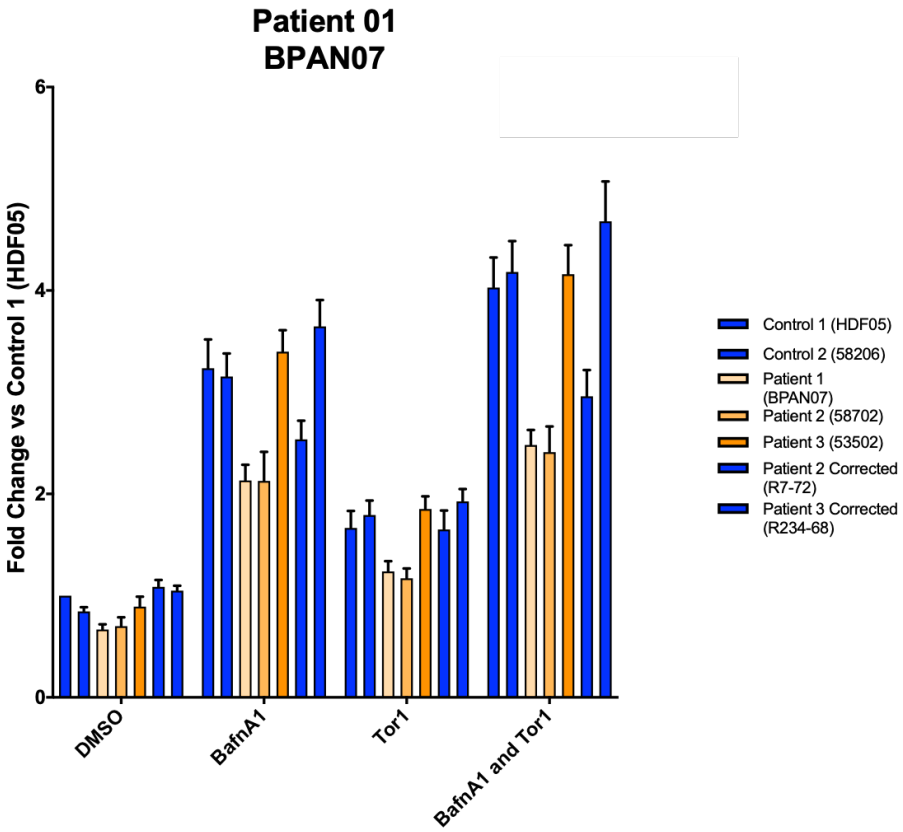

Figure 33. Treatments with autophagy-inhibiting and/or inducing compounds increases autophagosome production in all Day 11 lines. *Both Torin 1 (flux inducer) and Bafilomycin A1 (flux blocker) lead to increase in autophagosome numbers in each cell, in all cell lines. As expected from a physiological perspective, maximal puncta per nuclei increased is seen in the combined Bafilomycin A1 and Torin 1 treatments. Indication of Significance is not shown due to space limitations, but each treatment resulted in statistically significant increase in LC3 puncta per nuclei in every line, when compared to (DMSO-treated) basal conditions. As detailed in Figure 34, this increase could potentially be therapeutically beneficial in BPAN. n=8 independent differentiations/ biological replicates for each line. For statistical analysis, the unpaired two-tailed t test was used. Error bars represent the Standard Error of Mean.*

Importantly, treatment with Torin 1 led to a statistically significant increase in LC3 puncta formation for all lines, both patients and controls (**Figure 34**). This has potentially important implications, as previous studies have shown that autophagy induction (with Torin 1) leads to reversal of iron accumulation and endoplasmic reticulum stress in BPAN neurons (Seibler, Burbulla et al. 2018, Wan, Wang et al. 2019). As shown here, induction of the autophagy flux can overcome the LC3/ autophagosome production defect in BPAN Day 11 progenitors and therefore autophagy-inducing drugs might plausibly be of therapeutic benefit for BPAN.

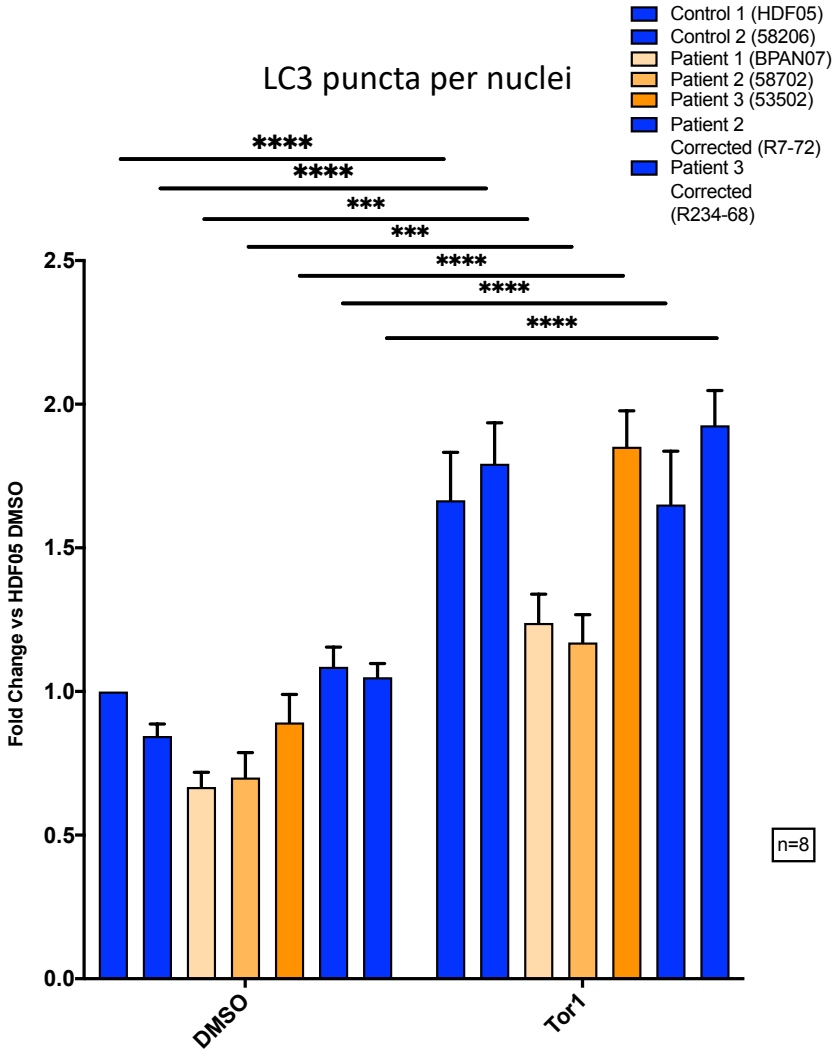

Figure 34. Torin1 leads to restoration of the LC3 defect in Day 11 patient lines. *Continuation of Figure 33. After treatment with Torin 1 for 3 hours, LC3 puncta are significantly increased in all Day 11 ventral midbrain progenitor lines. For BPAN lines, this is at levels comparable (Patients 01 and 02) or above (Patient 03) the ones seen in DMSO-treated control lines. n=8 independent differentiations/ biological replicates for each line. For statistical analysis, the unpaired two-tailed t test was used. Error bars represent the Standard Error of Mean.*

In summary, the LC3 ventral midbrain progenitor assay shows a robust and reproductible phenotypic defect in autophagosome formation in all patient lines. This is firstly important as it verifies my initial hypothesis that autophagy is defective in BPAN neuronal lines. Moreover, 1) the assay is amenable to high content imaging, 2) the defect shown is more prominent in basal conditions (hence a downstream drug screen would be easier to set up) and, finally, 3) LC3 defects are reversible by autophagy-inducing drugs, that might also have the capacity to reduce iron accumulation as per previous studies (hence any drug hits that increase LC3 production potentially might be of therapeutic benefit).

Additionally, Day 11 progenitors are optimal for performing a drug screen, since

- they are still in a mitotic stage (thus survive replating and seeding at low densities more easily)
- they can be produced in relative abundance compared to later stages of differentiation, which also allows downstream experiments on a large scale
- they are overall very well characterised cells, with established ventral midbrain identities
- attempts to dissociate and re-seed (post-mitotic, more fragile) Day 65 mDA neurons at low densities (and in a monolayer, in order to allow high content imaging and subsequent meaningful image analysis) had previously been unsuccessful, with very few TH-positive neurons surviving (data not shown).

Due to the above, I decided to perform the primary drug screen on Day 11 cells and validate hits on both Day 11 cells but also in more mature Day 65 mDA neurons.

4.3.2. RNAseq reveals Involvement of other pathways in disease pathogenesis

After establishing that autophagy is defective in BPAN, I also wanted to investigate other pathophysiological mechanisms leading to disease in BPAN neurons. For this, I firstly performed bulk RNA Sequencing (RNASeq) on Day 65 mDA neurons (Patients 01, 02 and 03, Controls 01 and 02 in the first instance). Analysis of RNASeq data was performed by using DESeq2 (Love, Huber et al. 2014). A p value of <0.05 and fold change of <-2 or >+2 [-1<log2(FC)<1] were set as statistically significant cut-offs. This process generated a list of 190 differentially expressed genes (20 upregulated and 170 downregulated simultaneously in all patients when compared to controls) in BPAN mDA neurons compared to controls (**Table 18, Figures 35 and 36**). Many upregulated genes belong in the long non-coding RNA category, with function so far not investigated or known.

Differentially Expressed genes in BPAN mDA neurons									
ABCB1	*CECR7*	*EDNRA*	*GPC4*	*KLHL4*	*OAS3*	*RP1-140K8.5*	*SHROOM4*	*TWIST2*	*RP11-341N2.1*
ABCG2	*CHST9*	*EGFR-AS1*	*GPR101*	*LAMP3*	*PALD1*	*RP11-262H14.3*	*SKA1*	*USH1C*	*RP11-350D17.3*
ACOT1	*CLDN5*	*EGR2*	*HAS2*	*LAMP5*	*PAPLN*	*RP11-491F9.5*	*SLC13A3*	*UTP14A*	*RP11-384L8.1*
ACTL8	*CMKLR1*	*EIF1AXP1*	*HFE*	*LEF1*	*PAPPA2*	*RP11-706O15.3*	*SLC25A5*	*VCAM1*	*RP11-817I4.2*
ADAMTS14	*COL1A1*	*ELK3*	*HK2P1*	*LEPR*	*PAX6*	*RP11-752L20.3*	*SLC2A14*	*XPNPEP2*	*RPL13P12*
ADCY8	*COL23A1*	*EMILIN2*	*HSFX2*	*LINC00907*	*PAXIP1-AS2*	*RP11-766F14.2*	*SLC5A12*	*ZIC2*	*SLC30A8*
AF011889.2	*COL4A1*	*EN1*	*HSPA2*	*LINC01139*	*PBK*	*RP11-88I21.2*	*SPINK1*	*ZIC3*	*SP6*
APCDD1	*COL4A2*	*ERMN*	*IFI44L*	*LPAR3*	*PCDHGA6*	*RP4-545C24.1*	*SRPX2*	*ZIC5*	*SYCP2L*
AQP1	*COL5A2*	*ERVV-1*	*IFI6*	*LRP2*	*PCDHGA7*	*RP4-755D9.1*	*TBC1D3G*	*ZNF600*	*TAS2R14*
ATP1A2	*CPED1*	*ERVV-2*	*IFIH1*	*LRP4*	*PCSK9*	*RRM2*	*TBC1D8B*	*ZRSR1*	*UNC5CL*
BAAT	*CRYBB1*	*ETV5*	*IFIT1*	*LY75-CD302*	*PDGFRA*	*RRP7A*	*TBX15*	*ARHGEF15*	
BIRC5	*CSF1*	*FAM129A*	*IGFBPL1*	*MELK*	*PDIA5*	*RSPO2*	*TCF19*	*CECR1*	
BUB1	*CTB-12O2.1*	*FAM64A*	*IKZF1*	*MTND4P12*	*PENK*	*RUNX3*	*TCP11X2*	*CTD-2270P14.5*	
CASC5	*CTC-575D19.1*	*FAM83D*	*IL17RA*	*MX1*	*PIEZO2*	*SCARA5*	*TESC*	*FAM157C*	
CCNB1	*CUZD1*	*FBLN2*	*INHBE*	*MX2*	*PLP1*	*SCN5A*	*TF*	*LHX8*	
CCR7	*CXCR4*	*FFAR4*	*IQCA1*	*NDST4*	*PLSCR5*	*SDHAP2*	*TFAP2B*	*LRRC37A*	
CD97	*DCT*	*FGFR1*	*ISG15*	*NOTUM*	*PRELP*	*SEMA5B*	*THBS2*	*NPPA-AS1*	
CDCA2	*DEPDC1*	*FOXF2*	*JAG1*	*NPAS4*	*RBP4*	*SERPING1*	*THSD7B*	*NUTM2E*	
CDH11	*DEPDC1B*	*FZD1*	*KAL1*	*NR0B1*	*REG1B*	*SFRP2*	*TMC6*	*PCDHA2*	
CDH7	*DTL*	*GALNT10*	*KIF14*	*OAS1*	*ROR1*	*SHE*	*TRIM29*	*RP11-11N5.1*	

Table 18. List of differentially expressed genes in mDA BPAN neurons when compared to controls 01 and 02. *Results presented from left to right in alphabetical order. White cells: downregulated genes. Shaded/ grey cells: upregulated genes.*

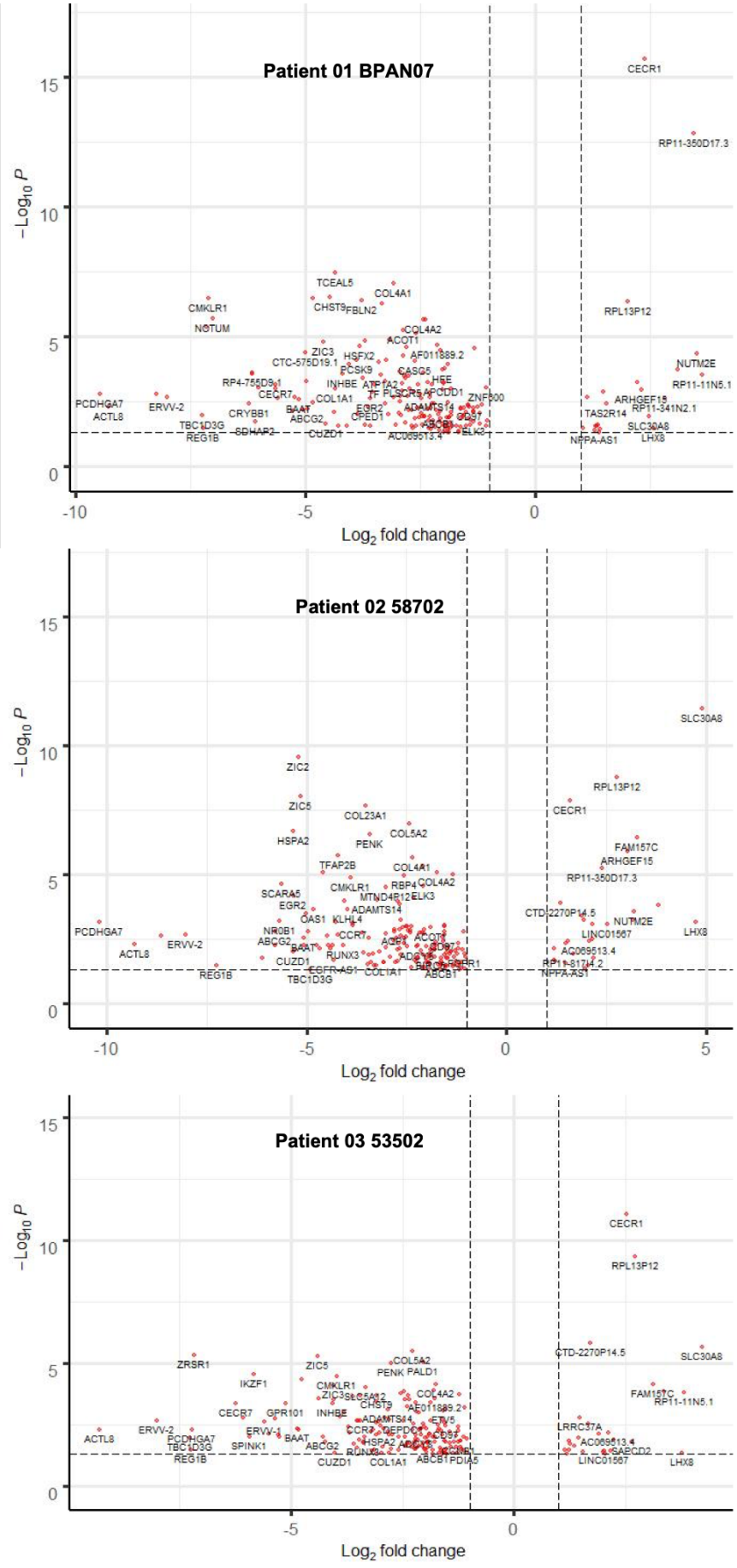

Figure 35. Bulk RNASeq reveals 190 differentially expressed genes in BPAN neurons compared to controls. *Volcano plots showing statistically significant differentially expressed genes in BPAN neurons (red dots). Upregulated genes are shown on the right of the X axis ($Log_2FC>1$) while downregulated genes of the left ($Log_2FC<-1$). p values in logarithmic scale are shown on the y axis (cut off p value <0.05).*

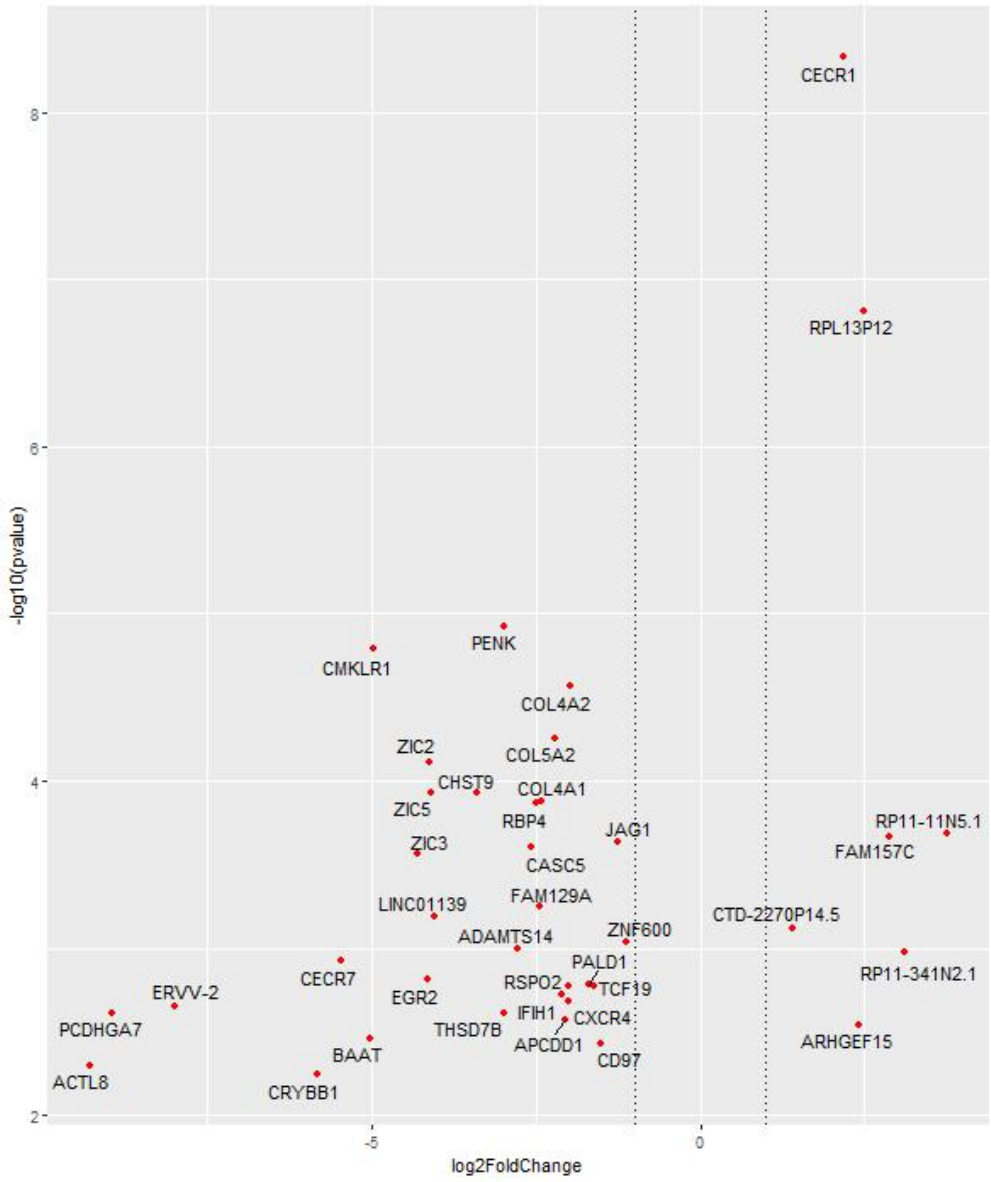

Figure 36. Volcano Plot showing top gene hits based on p value. *Top 100 genes, sorted based on p values (in ascending order) for all three patients, were compared and genes found in all three extracted. Subsequently, the p values and the log_2FC for these common genes were averaged and the volcano plot created, in order to provide a more focused view of the RNASeq results and the genes that differentially expressed in all 3 patients versus Controls 01 and 02. Upregulated genes are shown on the right of the X axis ($Log_2FC>1$) while downregulated genes of the left ($Log_2FC<-1$). p values in logarithmic scale are shown on the y axis (cut off p value <0.05).*

Patterns of gene expression sometimes differed between biological replicates for each line, and this was observed in all 5 lines tested (**Figure 37**). Additionally, gene expression patterns for particular genes were sometimes different in the two control lines, possibly reflecting differences in these controls' age at fibroblast harvesting and/ or sex (Control 01 coming from a 13 year old female and Control 02 from a 2 year old male, as described in **Section 3.4**). Due to time constraints in the project, and the CRISPR-corrected iPSCs becoming available only in the last few months of my time allocated in the lab, bulk RNAseq for Patient 02 Corrected and Patient 03 Corrected Day 65 mDA neurons has not been performed yet; however, this will be an important part of future work in order to establish which genes are truly differentially expressed due to WDR45 deficiency, rather than other genetic, epigenetic changes or iPSC line variability.

Moreover, I wanted to investigate the RNASeq data in order to identify molecular mechanisms that might lead to dysfunction in BPAN mDA neurons. For this purpose, Gene Ontology (GO) term annotation and molecular pathway enrichment analysis was performed (Mi, Muruganujan et al. 2013), showing that several intracellular pathways are affected in BPAN (**Figure 37**).

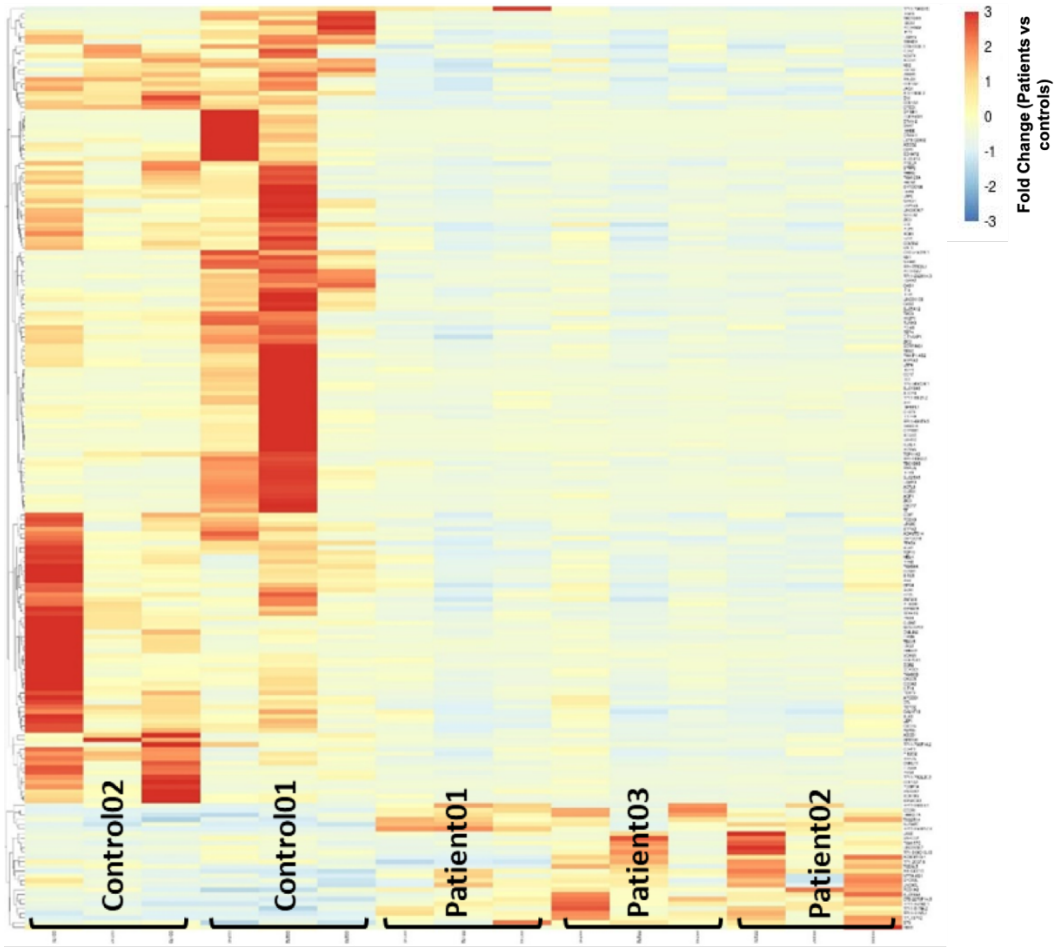

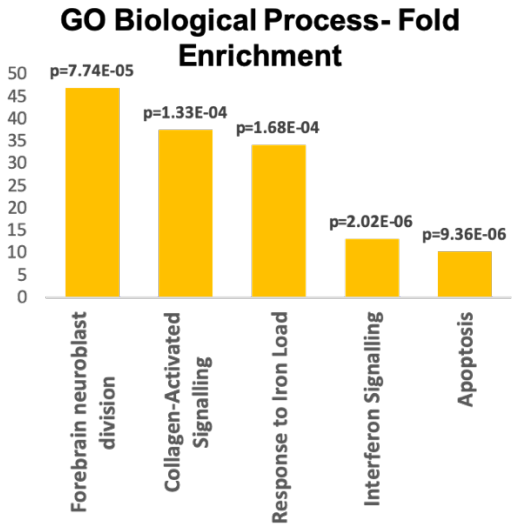

Figure 37. Differential gene expression patterns in BPAN neurons reveal several affected intracellular pathways that might lead to neuronal dysfunction and early death. Above: *downregulation and upregulation of gene expression are depicted in gradients of blue and red, respectively. Despite some differences in gene expression for each line in different biological replicates (n=3 for all 5 lines, seen as subcolumns), some genes are clearly downregulated (top of graph) or upregulated (bottom of graph) in all 3 BPAN lines versus controls.* ***Below:*** *GO Term analysis reveals that several intracellular pathways are affected in BPAN. Pathways with the most significant Fold Enrichment (Y axis) are shown and include neurogenesis and response to iron load. Relevant p values are shown at the top of each bar representing different pathways.*

The most significant pathway enrichment was seen for genes involved in neurogenesis, neurodevelopment and neuroblast division. These are very complicated, interconnected and sub-optimally understood pathways; however, our results show that the whole process of neurodevelopment is affected in BPAN. Representative examples include, firstly, that 3 of the 5 Zinc finger of the cerebellum (ZIC) genes*, ZIC2, ZIC3* and *ZIC5*, were downregulated. The zic genes play a central role in early neural patterning, development of the neural crest, and subsequent cerebellar development (Aruga 2004, Inoue, Ota et al. 2007, Merzdorf 2007). Paired Box Protein 6 (PAX6), a gene with important roles in cortical progenitor proliferation, neurogenesis, and formation of cortical layers (Manuel, Mi et al. 2015), was also downregulated. Similarly, Dopachrome tautomerase (DCT), involved in neural progenitor proliferation (Jiao, Zhang et al. 2006), and Fibroblast Growth Factor Receptor 1 (FGFR1) were also downregulated in BPAN lines. FGF signalling is essential for neurogenesis, anteroposterior patterning of the neural tube, establishing neural networks; in other instances, it promotes neuronal survival, proliferation, migration, or differentiation (Hebert 2011). Another gene downregulated in BPAN neurons was Jagged Canonical Notch Ligand 1 (JAG1), a Notch signalling pathway receptor ligand. As a crucial component of the Notch pathway, JAG1 plays an important role in neurophysiological processes such as learning and memory. JAG1 expression is significantly and progressively decreased in Alzheimer's disease, and knockout mice exhibit spatial memory loss and a reduction in exploration-dependent Notch signalling pathway activation (Marathe, Jaquet et al. 2017). CXCR4 (C-X-C motif chemokine receptor type 4), required for radial migration and fiber outgrowth of mDA neurons, was downregulated in patient neurons (Yang, Edman et al. 2013, Bodea, Spille et al. 2014) . Additionally, EN1, a ventral midbrain marker that is crucial for regulating terminal differentiation, as well as survival and maintenance of mDA neurons, was also downregulated in BPAN neurons (Arenas, Denham et al. 2015). PENK, another downregulated gene in BPAN neurons, has also been shown to be downregulated in the putamen and posterior cingulate cortex of Parkinson's disease patients when compared to controls (Henderson-Smith, Corneveaux et al. 2016) (Backman, Shan et al. 2007,

Henderson-Smith, Corneveaux et al. 2016). Finally, gene expression levels of LIM Homeobox 8 (LHX8), with roles in forebrain neuronal development (Mori, Yuxing et al. 2004, Zhou, Yang et al. 2015), were upregulated. Although the mechanisms leasing to disease are not clear, the above results support the clinical observation that BPAN is a neurodevelopmental disorder that not only affects the whole brain but also progresses to neuroregression, dementia and parkinsonism.

Significant fold enrichment was also seen for genes involved in collagen-activated signalling. In detail, expression of genes Collagen Type IV Chain Alpha 1 and 2 (COL4A1 and COL4A2) and Collagen Type I Chain Alpha 1 (COL1A1) was downregulated in BPAN neurons when compared to the Control lines 01 and 02. Again, the mechanisms linking this downregulation with BPAN pathogenesis are not well understood and likely to be multifactorial. Collagen signalling has been shown to be deregulated in Parkinson's disease and Dementia with Lewy Bodies (Paiva, Jain et al. 2018). COL4A1 and COL4A2 encode proteins that assemble to form Collagen IV, a heterotrimeric helix [consisting of 2 A1(IV) and 1 A2(IV) chains] which is a main constituent of basement membranes. Mutations in those genes disrupt the integrity of vascular basement membranes and predispose to a broad spectrum of disorders including periventricular leukomalacia, haemorrhagic stroke, aneurysm formation, epilepsy, developmental delay and also congenital cataracts and anterior eye segment dysgenesis (Shah, Ellard et al. 2012, Papandreou, Tisdall et al. 2014). COL1A1 mutations have been linked to Osteogenesis Imperfecta or Ehlers Danlos syndrome and are not known to directly affect the CNS (Ackermann and Levine 2017, Marini, Forlino et al. 2017). However, a recent study on cumulus cells showed that COL1A1 short interfering RNA (SiRNA)-mediated knockdown led to apoptosis, ROS production, abnormal mitochondrial membrane potential and autophagy dysregulation evident by LC3 accumulation (Fu, Chen et al. 2019).

The third most significant fold enrichment was seen for genes involved in Cellular Response to Iron. Gene expression of Hereditary hemochromatosis protein (*HFE*), Transferrin (*TF*), Scavenger Receptor Class A Member 5 (*SCARA5*) and G2/mitotic-specific Cyclin B1 (*CCNB1*) was downregulated

in BPAN neurons. HFE regulates hepcidin expression according to plasma iron levels; in turn, hepcidin leads to the lysosomal degradation of ferroportin, which releases iron from duodenal enterocytes and reticuloendothelial macrophages into the plasma in low-iron conditions. Transferrin, a crucial iron-binding protein in the body, then binds this iron and transports it into cells via transferrin receptor-mediated endocytosis. Cellular iron that is not required immediately for metabolic purposes can be sequestered in the cytosol within ferritin. SCARA5 has a role in endocytosis of serum ferritin (Gkouvatsos, Papanikolaou et al. 2012, Lawen and Lane 2013). Finally, the role of CCNB1 in iron metabolism is not clear but recent studies have shown upregulated levels of CCNB1 expression in iron-deficient rats (Clardy, Wang et al. 2006).

Moreover, Gene Ontology term analysis indicates that other molecular pathways might be involved in BPAN pathophysiology. Gene Ontology terms with significant fold enrichment included Type I interferon signalling pathway (Fold Enrichment 13.06) and Negative regulation of cysteine-type endopeptidase activity involved in apoptotic process (10.29) (**Figure 37**). Indeed, several genes downstream of Interferon I signalling (*ISG15, IFIT, IFI6, OAS1, OAS3, MX1, MX2*) were downregulated in BPAN neurons. It is unclear how this could lead to brain disease but the link between type I interferonopathies and neurological manifestations is well established (Crow and Manel 2015). Additionally, the dysregulation of the apoptotic pathway might indicate that BPAN neuronal cells are more susceptible to damage than controls.

Finally, RNAseq suggests that lysosomal function in BPAN might be impaired in a cell-specific manner. In detail, gene expression of *LAMP3* and *LAMP5* was downregulated in Day 65 patient neurons compared to Controls 01 and 02, while there were no differences in the other Lysosome-associated membrane glycoproteins (*LAMP*1, *LAMP2* and *LAMP4*). Compared to the ubiquitous expression of *LAMP1* and *LAMP2*, LAMP3 is reportedly only expressed in differentiating dendritic cells, type II pneumocytes and certain types of cancers and transformed lines (Dominguez-Bautista, Klinkenberg et al. 2015, Malaguarnera, Marsullo et al. 2017). Additionally, and despite studies

reporting absence of LAMP3 mRNA in human post-mortem and mouse brains (Dominguez-Bautista, Klinkenberg et al. 2015), the *LAMP3* locus has been identified as a risk factor for Parkinson's disease in Genome-Wide Association studies (Li, Tan et al. 2013, Pihlstrom, Axelsson et al. 2013). LAMP5 is the latest described Lysosome-associated membrane glycoprotein subtype and perhaps the least studied (Alessandrini, Pezze et al. 2017); in mice, it is only expressed in the brain and, more specifically, in subpopulations of GABAergic forebrain neurons in the striatonigral system and the olfactory bulb. In more detail, LAMP5 protein was present in high concentrations at synaptic terminals in the Globus Pallidus, the Substantia Nigra and the Olfactory bulb. Additionally, LAMP5 knockout mice exhibited subtle alterations in their synaptic plasticity and behaviour when compared to controls (Tiveron, Beurrier et al. 2016). In humans, LAMP5 is expressed in the brain at higher levels, but also in the type I Interferon-producing primary plasmacytoid dendritic cells (Defays, David et al. 2011). Overall, further studies are required in order to establish the role of LAMP3 and LAMP5 in BPAN pathogenesis, but these results indicate that lysosomal function could be affected in the patient neurons.

4.3.3. Western Blotting confirms that iron metabolism is dysregulated in BPAN neurons

Bulk RNAseq results provided back-up to my initial hypothesis that iron metabolism is dysregulated in BPAN, but also prompted me to consider how best to measure this in my cells in downstream experiments. Measuring intra- (or even extra-) cellular iron directly is complicated and requires special equipment (e.g. using inductively coupled plasma mass spectrometry, ICP-MS). Direct staining for iron is also complicated and used primarily in tissues/ histopathology studies, rather than cells in a dish (although rare studies using Perl's staining in cell culture also exist in the literature) (Meguro, Asano et al. 2007, Cozzi, Orellana et al. 2019). Examining iron metabolism indirectly is another, perhaps more straightforward option; one could, for example, perform RT-PCR, western blotting or immunofluorescence experiments using antibodies against proteins involved in the pathway, looking for differential expression in patients when compared to controls. In my

project, I started with the latter (indirect) approach, especially due to project time restrictions. However, I am also hoping to perform ICP-MS in my samples in future experiments, for more direct quantification of intracellular iron in BPAN neurons.

Hence, in order to examine the effects of *WDR45* mutations on Day 65 mDA neuronal iron metabolism, western blotting was performed. Day 65 BPAN neurons showed evidence of iron dysregulation. In detail, Ferritin (Heavy Chain) tended to accumulate in BPAN neurons versus controls; as ferritin is a major iron storage protein, this possibly reflects an overall increase in intracellular iron levels (**Figure 38**). Importantly, ferritin was reduced to levels comparable to controls after WDR45 mutation correction in both gene-edited lines Patient 02 Corrected (CRISPR01) and Patient 03 Corrected (CRISPR02). Protein levels of transferrin were similar in all patient and control lines (**Figure 39**). The above data, combined with the RNAseq, suggest that iron metabolism is, indeed, affected in BPAN neurons.

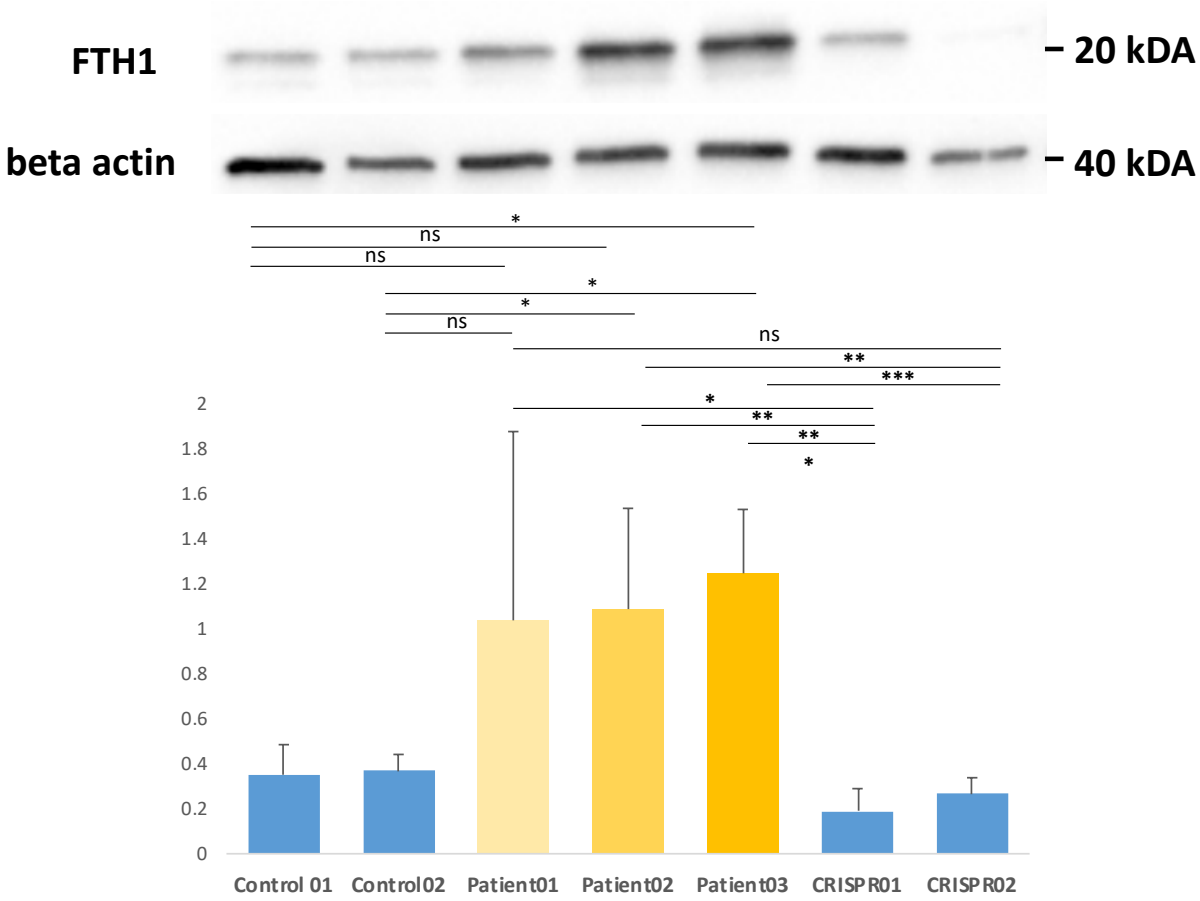

Figure 38. Ferritin accumulation in BPAN neurons. *DMSO-treated samples were tested for ferritin heavy chain 1 (FTH1) levels using the FTH1 D1D4 clone primary antibody. A representative blot is shown. The ratio of Ferritin versus beta actin, the house keeping gene/ loading control, was calculated. Levels are elevated in all patient lines, when compared to controls, and this is statistically significant in most cases. Importantly, CRISPR correction of the WDR45 disease-causing mutations in Patients 02 and 03 restores ferritin levels, suggesting that this phenotypic difference is indeed related to the mutations and not to line variability. n=4-5 independent biological replicates (from independent differentiations) for each line. Statistical analysis was performed using ANOVA. Error bars represent the Standard Error of Mean.*

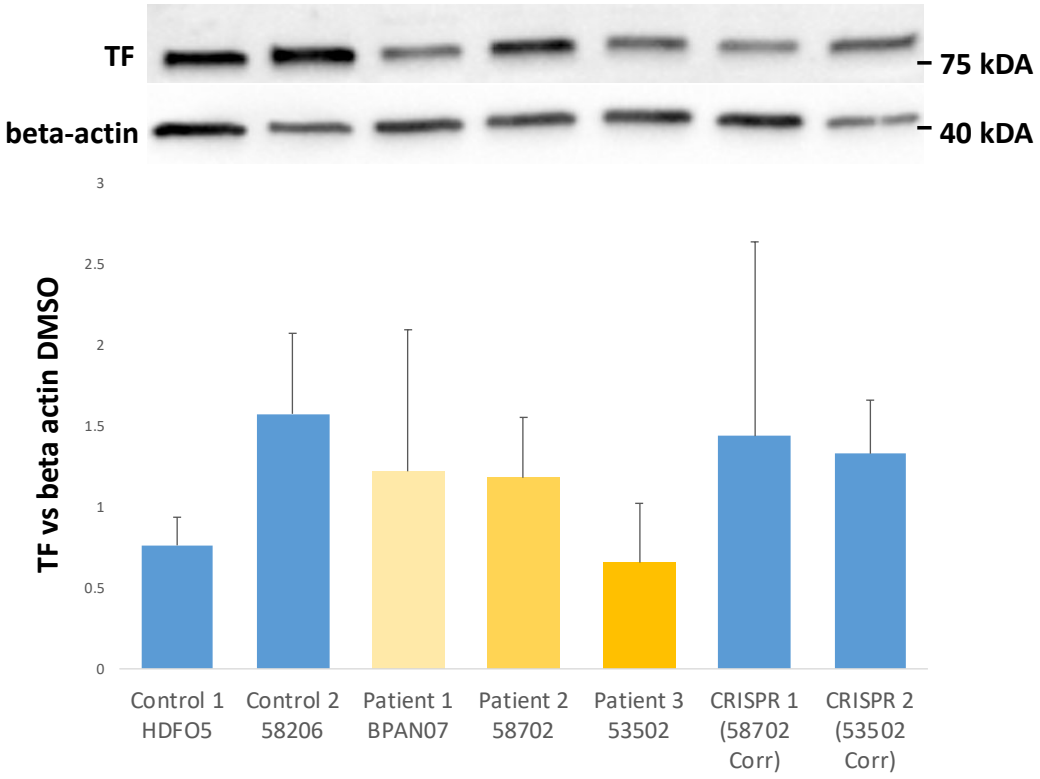

Figure 39. Transferrin levels in Day 65 mDA neurons. *DMSO-treated samples were tested for transferrin (TF) levels via western blotting. A representative blot is shown. No statistically significant difference in TF is seen between BPAN and control lines in basal (DMSO-treated) conditions, despite RNAseq data suggesting that transferrin is downregulated in BPAN neurons at the mRNA level. The ratio of TF versus beta actin, the house keeping gene/ loading control, is shown. n=4-5 independent biological replicates per line. Representative TF and beta actin bands are also depicted. band Statistical analysis was performed using the one-way Anova test. Error bars represent the Standard Error of Mean.*

4.4. Other Phenotypic comparisons between BPAN and control neurons show no obvious differences

4.4.1. High Content Assays

In order to examine pathogenic mechanisms in BPAN but also to develop phenotypic assays for potential hit validation after the primary drug screen, I continued to develop high content assays, both immunofluorescence-based and plate reader-based.

Firstly, I examined lysosomal function on Day 11 progenitor lysosomal function through LAMP1 staining, in an assay similar to the LC3 assay previously described. The rationale for developing this assay was that a recent study had showed a reduction in LAMP1 in BPAN lines (fibroblasts and dopaminergic neurons), evident via immunofluorescence and western blotting experiments (Seibler, Burbulla et al. 2018). Therefore, Day 11 progenitors were seeded onto 96-well Perkin-Elmer CellCarier Ultra plates, at a density of 10,000-15,000 cells/ well, and exposed to 3-hour treatments with DMSO, BafilomycinA1, Torin1, or a combination of BafilomycinA1 and Torin1. Cells were subsequently fixed and stained for LAMP1, with DAPI used as a nuclear stain. Image analysis revealed no obvious difference in LAMP1 puncta numbers per cell, both at basal conditions and after autophagy flux- inhibiting or inducing treatments (**Figure 40)**. Interestingly, and perhaps unexpectedly, there was no obvious difference in LAMP1 puncta numbers per nuclei after autophagy inducing- or inhibiting treatments, when compared to DMSO values. Theoretically, both Torin 1 (autophagy inducer, producing more autophagosomes, hence possibly more lysosomes) and Bafilomycin A1 (blocker of the autophagosome/ lysosome fusion) would have been expected to lead to production of more lysosomes per cell than in basal conditions. Admittedly, no other treatments, e.g. rapamycin (another autophagy flux inducer) or chloroquine (also causing reduction of autophagosomal/ lysosomal fusion) (Mauthe, Orhon et al. 2018) were used in order to verify these results. Hence, potential explanations for this observation could be that a) the treatments did not work (or the experiment failed) or b) there is an issue with autophagosomal/ lysosomal fusion in

BPAN lines (however, the absence of LAMP1 accumulation after treatments was also observed in controls). More investigations are warranted to investigate the above hypotheses, such as a) repeating the experiments with Torin 1 and Bafilomycin A1, but also possibly with other compound treatments (e.g. the aforementioned rapamycin or chloroquine) and/ or b) performing immunofluorescence for co-localisation

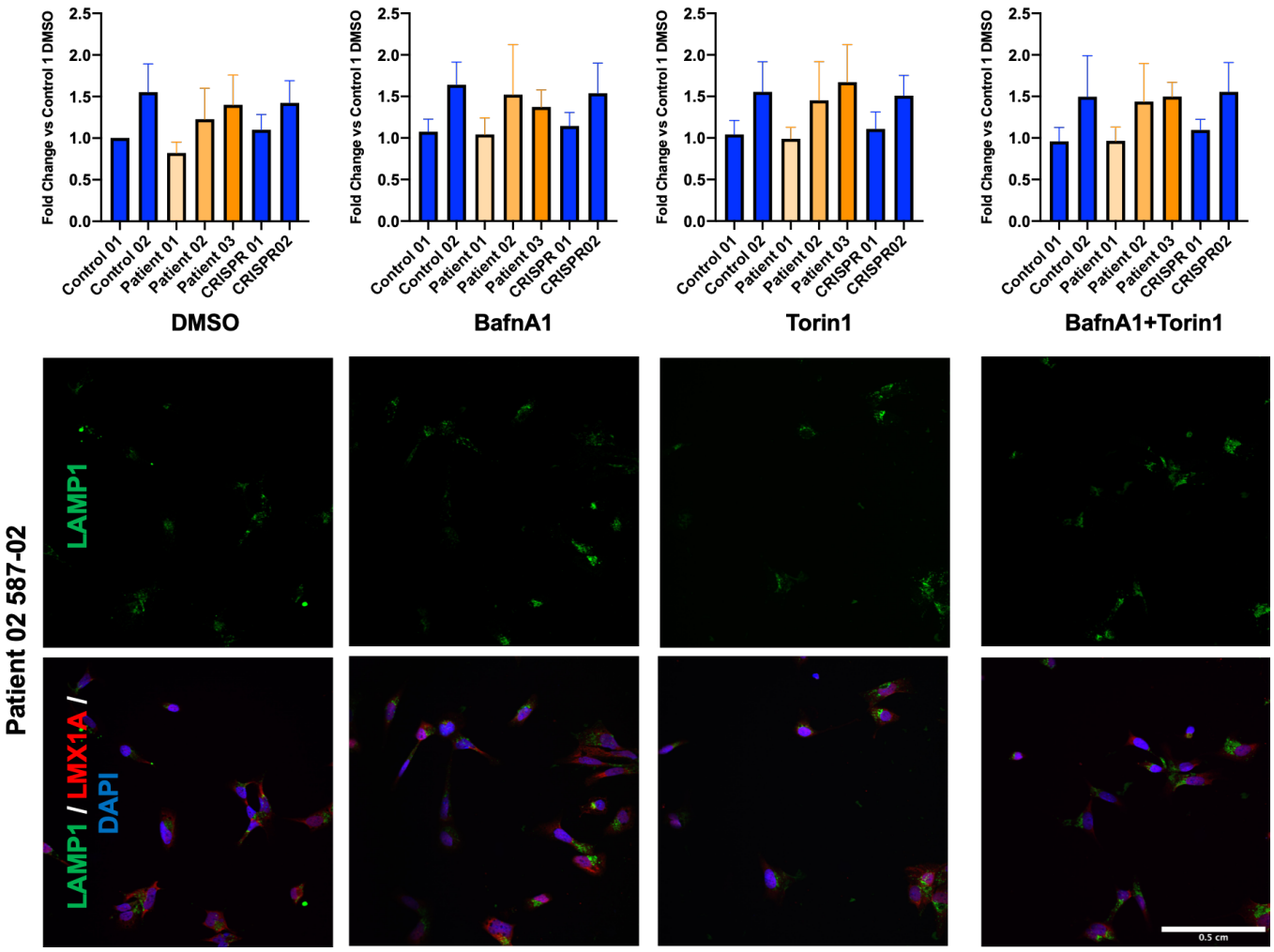

Figure 40. LAMP1 immunofluorescence on Day 11 ventral midbrain progenitors. *This experiment was set up in parallel to the LC3 immunofluorescence-based assay described above, and the methodology was similar. Day 11 ventral midbrain progenitors were seeded onto 96-well plates at low density and treated with autophagy-inducing or inhibiting drugs, then fixed and stained for LAMP1. After image analysis, no obvious difference in LAMP1 formation (representing lysosomes) was seen when comparing BPAN and control lines. n=8 biological replicates. Statistical analysis was performed using Repeated Measurements ANOVA. Error bars represent the Standard Error of Mean.*

Moreover, I wanted to examine cell viability in BPAN lines when compared to controls. For this purpose, I proceeded to develop a plate reader assay to examine Day 11 progenitor cell viability under different conditions. The action of WDR45 is induced in Glucose starvation (Bakula, Muller et al. 2017). Additionally, BPAN fibroblasts showed evidence of increased oxidative stress and mitochondrial dysfunction after treatments with the mitochondrial stressor (complex I inhibitor) 1-methyl-4-phenylpyridinium (MPP+, 1mM) or ferric chloride (FeCl3, 100 µM) in recent studies (Seibler, Burbulla et al. 2018). Hence, the rationale behind the treatments I chose when designing this experiment was to test whether glucose absence or oxidative stress had any effect on cell viability. Similarly to the LC3 and LAMP1 assays, 24 hours post seeding, Day 11 progenitors were exposed to the following conditions/ stressors (for a total of 24 hours):

1. H20 (negative control)
2. FD Medium without antioxidants B27 and L-Ascorbic Acid
3. FD Medium without Glucose
4. MPP+ at 0.5mM, 1mM and 2mM
5. FeCl3 at 100 µM and 200 µM

Each condition was tested on all 7 BPAN and control lines, and in 4 separate experiments/ biological replicates. After 24 hours of treatments, Alamar Blue Cell Viability Reagent (ThermoFisher) 10 µl was added in each well and plates incubated for a further 4-7 hours. Medium colour change from blue to pink indicated metabolically active and, hence, viable cells; at that point, fluorescence (excitation at 560/ emission at 590 nm) was measured on the PerkinElmer Envision II Microplate Reader. To correct for differences between 1) basal metabolic rates between lines, 2) numbers of cells seeded per well for each line and 3) background fluorescence, all values for each cell line were converted to a Fold Change from the H_20-treated value. No differences in cell viability were seen between patient and control lines, under any treatment condition (**Figure 41**). As 24 hours of treatment might not have been sufficient for phenotypes to be elicited, an experiment where cells were treated for a

total of 7 days was also performed. Again, no difference in metabolic activity/ cell viability was seen (preliminary results, n=1 biological replicate, **Figure 42**).

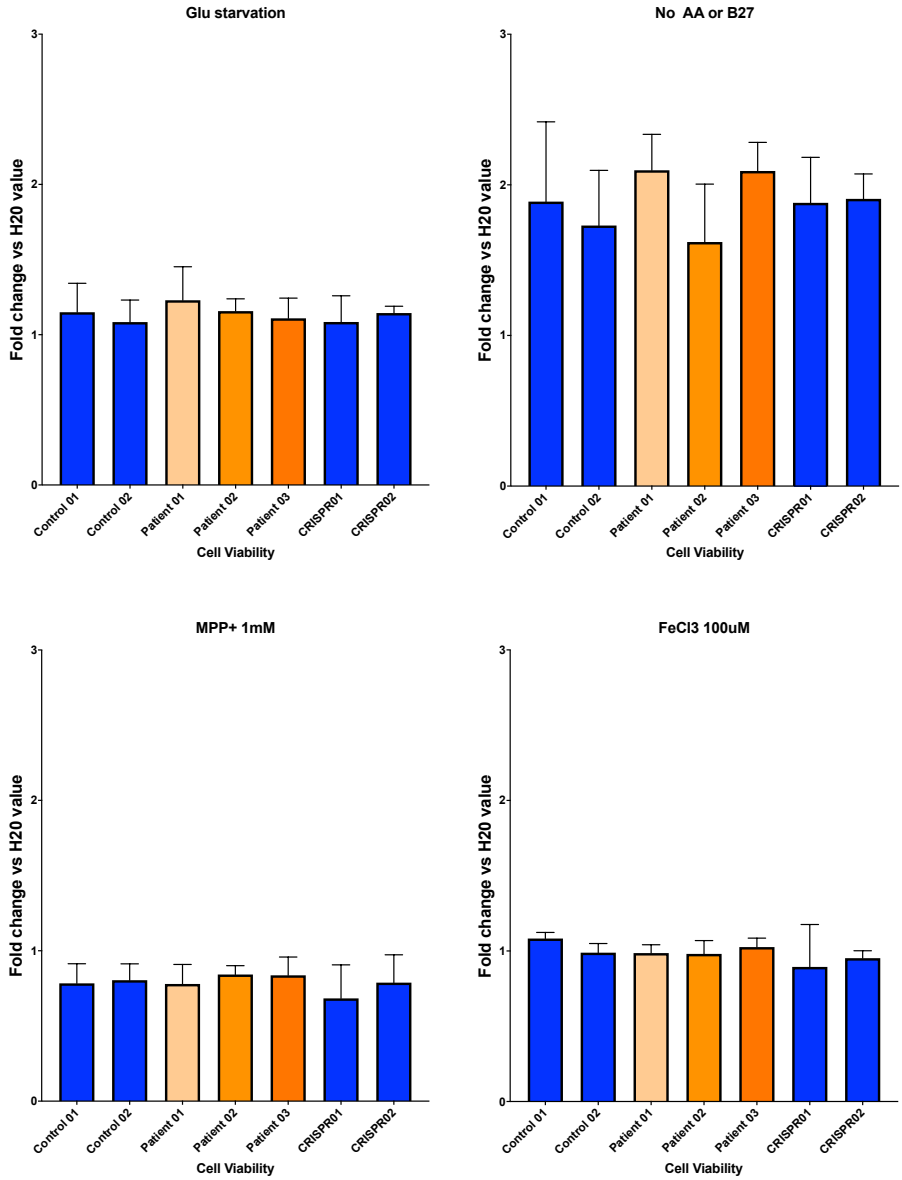

Figure 41. Alamar Blue Cell viability assay shows no significant difference between cell lines. *Some treatments such as glucose starvation and removal of antioxidants B27 and Ascorbic Acid from the medium resulted in metabolic rate increase, whereas treatment with MPP+ led to reduction of metabolic activities. Treatments lasted for 24 hours for all conditions. For each treatment, the Fold Chance of the fluorescence for each line when compared to the H20-treated value is shown. n=4 biological replicates for each line and each condition. Statistical analysis was performed using the ordinary one-way ANOVA test. Due to space restrictions, lack of statistical significance is not specifically indicated on the graphs.*

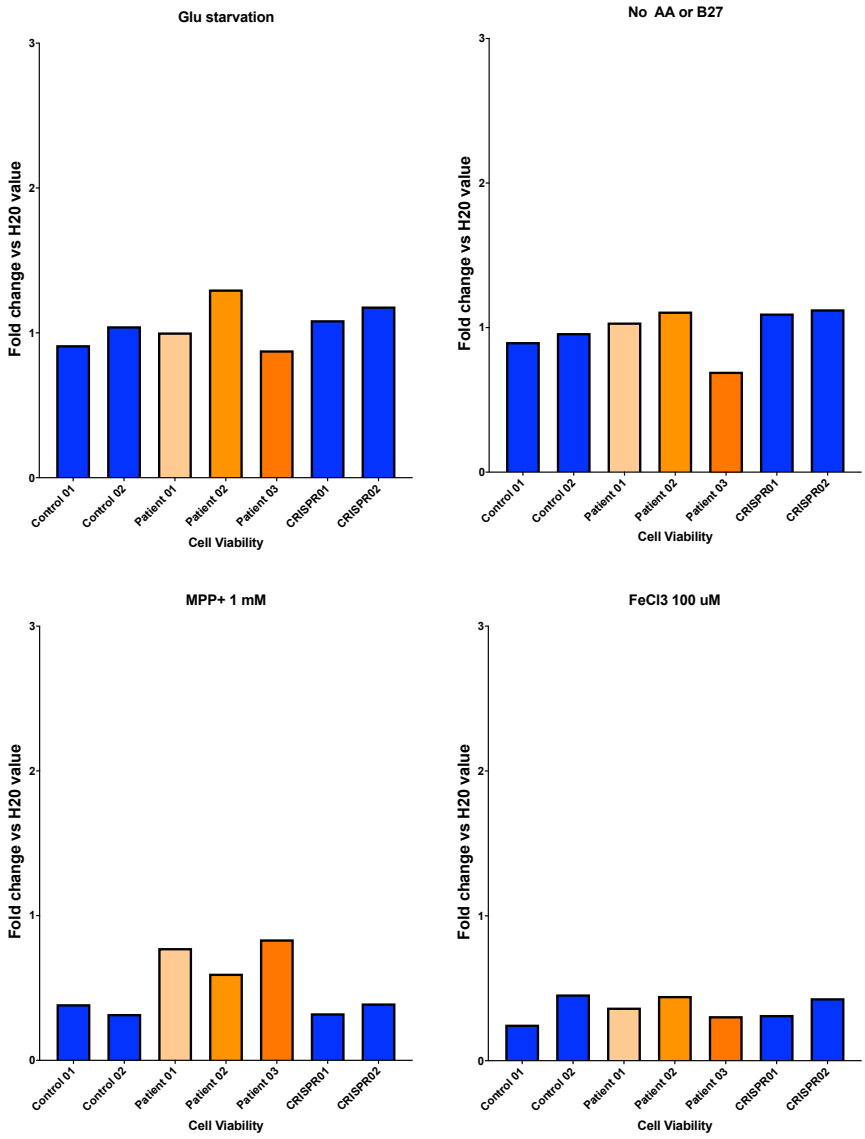

Figure 42. Alamar Blue Cell viability assay at 1 week of treatment. *Preliminary results (n=1 biological replicate for each line and each condition**).** Treatments with MPP+ and FeCl3 led to significant reduction of metabolic activities when compared to untreated samples. However, there seems to be no clear difference between the metabolic activity/ cell viability between patient and control lines for each treatment condition. For each treatment, the Fold Chance of the fluorescence for each line when compared to the H20-treated value is shown.*

4.4.2. Real Time quantitative RT PCR

I also wanted to compare gene expression levels of mature mDA markers at Day 65 of differentiation between BPAN and control neurons. For this, cDNA from Day 65 mDA neurons (all 7 lines, patients and controls) was tested for expression of markers TH, DAT, NURR1, SNCA, MAPT via real-time quantitative RT PCR. Moreover, the same internal control [an age-matched mDA neuronal line (Control 01, HDF05) from one single differentiation and also a single RNA extraction/ cDNA conversion] for each target was tested on each qRT PCR plate. The internal control was used to allow 1) normalisation for inter-plate variability and, hence, 2) comparisons of expression profiles in BPAN and control mDA neurons. For this purpose, an average of the internal control Delta CT mean values from each plate and for each target was calculated. Subsequently, the $\Delta\Delta C_T$ was calculated as below:

$$\Delta C_{T\ internal\ control} = C_T \text{ target} - C_T \text{ GADPH}$$

$$\Delta\Delta C_T = \Delta C_T \text{ sample} - (\Delta C_{T\ internal\ control})average$$

Overall, there was no significant difference in gene expression profiles for any mature marker between BPAN and control lines (**Figure 43**). Occasionally, values were up- or down-regulated in some BPAN (e.g. high *TH* levels in Patients 02 and 03) or control lines (e.g. low *SNCA* levels in Patient 03 Corrected, R234-68), but not consistently so when comparing across patient and control groups. Small sample numbers and large error bars also precluded any further conclusions from these experiments. Importantly, there was no evidence of SNCA or MAPT accumulation, although there was a trend towards MAPT being more expressed in BPAN neurons. There was also a trend for NURR1 to be upregulated in patient neurons. Other studies suggest that *NURR1* upregulation can be seen after hypoxic stress and other brain insults (Perlmann and Wallen-Mackenzie 2004, Jankovic, Chen et al. 2005). Hence, this trend could suggest that the patient neurons are in a stressed state, but more studies are warranted in order to understand the role of *NURR1* in BPAN pathophysiology.

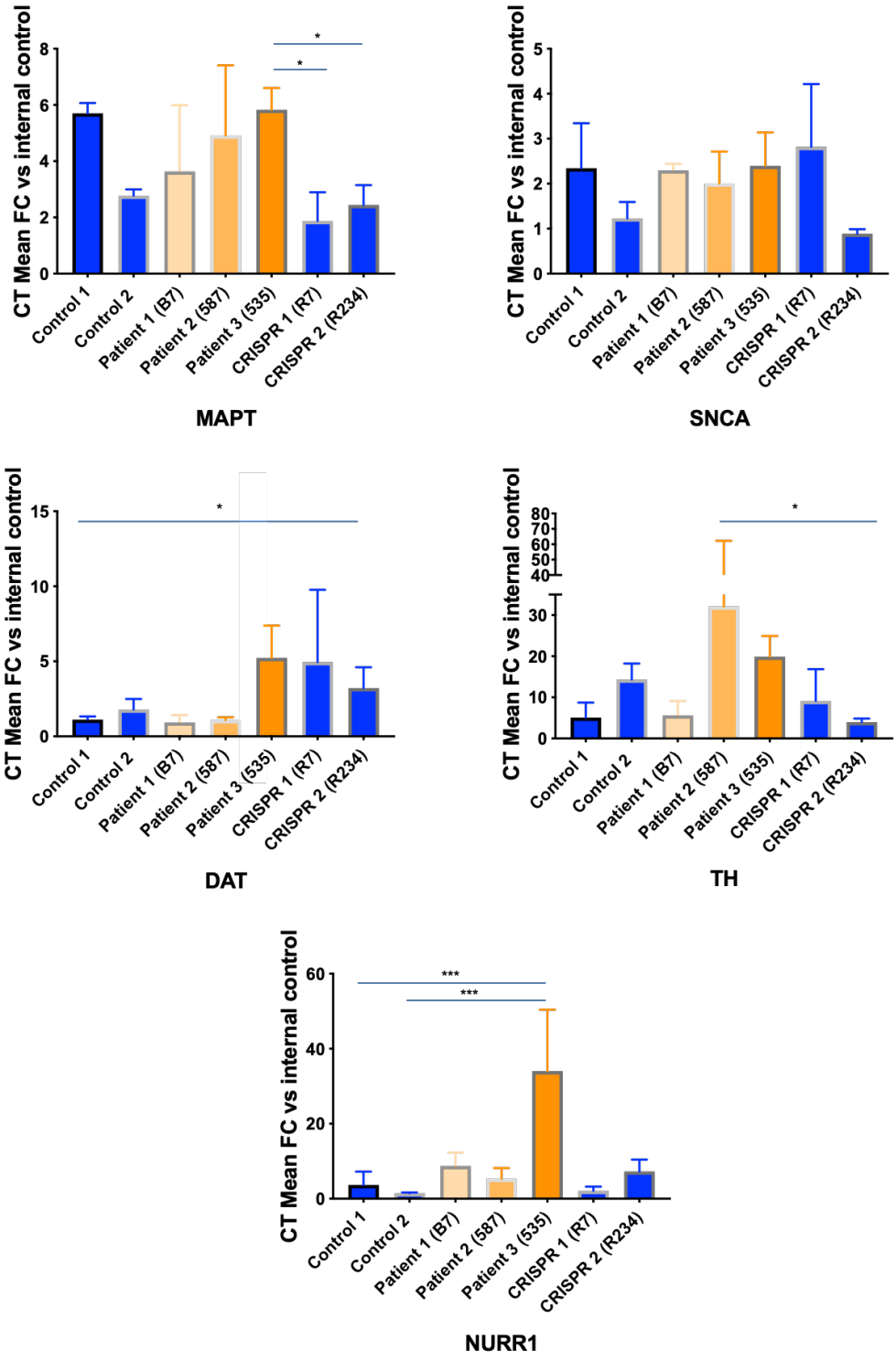

Figure 43. Gene expression levels of mature mDA markers are similar between patient and control lines*. qRT PCR data comparing mature mDA-related marker expression, with all values normalised to the same internal control.). On the graphs, the y axis is on a logarithmic scale. Gene expression is relative to the housekeeping gene (GAPDH) and normalised to the internal control. The fold Change of the* $\Delta\Delta C_T$ *[(*$\Delta\Delta C_T = \Delta C_T$ *sample –* ΔC_T *internal control average), and [(FC)= 2^-(ΔΔCT)] for each marker is shown. Importantly, no difference in SNCA gene expression was notable. MAPT levels tend to be higher in BPAN neurons, but large sample-to-sample variability and a relatively small number of biological replicates precludes any further conclusions. n=3-5 independent biological replicates for each line. Statistical analysis was performed using the ordinary one-way ANOVA test, with the majority of comparisons being non-significant. Error bars represent the Standard Error of Mean. Due to space restrictions, only statistically significant comparisons between patient and control values are shown.*

4.4.3. Western Blotting

In order to compare LC3 and LAMP1 protein levels between patient and control Day 65 mDA neurons, I performed Western blotting on Day 65 mDA neurons. For these experiments, the CRISPR-corrected lines were not analysed due to time constraints. Namely, iPSC lines Patient 02 Corrected and Patient 03 Corrected became available only 6 months before the end of my project and, subsequently, a long time was required for line expansion and neuronal differentiation; hence, there was no time to perform Western Blotting on the isogenic controls for all desired targets and only 5 lines [Controls 01 (HDF-05) and 02 (582-06), and Patients 01 (BPAN-07), 02 (587-02) and 03 (535-02)] were tested for LAMP1 and LC3 levels. Neurons were tested both at basal (DMSO-treated) conditions and after combined 3-hour treatments with Bafilomycin A1 and Torin 1. These treatments work jointly in inducing the formation of autophagomes (Torin 1) and blocking autophagosomal fusion to the lysosomes (Bafilomycin A1); hence, for LC3-II, the lipidated/ autophagosome-bound form of LC3, this should result in increased levels, while the effect on lysosomes is less clear. Overall, no significant difference was seen between patient and control neurons (**Figure 44**).

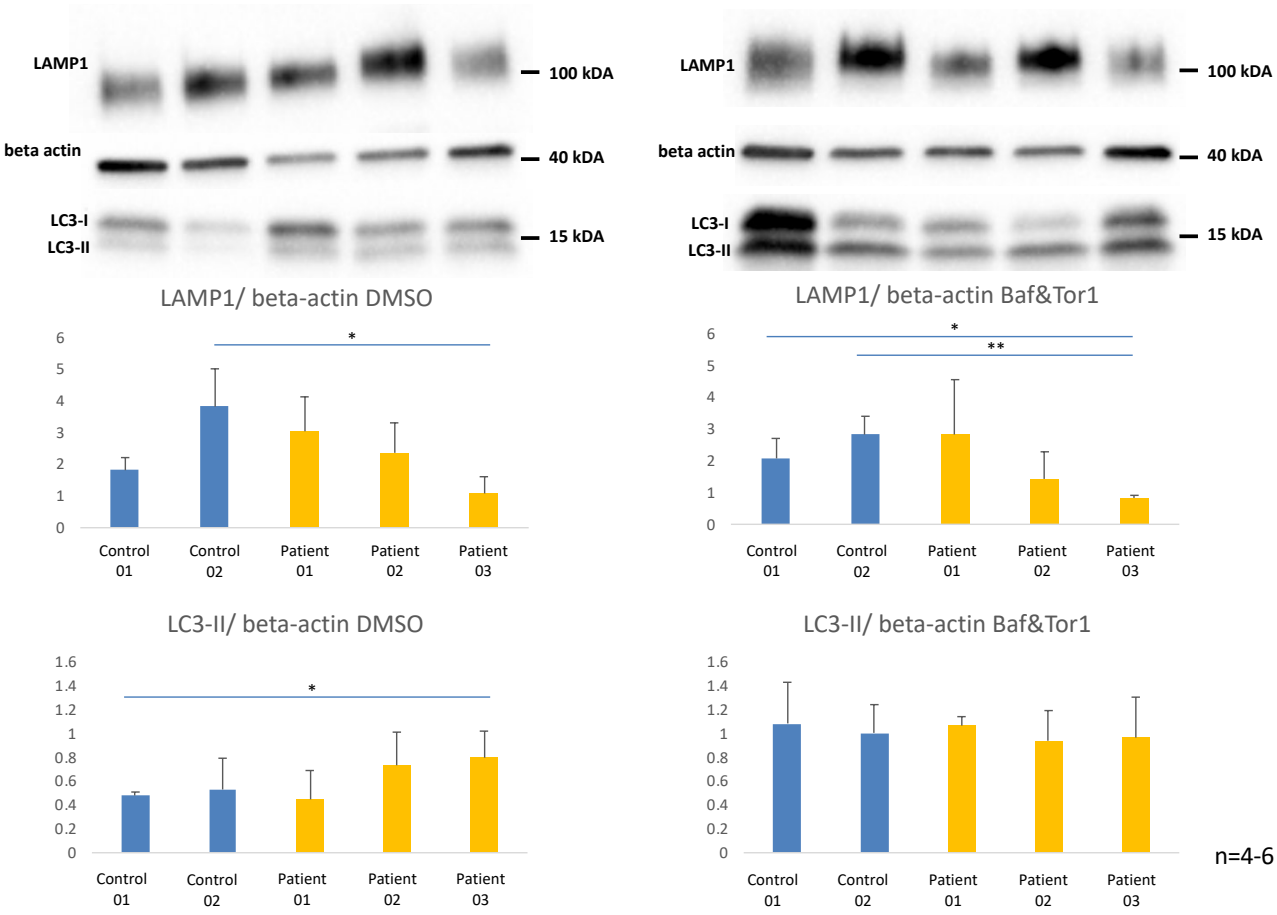

Figure 44. LC3 and LAMP1 Western Blotting. *Protein lysates were derived from control and BPAN mDA neuronal pellets harvested at Day 65 of differentiation. Neurons were tested at basal (DMSO-treated) conditions and also after combined Bafilomycin A1 and Torin1 treatments for 3 hours. LC3-II (lipidated, autophagosome-bound LC3) and LAMP1 protein levels were compared between patient and control lines. Beta-actin was used as a loading control. Representative blots are shown. There were only few statistically significant comparisons between patients and controls, and these were not seen consistently across all lines. For example, reduced LAMP1 was seen when comparing Bafilomycin and Torin-treated Control 01 and 02 (as well as DMSO-treated Control 01) to corresponding Patient 03 LAMP1 levels; however this difference was not seen in Patients 01 and 02. Similarly, DMSO-treated Patient 03 samples had higher LC3-II than Control 01, but not Control 02, and this difference was not observed in the other patients. Lack of statistical significance (in all other comparisons) is not shown due to space restrictions. The ratio of each marker versus beta actin, is shown. n=4-6 biological replicates, from independent differentiations, for each neuronal line. Statistical analysis was performed using ANOVA. Error bars represent the Standard Error of Mean.*

4.5. Discussion

4.5.1. The generated BPAN model recapitulates several disease-related phenotypes.

Firstly, this is a model of true WDR45 deficiency. All 3 patients harbour mutations leading to an early stop codon. Moreover, XCI studies and cDNA sequencing analysis at iPSC stage confirm that only the mutated WDR45 allele is expressed in BPAN female lines. Importantly, western blotting for WDR45 at Day 65 of differentiation shows absence of protein expression in patient neurons, which is restored after CRISPR-mediated mutation correction in the isogenic controls.

Additionally, RNAseq studies at Day 65 of differentiation (performed on Controls 01 and 02 and Patients 01, 02 and 03 in the first instance) have revealed the involvement of several intracellular pathways that might be important in disease pathogenesis. Firstly, neuronal homeostasis is defective in BPAN. Several genes involved in neurogenesis, neuroblast division and neurodevelopment were downregulated in patient Day 65 mDA neurons. There was also differential gene expression in other pathways such as the collagen signalling pathway, which is deregulated in synucleinopathies (Paiva, Jain et al. 2018) and the apoptotic pathway (which might possibly suggest that BPAN neurons are more susceptible to damage and early death). Moreover, the Response to Iron was also a GO term with a very significant fold enrichment, with *HFE, TF*, *CCNB1* and *SCARA5* downregulation in BPAN mDA neurons compared to controls. Western blotting showed no obvious difference in TF between patient and control lines at the protein level. However, Ferritin (Heavy Chain 1) accumulated in patient neurons, probably reflecting increased total intracellular iron levels; this accumulation resolved to normal levels after CRISPR/Cas9 WDR45 mutation correction in both Patients 02 and 03, again pointing towards WDR45 being important for iron metabolism. Iron levels (e.g. via Inductively coupled plasma mass spectrometry, ICP-MS) were not directly measured in patient and control neurons and this is an important experiment to be considered in the future. Additionally, RNAseq has not yet been performed on the CRISPR-corrected lines (as these became available only in the last 6 months of the project) and it would be crucial to show that WDR45

mutation correction leads to restoration of gene expression in affected pathways. Even despite this, these are very important findings confirming that neurodevelopment, neuronal homeostasis and iron metabolism are, indeed, defective in BPAN neurons.

BPAN neuronal lines also exhibit defective autophagy. To test autophagy, I designed a high content imaging-based assay that shows reduced LC3 puncta production (representing autophagosomes) in patient Day 11 ventral midbrain progenitors when compared to controls. This phenotypic defect is completely reversed after CRISPR/Cas9 mutation correction in both 'isogenic controls'. Moreover, this defect is reversible when cells are treated with autophagy inducers such as Torin 1. The mechanism through which this reversal occurs is unclear; it is possible that WDR45 deficiency causes a degree of autophagy flux block that can be, at least partially, overcome through compensatory signalling, for instance through activation of other WIPIs or other molecules acting downstream of WDR45/WIPI4. In any case, the autophagosome production in BPAN lines seems to be not completely blocked, just reduced (or even exhibit slower kinetics) compared to controls. The above not only confirms my initial hypothesis that WDR45 is required for autophagosome formation but might also have therapeutic implications for BPAN patients.

4.5.2. Other assays developed fail to exhibit any phenotypic differences between patient and control lines.

Firstly, there was no obvious lysosomal dysfunction in patient lines, despite this having been reported as a strong phenotype by other studies (Seibler, Burbulla et al. 2018). BPAN Day 11 mDA progenitors exhibited comparable LAMP1 immunofluorescence phenotypes to controls; data analysis included LAMP1 puncta per nuclei, mean intensity of LAMP1 staining per well, and area of LAMP1 staining per cell/ nuclei. Western blotting at Day 65 showed a similar picture, with only Patient 03 (535-02) showing reduced LAMP1 levels compared to Controls 01 and 02. However, LAMP1 western blotting did not include testing of the CRISPR-corrected lines (due to time constrictions, as the CRISPR iPSCs became available late in the project). Interestingly, RNAseq data

showed that *LAMP3* and *LAMP5* were downregulated in BPAN neurons, suggesting that the lysosomal function might indeed be perturbed but in a more cell-specific manner. LAMP5 western blotting was unsuccessful, with no bands visualised even at high concentrations (1:50) of primary anti-LAMP5 antibody (data not shown), and more work/ further antibody optimisation is required. Due to time constrictions in this project, LAMP3 western blotting has not been performed yet, although, again, relevant future experiments might be important to consider.

Western blotting for LC3-II, the lipidated, autophagosomal membrane-bound form of LC3, also failed to show any differences between patient and control lines. This is perhaps surprising, especially in view of the robust Day 11 LC3 immunofluorescence-based phenotypic defect (reduced LC3 puncta) seen in patient lines. However, autophagy (and, therefore, LC3 lipidation during autophagosome formation) is a very dynamic process regulated by many different stimuli. Hence, LC3-II levels can change very fast; for example, in this project I showed that even 3-hour treatments with Bafilomycin A1 and/or Torin 1 can increase autophagosome production. It is, therefore, possible that variable levels of LC3-II in samples differentiated independently from each other (e.g. with different starting dates of differentiation and harvesting) just reflect environmental processes (e.g. differences in incubator CO2/ O2 levels or in batch-to-batch variations in nutrient concentrations) around the time of harvesting the neuronal pellets. On the other hand, the Day 11 LC3 assay was designed with this variability in mind; for each biological replicate, differentiation for all cell lines started on the same day and, at Day 11, all cells were seeded onto the same 96-well plate. Hence, the samples were paired, and this pairing allowed the comparison of Fold Change values (versus the Control 01 DMSO value) between patients and controls, rather than actual LC3 puncta/ nuclei values. Indeed, in each particular 96-well plate (biological replicate), the LC3 puncta/ nuclei value in BPAN lines was lower than the paired controls, but this was not necessarily true when comparing one biological replicate to the other (data not shown). If such an experimental design was followed for LC3 Western Blotting, results could be different, although prolonged culture times might also plausibly increase variability between samples. Moreover, immunostaining allows better

discrimination of LC3 localised to the autophagosome by identification of puncta. On the other hand, Western Blotting could identify LC3 that is cytoplasmic or non-autophagosomal (e.g. in the endoplasmic reticulum). Importantly, recent studies suggest that lipidated LC3 does not only attach to autophagosomes but also cytoplasmic proteins (Agrotis, von Chamier et al. 2019). Hence, imaging based assays were more accurate for monitoring LC3 in my project. In any case, LC3-II levels in the CRISPR-corrected lines (Patient 02 Corrected and Patient 03 Corrected) have not yet been tested due to time constraints, and it would be important to compare these levels to the corresponding ones in Patients 02 (587-02) and 03 (535-02) in future experiments.

Another assay that did not show any phenotypic defects in BPAN lines was the Alamar Blue cell viability assay on Day 11 ventral midbrain progenitors. For this experiment, I used stressors that were either reportedly specific for WDR45 (e.g. glucose starvation, that induces WDR45 function) (Bakula, Muller et al. 2017) or had been used in other BPAN-related studies (e.g. MPP+ or FeCl3) (Seibler, Burbulla et al. 2018). Despite this, no phenotypic defect was seen in patient lines compared to controls; this might be because 1) I used incorrect concentrations or exposure times (even if I used a range of concentrations and treatments of both 24hours and 7 days) or 2) Day 11 cells are not susceptible to these stressors, or even because 3) Alamar Blue was the wrong assay to detect viability defects (as it focuses on respiratory chain-based metabolism, that might not be affected in BPAN). In any case, the application of these (and other similar) stressors on Day 11 and (perhaps more importantly) on Day 65 neurons, and the use of assays looking at cell viability and/ or apoptosis and other relevant readouts (e.g. mitochondrial or lysosomal function) might be warranted in future BPAN-related studies, in order to elucidate mechanisms leading to striatonigral degeneration.

5. The use of the BPAN model as a drug screening platform to identify novel therapies

5.1. Rationale behind drug screen

One of my major goals in this project was to perform a drug screen with the aim to identify compounds that reverse or ameliorate disease-related phenotypes in neuronal cells. These drugs would then have the capacity to be further validated and tested in other preclinical models, with the ultimate aim of clinical translation and establishment of novel, more targeted and effective therapies for BPAN patients.

For the purpose of the primary drug screen, as mentioned above, I had already 1) chosen Day 11 cells as the optimal platform and 2) identified a robust and reproducible high content imaging-based phenotypic defect in BPAN lines, namely that LC3 puncta production (reflecting autophagosome formation) is reduced in Day 11 patient ventral midbrain progenitors when compared to controls. Moreover, during the LC3 assay set up I also demonstrated that the BPAN LC3 defect is reversible upon autophagy induction with Torin1, which in turn has been shown by other studies to reduce iron accumulation in BPAN neurons. Hence, identifying drug hits that increase LC3 production by inducing autophagy might have future therapeutic implications for our patients. For all the above reasons I performed the primary drug screen using the LC3 assay on Day 11 mDA progenitors. The aim in this project was to, firstly, identify hits that increase LC3 puncta production and, secondly, perform a first validation of identified compound hits by testing their capacity to induce autophagy through another assay based on p62 degradation. Ultimately, more robust validation of these hits on our Day 11 and Day 65 neuronal model, as well as other models, will have to be performed in future projects.

The process of drug screening and counter-screening of identified hits is described in detail below.

5.2. Primary drug screen

For the actual screen, I used 2 separate small molecule libraries. Firstly, the **Prestwick Chemical Library** of 1280 compounds (95% FDA/ EMA approved) was used (http://www.prestwickchemical.com/libraries-screening-lib-pcl.html). Overall, 16% of the Prestwick library compounds also have known actions in the CNS. Moreover, the use of FDA-approved drugs provides opportunities for drug repurposing and shorter times to clinical translation and patient benefit. Compounds are provided on source plates at 10mM in DMSO.

Secondly, a **library of autophagy activators** was screened. This consists of a) novel compounds (available in the Kettleler lab and developed through collaboration with UCL School of Pharmacy and UCL Translational Research Office) that are known to enhance autophagy in several cell lines, b) well-known autophagy inducers and c) other drugs (e.g. autophagy inhibitors or toxins), effectively to be used as negative controls.

For both screens, DMSO (in column 1) and Bafilomycin A1 (in column 12) were used in all destination plates as negative and positive controls, respectively. This was because 1) Bafilomycin A1 blocks autophagosomal/ lysosomal fusion and leads to accumulation of autophagosomes, whereas 2) DMSO in low concentrations should have no (or little) effect and, finally, 3) almost all drugs in the screen were diluted in DMSO.

For each drug, 100 nl were dispensed into each destination well using the Labcyte Echo550 acoustic dispenser (initial concentrations detailed in the Methods section). Cells were fixed 24 hours post treatments. LC3 was detected using the anti-LC3 D11 clone rabbit monoclonal antibody (1:200, as per **Table 2**) and a corresponding Alexa Fluor 488 Goat Anti-Rabbit IgG secondary antibody (1:400); nuclei were detected via DAPI staining. Finally, plates were imaged for LC3 (488nm) and DAPI (375nm) and images analysed with ImageJ/Fiji and R Studio for hit detection (**Figure 45**).

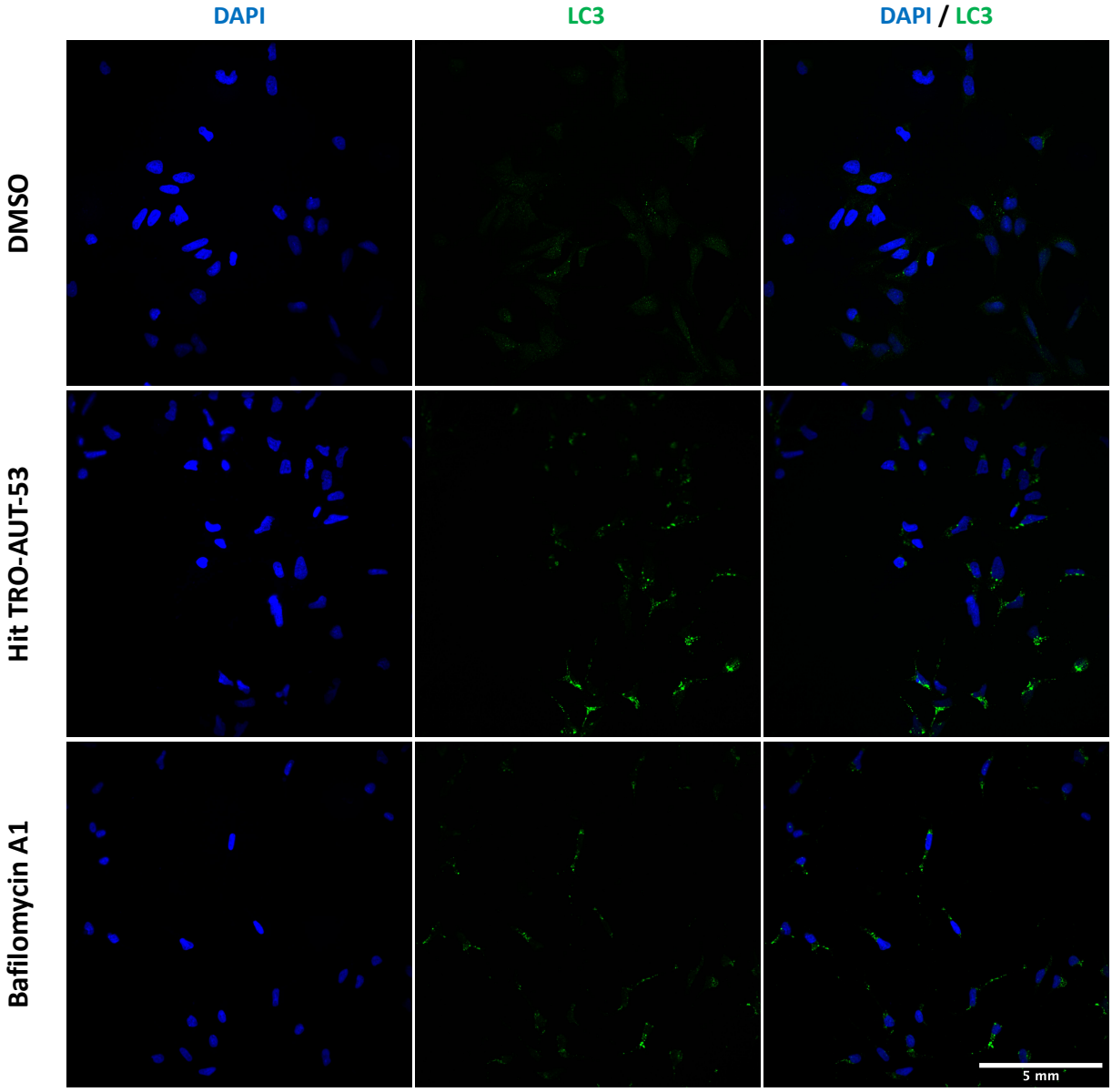

Figure 45. Representative images from primary drug screen. *For both compound libraries tested, Day 11 ventral midbrain progenitors were seeded onto 96-well plates and treated for 24 hours prior to fixing and staining for LC3 puncta (green) and DAPI (blue). Subsequently, images were acquired via the PerkinElmer Opera Phenix microscope, using a 40x water immersion objective (as detailed in the Methods section). Plates were imaged for LC3 (488nm) and DAPI (375nm) and representative examples from negative controls, hits and positive controls (top, middle and bottom rows, respectively) are shown. Results of the screen will be discussed below; however, some hits (e.g. the depicted hit TRO-AUT-53, from source plate well A8 in the autophagy inducer library) significantly enhanced autophagy with more LC3 puncta per nuclei than those seen with Bafilomycin A1 treatments. Image analysis for hit detection took place using with ImageJ/Fiji and R Studio, as well as Excel softwares. Importantly, ImageJ/Fiji parametres wet set appropriately so that only LC3 puncta within the cell, and background, were counted.*

5.2.1. Drug Screen using autophagy inducers

The source plate layout (96-well format) for the autophagy activator library is detailed in **Table 19**.

	1	2	3	4	5	6	7	8	9	10	11	12
A	DMSO	TRO-AUT-29	Chloroquine	TRO-AUT-37	BEZ235	TRO-AUT-45	PV-1019	TRO-AUT-53	JKV8C3-A	TRO-AUT-61	JKV8C3-C	Bafn A1
B	DMSO	TRO-AUT-30	JKV8C3	TRO-AUT-38	MG132	TRO-AUT-46	Etoposide	TRO-AUT-54	JKV8C3-B	TRO-AUT-62	STK964	Bafn A1
C	DMSO	TRO-AUT-31	Comp 5F4	TRO-AUT-39	Trehalose	TRO-AUT-47	3-methyl adenine	TRO-AUT-55	MRT68921	TRO-AUT-63	Compound C	Bafn A1
D	DMSO	TRO-AUT-32	Rapamycin	TRO-AUT-40	ABT-737	TRO-AUT-48	DMSO	TRO-AUT-56	MRT673074	TRO-AUT-64	Brefeldin A	Bafn A1
E	DMSO	TRO-AUT-33	Torin 1	TRO-AUT-41	SRT-1720	TRO-AUT-49	AZD8055	TRO-AUT-57	MHY-1485	TRO-AUT-65	Antimycin A	Bafn A1
F	DMSO	TRO-AUT-34	Resveratrol	TRO-AUT-42	STK693863	TRO-AUT-50	S6K inhibitor	TRO-AUT-58	SMER-28	TRO-AUT-66	Oligomycin	Bafn A1
G	DMSO	TRO-AUT-35	Flubendazole	TRO-AUT-43	Desferiox-amine	TRO-AUT-51	Spermidine	TRO-AUT-59	Biochanin A	Erlotinib	Rotenone	Bafn A1
H	DMSO	TRO-AUT-36	AZD1152	TRO-AUT-44	MK-2206	TRO-AUT-52	Valinomycin	TRO-AUT-60	Tamoxifen	CCCP	Digoxin	Bafn A1

Table 19. Source plate layout for autophagy activator screen. *DMSO and Bafilomycin A1 are used as negative controls (Columns 1 and 8, respectively). Stock concentrations for each compound are detailed in the Methods section; 100nl of each drug was dispensed in each well of the destination plates.*

In total, 3 lines (Control 01 HDF-05, Patient 02 587-02, Patient 03 535-02) and 9 x 96-well destination plates were used (1 source plate, 3 lines, tested in triplicates).

Results are summarised in **Figure 46**. After image analysis with ImageJ/Fiji, R Studio and Excel softwares, values of LC3 puncta per cell were calculated for each well, and representative heatmaps and graphs generated. Several tested compounds had the ability to significantly enhance LC3 puncta production in all lines; in some, this enhancement was more pronounced than the one seen after Bafilomycin A1 treatments. Some of the top hits [e.g. A08 (TRO-AUT-53), A03 (Chloroquine), B04 (TRO-AUT-38)] behaved similarly in all three lines, while others [e.g. H02 (AZD1152), F08 (TRO-AUT-58)] resulted in a pronounced LC3 puncta increase in the patient lines, but not in the controls. Most of the top, common, compound hits are novel, whereas others have different mechanisms of action. For example, chloroquine blocks autophagy flux by inhibiting autophagosomal/ lysosomal fusion (Mauthe, Orhon et al. 2018), in a mechanism of action similar to Bafilomycin A1. Such 'hits' (or treatments leading to results as expected) acted as additional controls and provided further validation that our screening results were robust.

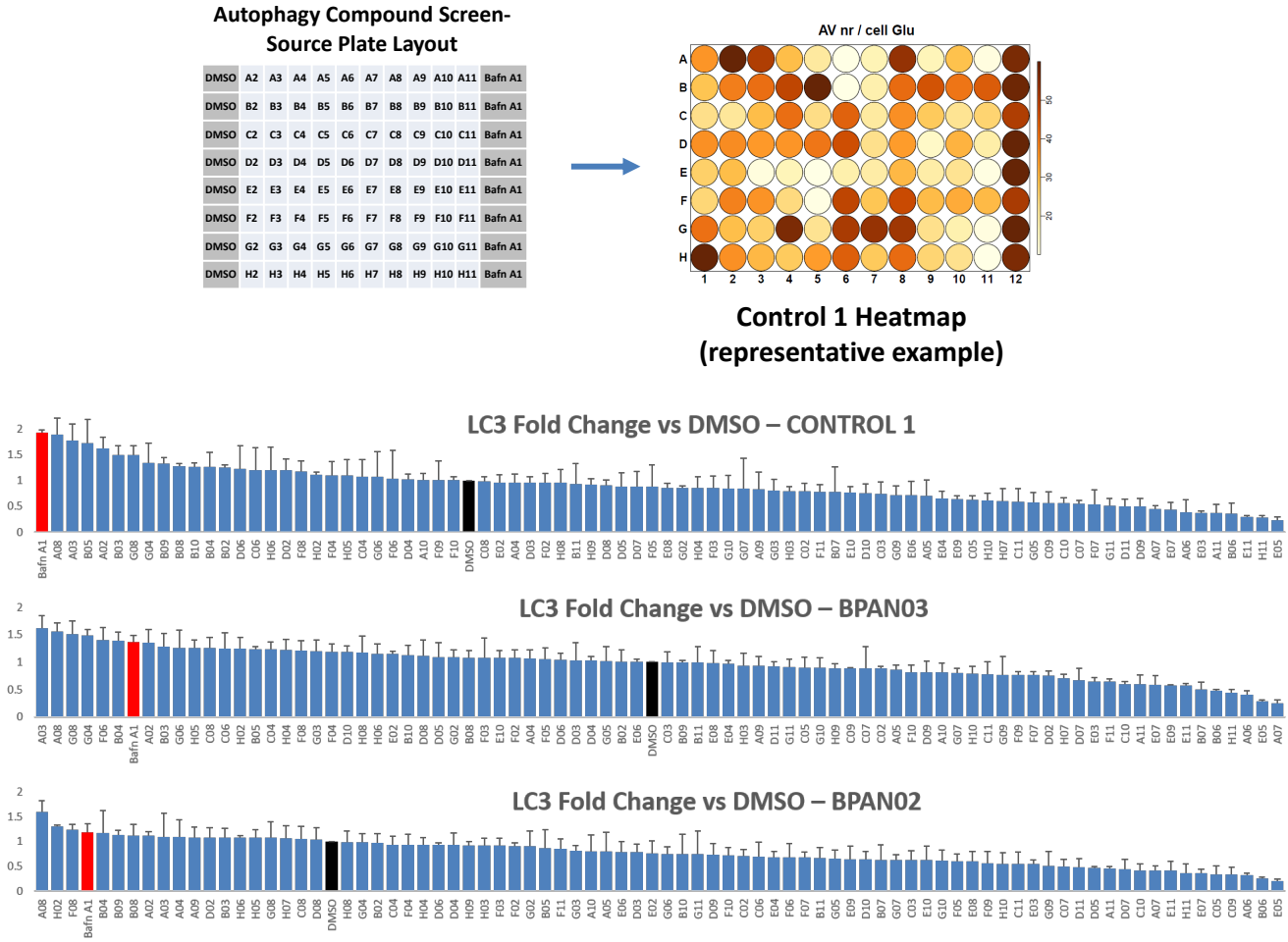

Figure 46. Autophagy Inducing Compound Screen: hits. Top Left: *the source plate layout is shown. DMSO (Column 1) and Bafilomycin A1 (Column 12) were used as negative and positive controls, respectively.* ***Top Right****: a representative heatmap is shown. Increasing puncta numbers per nuclei are depicted in increasingly darker shade of orange. Positive controls and hits show higher numbers of LC3 puncta per cell than negative controls, although in some wells (e.g. H1), occasional edge artefacts, due to moisture evaporation and resulting in falsely high counts, are seen.* ***Bottom:*** *DMSO values were averaged for each cell line. Subsequently, all Bafilomycin A1- and compound-related readouts from each technical replicate were also averaged and depicted as a Fold Change compared to the DMSO value. n=3 technical replicates for each compound. Error bars represent Standard Deviation.*

5.2.2. Drug Screen using the Prestwick Library

For the Prestwick screen, one patient line (Patient 02 587-02, with the biggest LC3-related phenotypic defect) was used and 48 x 96-well destination plates required (16 source plates, 80 compounds each, tested in triplicates). The choice of using only one line was due to capacity issues, namely the large number of source and destination plates required to conduct the screen, even using only Patient 02. Again, DMSO (in column 1) and Bafilomycin A1 (in column 12) were used in all destination plates as negative and positive controls, respectively.

Results for the Prestwick library screen are summarised in **Figure 47**. Similarly to the autophagy enhancer screen, values of LC3 puncta per cell were calculated for each well, and representative heatmaps and graphs produced. Image segmentation was used in order to remove background noise, and only puncta within cells were measured. Moreover, in some plates the quality control (performed by assessing the effect of the controls, but also the presence of non-specific puncta detectable in the image background) failed; in these cases, the whole process (cell seeding, drug treatments, fixing, blocking, staining and imaging) was repeated. Subsequently, values were normalised, within each plate but also throughout the screen based on negative control values, and corresponding z scores were calculated. Several compound hits had the ability to significantly enhance LC3 puncta production in all lines, with z scores much higher than those of positive controls. A list of the hits with the highest z scores is provided in **Table 20**.

	Destination plate	Destination well	z score	Well Annotation
1	14	A10	253.64	sample
2	6	D09	152.67	sample
3	14	C09	107.82	sample
4	10	F08	93.28	sample
5	7	A08	82.75	sample
6	9	D07	60.76	sample
7	15	F02	57	sample
8	9	B07	53.24	sample
9	12	A04	46.93	sample
10	12	E06	39.85	sample
11	11	B02	32.34	sample
12	8	H11	25.03	sample
13	16	G02	24.93	sample
14	16	B05	24.49	sample
15	9	G09	24.39	sample
16	6	D08	21.69	sample
17	5	G06	21.09	sample
18	9	G06	19.4	sample
19	7	G11	18.22	sample
20	6	D07	17.8	sample
21	5	H08	15.89	sample
22	9	A11	14.96	sample
23	4	E07	14.67	sample
24	13	C07	14.2	sample
25	1	H09	13.55	sample
26	6	A10	13.41	sample
27	2	F07	12.87	sample
28	7	E03	11.92	sample
29	13	H11	11.5	sample
30	4	H09	10.16	sample
31	5	F06	10.13	sample
32	10	G08	9.97	sample
33	9	A07	9.16	sample
34	2	E07	9.1	sample
35	2	G07	8.59	sample
36	5	E09	8.14	sample
37	14	A06	7.55	sample
38	7	H11	7.49	sample
39	13	A11	7.18	sample
40	5	G07	6.77	sample
41	16	E05	6.53	sample
42	2	G04	6.11	sample
43	4	H04	6.06	sample
44	6	F08	5.67	sample
45	3	D11	5.59	sample
46	4	C11	5.49	sample
47	11	A11	5.47	sample
48	10	C08	5.44	sample
49	14	C11	5.42	sample
50	9	B11	5.37	sample
51	5	E05	4.47	sample
52	13	H02	4.27	sample
53	9	C07	4.17	sample

54	4	H11	4.16	sample
55	1	H12	4	Positive Control
56	15	H11	3.94	sample
57	5	C09	3.91	sample
58	10	G12	3.51	Positive Control
59	7	G02	3.43	sample
60	4	G05	3.43	sample
61	12	A12	3.27	Positive Control
62	1	H07	3.13	sample
63	2	H12	3.12	Positive Control
64	4	H03	3.02	sample
65	11	G12	2.91	Positive Control
66	1	A12	2.85	Positive Control
67	11	G07	2.84	sample
68	3	A02	2.84	sample
69	2	E05	2.83	sample
70	13	F05	2.79	sample
71	2	G12	2.7	Positive Control
72	1	F12	2.69	Positive Control
73	11	F12	2.68	Positive Control
74	1	A02	2.66	sample
75	1	D12	2.6	Positive Control
76	10	F12	2.59	Positive Control
77	10	H12	2.56	Positive Control
78	6	B05	2.56	sample
79	16	G05	2.55	sample
80	11	G03	2.55	sample
81	5	H10	2.52	sample
82	5	G04	2.5	sample
83	5	H07	2.5	sample
84	2	D12	2.49	Positive Control
85	14	H12	2.48	Positive Control
86	13	F12	2.47	Positive Control
87	6	A11	2.46	sample
88	1	C12	2.45	Positive Control
89	16	H11	2.44	sample
90	11	A12	2.43	Positive Control
91	16	H10	2.3	sample
92	14	H06	2.29	sample
93	1	G12	2.27	Positive Control
94	4	H10	2.26	sample
95	1	F08	2.25	sample
96	11	G06	2.24	sample
97	5	F12	2.2	Positive Control
98	10	B11	2.19	sample
99	10	E12	2.16	Positive Control
100	3	B02	2.14	sample

Table 20. Prestwick Library hits. *After image analysis and value normalisation, firstly within each plate but also across the whole screen, z scores were calculated. Hits are evenly distributed amongst the 16 source plates and the highest z scores for wells representing (Bafilomycin A1-treated) positive controls were much lower than the top-scoring compound hits. .A list of the 100 highest scoring hits (in descending z score value) is shown. The 26 top hits (shaded in grey, with the highest z-score values) were further validated via a p62 high content imaging assay, as described below (Section 5.3).*

Prestwick Screen- Source Plate Layout

DMSO	A2	A3	A4	A5	A6	A7	A8	A9	A10	A11	Bafn A1
DMSO	B2	B3	B4	B5	B6	B7	B8	B9	B10	B11	Bafn A1
DMSO	C2	C3	C4	C5	C6	C7	C8	C9	C10	C11	Bafn A1
DMSO	D2	D3	D4	D5	D6	D7	D8	D9	D10	D11	Bafn A1
DMSO	E2	E3	E4	E5	E6	E7	E8	E9	E10	E11	Bafn A1
DMSO	F2	F3	F4	F5	F6	F7	F8	F9	F10	F11	Bafn A1
DMSO	G2	G3	G4	G5	G6	G7	G8	G9	G10	G11	Bafn A1
DMSO	H2	H3	H4	H5	H6	H7	H8	H9	H10	H11	Bafn A1

Heatmap (representative example)

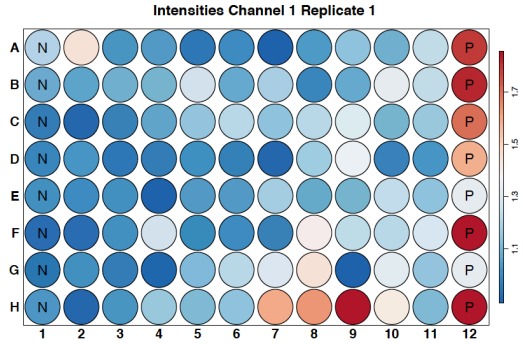

Prestwick Hits

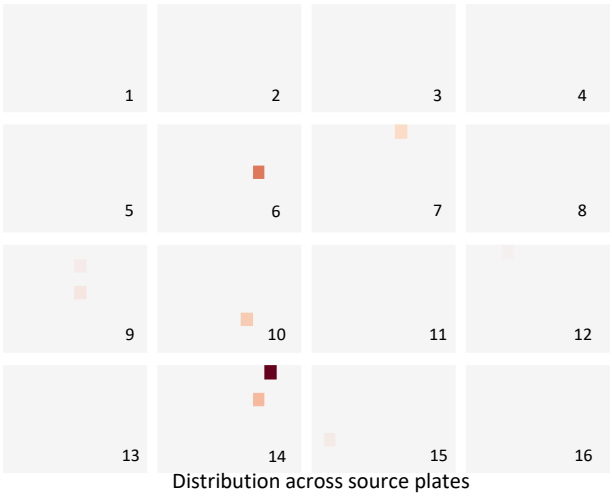

Distribution across source plates

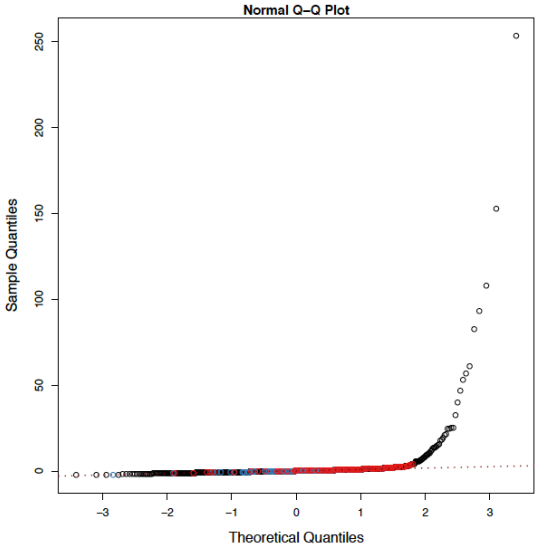

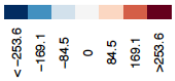

Figure 47. Prestwick screen hits. Top Left: *the source plate layout is shown. DMSO and Bafilomycin A1 were used as negative and positive controls, respectively.* ***Top Right****: a representative heatmap is shown. Increasing puncta numbers per nuclei are depicted in increasingly darker shade of red. Positive controls and hits show higher numbers of LC3 puncta per cell than negative controls.* ***Bottom:*** *after image analysis, Z scores were calculated for each treatment. The distribution of the top scoring hits is shown on the left. There is a fairly even distribution of hits across all 16 destination plates (as also detailed in Table 20). Several hits have z scores and theoretical quantiles that are much higher than their theoretical values and values from positive controls (in red).*

5.3. p62 assay for first pass hit validation

BPAN cells exhibit defective autophagy [as detailed above and also described in (Saitsu, Nishimura et al. 2013, Seibler, Burbulla et al. 2018)] and there is also a suggestion that autophagy induction might lead to restoration of intracellular iron accumulation in BPAN neurons (Seibler, Burbulla et al. 2018) and also endoplasmic reticulum stress (Wan, Wang et al. 2019). With this in mind, after hits (compounds that increased LC3 puncta production in Patient02) were identified in the Prestwick screen, I proceeded to perform their first validation by designing a p62 immunofluorescence-based assay. The rationale of this assay was to test the hits with the highest z-scores on 1) whether they cause autophagy induction or inhibition and also 2) their effects on cell viability. Firstly, LC3 puncta accumulation can occur either via autophagy induction (e.g. with mTOR inhibition via Torin1) or inhibition (e.g. through blockage of autophagosomal fusion with lysosomes via Bafilomycin A1). Both these processes would lead to a similar phenotype of LC3 puncta per cell number increase; however, due to reasons detailed above, I was interested in hits in the Prestwick library that actually induce autophagy and might therefore have the potential for future therapeutic benefits for BPAN patients. Secondly, compounds that cause major cell death or apoptosis were not desirable and/ or might appear as false hits on the screen (if, for example, autophagy were to be activated as a defence mechanism upon accumulation of damaged cellular organelles or protein aggregates). Therefore, Day 11 Patient 02 (587-02) cells were seeded onto 96-well plates, as above, and treated for 24 hours with the top 26 scoring Prestwick hits at a final concentration of 100 µM (**Table 20**). After, fixing and blocking, cells were stained for p62/ SQSTM1. For this assay, DMSO (1:1,000 in culture medium) and Torin1 (250 nM) were used as negative and positive controls, respectively; Torin 1 treatment should result in autophagy induction and, thereby, reduction of p62-positive puncta (representing autophagy cargo tagged for degradation and recycling) compared to DMSO, which should have no (or minimal) effect. Autophagy-inducing hits were expected to behave in a similar manner to Torin1, while flux-blocking drugs should lead to p62 accumulation. The layout of the source plate for the p62 counter-screen is detailed in **Table 21**.

	1	2	3	4	5	6	7	8	9	10	11	12
A	**DMSO**	**DMSO**	**DMSO**	**DMSO**	**DMSO**	**DMSO**	**DMSO**	**DMSO**	**DMSO**	1	1	1
B	2	2	2	3	3	3	4	4	4	5	5	5
C	6	6	6	7	7	7	8	8	8	9	9	9
D	10	10	10	11	11	11	12	12	12	13	13	13
E	14	14	14	15	15	15	16	16	16	17	17	17
F	18	18	18	19	19	19	20	20	20	21	21	21
G	22	22	22	23	23	23	24	24	24	25	25	25
H	26	26	26	**Torin1**	**Torin1**	**Torin1**	**Torin1**	**Torin1**	**Torin1**	**Torin1**	**Torin1**	**Torin1**

Table 21. Destination plate layout for the p62 assay. *Patient02 ventral midbrain progenitors were treated with the top hits (1 to 26, in triplicates) from the Prestwick screen and p62 puncta formation was examined 24 hours later. DMSO and Torin1 were used as negative and positive controls, respectively.*

After staining, imaging and image analysis, ratios of nuclei per well (crudely representing viability) and p62 puncta per nuclei were calculated and plotted as Fold Change compared to the DMSO-treated values (**Figure 48**). Several hits (namely Hits 2, 3, 6, 12, 15, 19, 21, 22, 23, 25, 26) increased p62 puncta production to values higher than the negative control, possibly representing autophagy flux inhibitors. Additionally, several compounds (Hits 1, 2, 4, 5, 7, 10, 11, 12, 13, 14, 15, 17, 18, 21) resulted in significant reduction in detectable nuclei per well when compared to DMSO; in other words, these were toxic for the Day 11 cells at the tested final drug concentration of 10 uM.

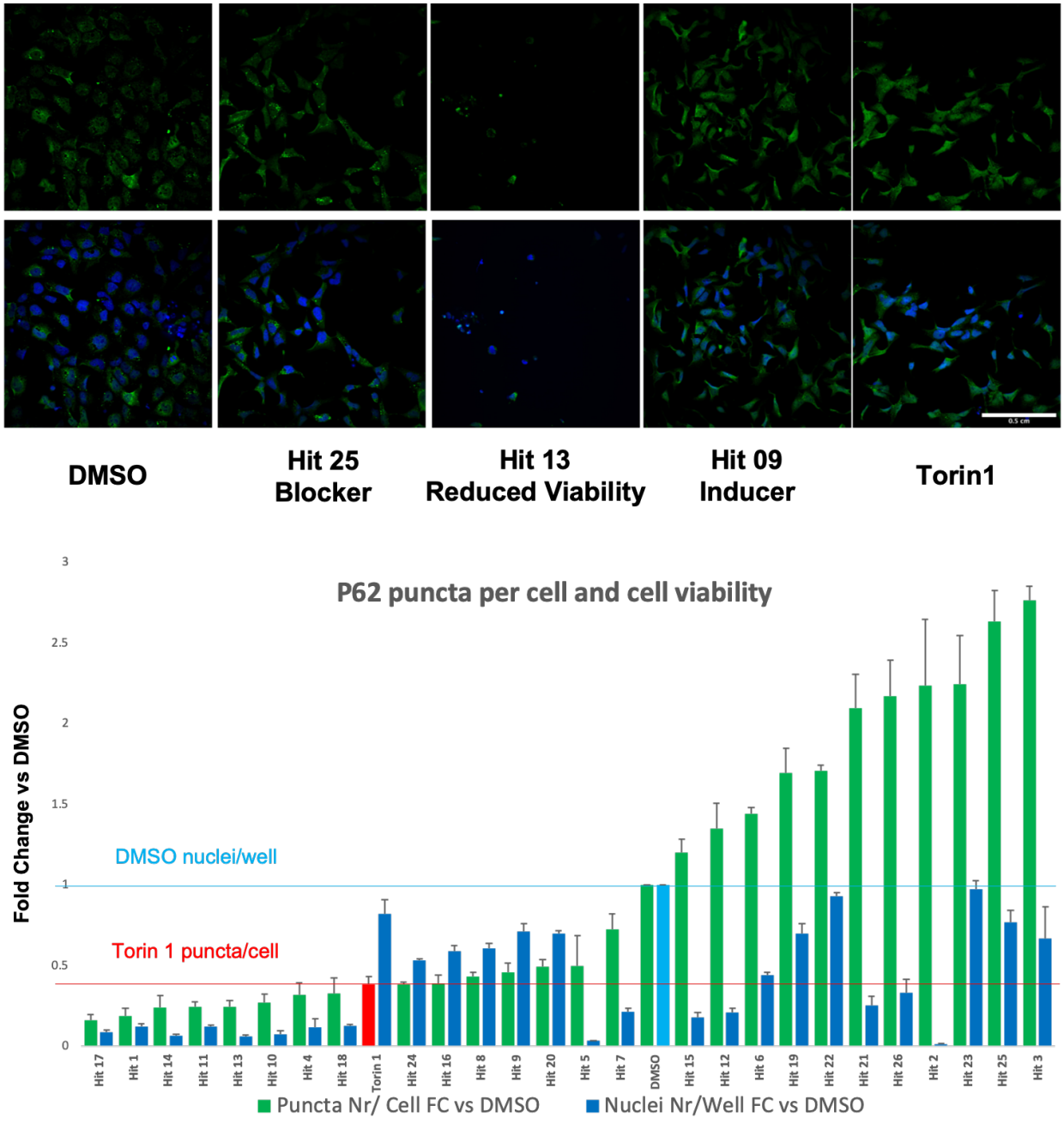

Figure 48. First validation of top Prestwick hits using a p62/SQSTM1 high content imaging-based assay. *The 26 hits from the Prestwick screen with the highest z-scores were used. The hits were tested on Patient 02 (587-02) Day 11 ventral midbrain progenitor cells, as per the actual primary screen. After fixing and staining for p62 puncta (green) and DAPI (blue), images were acquired via the PerkinElmer Opera Phenix microscope, using a 40x water immersion objective (as detailed in the Methods section). Plates were imaged for p62 (488nm) and DAPI (375nm) and representative images from negative controls (DMSO), positive controls (Torin 1), autophagy inducers and blockers, as well as 'false hits' (resulting in reduced cell viability) are shown. The graph depicts cell viability (fold change of nuclei number per well, compared to DMSO; blue bars) and p62 degradation (fold change of p62 puncta per nuclei, compared to DMSO; green bars) for each hit, as well as Torin and DMSO. Several compounds leading to LC3 puncta increase also result in p62 accumulation, hence work as autophagy flux blockers and are not of interest for BPAN. Other compounds have true autophagy flux inducing properties, leading to both LC3 puncta accumulation and also p62 degradation. However, a few of the latter are also associated with reduced cell viability, examined by numbers of nuclei per each well. The compounds of interest, namely the ones with properties similar to Torin 1 and associated with acceptable cell viability, are detailed in Figure 49. n=3 technical replicates for each compound, n=9 for DMSO and Torin 1, as per plate layout detailed in Table 21. Error bars represent Standard Deviation.*

However, 5 compounds resulted in both good levels of cell viability (nuclei numbers per well) and also p62 puncta numbers/ nuclei comparable to Torin 1 (**Figure 49**). Very interestingly, all of these compounds (Proscillaridin A, Digoxin, Lanatoside C, Digoxigenin, Digitoxigenin) belong in the category of cardiac glycosides. Notably, Digoxin at 10 mM was also used in the autophagy inducer screen with no obvious effect in increasing LC3 puncta production. However, this was from a very old batch with possibly reduced or absent efficacy at the time of the novel autophagy activator screen. In any case, the fact that all top 5 hits after the counter screen are cardiac glycosides points towards this category of drugs being of potential further interest in BPAN.

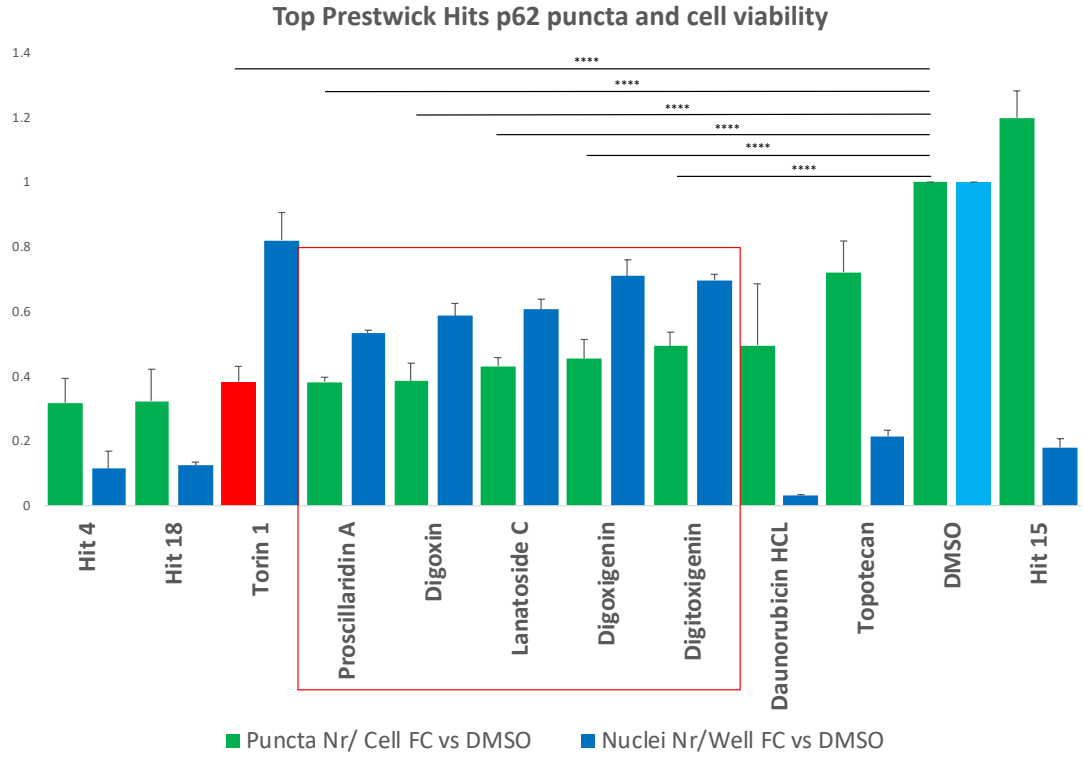

Figure 49. The top 5 Prestwick screen hits after the p62 validation assay belong to the same drug category. *Continuation of Figure 48, zooming into the compounds with properties similar to Torin 1 (inducers of autophagy, leading to LC3 accumulation and p62 degradation) and acceptable cell viability (red square). All 5 compounds belong to the drug category of cardiac glycosides. There is no statistical difference in p62 puncta per cell when comparing Torin 1 and the 5 cardiac glycosides. Additionally, all 5 compounds significantly degrade p62 when compared to DMSO. This is, firstly, of potential therapeutic interest for BPAN, as many cardiac glycosides are FDA approved and have known side effect profiles; hence there is a scope for drug repurposing and relatively quick translation to the clinic. Secondly, cardiac glycosides act on the Na(+)/K(+)-ATPase (Wang, Qiu et al. 2012); thus, it would be interesting to see whether Na(+)/K(+)-ATPase, or other molecules upstream or downstream in its pathway, are mechanistically involved in BPAN pathogenesis or could be appropriate drug targets for the disease. n=3 technical replicates for each compound, n=9 for DMSO and Torin 1, as per plate layout detailed in Table 21. Ordinary one-way Anova was used for statistical analysis. Error bars represent Standard Deviation. Abbreviations:FC= fold change, Nr= number*

Cardiac glycosides, such as digoxin, inhibit the Na+/K+- ATPase pump and, according to some studies, induce autophagy by activating AMPK (and subsequently inhibiting mTOR) and also regulating ERK1/2 signalling (Wang, Qiu et al. 2012). However, other studies have suggested that Na+/K+- ATPase inhibition leads to autophagy inhibition (and protection from autophagy induction-mediated cell death) in rat neurons (Liu, Shoji-Kawata et al. 2013). Cardiac glycosides have also been reported to be strong inhibitors of Hypoxia Inducible Factor 1a (HIF1a), a major protein in the regulation of cellular response to hypoxia (Zhang, Qian et al. 2008). However, hypoxia and HIF1a overexpression can induce autophagy (Lu, Li et al. 2018). Overall, the exact mechanism by which glycosides act in BPAN mDA progenitors is not clear. Nevertheless, they do seem to be potent and non-toxic autophagy inducers in patient Day 11 cells, with the ability to not only increase LC3 puncta production but also reduce p62 accumulation. In any case, the fact that all top hits identified after the Prestwick drug screen and the p62 counter-screen belong to the same drug category is of particular interest and further validation of cardiac glycosides' actions and effects on our model is warranted.

5.4. Discussion

Using the LC3 Day 11 assay, **I performed a drug screen looking for compounds that ameliorate the defective LC3 production in BPAN lines.** I tested two separate small molecule libraries; firstly, a series of novel autophagy activators and also the Prestwick library of 1280 FDA-approved compounds. After the screening, I identified several compound 'hits' that significantly increase LC3 production in both libraries. These hits need to be further validated in our Day 11 and/ or Day 65 neuronal model, looking for reversal of other disease-related phenotypes. However, a first validation of the top hits identified in the Prestwick library has helped identify a category of drugs that might prove of therapeutic benefit for BPAN patients in the future. The p62 assay identified the Prestwick screen hits that were, indeed, autophagy inducers (rather than autophagy flux blockers) but also non-toxic for cells.

I showed that cardiac glycosides (such as digoxin and derivatives) not only significantly enhance autophagy in BPAN but also result in levels of cell viability comparable to the ones seen after treatment with Torin 1, the assay's positive control. The autophagy inducing compound screen also included digoxin, which did not come up as a hit in any of the three tested lines; however, this treatment was from a different source plate and several factors might have plausibly altered that effect. For example, a miscalculation in the stock concentration might have occurred. Additionally, that particular stock digoxin sample was very old, hence possibly degraded in the tubes. To determine this, further testing including liquid chromatography- mass spectrometry would need to be undertaken. Overall, the fact that all top 5 hits identified after the Prestwick screen and the p62 validation assay belong in the cardiac glycoside category is of particular interest and might point towards a specific intracellular mechanism/ drug target through which WDR45 deficiency can be reversed in patient neurons. For example, cardiac glycosides inhibit the Na(+)/K(+)-ATPase (Wang, Qiu et al. 2012); hence the role of Na(+)/K(+)-ATPase in BPAN pathogenesis needs to be examined in future studies, while other molecules involved in its pathway could be appropriate drug targets for the disease. Additionally, the fact that cardiac glycosides are widely used, FDA-approved drugs with

known pharmacokinetics and side effect profiles could potentially provide a faster way to clinical translation and patient benefit through drug repurposing. One of the biggest bottlenecks for inhibiting the translation of digoxin into clinical practice would be that it does not cross the blood brain barrier (Wang, Portbury et al. 2006, Dunn, He et al. 2011). Hence, potentially, 1) modification of these compounds, 2) the use of structurally related compounds with better blood brain barrier permeability (Wang, Portbury et al. 2006) or even 3) intrathecal administration would have to be considered in the future. Moreover, cardiac glycosides are associated with CNS-related side effects in high doses (Greenaway, Abuaisha et al. 1996, Thacker and Sharma 2007). Therefore, further examination of the actions of cardiac glycosides in our model and their effects in autophagy, iron metabolism, cell viability and other relevant pathways is warranted for future studies.

Regarding further steps in hit validation, the development of a relevant high content assay on which to test identified hits for phenotypic reversal of disease-related defects (such as, for example, iron accumulation) was not feasible in this project. I have already described the lack of phenotypic differences seen in the LAMP1 and Alamar Blue assays between Day 11 patients and controls. Additionally, I have mentioned efforts to establish a high content imaging-based assay using primary antibodies against Transferrin and Ferritin Light Chain; however, these assays were not fully optimised and hence not used yet (data not shown). Such a high content assay might have proven useful if the number of hits was too large to validate in a conventional manner. On the other hand, the use of the p62 counter-screen assay as a 'first-pass' hit validation seems to substantially reduce the number of acceptable Prestwick library hits, whereas the 'common hits' increasing LC3 production in all lines in the autophagy inducer screen were not too numerous. Hence, conceivably, an assay such as Western blotting for Ferritin Heavy Chain 1 (which is already developed/ set up), or an ICP-MS assay for intracellular iron detection showing iron accumulation in patient lines, might be efficiently used for secondary hit validation in the future. In fact, during this project I tried to set up such a Day 11 high content-based assay for secondary hit validation. Finally, further work on identified hits should also include dose response curves for the most promising hits in order to

establish the lowest possible concentration that could lead to reversal of the observed phenotypic defects.

6. Discussion and Future Work

During my PhD I studied BPAN, a rare X-linked monogenic neurodegenerative condition of childhood onset. Having already met several patients with the condition during my clinical training, I was struck by 1) how severe, relentless and effectively life limiting BPAN is for most patients, 2) the poor understanding of molecular pathways leading to neurological dysfunction and, also, 3) the absence of effective, targeted treatments for the disorder. In order to address these issues, I created a human-derived, physiologically relevant, dopaminergic neuronal cell model of the disease. Studying this model, I showed that BPAN neurons recapitulate various patient-related phenotypes and elucidated several affected intracellular mechanisms that might contribute to downstream striatonigral degeneration. I also used this model as a platform for a drug screen in order to identify novel therapies for my patients. Testing two separate compound libraries, I identified hits that reverse disease-related phenotypes *in vitro* and have the potential to be translated to the clinic in the future, following further validation. Despite the limitations of this study and future work that needs to be completed, my work shows the creation of a comprehensive, robust model for studying BPAN and hopefully lays the foundations for future tangible benefits for affected children, both through better understanding of the disease and the development of new, improved and targeted treatments.

BPAN manifests clinically as a devastating brain iron accumulation condition. BPAN is one of the latest described subtypes of Neurodegeneration with Brain Iron Accumulation (Gregory and Hayflick 2014, Gregory, Kurian et al. 2016). Although already identified as a separate clinical entity (and initially labelled as 'Static Encephalopathy with Neurodegeneration in Adulthood, SENDA' due to its two-phased clinical course), *WDR45* (a gene with conserved function in early autophagy) was only identified as the causative gene in late 2012/ early 2013 (Haack, Hogarth et al. 2012, Saitsu, Nishimura et al. 2013). Unfortunately, BPAN is associated with significant morbidity and increased risk of mortality. Although there is a phenotypic spectrum of disease, most patients are very severely affected; they manifest neurodevelopmental problems (such as learning difficulties, epilepsy, autistic-like features and disordered sleep) early on in life and subsequently develop neurological

regression, dementia and a prominent movement disorder including dystonia and parkinsonism. Even if they previously had achieved independent walking, patients eventually become wheelchair or bed-bound and complications secondary to the dementia and the movement disorder ensue, such as dysphagia, poor nutrition and aspiration pneumonias or spinal deformities and restrictive lung disease. Ultimately, this deterioration leads to increased disease burden and early death. Brain imaging and neuropathological studies show abnormal levels of iron accumulation in BPAN, mainly in the substantia nigra but also in other brain areas. They also demonstrate that the substantia nigra is the most affected brain area, with loss of dopaminergic neurons and reactive astrogliosis (Hayflick, Kruer et al. 2013, Paudel, Li et al. 2015).

The poorly understood disease mechanisms and lack of effective treatments in BPAN constituted an unmet clinical need and a priority area for translational research. Firstly, WDR45, also known as WIPI4, has a conserved role in the early stages of autophagosome formation, as demonstrated by several studies (Lu, Yang et al. 2011, Saitsu, Nishimura et al. 2013, Bakula, Muller et al. 2017). Moreover, iron accumulation is a hallmark of BPAN; although the whole brain is affected, accumulation of iron and neuronal loss are more pronounced in the dopaminergic neuron-rich substantia nigra compared to other areas. However, the mechanisms linking autophagy, iron accumulation and striatonigral neurodegeneration are not well elucidated. Also importantly, while WDR45 is ubiquitously expressed (with high levels of expression in skeletal muscle), the symptoms of disease are, seemingly, purely neurological. Plausible explanations for this might be that WDR45/WIPI4 has a very important role in neuronal homeostasis, and/ or that the protein functions in a tissue-specific manner, with other proteins compensating for the deficiency of WDR45 outside the CNS (Saitsu, Nishimura et al. 2013). On the other hand, WDR45 deficiency-related phenotypes might just be more easily discernible in the brain, which largely consists of post-mitotic, relatively vulnerable cells. Indeed, several studies (including mine) have shown WDR45/WIPI4 deficiency-related cellular phenotypes in human lymphocytes, fibroblasts or transformed lines (Saitsu, Nishimura et al. 2013, Bakula, Muller et al. 2017, Seibler, Burbulla et al. 2018). Therefore, plausibly,

these phenotypic defects might reflect clinical phenotypes that are masked *in vivo* because 1) they are milder compared to the CNS-related symptoms and signs and/or because 2) patients pass away (due to neurological deterioration) before they have a chance to manifest clinically. This is also seen in other 'primarily neurological' disorders, such as the neuronal ceroid lipofuscinoses or other lysosomal storage disorders, where most or all tissues are affected but the symptomatology and complications arise prominently from the CNS (Platt, Boland et al. 2012, Johnson, Cain et al. 2019). In any case, all the above demonstrate the sub-optimal understanding of disease mechanisms in BPAN. Another major, and more immediately tangible, limitation is the current lack of available effective treatments for the disease. Unfortunately, management options for affected patients are not curative but only focus on symptom control and prevention of complications. Despite the best efforts of large and experienced multidisciplinary teams, management interventions often result in very little or no clinical benefit and, frequently, disease progression and early death cannot be halted. Hence, my project was conceived, set up and carried forward exactly in order to address these two major issues that constituted a translational research priority. Namely, the project aims were to create a BPAN disease model that would be used to 1) increase understanding of pathophysiological mechanisms leading to disease 2) identify drugs that could ameliorate/ reverse disease-related phenotypes in vitro, that could subsequently be developed into novel, targeted and effective treatments with substantial clinical benefit affected individuals.

A human-derived mDA neuronal model was optimal in order to appropriately address the aims of my project. A number of models have already been described for studying BPAN, and all can be perceived to have advantages and disadvantages (Lu, Yang et al. 2011, Zhao, Sun et al. 2015, Bakula, Muller et al. 2017, Seibler, Burbulla et al. 2018). For my project, the considerations for the choice of model are summarised as follows: firstly, a neuronal model of the disease would be ideal, since BPAN seems to exclusively affect the CNS. Secondly, since the mDA-rich substantia nigra is the most affected brain area and parkinsonism is a very prominent disease feature, studying dopaminergic neurons (and elucidating affected molecular pathways in this cell subtype) is highly

relevant from a pathophysiological aspect. Thirdly, a patient-derived model was preferable, as animal models often fail to recapitulate human disease-related phenotypes; for example, in WDR45 CNS-specific knockout mice there is lack of iron accumulation (Zhao, Sun et al. 2015). Additionally, fundamental differences in the neurobiology of humans when compared to animals might mean that any drug testing performed might not be relevant to patients in the clinic (Scannell, Blanckley et al. 2012). Finally, a cellular, as opposed to an animal, model was required in order to perform large-scale applications such as the proposed drug screen. For all the above reasons, I chose to create an iPSC-based mDA neuronal model of BPAN. The use of iPSCs has provided a way around the historical problem of tissue unavailability for research in neurological disorders (Barral and Kurian 2016). An iPSC-based model of BPAN allowed the study of the neuronal subtypes of interest that had also derived from patients with known genetic backgrounds and clinical phenotypes. Additionally, due to their capacity for renewal and proliferation, iPSCs enabled the downstream drug screen that was a main focus of our project.

Afterwards, I aimed to eliminate or address factors that could influence iPSC-based disease modelling or mask disease-related phenotypes. There were several caveats of iPSC-based models that I addressed such as the inherent issue of iPSC line variability (for which I used multiple lines including isogenic controls) and the XCI (for which I established that only the mutated WDR45 allele was expressed in female BPAN lines). After addressing the above and stringently characterising all iPSC lines, I was confident that my model was robust enough to ensure accurate and reproducible results in downstream experiments.

I have shown that all BPAN and control iPSCs can be successfully differentiated, firstly into typical mDA neuronal progenitors and subsequently into mature day 65 mDA neurons that show characteristic mDA identities. Importantly, the differentiation process in BPAN lines was equally effective to the ones in the controls, both at progenitor and mature stage (as reflected by comparable LMX1A/ FOXA2 and TH/DAPI ratios, respectively). Overall, the differentiation efficiency

was similar to ones reported in other studies (Kirkeby, Grealish et al. 2012). As mentioned above, when compared to control lines, patient-derived Day 65 neurons in basal conditions show no evidence of spontaneous neurodegeneration (in terms of TH/DAPI ratios) detectable via immunofluorescence. Moreover, all Day 65 neurons have upregulation in gene expression of several mature mDA-related markers (*TH, SNCA, NURR1, DAT*), as well as *MAPT*, as detected through qRT PCR. Again, there is no obvious difference between patients and controls when comparing the expression profiles of these markers, although there was a trend for MAPT to be higher in Patients 02 and 03 when compared to the CRISPR-generated isogenic controls (Patient 02 Corrected and Patient 03 Corrected, respectively). These results a) are in line with the clinical observation that patients present with early-onset neurodevelopmental issues but manifest neurodegeneration later on in life and, importantly, b) suggest that applying stress to Day 65 neurons in order to elicit neurodegenerative phenotypes *in vitro* might be an important experiment to consider in future studies.

Importantly, I have shown that BPAN mDA neurons recapitulate a number of key disease-related features. Firstly, this is a model of WDR45 deficiency, with absence of protein expression in patient neurons. Additionally, several intracellular pathways were shown to be defective in our model via RNAseq experiments, including neuronal homeostasis (neurogenesis, neuroblast division and neurodevelopment) and iron metabolism. Iron levels (e.g. via Inductively coupled plasma mass spectrometry, ICP-MS) were not directly measured in patient and control neurons and this is an important experiment to be considered in the future. However, apart from the RNAseq, western blotting also showed indirect evidence of impaired iron homeostasis in the form of ferritin accumulation in BPAN neurons; importantly, this was reversed after CRISPR-mediated mutation correction in two patient lines. In summary, the model I generated recapitulates several disease-related profiles and, therefore, can be useful for downstream applications such as a drug screen to identify potential new therapies.

I have also shown that BPAN neuronal lines exhibit defective autophagy. WDR45 is considered a key regulator of autophagy, required for early stages of autophagosome formation (Proikas-Cezanne, Takacs et al. 2015, Bakula, Muller et al. 2017). To test autophagy in my model, I designed a high content imaging-based assay that shows reduced LC3 puncta production (representing autophagosomes) in patient Day 11 ventral midbrain progenitors when compared to controls. Very importantly, this phenotypic defect is completely reversed after CRISPR/Cas9 mutation correction in both 'isogenic controls'. Moreover, this defect is reversible when cells are treated with autophagy inducers such as Torin 1. Additionally, the fact that this defect can be reversed with autophagy inducers [and might even lead to reduction of iron accumulation according to recent studies (Seibler, Burbulla et al. 2018)] could have therapeutic implications for patients. The LC3 assay was eventually used as the primary drug screening assay in downstream experiments, as the phenotypic defect was reproducible and also observed more prominently in basal (DMSO-treated) conditions.

Other phenotypic assays I developed showed no obvious differences between patient and control lines. Firstly, there was no evidence of lysosomal dysfunction in patient lines (examined by immunofluorescence and western blotting using anti-LAMP1 antibodies); however, RNAseq data showed that *LAMP3* and *LAMP5* were downregulated in BPAN neurons, suggesting that the lysosomal function might indeed be perturbed but in a more cell-specific manner. Secondly, western blotting for LC3-II, the lipidated, autophagosomal membrane-bound form of LC3, also failed to show any differences between patient and control lines. Again, this experiment is incomplete and the CRISPR-corrected lines also need to be tested in future experiments for more robust conclusions. Thirdly, the Alamar Blue cell viability assay on Day 11 ventral midbrain progenitors did not show any phenotypic defects in BPAN lines but, as discussed in the relevant results section, it is unclear whether the correct cell line, or even the correct assay or stressors, were used. Overall, more experiments are needed to further investigate the cell viability, lysosomal function and autophagy flux in 'mature' BPAN neurons.

After establishing the disease model and developing high content imaging-based phenotypic assays, I performed a drug screen with the ultimate aim of identifying potential novel and effective treatments for BPAN patients. Using the LC3 Day 11 assay, I tested two separate small molecule libraries; firstly, one mainly consisting of novel autophagy activators and also the Prestwick library of 1280 FDA-approved compounds. After the screening, several compound 'hits' that significantly increase LC3 production were identified in both libraries. These hits need to be further validated in our Day 11 and/ or Day 65 neuronal model, looking for reversal of other disease-related phenotypes. For example, it would be interesting to see if the most promising hits also result in reversal of iron accumulation, which could be measured directly (e.g. via ICP-MS) or indirectly (e.g. through an immunofluorescence- or western blot-based assay examining ferritin staining).

A first validation of the top hits identified in the Prestwick library has helped identify a category of drugs that might prove of therapeutic benefit for BPAN patients in the future. The p62 assay was designed to examine if the Prestwick screen hits were, indeed, 1) autophagy inducers (rather than autophagy flux blockers) and also 2) not toxic for cells. Using the p62 counter-screen assay on the 26 top-scoring hits in the Prestwick screen, I showed that cardiac glycosides (such as digoxin and derivatives) not only significantly enhance autophagy in BPAN but also result in levels of cell viability comparable to the ones seen after treatment with Torin 1, the assay's positive control. The fact that all top 5 hits identified after the Prestwick screen and the p62 validation assay belong in the cardiac glycoside category is of particular interest and might point towards a specific intracellular mechanism/ drug target through which WDR45 deficiency can be reversed in patient neurons. Therefore, further examination of the actions of cardiac glycosides in our model and their effects in autophagy, iron metabolism, cell viability and other relevant pathways is warranted for future studies. Hopefully, assays such as the already developed Ferritin Heavy Chain western blot, or even ICP-MS studies on Day 65 neurons, will prove to be robust enough to be used for second hit validation. Overall, I hope that the top hits identified from this work will also be tested in other preclinical models and eventually onto patients, with the ultimate aim of clinical translation,

amelioration or reversal of BPAN-related symptoms and signs, and tangible quality of life improvements for my patients.

There are a number of limitations to this work. Firstly, I used 7 patient and age-matched control lines in total, including 2 CRISPR-generated isogenic controls; however, the CRISPR/Cas9 genome editing took place during the latter parts of the project and lines Patient 02 Corrected and Patient 03 Corrected only became available to me in the final 6 months of the project. Hence, I did not have time to perform all assays (e.g. Western Blotting for LAMP1 or LC3 levels or, more importantly, RNAseq) using all 7 lines, and this needs to be completed in future studies.

Secondly, I did not expose Day 65 mDA neurons to stressful conditions in order to make the neurodegenerative processes governing BPAN more discernible *in vitro*. Instead, in the time constraints of my PhD, I chose to expose the Day 11 progenitors to certain potentially stressful conditions. Although the rational/ intention was to develop another high content assay to be used for secondary hit validation, Day 11 progenitors are still mitotic and likely less vulnerable to stressors than mature mDA neurons, hence possibly not the right cell type to stress in order to elicit neurodegeneration-related phenotypic defects in patient lines. Hence, more relevant experiments at mature mDA neuronal stage (and the examination of more phenotypic readouts) are warranted in the future in order to elucidate mechanisms leading to striatonigral degeneration in BPAN.

Thirdly, I generated RNAseq and Western Blotting data which indirectly indicate that iron metabolism is disturbed in BPAN and that iron levels are probably elevated in patient neurons versus controls. However, a definitive, direct measurement of intracellular and/ or extracellular iron levels was not performed. Future work will need to focus on setting up such assays or even establishing collaborations with ICP-MS groups, as ICP-MS is a reliable way of measuring metals including iron. Also importantly, if such an assay showed the expected phenotype of iron accumulation in patient lines, it could serve as a robust secondary validation assay for hits identified in our drug screen.

Finally, the model I generated is 2-dimensional. This was mainly for two reasons: firstly, at the start of the project, protocols for generating MLOs had not yet been established. Secondly, the drug screen was a main focus of my work and, at least at the start of the project (but even now), the use of iPSC-derived 2-dimensional models for drug screening is much better established. Nevertheless, this is a model with relatively limited network connectivity and cell types. Hence, future development or three-dimensional BPAN organoid models (both MLO but also CLO, as all brain areas are affected) may allow development of a more complex system that will allow a more robust study of WDR45 deficiency.

In Conclusion, my PhD-related work includes the successful generation of a patient-derived iPSC-based mDA neuronal model of BPAN, which recapitulates some key features of WDR45 deficiency and provides insights into the downstream affected pathways leading to neuronal dysfunction and striatonigral degeneration. Moreover, the use of this model as a platform for a high content imaging-based drug screen has identified several compound hits that 1) are in need of further validation but 2) have the potential to lead to the development of new, targeted and more effective treatments for this devastating, life-limiting condition. Overall, I am confident that this work provides a solid basis for future BPAN-related basic science and translational studies; I also truly hope that my efforts will contribute towards the ultimate goal of, one day, actually curing BPAN.

6. REFERENCES

Abidi, A., C. Mignon-Ravix, P. Cacciagli, N. Girard, M. Milh and L. Villard (2016). "Early-onset epileptic encephalopathy as the initial clinical presentation of WDR45 deletion in a male patient." Eur J Hum Genet **24**(4): 615-618.

Abidi, A., C. Mignon-Ravix, P. Cacciagli, N. Girard, M. Milh and L. Villard (2016). "Early-onset epileptic encephalopathy as the initial clinical presentation of WDR45 deletion in a male patient." **24**(4): 615-618.

Ackermann, A. M. and M. A. Levine (2017). "Compound heterozygous mutations in COL1A1 associated with an atypical form of type I osteogenesis imperfecta." Am J Med Genet A **173**(7): 1907-1912.

Agrotis, A. and R. Ketteler (2015). "A new age in functional genomics using CRISPR/Cas9 in arrayed library screening." Front Genet **6**: 300.

Agrotis, A., N. Pengo, J. J. Burden and R. Ketteler (2019). "Redundancy of human ATG4 protease isoforms in autophagy and LC3/GABARAP processing revealed in cells." Autophagy **15**(6): 976-997.

Agrotis, A., L. von Chamier, H. Oliver, K. Kiso, T. Singh and R. Ketteler (2019). "Human ATG4 autophagy proteases counteract attachment of ubiquitin-like LC3/GABARAP proteins to other cellular proteins." J Biol Chem **294**(34): 12610-12621.

Akizu, N., V. Cantagrel, M. S. Zaki, L. Al-Gazali, X. Wang, R. O. Rosti, E. Dikoglu, A. B. Gelot, B. Rosti, K. K. Vaux, E. M. Scott, J. L. Silhavy, J. Schroth, B. Copeland, A. E. Schaffer, P. L. Gordts, J. D. Esko, M. D. Buschman, S. J. Field, G. Napolitano, G. M. Abdel-Salam, R. K. Ozgul, M. S. Sagiroglu, M. Azam, S. Ismail, M. Aglan, L. Selim, I. G. Mahmoud, S. Abdel-Hadi, A. E. Badawy, A. A. Sadek, F. Mojahedi, H. Kayserili, A. Masri, L. Bastaki, S. Temtamy, U. Muller, I. Desguerre, J. L. Casanova, A. Dursun, M. Gunel, S. B. Gabriel, P. de Lonlay and J. G. Gleeson (2015). "Biallelic mutations in SNX14 cause a syndromic form of cerebellar atrophy and lysosome-autophagosome dysfunction." Nat Genet **47**(5): 528-534.

Alessandrini, F., L. Pezze and Y. Ciribilli (2017). "LAMPs: Shedding light on cancer biology." Semin Oncol **44**(4): 239-253.

Ang, S. L. and J. Rossant (1994). "HNF-3 beta is essential for node and notochord formation in mouse development." Cell **78**(4): 561-574.

Arenas, E., M. Denham and J. C. Villaescusa (2015). "How to make a midbrain dopaminergic neuron." Development **142**(11): 1918-1936.

Aruga, J. (2004). "The role of Zic genes in neural development." Mol Cell Neurosci **26**(2): 205-221.

Backman, C. M., L. Shan, Y. Zhang, B. J. Hoffer and A. C. Tomac (2007). "Alterations in prodynorphin, proenkephalin, and GAD67 mRNA levels in the aged human putamen: correlation with Parkinson's disease." J Neurosci Res **85**(4): 798-804.

Bahi-Buisson, N., J. Nectoux, B. Girard, H. Van Esch, T. De Ravel, N. Boddaert, P. Plouin, M. Rio, Y. Fichou, J. Chelly and T. Bienvenu (2010). "Revisiting the phenotype associated with FOXG1 mutations: two novel cases of congenital Rett variant." Neurogenetics **11**(2): 241-249.

Bahi-Buisson, N., J. Nectoux, H. Rosas-Vargas, M. Milh, N. Boddaert, B. Girard, C. Cances, D. Ville, A. Afenjar, M. Rio, D. Heron, M. A. N'Guyen Morel, A. Arzimanoglou, C. Philippe, P. Jonveaux, J. Chelly and T. Bienvenu (2008). "Key clinical features to identify girls with CDKL5 mutations." Brain **131**(Pt 10): 2647-2661.

Bakula, D., A. J. Muller, T. Zuleger, Z. Takacs, M. Franz-Wachtel, A. K. Thost, D. Brigger and M. P. Tschan (2017). "WIPI3 and WIPI4 beta-propellers are scaffolds for LKB1-AMPK-TSC signalling circuits in the control of autophagy." **8**: 15637.

Bar, S., L. R. Seaton, U. Weissbein, T. Eldar-Geva and N. Benvenisty (2019). "Global Characterization of X Chromosome Inactivation in Human Pluripotent Stem Cells." Cell Rep **27**(1): 20-29.e23.

Barral, S. and M. A. Kurian (2016). "Utility of Induced Pluripotent Stem Cells for the Study and Treatment of Genetic Diseases: Focus on Childhood Neurological Disorders." Front Mol Neurosci **9**: 78.

Barrangou, R., C. Fremaux, H. Deveau, M. Richards, P. Boyaval, S. Moineau, D. A. Romero and P. Horvath (2007). "CRISPR provides acquired resistance against viruses in prokaryotes." Science **315**(5819): 1709-1712.
Barrett, R., L. Ornelas, N. Yeager, B. Mandefro, A. Sahabian, L. Lenaeus, S. R. Targan, C. N. Svendsen and D. Sareen (2014). "Reliable generation of induced pluripotent stem cells from human lymphoblastoid cell lines." Stem Cells Transl Med **3**(12): 1429-1434.
Baskaran, S., M. J. Ragusa, E. Boura and J. H. Hurley (2012). "Two-site recognition of phosphatidylinositol 3-phosphate by PROPPINs in autophagy." Mol Cell **47**(3): 339-348.
Basson, M. A., D. Echevarria, C. P. Ahn, A. Sudarov, A. L. Joyner, I. J. Mason, S. Martinez and G. R. Martin (2008). "Specific regions within the embryonic midbrain and cerebellum require different levels of FGF signaling during development." Development **135**(5): 889-898.
Baud, A., W. E. Heywood, D. Little, P. Gissen and K. Mills (2019). "Preparation of iPSCs for Targeted Proteomic Analysis." Methods Mol Biol **1994**: 131-139.
Beirowski, B., A. Nogradi, E. Babetto, G. Garcia-Alias and M. P. Coleman (2010). "Mechanisms of axonal spheroid formation in central nervous system Wallerian degeneration." J Neuropathol Exp Neurol **69**(5): 455-472.
Bento, C. F., M. Renna, G. Ghislat, C. Puri, A. Ashkenazi, M. Vicinanza, F. M. Menzies and D. C. Rubinsztein (2016). "Mammalian Autophagy: How Does It Work?" Annu Rev Biochem **85**: 685-713.
Berger, K., M. M. Breteler, C. Helmer, D. Inzitari, L. Fratiglioni, C. Trenkwalder, A. Hofman and L. J. Launer (2000). "Prognosis with Parkinson's disease in europe: A collaborative study of population-based cohorts. Neurologic Diseases in the Elderly Research Group." Neurology **54**(11 Suppl 5): S24-27.
Bock, C., E. Kiskinis, G. Verstappen, H. Gu, G. Boulting, Z. D. Smith, M. Ziller, G. F. Croft, M. W. Amoroso, D. H. Oakley, A. Gnirke, K. Eggan and A. Meissner (2011). "Reference Maps of human ES and iPS cell variation enable high-throughput characterization of pluripotent cell lines." Cell **144**(3): 439-452.
Bodea, G. O., J. H. Spille, P. Abe, A. S. Andersson, A. Acker-Palmer, R. Stumm, U. Kubitscheck and S. Blaess (2014). "Reelin and CXCL12 regulate distinct migratory behaviors during the development of the dopaminergic system." Development **141**(3): 661-673.
Bolam, J. P. and E. K. Pissadaki (2012). "Living on the edge with too many mouths to feed: why dopamine neurons die." Mov Disord **27**(12): 1478-1483.
Brichta, L. and P. Greengard (2014). "Molecular determinants of selective dopaminergic vulnerability in Parkinson's disease: an update." Front Neuroanat **8**: 152.
Briscoe, J. and J. Ericson (1999). "The specification of neuronal identity by graded Sonic Hedgehog signalling." Semin Cell Dev Biol **10**(3): 353-362.
Broccoli, V., E. Boncinelli and W. Wurst (1999). "The caudal limit of Otx2 expression positions the isthmic organizer." Nature **401**(6749): 164-168.
Brownjohn, P. W., J. Smith, E. Portelius, L. Serneels, H. Kvartsberg, B. De Strooper, K. Blennow, H. Zetterberg and F. J. Livesey (2017). "Phenotypic Screening Identifies Modulators of Amyloid Precursor Protein Processing in Human Stem Cell Models of Alzheimer's Disease." Stem Cell Reports **8**(4): 870-882.
Burkhardt, M. F., F. J. Martinez, S. Wright, C. Ramos, D. Volfson, M. Mason, J. Garnes, V. Dang, J. Lievers, U. Shoukat-Mumtaz, R. Martinez, H. Gai, R. Blake, E. Vaisberg, M. Grskovic, C. Johnson, S. Irion, J. Bright, B. Cooper, L. Nguyen, I. Griswold-Prenner and A. Javaherian (2013). "A cellular model for sporadic ALS using patient-derived induced pluripotent stem cells." Mol Cell Neurosci **56**: 355-364.
Byrne, S., L. Jansen, U. K.-I. JM, A. Siddiqui, H. G. Lidov, I. Bodi, L. Smith, R. Mein, T. Cullup, C. Dionisi-Vici, L. Al-Gazali, M. Al-Owain, Z. Bruwer, K. Al Thihli, R. El-Garhy, K. M. Flanigan, K. Manickam, E. Zmuda, W. Banks, R. Gershoni-Baruch, H. Mandel, E. Dagan, A. Raas-Rothschild, H. Barash, F. Filloux, D. Creel, M. Harris, A. Hamosh, S. Kolker, D. Ebrahimi-Fakhari, G. F. Hoffmann, D. Manchester, P. J. Boyer, A. Y. Manzur, C. M. Lourenco, D. T. Pilz, A. Kamath, P. Prabhakar, V. K. Rao, R. C. Rogers, M.

M. Ryan, N. J. Brown, C. A. McLean, E. Said, U. Schara, A. Stein, C. Sewry, L. Travan, F. A. Wijburg, M. Zenker, S. Mohammed, M. Fanto, M. Gautel and H. Jungbluth (2016). "EPG5-related Vici syndrome: a paradigm of neurodevelopmental disorders with defective autophagy." Brain **139**(Pt 3): 765-781.
Caccamo, A., S. Majumder, A. Richardson, R. Strong and S. Oddo (2010). "Molecular interplay between mammalian target of rapamycin (mTOR), amyloid-beta, and Tau: effects on cognitive impairments." J Biol Chem **285**(17): 13107-13120.
Caiazzo, M., M. T. Dell'Anno, E. Dvoretskova, D. Lazarevic, S. Taverna, D. Leo, T. D. Sotnikova, A. Menegon, P. Roncaglia, G. Colciago, G. Russo, P. Carninci, G. Pezzoli, R. R. Gainetdinov, S. Gustincich, A. Dityatev and V. Broccoli (2011). "Direct generation of functional dopaminergic neurons from mouse and human fibroblasts." Nature **476**(7359): 224-227.
Caraballo, R. H., R. Aldao Mdel and P. Cachia (2011). "Benign childhood seizure susceptibility syndrome: three case reports." Epileptic Disord **13**(2): 133-139.
Carvill, G. L., A. Liu, S. Mandelstam, A. Schneider, A. Lacroix, M. Zemel, J. M. McMahon, L. Bello-Espinosa, M. Mackay, G. Wallace, M. Waak, J. Zhang, X. Yang, S. Malone, Y. H. Zhang, H. C. Mefford and I. E. Scheffer (2018). "Severe infantile onset developmental and epileptic encephalopathy caused by mutations in autophagy gene WDR45." Epilepsia **59**(1): e5-e13.
Cheng, L., Q. Lei, C. Yin, H. Y. Wang, K. Jin and M. Xiang (2017). "Generation of Urine Cell-Derived Non-integrative Human iPSCs and iNSCs: A Step-by-Step Optimized Protocol." Front Mol Neurosci **10**: 348.
Choi, A. M., S. W. Ryter and B. Levine (2013). "Autophagy in human health and disease." N Engl J Med **368**(7): 651-662.
Clardy, S. L., X. Wang, W. Zhao, W. Liu, G. A. Chase, J. L. Beard, B. True Felt and J. R. Connor (2006). "Acute and chronic effects of developmental iron deficiency on mRNA expression patterns in the brain." J Neural Transm Suppl(71): 173-196.
Comertpay, S., S. Pastorino, M. Tanji, R. Mezzapelle, O. Strianese, A. Napolitano, F. Baumann, T. Weigel, J. Friedberg, P. Sugarbaker, T. Krausz, E. Wang, A. Powers, G. Gaudino, S. Kanodia, H. I. Pass, B. L. Parsons, H. Yang and M. Carbone (2014). "Evaluation of clonal origin of malignant mesothelioma." J Transl Med **12**: 301.
Corti, S., M. Nizzardo, C. Simone, M. Falcone, M. Nardini, D. Ronchi, C. Donadoni, S. Salani, G. Riboldi, F. Magri, G. Menozzi, C. Bonaglia, F. Rizzo, N. Bresolin and G. P. Comi (2012). "Genetic correction of human induced pluripotent stem cells from patients with spinal muscular atrophy." Sci Transl Med **4**(165): 165ra162.
Cozzi, A., D. I. Orellana, P. Santambrogio, A. Rubio, C. Cancellieri, S. Giannelli, M. Ripamonti, S. Taverna, G. Di Lullo, E. Rovida, M. Ferrari, G. L. Forni, C. Fiorillo, V. Broccoli and S. Levi (2019). "Stem Cell Modeling of Neuroferritinopathy Reveals Iron as a Determinant of Senescence and Ferroptosis during Neuronal Aging." Stem Cell Reports **13**(5): 832-846.
Crow, Y. J. and N. Manel (2015). "Aicardi-Goutieres syndrome and the type I interferonopathies." Nat Rev Immunol **15**(7): 429-440.
Cuervo, A. M., L. Stefanis, R. Fredenburg, P. T. Lansbury and D. Sulzer (2004). "Impaired degradation of mutant alpha-synuclein by chaperone-mediated autophagy." Science **305**(5688): 1292-1295.
Decressac, M., B. Mattsson, P. Weikop, M. Lundblad, J. Jakobsson and A. Bjorklund (2013). "TFEB-mediated autophagy rescues midbrain dopamine neurons from alpha-synuclein toxicity." Proc Natl Acad Sci U S A **110**(19): E1817-1826.
Defays, A., A. David, A. de Gassart, F. De Angelis Rigotti, T. Wenger, V. Camossetto, P. Brousset, T. Petrella, M. Dalod, E. Gatti and P. Pierre (2011). "BAD-LAMP is a novel biomarker of nonactivated human plasmacytoid dendritic cells." Blood **118**(3): 609-617.
Dell'Anno, M. T., M. Caiazzo, D. Leo, E. Dvoretskova, L. Medrihan, G. Colasante, S. Giannelli, I. Theka, G. Russo, L. Mus, G. Pezzoli, R. R. Gainetdinov, F. Benfenati, S. Taverna, A. Dityatev and V. Broccoli (2014). "Remote control of induced dopaminergic neurons in parkinsonian rats." J Clin Invest **124**(7): 3215-3229.

Desai, M., R. Fang and J. Sun (2015). "The role of autophagy in microbial infection and immunity." Immunotargets Ther **4**: 13-26.
Devine, M. J., M. Ryten, P. Vodicka, A. J. Thomson, T. Burdon, H. Houlden, F. Cavaleri, M. Nagano, N. J. Drummond, J. W. Taanman, A. H. Schapira, K. Gwinn, J. Hardy, P. A. Lewis and T. Kunath (2011). "Parkinson's disease induced pluripotent stem cells with triplication of the alpha-synuclein locus." Nat Commun **2**: 440.
Disteche, C. M. and J. B. Berletch (2015). "X-chromosome inactivation and escape." J Genet **94**(4): 591-599.
Dominguez-Bautista, J. A., M. Klinkenberg, N. Brehm, M. Subramaniam, B. Kern, J. Roeper, G. Auburger and M. Jendrach (2015). "Loss of lysosome-associated membrane protein 3 (LAMP3) enhances cellular vulnerability against proteasomal inhibition." Eur J Cell Biol **94**(3-4): 148-161.
Dunn, D. E., D. N. He, P. Yang, M. Johansen, R. A. Newman and D. C. Lo (2011). "In vitro and in vivo neuroprotective activity of the cardiac glycoside oleandrin from Nerium oleander in brain slice-based stroke models." J Neurochem **119**(4): 805-814.
Ebrahimi-Fakhari, D., A. Saffari, L. Wahlster, J. Lu, S. Byrne, G. F. Hoffmann, H. Jungbluth and M. Sahin (2016). "Congenital disorders of autophagy: an emerging novel class of inborn errors of neuro-metabolism." Brain **139**(Pt 2): 317-337.
Ebrahimi-Fakhari, D., L. Wahlster, G. F. Hoffmann and S. Kolker (2014). "Emerging role of autophagy in pediatric neurodegenerative and neurometabolic diseases." Pediatr Res **75**(1-2): 217-226.
Esner, M., F. Meyenhofer and M. Bickle (2018). "Live-Cell High Content Screening in Drug Development." Methods Mol Biol **1683**: 149-164.
Forozan, F., R. Karhu, J. Kononen, A. Kallioniemi and O. P. Kallioniemi (1997). "Genome screening by comparative genomic hybridization." Trends Genet **13**(10): 405-409.
Fu, X. H., C. Z. Chen, Y. Wang, Y. X. Peng, W. H. Wang, B. Yuan, Y. Gao, H. Jiang and J. B. Zhang (2019). "COL1A1 affects apoptosis by regulating oxidative stress and autophagy in bovine cumulus cells." Theriogenology **139**: 81-89.
Fujikake, N., M. Shin and S. Shimizu (2018). "Association Between Autophagy and Neurodegenerative Diseases." Front Neurosci **12**: 255.
Fujita, N., T. Itoh, H. Omori, M. Fukuda, T. Noda and T. Yoshimori (2008). "The Atg16L complex specifies the site of LC3 lipidation for membrane biogenesis in autophagy." Mol Biol Cell **19**(5): 2092-2100.
Fukasawa, J. T., R. W. de Labio, L. T. Rasmussen, L. C. de Oliveira, E. Chen, J. Villares, G. Tureck, C. S. M. de Arruda and S. L. M. Payao (2018). "CDK5 and MAPT Gene Expression in Alzheimer's Disease Brain Samples." Curr Alzheimer Res **15**(2): 182-186.
Funderburk, S. F., Q. J. Wang and Z. Yue (2010). "The Beclin 1-VPS34 complex--at the crossroads of autophagy and beyond." Trends Cell Biol **20**(6): 355-362.
Fusaki, N., H. Ban, A. Nishiyama, K. Saeki and M. Hasegawa (2009). "Efficient induction of transgene-free human pluripotent stem cells using a vector based on Sendai virus, an RNA virus that does not integrate into the host genome." Proc Jpn Acad Ser B Phys Biol Sci **85**(8): 348-362.
Gao, F., J. Yang, D. Wang, C. Li, Y. Fu, H. Wang, W. He and J. Zhang (2017). "Mitophagy in Parkinson's Disease: Pathogenic and Therapeutic Implications." Front Neurol **8**: 527.
Gkouvatsos, K., G. Papanikolaou and K. Pantopoulos (2012). "Regulation of iron transport and the role of transferrin." Biochim Biophys Acta **1820**(3): 188-202.
Gottlieb, R. A., A. M. Andres, J. Sin and D. P. Taylor (2015). "Untangling autophagy measurements: all fluxed up." Circ Res **116**(3): 504-514.
Grace, A. A. and S. P. Onn (1989). "Morphology and electrophysiological properties of immunocytochemically identified rat dopamine neurons recorded in vitro." J Neurosci **9**(10): 3463-3481.
Greenaway, J. R., B. Abuaisha and M. G. Bramble (1996). "Digoxin toxicity presenting as encephalopathy." Postgrad Med J **72**(848): 367-368.

Gregory, A. and S. Hayflick (2014). Neurodegeneration with Brain Iron Accumulation Disorders Overview. GeneReviews((R)). M. P. Adam, H. H. Ardinger, R. A. Pagon et al. Seattle (WA), University of Washington, Seattle

Gregory, A., M. A. Kurian, T. Haack, S. J. Hayflick and P. Hogarth (2016). Beta-Propeller Protein-Associated Neurodegeneration. GeneReviews((R)). M. P. Adam, H. H. Ardinger, R. A. Pagon et al. Seattle (WA), University of Washington, Seattle

Grskovic, M., A. Javaherian, B. Strulovici and G. Q. Daley (2011). "Induced pluripotent stem cells--opportunities for disease modelling and drug discovery." Nat Rev Drug Discov **10**(12): 915-929.
Guo, F., X. Liu, H. Cai and W. Le (2018). "Autophagy in neurodegenerative diseases: pathogenesis and therapy." Brain Pathol **28**(1): 3-13.
Guzman, J. N., J. Sanchez-Padilla, D. Wokosin, J. Kondapalli, E. Ilijic, P. T. Schumacker and D. J. Surmeier (2010). "Oxidant stress evoked by pacemaking in dopaminergic neurons is attenuated by DJ-1." Nature **468**(7324): 696-700.
Haack, T. B., P. Hogarth, M. C. Kruer, A. Gregory, T. Wieland, T. Schwarzmayr, E. Graf, L. Sanford, E. Meyer, E. Kara, S. M. Cuno, S. I. Harik, V. H. Dandu, N. Nardocci, G. Zorzi, T. Dunaway, M. Tarnopolsky, S. Skinner, S. Frucht, E. Hanspal, C. Schrander-Stumpel, D. Heron, C. Mignot, B. Garavaglia, K. Bhatia, J. Hardy, T. M. Strom, N. Boddaert, H. H. Houlden, M. A. Kurian, T. Meitinger, H. Prokisch and S. J. Hayflick (2012). "Exome sequencing reveals de novo WDR45 mutations causing a phenotypically distinct, X-linked dominant form of NBIA." Am J Hum Genet **91**(6): 1144-1149.
Haack, T. B., E. Ignatius, J. Calvo-Garrido, A. Iuso, P. Isohanni, C. Maffezzini, T. Lonnqvist, A. Suomalainen, M. Gorza, L. S. Kremer, E. Graf, M. Hartig, R. Berutti, M. Paucar, P. Svenningsson, H. Stranneheim, G. Brandberg, A. Wedell, M. A. Kurian, S. A. Hayflick, P. Venco, V. Tiranti, T. M. Strom, M. Dichgans, R. Horvath, E. Holinski-Feder, C. Freyer, T. Meitinger, H. Prokisch, J. Senderek, A. Wredenberg, C. J. Carroll and T. Klopstock (2016). "Absence of the Autophagy Adaptor SQSTM1/p62 Causes Childhood-Onset Neurodegeneration with Ataxia, Dystonia, and Gaze Palsy." Am J Hum Genet **99**(3): 735-743.
Haddad, D. and K. Nakamura (2015). "Understanding the susceptibility of dopamine neurons to mitochondrial stressors in Parkinson's disease." FEBS Lett **589**(24 Pt A): 3702-3713.
Hanaway, J., J. A. McConnell and M. G. Netsky (1971). "Histogenesis of the substantia nigra, ventral tegmental area of Tsai and interpeduncular nucleus: an autoradiographic study of the mesencephalon in the rat." J Comp Neurol **142**(1): 59-73.
Hara, T., K. Nakamura, M. Matsui, A. Yamamoto, Y. Nakahara, R. Suzuki-Migishima, M. Yokoyama, K. Mishima, I. Saito, H. Okano and N. Mizushima (2006). "Suppression of basal autophagy in neural cells causes neurodegenerative disease in mice." Nature **441**(7095): 885-889.
Hartfield, E. M., M. Yamasaki-Mann, H. J. Ribeiro Fernandes, J. Vowles, W. S. James, S. A. Cowley and R. Wade-Martins (2014). "Physiological characterisation of human iPS-derived dopaminergic neurons." PLoS One **9**(2): e87388.
Hayflick, S. J., M. C. Kruer, A. Gregory, T. B. Haack, M. A. Kurian, H. H. Houlden, J. Anderson, N. Boddaert, L. Sanford, S. I. Harik, V. H. Dandu, N. Nardocci, G. Zorzi, T. Dunaway, M. Tarnopolsky, S. Skinner, K. R. Holden, S. Frucht, E. Hanspal, C. Schrander-Stumpel, C. Mignot, D. Heron, D. E. Saunders, M. Kaminska, J. P. Lin, K. Lascelles, S. M. Cuno, E. Meyer, B. Garavaglia, K. Bhatia, R. de Silva, S. Crisp, P. Lunt, M. Carey, J. Hardy, T. Meitinger, H. Prokisch and P. Hogarth (2013). "beta-Propeller protein-associated neurodegeneration: a new X-linked dominant disorder with brain iron accumulation." Brain **136**(Pt 6): 1708-1717.
Hayflick, S. J., M. A. Kurian and P. Hogarth (2018). "Neurodegeneration with brain iron accumulation." Handb Clin Neurol **147**: 293-305.

Hebert, J. M. (2011). "FGFs: Neurodevelopment's Jack-of-all-Trades - How Do They Do it?" Front Neurosci **5**: 133.
Hefti, M. M., K. Farrell, S. Kim, K. R. Bowles, M. E. Fowkes, T. Raj and J. F. Crary (2018). "High-resolution temporal and regional mapping of MAPT expression and splicing in human brain development." PLoS One **13**(4): e0195771.
Heller, J. P. and D. A. Rusakov (2015). "Morphological plasticity of astroglia: Understanding synaptic microenvironment." Glia **63**(12): 2133-2151.
Henderson-Smith, A., J. J. Corneveaux, M. De Both, L. Cuyugan, W. S. Liang, M. Huentelman, C. Adler, E. Driver-Dunckley, T. G. Beach and T. L. Dunckley (2016). "Next-generation profiling to identify the molecular etiology of Parkinson dementia." Neurol Genet **2**(3): e75.
Ihry, R. J., K. A. Worringer, M. R. Salick, E. Frias, D. Ho, K. Theriault, S. Kommineni, J. Chen, M. Sondey, C. Ye, R. Randhawa, T. Kulkarni, Z. Yang, G. McAllister, C. Russ, J. Reece-Hoyes, W. Forrester, G. R. Hoffman, R. Dolmetsch and A. Kaykas (2018). "p53 inhibits CRISPR-Cas9 engineering in human pluripotent stem cells." Nat Med **24**(7): 939-946.
Inoue, T., M. Ota, K. Mikoshiba and J. Aruga (2007). "Zic2 and Zic3 synergistically control neurulation and segmentation of paraxial mesoderm in mouse embryo." Dev Biol **306**(2): 669-684.
Jaeger, P. A., F. Pickford, C. H. Sun, K. M. Lucin, E. Masliah and T. Wyss-Coray (2010). "Regulation of amyloid precursor protein processing by the Beclin 1 complex." PLoS One **5**(6): e11102.
Jankovic, J., S. Chen and W. D. Le (2005). "The role of Nurr1 in the development of dopaminergic neurons and Parkinson's disease." Prog Neurobiol **77**(1-2): 128-138.
Jiao, Z., Z. G. Zhang, T. J. Hornyak, A. Hozeska, R. L. Zhang, Y. Wang, L. Wang, C. Roberts, F. M. Strickland and M. Chopp (2006). "Dopachrome tautomerase (Dct) regulates neural progenitor cell proliferation." Dev Biol **296**(2): 396-408.
Jinek, M., K. Chylinski, I. Fonfara, M. Hauer, J. A. Doudna and E. Charpentier (2012). "A programmable dual-RNA-guided DNA endonuclease in adaptive bacterial immunity." Science **337**(6096): 816-821.
Jo, J., Y. Xiao, A. X. Sun, E. Cukuroglu, H. D. Tran, J. Goke, Z. Y. Tan, T. Y. Saw, C. P. Tan, H. Lokman, Y. Lee, D. Kim, H. S. Ko, S. O. Kim, J. H. Park, N. J. Cho, T. M. Hyde, J. E. Kleinman, J. H. Shin, D. R. Weinberger, E. K. Tan, H. S. Je and H. H. Ng (2016). "Midbrain-like Organoids from Human Pluripotent Stem Cells Contain Functional Dopaminergic and Neuromelanin-Producing Neurons." Cell Stem Cell **19**(2): 248-257.
Johnson, T. B., J. T. Cain, K. A. White, D. Ramirez-Montealegre, D. A. Pearce and J. M. Weimer (2019). "Therapeutic landscape for Batten disease: current treatments and future prospects." Nat Rev Neurol **15**(3): 161-178.
Joyner, A. L., A. Liu and S. Millet (2000). "Otx2, Gbx2 and Fgf8 interact to position and maintain a mid-hindbrain organizer." Curr Opin Cell Biol **12**(6): 736-741.
Kageyama, S., H. Omori, T. Saitoh, T. Sone, J. L. Guan, S. Akira, F. Imamoto, T. Noda and T. Yoshimori (2011). "The LC3 recruitment mechanism is separate from Atg9L1-dependent membrane formation in the autophagic response against Salmonella." Mol Biol Cell **22**(13): 2290-2300.
Kaushik, S. and A. M. Cuervo (2012). "Chaperone-mediated autophagy: a unique way to enter the lysosome world." Trends Cell Biol **22**(8): 407-417.
Kawano, H., K. Ohyama, K. Kawamura and I. Nagatsu (1995). "Migration of dopaminergic neurons in the embryonic mesencephalon of mice." Brain Res Dev Brain Res **86**(1-2): 101-113.
Kazlauskaite, A. and M. M. Muqit (2015). "PINK1 and Parkin - mitochondrial interplay between phosphorylation and ubiquitylation in Parkinson's disease." Febs j **282**(2): 215-223.
Kerr, J. S., B. A. Adriaanse, N. H. Greig, M. P. Mattson, M. Z. Cader, V. A. Bohr and E. F. Fang (2017). "Mitophagy and Alzheimer's Disease: Cellular and Molecular Mechanisms." Trends Neurosci **40**(3): 151-166.
Kikuchi, T., A. Morizane, D. Doi, H. Magotani, H. Onoe, T. Hayashi, H. Mizuma, S. Takara, R. Takahashi, H. Inoue, S. Morita, M. Yamamoto, K. Okita, M. Nakagawa, M. Parmar and J. Takahashi

(2017). "Human iPS cell-derived dopaminergic neurons function in a primate Parkinson's disease model." Nature **548**(7669): 592-596.
Kilpatrick, K., Y. Zeng, T. Hancock and L. Segatori (2015). "Genetic and chemical activation of TFEB mediates clearance of aggregated alpha-synuclein." PLoS One **10**(3): e0120819.
Kim, J., M. Kundu, B. Viollet and K. L. Guan (2011). "AMPK and mTOR regulate autophagy through direct phosphorylation of Ulk1." Nat Cell Biol **13**(2): 132-141.
Kim, M., E. Sandford, D. Gatica, Y. Qiu, X. Liu, Y. Zheng, B. A. Schulman, J. Xu, I. Semple, S. H. Ro, B. Kim, R. N. Mavioglu, A. Tolun, A. Jipa, S. Takats, M. Karpati, J. Z. Li, Z. Yapici, G. Juhasz, J. H. Lee, D. J. Klionsky and M. Burmeister (2016). "Mutation in ATG5 reduces autophagy and leads to ataxia with developmental delay." Elife **5**.
Kirkeby, A., S. Grealish, D. A. Wolf, J. Nelander, J. Wood, M. Lundblad, O. Lindvall and M. Parmar (2012). "Generation of regionally specified neural progenitors and functional neurons from human embryonic stem cells under defined conditions." Cell Rep **1**(6): 703-714.
Kirkeby, A., J. Nelander and M. Parmar (2012). "Generating regionalized neuronal cells from pluripotency, a step-by-step protocol." Front Cell Neurosci **6**: 64.
Kocaturk, N. M. and D. Gozuacik (2018). "Crosstalk Between Mammalian Autophagy and the Ubiquitin-Proteasome System." Front Cell Dev Biol **6**: 128.
Komatsu, M., S. Waguri, T. Chiba, S. Murata, J. Iwata, I. Tanida, T. Ueno, M. Koike, Y. Uchiyama, E. Kominami and K. Tanaka (2006). "Loss of autophagy in the central nervous system causes neurodegeneration in mice." Nature **441**(7095): 880-884.
Kondo, T., K. Imamura, M. Funayama, K. Tsukita, M. Miyake, A. Ohta, K. Woltjen, M. Nakagawa, T. Asada, T. Arai, S. Kawakatsu, Y. Izumi, R. Kaji, N. Iwata and H. Inoue (2017). "iPSC-Based Compound Screening and In Vitro Trials Identify a Synergistic Anti-amyloid beta Combination for Alzheimer's Disease." Cell Rep **21**(8): 2304-2312.
Kriks, S., J. W. Shim, J. Piao, Y. M. Ganat, D. R. Wakeman, Z. Xie, L. Carrillo-Reid, G. Auyeung, C. Antonacci, A. Buch, L. Yang, M. F. Beal, D. J. Surmeier, J. H. Kordower, V. Tabar and L. Studer (2011). "Dopamine neurons derived from human ES cells efficiently engraft in animal models of Parkinson's disease." Nature **480**(7378): 547-551.
Kruer, M. C. (2013). "The neuropathology of neurodegeneration with brain iron accumulation." Int Rev Neurobiol **110**: 165-194.
Kuma, A., N. Mizushima, N. Ishihara and Y. Ohsumi (2002). "Formation of the approximately 350-kDa Apg12-Apg5.Apg16 multimeric complex, mediated by Apg16 oligomerization, is essential for autophagy in yeast." J Biol Chem **277**(21): 18619-18625.
Lancaster, M. A. and J. A. Knoblich (2014). "Organogenesis in a dish: modeling development and disease using organoid technologies." Science **345**(6194): 1247125.
Lancaster, M. A., M. Renner, C. A. Martin, D. Wenzel, L. S. Bicknell, M. E. Hurles, T. Homfray, J. M. Penninger, A. P. Jackson and J. A. Knoblich (2013). "Cerebral organoids model human brain development and microcephaly." Nature **501**(7467): 373-379.
Lawen, A. and D. J. Lane (2013). "Mammalian iron homeostasis in health and disease: uptake, storage, transport, and molecular mechanisms of action." Antioxid Redox Signal **18**(18): 2473-2507.
Lee, J. H., W. H. Yu, A. Kumar, S. Lee, P. S. Mohan, C. M. Peterhoff, D. M. Wolfe, M. Martinez-Vicente, A. C. Massey, G. Sovak, Y. Uchiyama, D. Westaway, A. M. Cuervo and R. A. Nixon (2010). "Lysosomal proteolysis and autophagy require presenilin 1 and are disrupted by Alzheimer-related PS1 mutations." Cell **141**(7): 1146-1158.
Lenz, M., R. Goetzke, A. Schenk, C. Schubert, J. Veeck, H. Hemeda, S. Koschmieder, M. Zenke, A. Schuppert and W. Wagner (2015). "Epigenetic biomarker to support classification into pluripotent and non-pluripotent cells." Sci Rep **5**: 8973.
Li, D. and R. Roberts (2001). "WD-repeat proteins: structure characteristics, biological function, and their involvement in human diseases." Cell Mol Life Sci **58**(14): 2085-2097.
Li, L., J. Chao and Y. Shi (2018). "Modeling neurological diseases using iPSC-derived neural cells : iPSC modeling of neurological diseases." Cell Tissue Res **371**(1): 143-151.

Li, N. N., E. K. Tan, X. L. Chang, X. Y. Mao, D. M. Zhao, J. H. Zhang, Q. Liao and R. Peng (2013). "MCCC1/LAMP3 reduces risk of sporadic Parkinson's disease in Han Chinese." Acta Neurol Scand **128**(2): 136-139.
Li, W. W., J. Li and J. K. Bao (2012). "Microautophagy: lesser-known self-eating." Cell Mol Life Sci **69**(7): 1125-1136.
Lim, S. Y., A. H. Tan, A. Ahmad-Annuar, S. A. Schneider, P. C. Bee, J. L. Lim, N. Ramli and M. I. Idris (2018). "A Patient with Beta-Propeller Protein-Associated Neurodegeneration: Treatment with Iron Chelation Therapy." J Mov Disord **11**(2): 89-92.
Little, D., R. Ketteler, P. Gissen and M. J. Devine (2019). "Using stem cell-derived neurons in drug screening for neurological diseases." Neurobiol Aging **78**: 130-141.
Liu, Y., S. Shoji-Kawata, R. M. Sumpter, Jr., Y. Wei, V. Ginet, L. Zhang, B. Posner, K. A. Tran, D. R. Green, R. J. Xavier, S. Y. Shaw, P. G. Clarke, J. Puyal and B. Levine (2013). "Autosis is a Na+,K+-ATPase-regulated form of cell death triggered by autophagy-inducing peptides, starvation, and hypoxia-ischemia." Proc Natl Acad Sci U S A **110**(51): 20364-20371.
Lo Giudice, T., F. Lombardi, F. M. Santorelli, T. Kawarai and A. Orlacchio (2014). "Hereditary spastic paraplegia: clinical-genetic characteristics and evolving molecular mechanisms." Exp Neurol **261**: 518-539.
Lojewski, X., J. F. Staropoli, S. Biswas-Legrand, A. M. Simas, L. Haliw, M. K. Selig, S. H. Coppel, K. A. Goss, A. Petcherski, U. Chandrachud, S. D. Sheridan, D. Lucente, K. B. Sims, J. F. Gusella, D. Sondhi, R. G. Crystal, P. Reinhardt, J. Sterneckert, H. Scholer, S. J. Haggarty, A. Storch, A. Hermann and S. L. Cotman (2014). "Human iPSC models of neuronal ceroid lipofuscinosis capture distinct effects of TPP1 and CLN3 mutations on the endocytic pathway." Hum Mol Genet **23**(8): 2005-2022.
Long, M., N. Abdeen, M. T. Geraghty, P. Hogarth, S. Hayflick and S. Venkateswaran (2015). "Novel WDR45 Mutation and Pathognomonic BPAN Imaging in a Young Female With Mild Cognitive Delay." Pediatrics **136**(3): e714-717.
Love, M. I., W. Huber and S. Anders (2014). "Moderated estimation of fold change and dispersion for RNA-seq data with DESeq2." Genome Biol **15**(12): 550.
Lu, N., X. Li, R. Tan, J. An, Z. Cai, X. Hu, F. Wang, H. Wang, C. Lu and H. Lu (2018). "HIF-1alpha/Beclin1-Mediated Autophagy Is Involved in Neuroprotection Induced by Hypoxic Preconditioning." J Mol Neurosci **66**(2): 238-250.
Lu, Q., P. Yang, X. Huang, W. Hu, B. Guo, F. Wu, L. Lin, A. L. Kovacs, L. Yu and H. Zhang (2011). "The WD40 repeat PtdIns(3)P-binding protein EPG-6 regulates progression of omegasomes to autophagosomes." Dev Cell **21**(2): 343-357.
Makarova, K. S., D. H. Haft, R. Barrangou, S. J. Brouns, E. Charpentier, P. Horvath, S. Moineau, F. J. Mojica, Y. I. Wolf, A. F. Yakunin, J. van der Oost and E. V. Koonin (2011). "Evolution and classification of the CRISPR-Cas systems." Nat Rev Microbiol **9**(6): 467-477.
Malaguarnera, L., A. Marsullo, K. Zorena, G. Musumeci and M. Di Rosa (2017). "Vitamin D3 regulates LAMP3 expression in monocyte derived dendritic cells." Cell Immunol **311**: 13-21.
Manuel, M. N., D. Mi, J. O. Mason and D. J. Price (2015). "Regulation of cerebral cortical neurogenesis by the Pax6 transcription factor." Front Cell Neurosci **9**: 70.
Marathe, S., M. Jaquet, J. M. Annoni and L. Alberi (2017). "Jagged1 Is Altered in Alzheimer's Disease and Regulates Spatial Memory Processing." Front Cell Neurosci **11**: 220.
Marchand, R. and L. J. Poirier (1983). "Isthmic origin of neurons of the rat substantia nigra." Neuroscience **9**(2): 373-381.
Mariani, J., G. Coppola, P. Zhang, A. Abyzov, L. Provini, L. Tomasini, M. Amenduni, A. Szekely, D. Palejev, M. Wilson, M. Gerstein, E. L. Grigorenko, K. Chawarska, K. A. Pelphrey, J. R. Howe and F. M. Vaccarino (2015). "FOXG1-Dependent Dysregulation of GABA/Glutamate Neuron Differentiation in Autism Spectrum Disorders." Cell **162**(2): 375-390.
Marini, J. C., A. Forlino, H. P. Bachinger, N. J. Bishop, P. H. Byers, A. Paepe, F. Fassier, N. Fratzl-Zelman, K. M. Kozloff, D. Krakow, K. Montpetit and O. Semler (2017). "Osteogenesis imperfecta." Nat Rev Dis Primers **3**: 17052.

Mauthe, M., I. Orhon, C. Rocchi, X. Zhou, M. Luhr, K. J. Hijlkema, R. P. Coppes, N. Engedal, M. Mari and F. Reggiori (2018). "Chloroquine inhibits autophagic flux by decreasing autophagosome-lysosome fusion." Autophagy **14**(8): 1435-1455.
Mayeux, R. and Y. Stern (2012). "Epidemiology of Alzheimer disease." Cold Spring Harb Perspect Med **2**(8).
Mayshar, Y., U. Ben-David, N. Lavon, J. C. Biancotti, B. Yakir, A. T. Clark, K. Plath, W. E. Lowry and N. Benvenisty (2010). "Identification and classification of chromosomal aberrations in human induced pluripotent stem cells." Cell Stem Cell **7**(4): 521-531.
Mazure, N. M. and J. Pouyssegur (2010). "Hypoxia-induced autophagy: cell death or cell survival?" Curr Opin Cell Biol **22**(2): 177-180.
Meguro, R., Y. Asano, S. Odagiri, C. Li, H. Iwatsuki and K. Shoumura (2007). "Nonheme-iron histochemistry for light and electron microscopy: a historical, theoretical and technical review." Arch Histol Cytol **70**(1): 1-19.
Mekhoubad, S., C. Bock, A. S. de Boer, E. Kiskinis, A. Meissner and K. Eggan (2012). "Erosion of dosage compensation impacts human iPSC disease modeling." Cell Stem Cell **10**(5): 595-609.
Meng, T., S. Lin, H. Zhuang, H. Huang, Z. He, Y. Hu, Q. Gong and D. Feng (2019). "Recent progress in the role of autophagy in neurological diseases." Cell Stress **3**(5): 141-161.
Menzies, F. M., A. Fleming, A. Caricasole, C. F. Bento, S. P. Andrews, A. Ashkenazi, J. Fullgrabe, A. Jackson, M. Jimenez Sanchez, C. Karabiyik, F. Licitra, A. Lopez Ramirez, M. Pavel, C. Puri, M. Renna, T. Ricketts, L. Schlotawa, M. Vicinanza, H. Won, Y. Zhu, J. Skidmore and D. C. Rubinsztein (2017). "Autophagy and Neurodegeneration: Pathogenic Mechanisms and Therapeutic Opportunities." Neuron **93**(5): 1015-1034.
Merkle, F. T., S. Ghosh, N. Kamitaki, J. Mitchell, Y. Avior, C. Mello, S. Kashin, S. Mekhoubad, D. Ilic, M. Charlton, G. Saphier, R. E. Handsaker, G. Genovese, S. Bar, N. Benvenisty, S. A. McCarroll and K. Eggan (2017). "Human pluripotent stem cells recurrently acquire and expand dominant negative P53 mutations." Nature **545**(7653): 229-233.
Merzdorf, C. S. (2007). "Emerging roles for zic genes in early development." Dev Dyn **236**(4): 922-940.
Metzakopian, E., W. Lin, M. Salmon-Divon, H. Dvinge, E. Andersson, J. Ericson, T. Perlmann, J. A. Whitsett, P. Bertone and S. L. Ang (2012). "Genome-wide characterization of Foxa2 targets reveals upregulation of floor plate genes and repression of ventrolateral genes in midbrain dopaminergic progenitors." Development **139**(14): 2625-2634.
Meyer, E., M. A. Kurian and S. J. Hayflick (2015). "Neurodegeneration with Brain Iron Accumulation: Genetic Diversity and Pathophysiological Mechanisms." Annu Rev Genomics Hum Genet **16**: 257-279.
Mi, H., A. Muruganujan and P. D. Thomas (2013). "PANTHER in 2013: modeling the evolution of gene function, and other gene attributes, in the context of phylogenetic trees." Nucleic Acids Res **41**(Database issue): D377-386.
Miller, J. D., Y. M. Ganat, S. Kishinevsky, R. L. Bowman, B. Liu, E. Y. Tu, P. K. Mandal, E. Vera, J. W. Shim, S. Kriks, T. Taldone, N. Fusaki, M. J. Tomishima, D. Krainc, T. A. Milner, D. J. Rossi and L. Studer (2013). "Human iPSC-based modeling of late-onset disease via progerin-induced aging." Cell Stem Cell **13**(6): 691-705.
Millet, S., K. Campbell, D. J. Epstein, K. Losos, E. Harris and A. L. Joyner (1999). "A role for Gbx2 in repression of Otx2 and positioning the mid/hindbrain organizer." Nature **401**(6749): 161-164.
Mizushima, N. and M. Komatsu (2011). "Autophagy: renovation of cells and tissues." Cell **147**(4): 728-741.
Mizushima, N. and B. Levine (2010). "Autophagy in mammalian development and differentiation." Nat Cell Biol **12**(9): 823-830.
Mizushima, N., T. Yoshimori and Y. Ohsumi (2011). "The role of Atg proteins in autophagosome formation." Annu Rev Cell Dev Biol **27**: 107-132.

Mori, T., Z. Yuxing, H. Takaki, M. Takeuchi, K. Iseki, S. Hagino, J. Kitanaka, M. Takemura, H. Misawa, M. Ikawa, M. Okabe and A. Wanaka (2004). "The LIM homeobox gene, L3/Lhx8, is necessary for proper development of basal forebrain cholinergic neurons." Eur J Neurosci **19**(12): 3129-3141.
Mosharov, E. V., K. E. Larsen, E. Kanter, K. A. Phillips, K. Wilson, Y. Schmitz, D. E. Krantz, K. Kobayashi, R. H. Edwards and D. Sulzer (2009). "Interplay between cytosolic dopamine, calcium, and alpha-synuclein causes selective death of substantia nigra neurons." Neuron **62**(2): 218-229.
Nakamura, K., H. Kodera, T. Akita, M. Shiina, M. Kato, H. Hoshino, H. Terashima, H. Osaka, S. Nakamura, J. Tohyama, T. Kumada, T. Furukawa, S. Iwata, T. Shiihara, M. Kubota, S. Miyatake, E. Koshimizu, K. Nishiyama, M. Nakashima, Y. Tsurusaki, N. Miyake, K. Hayasaka, K. Ogata, A. Fukuda, N. Matsumoto and H. Saitsu (2013). "De Novo mutations in GNAO1, encoding a Galphao subunit of heterotrimeric G proteins, cause epileptic encephalopathy." Am J Hum Genet **93**(3): 496-505.
Nakashima, M., K. Takano, Y. Tsuyusaki, S. Yoshitomi, M. Shimono, Y. Aoki, M. Kato, N. Aida, T. Mizuguchi, S. Miyatake, N. Miyake, H. Osaka and H. Saitsu (2016). "WDR45 mutations in three male patients with West syndrome." **61**(7): 653-661.
Nakatogawa, H., K. Suzuki, Y. Kamada and Y. Ohsumi (2009). "Dynamics and diversity in autophagy mechanisms: lessons from yeast." Nat Rev Mol Cell Biol **10**(7): 458-467.
Neul, J. L., W. E. Kaufmann, D. G. Glaze, J. Christodoulou, A. J. Clarke, N. Bahi-Buisson, H. Leonard, M. E. Bailey, N. C. Schanen, M. Zappella, A. Renieri, P. Huppke and A. K. Percy (2010). "Rett syndrome: revised diagnostic criteria and nomenclature." Ann Neurol **68**(6): 944-950.
Nguyen, H. N., B. Byers, B. Cord, A. Shcheglovitov, J. Byrne, P. Gujar, K. Kee, B. Schule, R. E. Dolmetsch, W. Langston, T. D. Palmer and R. R. Pera (2011). "LRRK2 mutant iPSC-derived DA neurons demonstrate increased susceptibility to oxidative stress." Cell Stem Cell **8**(3): 267-280.
Nishioka, K., G. Oyama, H. Yoshino, Y. Li, T. Matsushima, C. Takeuchi, Y. Mochizuki, M. Mori-Yoshimura, M. Murata, C. Yamasita, N. Nakamura, Y. Konishi, K. Ohi, K. Ichikawa, T. Terada, T. Obi, M. Funayama, S. Saiki and N. Hattori (2015). "High frequency of beta-propeller protein-associated neurodegeneration (BPAN) among patients with intellectual disability and young-onset parkinsonism." Neurobiol Aging **36**(5): 2004.e2009-2004.e2015.
Nixon, R. A. (2013). "The role of autophagy in neurodegenerative disease." Nat Med **19**(8): 983-997.
Nixon, R. A., J. Wegiel, A. Kumar, W. H. Yu, C. Peterhoff, A. Cataldo and A. M. Cuervo (2005). "Extensive involvement of autophagy in Alzheimer disease: an immuno-electron microscopy study." J Neuropathol Exp Neurol **64**(2): 113-122.
Nordstrom, U., T. M. Jessell and T. Edlund (2002). "Progressive induction of caudal neural character by graded Wnt signaling." Nat Neurosci **5**(6): 525-532.
Obara, K., T. Sekito, K. Niimi and Y. Ohsumi (2008). "The Atg18-Atg2 complex is recruited to autophagic membranes via phosphatidylinositol 3-phosphate and exerts an essential function." J Biol Chem **283**(35): 23972-23980.
Ohba, C., S. Nabatame, Y. Iijima, K. Nishiyama, Y. Tsurusaki, M. Nakashima, N. Miyake, F. Tanaka, K. Ozono, H. Saitsu and N. Matsumoto (2014). "De novo WDR45 mutation in a patient showing clinically Rett syndrome with childhood iron deposition in brain." J Hum Genet **59**(5): 292-295.
Ortmann, D. and L. Vallier (2017). "Variability of human pluripotent stem cell lines." Curr Opin Genet Dev **46**: 179-185.
Osafune, K., L. Caron, M. Borowiak, R. J. Martinez, C. S. Fitz-Gerald, Y. Sato, C. A. Cowan, K. R. Chien and D. A. Melton (2008). "Marked differences in differentiation propensity among human embryonic stem cell lines." Nat Biotechnol **26**(3): 313-315.
Paiva, I., G. Jain, D. F. Lazaro, K. G. Jercic, T. Hentrich, C. Kerimoglu, R. Pinho, E. M. Szego, S. Burkhardt, V. Capece, R. Halder, R. Islam, M. Xylaki, L. A. Caldi Gomes, A. E. Roser, P. Lingor, J. M. Schulze-Hentrich, F. Borovecki, A. Fischer and T. F. Outeiro (2018). "Alpha-synuclein deregulates the expression of COL4A2 and impairs ER-Golgi function." Neurobiol Dis **119**: 121-135.
Pan, T., S. Kondo, W. Le and J. Jankovic (2008). "The role of autophagy-lysosome pathway in neurodegeneration associated with Parkinson's disease." Brain **131**(Pt 8): 1969-1978.

Panayiotopoulos, C. P. (1993). "Benign childhood partial epilepsies: benign childhood seizure susceptibility syndromes." J Neurol Neurosurg Psychiatry **56**(1): 2-5.
Panning, B. (2008). "X-chromosome inactivation: the molecular basis of silencing." J Biol **7**(8): 30.
Papandreou, A., M. M. Tisdall, W. K. Chong, J. H. Cross, W. F. Harkness and S. M. Varadkar (2014). "COL4A1 mutations should not be a contraindication for epilepsy surgery." Childs Nerv Syst **30**(8): 1467-1469.
Pathak, D., L. Y. Shields, B. A. Mendelsohn, D. Haddad, W. Lin, A. A. Gerencser, H. Kim, M. D. Brand, R. H. Edwards and K. Nakamura (2015). "The role of mitochondrially derived ATP in synaptic vesicle recycling." J Biol Chem **290**(37): 22325-22336.
Paudel, R., A. Li, S. Wiethoff, R. Bandopadhyay, K. Bhatia, R. de Silva, H. Houlden and J. L. Holton (2015). "Neuropathology of Beta-propeller protein associated neurodegeneration (BPAN): a new tauopathy." Acta Neuropathol Commun **3**: 39.
Perlmann, T. and A. Wallen-Mackenzie (2004). "Nurr1, an orphan nuclear receptor with essential functions in developing dopamine cells." Cell Tissue Res **318**(1): 45-52.
Pickford, F., E. Masliah, M. Britschgi, K. Lucin, R. Narasimhan, P. A. Jaeger, S. Small, B. Spencer, E. Rockenstein, B. Levine and T. Wyss-Coray (2008). "The autophagy-related protein beclin 1 shows reduced expression in early Alzheimer disease and regulates amyloid beta accumulation in mice." J Clin Invest **118**(6): 2190-2199.
Pihlstrom, L., G. Axelsson, K. A. Bjornara, N. Dizdar, C. Fardell, L. Forsgren, B. Holmberg, J. P. Larsen, J. Linder, H. Nissbrandt, O. B. Tysnes, E. Ohman, E. Dietrichs and M. Toft (2013). "Supportive evidence for 11 loci from genome-wide association studies in Parkinson's disease." Neurobiol Aging **34**(6): 1708.e1707-1713.
Placzek, M. and J. Briscoe (2005). "The floor plate: multiple cells, multiple signals." Nat Rev Neurosci **6**(3): 230-240.
Platt, F. M., B. Boland and A. C. van der Spoel (2012). "The cell biology of disease: lysosomal storage disorders: the cellular impact of lysosomal dysfunction." J Cell Biol **199**(5): 723-734.
Prak, K., J. Kriston-Vizi, A. W. Chan, C. Luft, J. R. Costa, N. Pengo and R. Ketteler (2016). "Benzobisthiazoles Represent a Novel Scaffold for Kinase Inhibitors of CLK Family Members." Biochemistry **55**(3): 608-617.
Proikas-Cezanne, T., Z. Takacs, P. Donnes and O. Kohlbacher (2015). "WIPI proteins: essential PtdIns3P effectors at the nascent autophagosome." J Cell Sci **128**(2): 207-217.
Puelles, E., A. Annino, F. Tuorto, A. Usiello, D. Acampora, T. Czerny, C. Brodski, S. L. Ang, W. Wurst and A. Simeone (2004). "Otx2 regulates the extent, identity and fate of neuronal progenitor domains in the ventral midbrain." Development **131**(9): 2037-2048.
Qi, Y., X. J. Zhang, N. Renier, Z. Wu, T. Atkin, Z. Sun, M. Z. Ozair, J. Tchieu, B. Zimmer, F. Fattahi, Y. Ganat, R. Azevedo, N. Zeltner, A. H. Brivanlou, M. Karayiorgou, J. Gogos, M. Tomishima, M. Tessier-Lavigne, S. H. Shi and L. Studer (2017). "Combined small-molecule inhibition accelerates the derivation of functional cortical neurons from human pluripotent stem cells." Nat Biotechnol **35**(2): 154-163.
Raab, S., M. Klingenstein, S. Liebau and L. Linta (2014). "A Comparative View on Human Somatic Cell Sources for iPSC Generation." Stem Cells Int **2014**: 768391.
Rasool, S., N. Soya, L. Truong, N. Croteau, G. L. Lukacs and J. F. Trempe (2018). "PINK1 autophosphorylation is required for ubiquitin recognition." EMBO Rep **19**(4).
Reggiori, F. and C. Ungermann (2017). "Autophagosome Maturation and Fusion." J Mol Biol **429**(4): 486-496.
Robert Finestra, T. and J. Gribnau (2017). "X chromosome inactivation: silencing, topology and reactivation." Curr Opin Cell Biol **46**: 54-61.
Rubinsztein, D. C. and R. A. Frake (2016). "Yoshinori Ohsumi's Nobel Prize for mechanisms of autophagy: from basic yeast biology to therapeutic potential." J R Coll Physicians Edinb **46**(4): 228-233.

Rubinsztein, D. C., T. Shpilka and Z. Elazar (2012). "Mechanisms of autophagosome biogenesis." Curr Biol **22**(1): R29-34.
Russell, R. C., Y. Tian, H. Yuan, H. W. Park, Y. Y. Chang, J. Kim, H. Kim, T. P. Neufeld, A. Dillin and K. L. Guan (2013). "ULK1 induces autophagy by phosphorylating Beclin-1 and activating VPS34 lipid kinase." Nat Cell Biol **15**(7): 741-750.
Russell, R. C., H. X. Yuan and K. L. Guan (2014). "Autophagy regulation by nutrient signaling." Cell Res **24**(1): 42-57.
Ryan, S. D., N. Dolatabadi, S. F. Chan, X. Zhang, M. W. Akhtar, J. Parker, F. Soldner, C. R. Sunico, S. Nagar, M. Talantova, B. Lee, K. Lopez, A. Nutter, B. Shan, E. Molokanova, Y. Zhang, X. Han, T. Nakamura, E. Masliah, J. R. Yates, 3rd, N. Nakanishi, A. Y. Andreyev, S. Okamoto, R. Jaenisch, R. Ambasudhan and S. A. Lipton (2013). "Isogenic human iPSC Parkinson's model shows nitrosative stress-induced dysfunction in MEF2-PGC1alpha transcription." Cell **155**(6): 1351-1364.
Sachs, N., J. de Ligt, O. Kopper, E. Gogola, G. Bounova, F. Weeber, A. V. Balgobind, K. Wind, A. Gracanin, H. Begthel, J. Korving, R. van Boxtel, A. A. Duarte, D. Lelieveld, A. van Hoeck, R. F. Ernst, F. Blokzijl, I. J. Nijman, M. Hoogstraat, M. van de Ven, D. A. Egan, V. Zinzalla, J. Moll, S. F. Boj, E. E. Voest, L. Wessels, P. J. van Diest, S. Rottenberg, R. G. J. Vries, E. Cuppen and H. Clevers (2018). "A Living Biobank of Breast Cancer Organoids Captures Disease Heterogeneity." Cell **172**(1-2): 373-386.e310.
Saha, S., D. P. Panigrahi, S. Patil and S. K. Bhutia (2018). "Autophagy in health and disease: A comprehensive review." Biomed Pharmacother **104**: 485-495.
Saitsu, H., T. Nishimura, K. Muramatsu, H. Kodera, S. Kumada, K. Sugai, E. Kasai-Yoshida, N. Sawaura, H. Nishida, A. Hoshino, F. Ryujin, S. Yoshioka, K. Nishiyama, Y. Kondo, Y. Tsurusaki, M. Nakashima, N. Miyake, H. Arakawa, M. Kato, N. Mizushima and N. Matsumoto (2013). "De novo mutations in the autophagy gene WDR45 cause static encephalopathy of childhood with neurodegeneration in adulthood." Nat Genet **45**(4): 445-449, 449e441.
Scannell, J. W., A. Blanckley, H. Boldon and B. Warrington (2012). "Diagnosing the decline in pharmaceutical R&D efficiency." Nat Rev Drug Discov **11**(3): 191-200.
Schneider, S. A. and K. P. Bhatia (2010). "Rare causes of dystonia parkinsonism." Curr Neurol Neurosci Rep **10**(6): 431-439.
Seibler, P., L. F. Burbulla, M. Dulovic, S. Zittel, J. Heine, T. Schmidt, F. Rudolph, A. Westenberger, A. Rakovic, A. Munchau, D. Krainc and C. Klein (2018). "Iron overload is accompanied by mitochondrial and lysosomal dysfunction in WDR45 mutant cells." Brain.
Seibler, P., J. Graziotto, H. Jeong, F. Simunovic, C. Klein and D. Krainc (2011). "Mitochondrial Parkin recruitment is impaired in neurons derived from mutant PINK1 induced pluripotent stem cells." J Neurosci **31**(16): 5970-5976.
Shah, S., S. Ellard, R. Kneen, M. Lim, N. Osborne, J. Rankin, N. Stoodley, M. van der Knaap, A. Whitney and P. Jardine (2012). "Childhood presentation of COL4A1 mutations." Dev Med Child Neurol **54**(6): 569-574.
Sinha, S. and J. K. Chen (2006). "Purmorphamine activates the Hedgehog pathway by targeting Smoothened." Nat Chem Biol **2**(1): 29-30.
Smith, T. F., C. Gaitatzes, K. Saxena and E. J. Neer (1999). "The WD repeat: a common architecture for diverse functions." Trends Biochem Sci **24**(5): 181-185.
Son, J. H., J. H. Shim, K. H. Kim, J. Y. Ha and J. Y. Han (2012). "Neuronal autophagy and neurodegenerative diseases." Exp Mol Med **44**(2): 89-98.
Sonntag, K. C., B. Song, N. Lee, J. H. Jung, Y. Cha, P. Leblanc, C. Neff, S. W. Kong, B. S. Carter, J. Schweitzer and K. S. Kim (2018). "Pluripotent stem cell-based therapy for Parkinson's disease: Current status and future prospects." Prog Neurobiol **168**: 1-20.
Spilman, P., N. Podlutskaya, M. J. Hart, J. Debnath, O. Gorostiza, D. Bredesen, A. Richardson, R. Strong and V. Galvan (2010). "Inhibition of mTOR by rapamycin abolishes cognitive deficits and reduces amyloid-beta levels in a mouse model of Alzheimer's disease." PLoS One **5**(4): e9979.

Srikanth, P. and T. L. Young-Pearse (2014). "Stem cells on the brain: modeling neurodevelopmental and neurodegenerative diseases using human induced pluripotent stem cells." J Neurogenet **28**(1-2): 5-29.
Surmeier, D. J. and P. T. Schumacker (2013). "Calcium, bioenergetics, and neuronal vulnerability in Parkinson's disease." J Biol Chem **288**(15): 10736-10741.
Takahashi, J. (2019). "Preparing for first human trial of induced pluripotent stem cell-derived cells for Parkinson's disease: an interview with Jun Takahashi." Regen Med **14**(2): 93-95.
Takahashi, K., K. Tanabe, M. Ohnuki, M. Narita, T. Ichisaka, K. Tomoda and S. Yamanaka (2007). "Induction of pluripotent stem cells from adult human fibroblasts by defined factors." Cell **131**(5): 861-872.
Tchieu, J., E. Kuoy, M. H. Chin, H. Trinh, M. Patterson, S. P. Sherman, O. Aimiuwu, A. Lindgren, S. Hakimian, J. A. Zack, A. T. Clark, A. D. Pyle, W. E. Lowry and K. Plath (2010). "Female human iPSCs retain an inactive X chromosome." Cell Stem Cell **7**(3): 329-342.
Teinert, J., R. Behne, M. Wimmer and D. Ebrahimi-Fakhari (2019). "Novel insights into the clinical and molecular spectrum of congenital disorders of autophagy." J Inherit Metab Dis.
Thacker, D. and J. Sharma (2007). "Digoxin toxicity." Clin Pediatr (Phila) **46**(3): 276-279.
Thomas, A. C., H. Williams, N. Seto-Salvia, C. Bacchelli, D. Jenkins, M. O'Sullivan, K. Mengrelis, M. Ishida, L. Ocaka, E. Chanudet, C. James, F. Lescai, G. Anderson, D. Morrogh, M. Ryten, A. J. Duncan, Y. J. Pai, J. M. Saraiva, F. Ramos, B. Farren, D. Saunders, B. Vernay, P. Gissen, A. Straatmaan-Iwanowska, F. Baas, N. W. Wood, J. Hersheson, H. Houlden, J. Hurst, R. Scott, M. Bitner-Glindzicz, G. E. Moore, S. B. Sousa and P. Stanier (2014). "Mutations in SNX14 cause a distinctive autosomal-recessive cerebellar ataxia and intellectual disability syndrome." Am J Hum Genet **95**(5): 611-621.
Thumm, M., R. A. Busse, A. Scacioc, M. Stephan, A. Janshoff, K. Kuhnel and R. Krick (2013). "It takes two to tango: PROPPINs use two phosphoinositide-binding sites." Autophagy **9**(1): 106-107.
Tiveron, M. C., C. Beurrier, C. Ceni, N. Andriambao, A. Combes, M. Koehl, N. Maurice, E. Gatti, D. N. Abrous, L. Kerkerian-Le Goff, P. Pierre and H. Cremer (2016). "LAMP5 Fine-Tunes GABAergic Synaptic Transmission in Defined Circuits of the Mouse Brain." PLoS One **11**(6): e0157052.
Tomoda, K., K. Takahashi, K. Leung, A. Okada, M. Narita, N. A. Yamada, K. E. Eilertson, P. Tsang, S. Baba, M. P. White, S. Sami, D. Srivastava, B. R. Conklin, B. Panning and S. Yamanaka (2012). "Derivation conditions impact X-inactivation status in female human induced pluripotent stem cells." Cell Stem Cell **11**(1): 91-99.
Trabzuni, D., S. Wray, J. Vandrovcova, A. Ramasamy, R. Walker, C. Smith, C. Luk, J. R. Gibbs, A. Dillman, D. G. Hernandez, S. Arepalli, A. B. Singleton, M. R. Cookson, A. M. Pittman, R. de Silva, M. E. Weale, J. Hardy and M. Ryten (2012). "MAPT expression and splicing is differentially regulated by brain region: relation to genotype and implication for tauopathies." Hum Mol Genet **21**(18): 4094-4103.
Turinetto, V., L. Orlando and C. Giachino (2017). "Induced Pluripotent Stem Cells: Advances in the Quest for Genetic Stability during Reprogramming Process." Int J Mol Sci **18**(9).
van der Kant, R., V. F. Langness, C. M. Herrera, D. A. Williams, L. K. Fong, Y. Leestemaker, E. Steenvoorden, K. D. Rynearson, J. F. Brouwers, J. B. Helms, H. Ovaa, M. Giera, S. L. Wagner, A. G. Bang and L. S. B. Goldstein (2019). "Cholesterol Metabolism Is a Druggable Axis that Independently Regulates Tau and Amyloid-beta in iPSC-Derived Alzheimer's Disease Neurons." Cell Stem Cell **24**(3): 363-375.e369.
Vogiatzi, T., M. Xilouri, K. Vekrellis and L. Stefanis (2008). "Wild type alpha-synuclein is degraded by chaperone-mediated autophagy and macroautophagy in neuronal cells." J Biol Chem **283**(35): 23542-23556.
Wan, H., Q. Wang, X. Chen, Q. Zeng, Y. Shao, H. Fang, X. Liao, H. S. Li, M. G. Liu, T. L. Xu, M. Diao, D. Li, B. Meng, B. Tang, Z. Zhang and L. Liao (2019). "WDR45 contributes to neurodegeneration through regulation of ER homeostasis and neuronal death." Autophagy: 1-17.

Wang, J. K. T., S. Portbury, M. B. Thomas, S. Barney, D. J. Ricca, D. L. Morris, D. S. Warner and D. C. Lo (2006). "Cardiac glycosides provide neuroprotection against ischemic stroke: discovery by a brain slice-based compound screening platform." Proc Natl Acad Sci U S A **103**(27): 10461-10466.
Wang, Y., L. Li, C. Hou, Y. Lai, J. Long, J. Liu, Q. Zhong and J. Diao (2016). "SNARE-mediated membrane fusion in autophagy." Semin Cell Dev Biol **60**: 97-104.
Wang, Y., Q. Qiu, J. J. Shen, D. D. Li, X. J. Jiang, S. Y. Si, R. G. Shao and Z. Wang (2012). "Cardiac glycosides induce autophagy in human non-small cell lung cancer cells through regulation of dual signaling pathways." Int J Biochem Cell Biol **44**(11): 1813-1824.
Wassarman, K. M., M. Lewandoski, K. Campbell, A. L. Joyner, J. L. Rubenstein, S. Martinez and G. R. Martin (1997). "Specification of the anterior hindbrain and establishment of a normal mid/hindbrain organizer is dependent on Gbx2 gene function." Development **124**(15): 2923-2934.
Watanabe, K., M. Ueno, D. Kamiya, A. Nishiyama, M. Matsumura, T. Wataya, J. B. Takahashi, S. Nishikawa, S. Nishikawa, K. Muguruma and Y. Sasai (2007). "A ROCK inhibitor permits survival of dissociated human embryonic stem cells." Nat Biotechnol **25**(6): 681-686.
Weinstein, D. C., A. Ruiz i Altaba, W. S. Chen, P. Hoodless, V. R. Prezioso, T. M. Jessell and J. E. Darnell, Jr. (1994). "The winged-helix transcription factor HNF-3 beta is required for notochord development in the mouse embryo." Cell **78**(4): 575-588.
Xu, C. C., K. R. Denton, Z. B. Wang, X. Zhang and X. J. Li (2016). "Abnormal mitochondrial transport and morphology as early pathological changes in human models of spinal muscular atrophy." Dis Model Mech **9**(1): 39-49.
Xu, X., Y. Lei, J. Luo, J. Wang, S. Zhang, X. J. Yang, M. Sun, E. Nuwaysir, G. Fan, J. Zhao, L. Lei and Z. Zhong (2013). "Prevention of beta-amyloid induced toxicity in human iPS cell-derived neurons by inhibition of Cyclin-dependent kinases and associated cell cycle events." Stem Cell Res **10**(2): 213-227.
Xu, Y., X. Zhu, H. S. Hahm, W. Wei, E. Hao, A. Hayek and S. Ding (2010). "Revealing a core signaling regulatory mechanism for pluripotent stem cell survival and self-renewal by small molecules." Proc Natl Acad Sci U S A **107**(18): 8129-8134.
Yamamoto, H., S. Kakuta, T. M. Watanabe, A. Kitamura, T. Sekito, C. Kondo-Kakuta, R. Ichikawa, M. Kinjo and Y. Ohsumi (2012). "Atg9 vesicles are an important membrane source during early steps of autophagosome formation." J Cell Biol **198**(2): 219-233.
Yang, S., L. C. Edman, J. A. Sanchez-Alcaniz, N. Fritz, S. Bonilla, J. Hecht, P. Uhlen, S. J. Pleasure, J. C. Villaescusa, O. Marin and E. Arenas (2013). "Cxcl12/Cxcr4 signaling controls the migration and process orientation of A9-A10 dopaminergic neurons." Development **140**(22): 4554-4564.
Yang, Z. and D. J. Klionsky (2010). "Eaten alive: a history of macroautophagy." Nat Cell Biol **12**(9): 814-822.
Ye, W., M. D. Pitlock, M. A. Javors, B. J. Thompson, J. D. Lechleiter and J. G. Hensler (2018). "The long-term effect of maternal dietary protein restriction on 5-HT1A receptor function and behavioral responses to stress in adulthood." Behav Brain Res **349**: 116-124.
Ye, W., K. Shimamura, J. L. Rubenstein, M. A. Hynes and A. Rosenthal (1998). "FGF and Shh signals control dopaminergic and serotonergic cell fate in the anterior neural plate." Cell **93**(5): 755-766.
Yoshii, S. R. and N. Mizushima (2017). "Monitoring and Measuring Autophagy." Int J Mol Sci **18**(9).
Yu, L., Y. Chen and S. A. Tooze (2018). "Autophagy pathway: Cellular and molecular mechanisms." Autophagy **14**(2): 207-215.
Zachari, M. and I. G. Ganley (2017). "The mammalian ULK1 complex and autophagy initiation." Essays Biochem **61**(6): 585-596.
Zarate, Y. A., J. R. Jones, M. A. Jones, F. Millan, J. Juusola, A. Vertino-Bell, G. B. Schaefer and M. C. Kruer (2016). "Lessons from a pair of siblings with BPAN." Eur J Hum Genet **24**(7): 1080-1083.
Zavodszky, E., M. N. Seaman, K. Moreau, M. Jimenez-Sanchez, S. Y. Breusegem, M. E. Harbour and D. C. Rubinsztein (2014). "Mutation in VPS35 associated with Parkinson's disease impairs WASH complex association and inhibits autophagy." Nat Commun **5**: 3828.

Zhang, H., D. Z. Qian, Y. S. Tan, K. Lee, P. Gao, Y. R. Ren, S. Rey, H. Hammers, D. Chang, R. Pili, C. V. Dang, J. O. Liu and G. L. Semenza (2008). "Digoxin and other cardiac glycosides inhibit HIF-1alpha synthesis and block tumor growth." Proc Natl Acad Sci U S A **105**(50): 19579-19586.
Zhao, Y. G., L. Sun, G. Miao, C. Ji, H. Zhao, H. Sun, L. Miao, S. R. Yoshii, N. Mizushima, X. Wang and H. Zhang (2015). "The autophagy gene Wdr45/Wipi4 regulates learning and memory function and axonal homeostasis." Autophagy **11**(6): 881-890.
Zhou, C., G. Yang, M. Chen, L. He, L. Xiang, C. Ricupero, J. J. Mao and J. Ling (2015). "Lhx6 and Lhx8: cell fate regulators and beyond." Faseb j **29**(10): 4083-4091.
Zhou, T., C. Benda, S. Dunzinger, Y. Huang, J. C. Ho, J. Yang, Y. Wang, Y. Zhang, Q. Zhuang, Y. Li, X. Bao, H. F. Tse, J. Grillari, R. Grillari-Voglauer, D. Pei and M. A. Esteban (2012). "Generation of human induced pluripotent stem cells from urine samples." Nat Protoc **7**(12): 2080-2089.
Zhu, B. and S. K. Murthy (2013). "Stem Cell Separation Technologies." Curr Opin Chem Eng **2**(1): 3-7.
Zhu, Y., G. Runwal, P. Obrocki and D. C. Rubinsztein (2019). "Autophagy in childhood neurological disorders." Dev Med Child Neurol **61**(6): 639-645.

7. APPENDIX

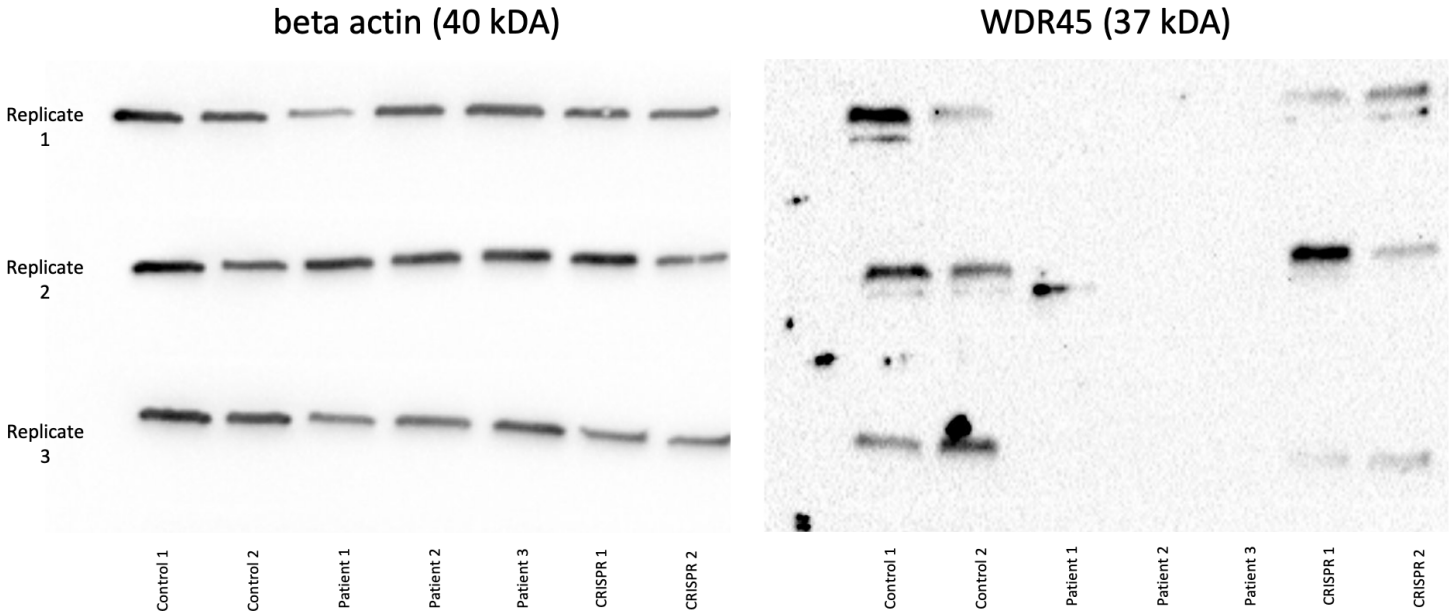

Appendix Figure 1. WDR45 western blotting on Day 65 neurons. *All 3 biological replicates tested are shown (n=3). Beta actin (as loading control) is shown on the left, whereas WDR45 bands on the right. Despite the occasional unequal loading and the WDR45 antibody (used at 1:200 dilution) leading to production of weak bands, it is clear that there WDR45 is present in both Controls 1 and 2 but absent in all three patient lines. This absence of expression is corrected in the isogenic controls CRISPR 1 and CRISPR 2. For this image to be produced, membrane strips were cut between approximately 25kDA and 75kDA and imaged together on an ImageQuant chemilumenscent imaging system (GE). Images were exported to .tiff format prior to quantification of band intensities with ImageJ/Fiji software.*